Diffusion of sorbed cations in clays: Development, improvement and application of new and existing models

Inauguraldissertation
der Philosophisch-naturwissenschaftlichen Fakultät
der Universität Bern

vorgelegt von

Philipp Krejci

aus Deutschland

Leiter der Arbeit:
PD Dr. Thomas Gimmi
Institut für Geologie, Universität Bern und Paul Scherrer Institut

Co-Leiter der Arbeit:
Dr. Luc R. Van Loon
Labor für Endlagersicherheit, Paul Scherrer Institut

Diffusion of sorbed cations in clays: Development, improvement and application of new and existing models

Inauguraldissertation
der Philosophisch-naturwissenschaftlichen Fakultät
der Universität Bern

vorgelegt von

Philipp Krejci

aus Deutschland

Leiter der Arbeit:
PD Dr. Thomas Gimmi
Institut für Geologie, Universität Bern und Paul Scherrer Institut

Co-Leiter der Arbeit:
Dr. Luc R. Van Loon
Labor für Endlagersicherheit, Paul Scherrer Institut

Von der Philosophisch-naturwissenschaftlichen Fakultät angenommen.

Bern, 03.03.2023

Der Dekan
Prof. Dr. Marco Herwegh

Acknowledgments

First and most importantly, I want to thank PD Dr. Thomas Gimmi for his outstanding supervision. He gave me the space to conduct my research independently, while he was there for giving me advice, when needed, and always made time for having very helpful discussions. Throughout the thesis we had a very pleasant and constructive work relationship.

Many thanks go to my co-supervisor Dr. Luc Van Loon, who answered all my questions about experiments, provided me with experimental data and gave helpful input to improve this thesis.

I am very grateful to Prof. Dr. Sergey Churakov, who was of great support in designing chapter 5. His constructive and analytical comments and advice on manuscripts and simulations definitely helped to improve this thesis.

I also want to thank Dr. Martin Glaus for having fruitful discussions and giving helpful insights into experiments and modeling, Dr. Wilfried Pfingsten for specific and general advice in all kind of things, Dr. Bart Baeyens for discussions about cation adsorption, Dr. Nikolaos Prasianakis for his support, Dr. Konstantinos Karalis for his help with molecular dynamics simulations, Dr. Peter Alt-Epping for sharing his knowledge about Flotran, and Dr. Dan Miron for helpful input and discussions, that improved my work.

I am happy that I was a part of the great community of PhD students and Postdocs at LES. We shared a lot of good moments together. I also want to thank all other LES members for making my time at PSI enjoyable.

Finally, I want to thank my parents and my sister, who were of great support and without whom I would not be where and who I am today, my friends who were always there for me, and last but not least, my partner and love Tonja, she is the best.

Financial support:

Financial support for the project by the Swiss National Science Foundation (grant no. 200021_166287) is kindly acknowledged.

Abstract

Clays and clay rocks play an important part in the foreseen multi-barrier system of the Swiss radioactive waste repository. The understanding of the transport behavior of ions through clays and clay rocks is crucial to assess the long-term safety of clay barrier systems. A low permeability and a high capacity to adsorb positively charged contaminants make clays and clay rocks suitable materials for such barriers. Many experimental studies revealed that diffusion of cations and anions in clays cannot be explained by pore diffusion alone, as diffusion coefficients derived from experiments were higher for cations and lower for anions than expected for pure pore diffusion. These observations can be attributed to the interactions of cations and anions with the negatively charged clay surfaces. Anions are (partially) excluded from the pore space close to the clay surfaces, while cations are enriched and maintain a certain mobility. These phenomena are called anion exclusion and surface diffusion.

The latter is subject to detailed investigations in this thesis. The main focus of this thesis lies on the development of new reactive transport models for the diffusion of sorbed cations in clays and their application to experimental data. The goal is to gain further insights into the diffusion processes of cations at the clay surfaces. The different modeling approaches used in this thesis are briefly summarized below.

A multi-site surface diffusion model was implemented in the continuum-scale reactive transport code Flotran (chapter 2). This model accounts for pore and surface diffusion by combining their contributions in a single diffusion coefficient that includes surface mobilities as model parameters. The surface mobilities are a measure of how mobile sorbed cations on different adsorption sites are compared to those in bulk pore water. They are used as fit parameters to match experimental data. This model was applied to diffusion data of Cs in Opalinus Clay (chapter 2). A set of surface mobilities could be derived, which describe the concentration-dependent diffusion of Cs consistently over a large range of Cs concentrations. The model results revealed that Cs remains a significant mobility on the so-called frayed-edge sites. The model was then also successfully applied to Na and Sr diffusion in Opalinus Clay (chapter 4), and to Na, Sr and Cs diffusion in Volclay bentonite (chapter 3) using a one-site cation exchange model with a respective cation-specific mobility. However, it became clear that the derived mobilities are not universal parameters, but are dependent on the specific experimental conditions (e.g., ionic strength).

A more detailed model that accounts for diffusion in ‘free’ pore water, in the diffuse layer, in the Stern layer and in interlayers (DL-SL-IL model) was implemented in Flotran (chapter 3). The model is parametrized by data of the clay microstructure and mobilities of cations in the Stern layer and in the interlayers. From this model, a combined diffusion coefficient can be derived, which can be directly compared to experimentally determined diffusion coefficients. Predictions of the DL-SL-IL model for Na, Sr and Cs diffusion were compared to experimental data of Volclay bentonite (chapter 3) and Opalinus Clay (chapter 4). The results of the comparison showed that the DL-SL-IL model is capable of predicting diffusion coefficients of cations under varying bentonite dry density as well as for different Opalinus Clay samples with different pore waters.

Molecular dynamics simulations were performed in order to investigate the mobility of Cs at illite edge surfaces (chapter 5). The simulations were carried out using the code LAMMPS. Various adsorption sites for Cs in the edge region could be identified. Constrained forces MD simulations were used to calculate the potential of mean force at the different sites, from which activation energies and attempt frequencies were determined. The latter were used as input for a jump diffusion model. Based on an effective medium approach a jump diffusion coefficient of Cs at the various illite edge surface sites was

calculated. A comparable but somewhat larger mobility of Cs on the illite edges was found than the mobility on the frayed-edge sites determined in chapter 2.

Table of Contents

Chapter 1:
Introduction

1 Background and significance

In September 2022, the Swiss National Cooperative for the Disposal of Radioactive Waste (Nagra) announced its proposal for the site of a deep geological nuclear waste repository. Nagra argued that the location 'Nördlich Lägern' is best suited because of its geological properties. The nuclear waste repository is proposed to be built in the Opalinus Clay formation several hundred meters below the surface. Opalinus Clay is an argillaceous rock which exhibits a very low permeability, a high sorption capacity and the ability to self-seal fissures (Nagra, 2002). The Opalinus Clay formation is sandwiched by geological confining units, summarized as 'Brauner Dogger' and the 'Effingen Member' of the Wildegg Formation above and the Staffelegg and Klettgau Formations below (Nagra, 2014a). The confining units consist mainly of marl and claystones, partly also of limestones and sandstones, which still exhibit low permeability but larger than that of Opalinus Clay. They increase the distance between the Opalinus Clay Formation and water-conducting aquifers that may act as potential exfiltration paths. Several other countries consider deep geological repositories as their preferred concept for storage of nuclear waste, *inter alia* France (Callovo-Oxfordian clay formation), Belgium (Boom Clay) and Finland (crystalline bedrock).

According to the current plans, the Swiss nuclear waste repositories for high-level and low- and intermediate-level waste may share common access and surface infrastructure. The high-level waste repository mainly contains spent fuel assemblies from nuclear power plants and vitrified high-level waste from reprocessing, i.e., from the recycling of spent fuel, which has been prohibited after the revision of the Nuclear Energy Act (The Federal Assembly of the Swiss Confederation, 2003) in 2018 (Nagra, n.d.). Its radiotoxicity will reach natural background radiation levels after a million of years of storage. Low- and intermediate-level waste contain contaminated material from nuclear power plants, other industries, medicine and research. Its radiotoxicity will decay to the level of background radiation within hundred of thousands of years.

In the repository, the radioactive waste will be isolated from the environment by a multi-barrier system, which includes natural and engineered barriers (Nagra, 2002, 2014b). Spent fuel assemblies and high-level waste from reprocessing are confined in steel canisters, which prevent the release of radionuclides for several thousands of years. The steel canisters are disposed of in tunnels, that are back-filled by highly compacted bentonite, which creates a buffer around the steel canisters. Bentonite contains large amounts of swelling clay minerals, notably montmorillonite; it has a very low permeability, and it expands when in contact with water and therefore has the ability to seal potential fractures. Intermediate- and low-level waste is embedded in a cement matrix within steel drums. The drums are placed in concrete containers. The last barrier in the multi-barrier system is the host rock, that is, the Opalinus Clay itself. It is mostly relevant for the long-term safety and stability of the repository system, by providing geochemically favorable and stable conditions. These engineered and natural barriers have to prevent or sufficiently delay the release of radionuclides into surface-near regions of the geosphere, where the environment and humanity are at risk of exposure and contamination.

2 Aim of the thesis

In order to assess the safety of the radioactive waste repository concept, it is crucial to understand and quantify the relevant transport processes of radionuclides in the various materials, which include cement, the bentonite buffer material and the host rock Opalinus Clay. Focusing on the clayey materials in this thesis, these processes depend, among other things, on the clay structure, on the interactions of the radionuclides with the clay surfaces, on the pore water chemistry, on the specific transport properties of the radionuclides, as well as on any further chemical reactions of the radionuclides. Insightful knowledge about the relevant chemical and physical processes can be gained by conducting adequate laboratory or in-situ experiments. The data obtained in the experiments can then be the basis of representative theoretical and numerical models, which, in the ideal case, accurately describe the transport behavior of radionuclides in clays and allow for a well-founded statement about the long-term safety of the nuclear waste repository.

In this thesis the transport of sorbing tracers (that serve as analogues for relevant radionuclides) through clays is investigated with the help of reactive transport models, in particular, with the focus on advancing the understanding of the aspect and relevance of surface diffusion of cations in clays.

The objectives of this thesis are:

- the development of new models for cation transport in clays and their implementation in reactive transport codes
- the comparison of different model concepts
- the application of new and existing model approaches to experimental data
- derive consistent sets of model parameters for cation diffusion that can be used under various experimental conditions
- provide further insights into the processes of cation diffusion at the clay surfaces
- increase the reliability of long-term predictions of cation transport through clay barriers

3 Clay properties

3.1 Clay structure

The Association Internationale pour l'Etude des Argiles (AIPEA) and the Clay Minerals Society (CMS) define clay as "*... a naturally occurring material composed primarily of fine-grained minerals, which is generally plastic at appropriate water contents and will harden when dried or fired ...*" (Guggenheim et al., 1995). Clays usually contain phyllosilicates, but may also contain other materials (e.g., organic matter). Clay particle sizes are defined (depending on discipline) to be smaller than 1-4 µm, and often a limit of 2 µm is used. Clays can be major constituents of rocks, sedimentary deposits and weathering products of primary silicate minerals (Bergaya and Lagaly, 2006). Clay minerals are phyllosilicate minerals, which impart plasticity and harden upon drying or firing (Guggenheim et al., 1995). Clay minerals can be natural or synthetic.

Opalinus Clay, for example, contains mainly clay minerals such as illite, kaolinite, chlorite and illite/smectite mixed layers, as well as other constituents, such as calcite, siderite and quartz (Nagra, 2002). With respect to the nuclear waste disposal planned in Switzerland, the clay minerals illite and montmorillonite (smectite group) are of special interest. Illites and smectites in Opalinus Clay are the minerals that dominate the sorption behavior of cations (Bradbury and Baeyens, 2000; Van Loon et al., 2009). Montmorillonite is the main constituent of the bentonite buffer material.

Both illite and montmorillonite have a TOT layer structure. The TOT layer consists of one octahedral sheet (O) sandwiched by two tetrahedral sheets (T) with a thickness of about one nanometer. In the octahedral sheet, octahedra formed by metal cations (Al^{3+}) coordinated with six oxygen are connected through shared edge oxygen with neighboring octahedra. The tetrahedral sheets consist of tetrahedra of a metal cation (Si^{4+}) in coordination with four oxygen atoms. Neighboring tetrahedra are connected by sharing corner oxygen.

The idealized structural formula of the illite and montmorillonite layers is $Si_4Al_2O_{10}(OH)_2$. The replacements of octahedral Al^{3+} by Fe^{3+}, Mg^{2+} or Fe^{2+} and of tetrahedral Si^{4+} by Al^{3+} or Fe^{3+} are called isomorphic substitutions. Montmorillonite exhibits predominately octahedral isomorphic substitutions, while illite has isomorphic substitutions in the octahedral and predominantly in the tetrahedral sheets. A net negative surface charge arises from these isomorphic substitutions. For montmorillonite this charge ranges between 0.2 and 0.6 $mol_c\ mol^{-1}$, for illite between 0.6 and 0.9 $mol_c\ mol^{-1}$ (Brigatti et al., 2006). This charge is compensated by (more or less strongly bound) cations on the mineral surfaces. Depending on the clay mineral, some or most of these cations can be exchanged by other cations in the pore solution in exchange reactions. The total charge compensated at the clay mineral surfaces by exchangeable cations is called cation exchange capacity (CEC).

Clay particles are composed of stacks of clay layers. Illite particles typically contain 5-20 stacked layers (Tournassat et al., 2015). Stack sizes of smectite/montmorillonite particles were reported between 3-5 (Pusch, 2001) layers per clay particle for compacted Na-montmorillonite and 6-8 (Matusewicz et al., 2013) layers per clay particle for compacted Ca-montmorillonite.

The space between two stacked clay layers is called interlayer. Montmorillonite is a swelling clay mineral, meaning that the interlayers are able to take up water and expand. Discrete interlayer distances of one, two, three and even four (average) water layers in the montmorillonite interlayers were found in several studies (e.g., Holmboe et al., 2012; Ohkubo et al., 2016, 2021). The distribution of these discrete steps varies with clay dry density and pore water chemistry (ionic strength and type of background cations). Interlayer distances decrease with increasing dry density, cation valence and

ionic strength. The discrete swelling behavior is referred to as crystalline swelling and is probably related to hydration of interlayer cations (Chen et al., 2022). Norrish (1954) found a continuous increase of interlayer distances up to 40 Å for Li^+ and Na^+ montmorillonite with increasing water content. This swelling behavior is called osmotic swelling. Illite is a non-swelling clay mineral meaning that illite interlayers are anhydrous. The net negative surface charge in illite interlayers is typically compensated by K^+ ions, which are generally considered as not or not easily exchangeable. The comparably strong binding is attributed to the location of the clay charge in the T layer as well as a good fit of the K^+ ions into the hexagonal cavities of the T layers.

The total porosity of a clay is composed of water filled volumes in the interlayer spaces and in the spaces between single and aggregated clay particles. The porosity of a clay can be calculated from the clay bulk density ρ_{bd} and the clay mineral grain density ρ_s:

$$\epsilon = 1 - \frac{\rho_{bd}}{\rho_s} \quad (1)$$

It is an important continuum-scale parameter that is related to permeability and diffusivity of clay in continuum-scale transport models. The mobility of solvents and solutes depends, however, also on sub-scale properties, such as the distribution of the clay pore water to different pore environments.

3.2 Cation adsorption

3.2.1 Empirical relations

Adsorption of ions is related to specific physical and chemical interaction with the structural units at the mineral surface. Cations can sorb onto clay minerals at different sorption sites. At the basal planes of interlayer and external surfaces, where cations compensate the negative surface charge, cations are readily exchangeable (Tournassat et al., 2015). These sites have the highest capacity for cation adsorption. Cations can also sorb onto the edges of clay particles. Here, cations exhibit different sorption behavior. While very selective Cs sorption onto illite frayed-edge sites at the entrance of anhydrous interlayers is explained by its large ionic radius and low hydration energy (Bradbury and Baeyens, 2000; Brouwer et al., 1983; Poinssot et al., 1999; Sawhney, 1972), the adsorption of transition metals such as Ni, Zn or Co onto clay edges shows a pH dependency explained by protonation/deprotonation of edge surface functional OH-groups (Bradbury and Baeyens, 1997; Churakov and Dähn, 2012; Kéri et al., 2020; Montoya et al., 2018).

Commonly batch experiments are carried out to determine cation adsorption in clays. Dispersed or compacted clay samples are equilibrated with pore solutions with different predefined cation concentrations. From experiments with different cation pore water concentrations the corresponding sorbed cation concentrations can be determined. The resulting relationship between the cation concentration sorbed onto the clay mineral and the concentration in solution is called adsorption isotherm. The empirical adsorption behavior displayed through adsorption isotherms is often described by cation exchange reactions.

A general cation exchange reaction between cations A and B with their respective charges z_A and z_B onto a surface sorption site $\equiv S$ can be written as:

$$\equiv S - z_B A^{z_A} + z_A B^{z_B} \Leftrightarrow \equiv S - z_A B^{z_B} + z_B A^{z_A} \quad (2)$$

The corresponding mass action law can be described for example according to the Gaines-Thomas convention (Gaines and Thomas, 1953):

$$ {}^{k}_{1}K_c = \frac{N_k^{z_1} a_1^{z_k}}{N_1^{z_k} a_k^{z_1}} \quad (3) $$

where ${}^{k}_{1}K_c$ is the selectivity coefficient of cation k with respect to the reference cation 1, z is the cation charge, N is the fractional occupancy on the exchanger solid, i.e., the moles charge of cation k on the exchanger per cation exchange capacity, and a is the cation activity in solution. Several other definitions of the selectivity coefficient have been developed (e.g., Gapon, 1933; Vanselow, 1932). For alkali metals selectivity coefficients increase in the sequence Li < Na < K < Rb < Cs (i.e., with decreasing hydration energy and increasing ionic radius of the cation).

Cation exchange in clays has been extensively studied (e.g., Bradbury and Baeyens, 2000a; Brouwer et al., 1983; Elprince et al., 1980; Lewis, 1949; Missana et al., 2014; Shainberg et al., 1987). Sorption of Na and Sr in Opalinus Clay determined in batch sorption experiments of dispersed samples and in through- and out-diffusion experiments of compacted samples were found to be in very good agreement (Van Loon et al., 2005). However, Maes et al. (2008) found that batch sorption overestimated Cs sorption in Boom Clay compared to results of Cs migration experiments. Cs sorption in Opalinus Clay was found to be identical for batch experiments with dispersed (crushed) and with intact clay samples (Van Loon et al., 2009). Van Loon and Glaus (2008) found Cs sorption in compacted Volclay bentonite to increase with bentonite dry density. In comparison to batch sorption experiments on dispersed samples, the compacted samples exhibited higher Cs sorption. This was explained with changes in the thermodynamics of ion exchange at different degrees of mechanical compaction, i.e., with the tendency of Cs with a lower hydration energy than Na to preferably occupy smaller interlayer pore spaces.

The cation exchange reactions with the corresponding selectivity coefficients are a rather simple and practical method to describe cation adsorption at clay mineral surfaces. The selectivity coefficients depend on the geochemical conditions and can vary with different pore water composition and different type of clay.

3.2.2 Theoretical models

More detailed models of cation adsorption exist. These models consider the electrostatic interactions between charged ions and the negatively charged clay surfaces. The region at the water-clay interface, where cations adsorb, can be divided into a so-called Stern layer and a diffuse layer. This structure (Stern layer and diffuse layer) has been more or less confirmed by molecular dynamics studies for smectite or montmorillonite (Bourg and Sposito, 2011; Tinnacher et al., 2016) and illite (Lammers et al., 2017). The first layer (closest to the surface) represents the Stern layer. Here, cations form both outer-sphere complexes and inner-sphere complexes that compensate a part of the negative surface charge. Outer-sphere complexes form mainly because of electrostatic forces or ion pairing (Dzombak and Hudson, 1995), while inner-sphere complexes are formed by more specifically adsorbed cations (without intervening water molecules). The second layer is the diffuse layer. Here, the remaining surface charge (not compensated in the Stern layer) is balanced by a swarm of cations, which are electrostatically attracted towards the surface, but at the same time tend to diffuse away from the surface. The concentrations of cations in the diffuse layer increase approximately exponentially with proximity to the surface, while anion concentrations decrease. The concentrations of cations and anions in the diffuse layer can be related to their concentration in the bulk solution by the Boltzmann equation. Classical diffuse double-layer models, as the Gouy-Chapman model (e.g., Bolt, 1979a, 1979b), do not include adsorption in the Stern layer and the total negative surface charge is considered to be compensated in the diffuse layer. The Gouy-Chapman model describes the balance of thermal forces and the long range electrostatic interactions of cations and anions with the surface, which are caused

by the negative electrostatic potential, via the Poisson-Boltzmann equation. This theory has been modified to account for the finite size of ions by shifting the origin of the diffuse layer by one ion radius away from the surface (Carnie and Torrie, 1984; Tournassat et al., 2009). The Gouy-Chapman model alone cannot sufficiently describe cation adsorption in clays (Dzombak and Hudson, 1995), because different selectivities of cations with identical charge cannot be explained. Triple-layer models (Davis et al., 1978; Leroy et al., 2007; Revil et al., 2005) do account for specific adsorption of cations in the Stern layer. Such models as well as other physico-chemical models (Dzombak and Hudson, 1995), which link diffuse layer sorption with surface complexation models, can account for overall observed ion selectivities.

4 Reactive transport in clays

The continuum representation of porous media is very helpful when describing reactive transport at a macroscopic scale, including diffusion experiments with characteristic dimensions in a range from millimeter to meter. At the continuum scale, the true heterogeneous structure of a porous medium (e.g., the complex distribution of solid and fluid phases) is not explicitly considered. Instead, all equations and parameters are defined at a larger scale, termed representative elementary volume (REV) scale, where averaged physical and chemical properties such as phase fractions, permeability, diffusion coefficients for the entire porous medium, or sorption capacities apply. Transport of fluids and solutes and their interaction with rocks is then quantitatively described by differential equations based on an idealization of the real physical system (Lichtner, 1996).

Transport of solutes in porous media in the water phase in one dimension can be described by advection (J_{adv}), dispersion (J_{disp}) and diffusion (J_{diff}) (e.g., Steefel and Maher, 2009). The total mass flux J_{tot} is written as:

$$J_{tot} = J_{adv} + J_{disp} + J_{diff} \tag{4}$$

The advective flux is:

$$J_{adv} = \epsilon C v \tag{5}$$

where ϵ is the porosity of the medium, C is the solute concentration in the pore water and v is the average linear velocity in the medium, which is usually expressed by the Darcy velocity $q = v/\epsilon$.

Mechanical dispersion accounts for the heterogeneity of flow pathways in porous media. It is scale-dependent and typically described by the empirical dispersivity factor α. The contribution of mechanical dispersion is:

$$J_{disp} = -\alpha v \frac{\partial C}{\partial x} \tag{6}$$

where $\partial C/\partial x$ is the concentration gradient.

The diffusive flux is described by Fick's first law:

$$J_{diff} = -D_e \frac{\partial C}{\partial x} \tag{7}$$

where D_e is the effective diffusion coefficient:

$$D_e = \frac{\epsilon}{G} D_0 \tag{8}$$

Here, D_0 is the self diffusion coefficient in bulk water and G is the geometrical factor. The geometrical factor accounts for constricted and tortuous pathways of solutes caused by the complex pore geometry.

Because clay rocks (Gimmi et al., 2007; Mazurek et al., 2011; Yu et al., 2018) and bentonite (Pusch, 2006) exhibit very low hydraulic conductivity (10^{-10}-10^{-15} m s^{-1}) advective-dispersive transport is negligible under natural gradients, and the only relevant transport process is diffusion.

The mass balance when considering diffusion and adsorption is expressed by:

$$\left(\epsilon + \rho_{bd} \frac{\partial S}{\partial C}\right) \frac{\partial C}{\partial t} = \frac{\partial}{\partial x} \left(\varepsilon \frac{D_0}{G}\right) \frac{\partial C}{\partial x} \tag{9}$$

Here, ρ_{bd} is the bulk dry density of the clay and S is the concentration of a solute sorbed on the clay surfaces (moles per mass of dry solid). The derivative $\partial S/\partial C$ describes the relationship between the concentration in bulk water and the sorbed concentration. Sorption can involve ion exchange or surface complexation reactions, and it can be described by corresponding equations or by a measured adsorption isotherm.

For linear sorption $\partial S/\partial C$ equals the distribution coefficient R_d and the rock capacity factor can then be defined as

$$\alpha = \epsilon + \rho_{bd} R_D \tag{10}$$

The apparent diffusion coefficient describes the transient diffusion behavior of a sorbing species, for example at the beginning of a diffusion experiment with about constant boundary conditions before the system reaches a steady-state. It is calculated by dividing the effective diffusion coefficient by the rock capacity factor:

$$D_a = \frac{D_e}{\alpha} \tag{11}$$

Typically, when through-diffusion experiments in clays are evaluated with the classical Fickian law (Eq. (7)) and the rock capacity α and the effective diffusion coefficient D_e are fitted to the data.

In natural, complex pore waters as in Opalinus Clay, where ions of different charge and with different self-diffusion coefficients are present, the diffusion of a single ion is influenced by all other diffusing ions because of electrostatic interactions. The so-called multi-component transport of ions can be accounted for by applying the Nernst-Planck equation. In a system where no net current occurs, the diffuse flux of an ion *i* is (Appelo and Wersin, 2007; Tournassat and Steefel, 2015):

$$J_i = -D_{e,i}\frac{\partial C_i}{\partial x} + z_i C_i D_{e,i}\frac{\sum_j z_j D_{e,j}\frac{\partial C_j}{\partial x}}{\sum_j z_j^2 D_{e,j} C_j} \tag{12}$$

The first term of the right hand-side corresponds to Fickian diffusion (Eq. (7)) and the second term accounts for an additional migration of an ion *i* caused by the electrostatic effects between ion *i* and all other ions *j*. This electrochemical migration term depends on the charge of ion *i* and the charges, concentrations, concentration gradients and diffusion coefficients of all other ions. Depending on the geochemical conditions, the flux resulting from electrochemical migration adds to or subtracts from the diffusive flux. A mass balance equation including electrochemical migration can be written analogously to Eq. (9):

$$\left(\epsilon + \rho_{bd}\frac{\partial S_i}{\partial C_i}\right)\frac{\partial C_i}{\partial t} = \frac{\partial}{\partial x}\left(-D_{e,i}\frac{\partial C_i}{\partial x} + z_i C_i D_{e,i}\frac{\sum_j z_j D_{e,j}\frac{\partial C_j}{\partial x}}{\sum_j z_j^2 D_{e,j} C_j}\right) \tag{13}$$

5 Transport codes

The transport of radionuclides in clays can be calculated by solving Eq. (9) or Eq. (13) numerically. In this thesis, the reactive transport code Flotran (Lichtner, 2007) was used to model the reactive transport of cations at the continuum scale. Flotran is capable of calculating multi-component (species-dependent transport properties solved by the Nernst-Planck equation), multiphase (in liquid and gas phase), non-isothermal (temperature dependent) and reactive (chemical and mineralogical reactions) transport. Flotran uses a finite difference scheme (discretization in time and space) to solve the advection-diffusion equation with the option to choose between implicit, explicit and operator splitting solution methods. The chemical reactions include homogeneous aqueous equilibrium reactions, redox reactions, mineral precipitation/dissolution reactions and ion exchange reactions. Gimmi and Alt-Epping (2018) showed that Flotran (or any other code that includes multi-component transport) can be extended to calculate transport in a Donnan layer (similar to a diffuse layer) by introducing an immobile negative charge as solution species. The negatively charged immobile species create a mean negative potential (Donnan potential) over a specific diffuse or Donnan layer volume, which in turn leads to exclusion of anions and enrichment of cations from this Donnan layer.

Several other transport codes have been developed, which are comparable to Flotran. A comprehensive overview over these transport codes and their capabilities is found in Steefel et al. (2015). Here, two other transport codes are highlighted, namely PHREEQC (Parkhurst and Appelo, 2013) and CrunchFlow (Steefel, 2009). Both codes are capable of considering transport of ions in a Donnan (or diffuse) layer. They use a dual continuum approach, where the total porosity of the clay is split into a charge-neutral bulk water porosity and a Donnan layer porosity. The average ion concentrations in the Donnan layer are explicitly calculated in these codes by calculating the mean electrostatic (Donnan) potential from balancing the charges.

6 Diffusion coefficients of ions in clays

Through-diffusion (e.g., Tachi and Yotsuji, 2014) and in-diffusion (e.g., Van Loon and Müller, 2014) experiments are the two most common methods to measure diffusion of tracers in clays. Also, other techniques such as out-diffusion (Jakob and Spieler, 1999) or a closed cell (Shackelford, 1991) can be used to measure diffusion in clays.

In through-diffusion set-ups a clay sample is sandwiched by two filters and connected to two pore solution reservoirs. The pore solution in the upstream reservoir is spiked with the tracer of interest. The tracer concentration in the upstream boundary is either kept constant (regular exchange with the same pore solution including the tracer) or is variable as a result of diffusive transport (no exchange of pore solution). At the downstream reservoir the tracer concentration is kept at approximately zero by exchanging the reservoir regularly with fresh pore solution. The flux at the downstream boundary and, if not kept constant, the concentration in the upstream reservoir are measured. In addition, the tracer profile can be measured at the end of the experiment, which gives information on the final spatial distribution of a tracer in the clay sample.

In in-diffusion experiments the clay sample is in contact with a single reservoir, which is spiked with the tracer of interest. The tracer diffuses into the clay sample due to the concentration gradient. The decrease of tracer concentration in the reservoir is measured. Additionally, the tracer concentration profile can be measured, for example by abrasive peeling (Van Loon and Eikenberg, 2005).

The evaluation of through-diffusion experiments is typically based on Fick's Law (Eq. (7)), and D_e and α are fitted to the experimental data by applying numerical (i.e., application of transport codes) or analytical (Crank, 1975; Shackelford, 1991) solutions for the different set-ups. The advantage of using more sophisticated (reactive) transport codes in the evaluation of diffusion experiments is that the pore water chemistry (speciation calculation of aquatic complexes) and tracer-clay interaction (non-linear sorption) can be considered explicitly.

One difficulty in the evaluation of diffusion experiments arises from the filters used in experiments. Stainless steel filters, for example, have a non-negligible diffusive resistance, which is different for fresh or used filter discs, probably because of partial clogging of some of the filter pores with clay particles during the experiments (Glaus et al., 2008). Another difficulty is that the application of a zero-concentration boundary condition for strongly sorbing tracers may be an oversimplification. It can lead to an underestimation of diffusion coefficients when compared to an explicit consideration of a time-dependent boundary concentration according to measured values at the downstream boundary (Glaus et al., 2015). Furthermore, for samples of swelling clay minerals, higher water contents and therefore lower clay bulk dry density have been found near the inlet and outlet boundaries, which also influence the determination of tracer diffusion coefficients (Glaus et al., 2011; Van Loon et al., 2007).

The diffusion of water, anions and cations in clays and clay rocks has been extensively investigated in numerous studies (Appelo et al., 2010; Fukatsu et al., 2021; Glaus et al., 2007, 2011; González Sánchez et al., 2008; Maes et al., 2008; Melkior et al., 2009; Melkior et al., 2005; Tachi and Yotsuji, 2014; Tournassat and Appelo, 2011; Van Loon et al., 2003; Wersin et al., 2008; Wigger and Van Loon, 2017, 2018). It was generally found that anion fluxes were decreased compared to the fluxes of water tracers, while fluxes of cations were increased. This results in comparably lower effective diffusion coefficients for anions and larger effective diffusion coefficients for cations when applying Fick's law. Gimmi and Kosakowski (2011) analyzed cation diffusion data in clays and clay rocks with a surface diffusion model. Their findings show that cations considered to be sorbed exhibit an ion-specific mobility at the clay surfaces. They did not differentiate between diffuse layer and Stern layer diffusion. A

comprehensive summary and analysis of experimental diffusion data of water, anion and cations in clays and clay rocks is found in Bourg and Tournassat (2015). Their compilation of diffusion data shows that apparent diffusion coefficients of water, anions and cations decreased with increasing clay dry density. The diffusion accessible porosity of water determined in diffusion experiments agrees very well with porosity calculations based on measured densities (so-called pycnometer porosities, Eq. (1)). The anisotropy in clays (ratio of diffusion coefficients parallel to bedding and normal to bedding) increases with increasing clay dry density. The anion accessible porosity increases with increasing ionic strength of the pore water, which is in agreement with the diffuse layer theory. No influence of the ionic strength on the apparent diffusion coefficients of cations were found.

The phenomena of decreased anion diffusion and increased cation diffusion are referred to as anion exclusion and surface diffusion. They can be explained by the interactions of negatively charged anions and positively charged cations with the negatively charged clay surface, more specifically in the electrical double layer. Anion concentrations are depleted in the diffuse layer because of electrostatic forces (see section 2), which then results in a lower effective (anion accessible) porosity in the application of simple Fick's law, and a lower anion flux compared to that of a water tracer. Cation concentrations on the other hand are increased in the diffuse layer, which leads to an increased overall mass flux. Several studies were published that explicitly account for cation and/or anion diffusion in the diffuse layer. Tournassat and Appelo (2011) modeled anion exclusion in bentonite using a single porosity (Birgersson and Karnland, 2009) and dual porosity (Appelo et al., 2010) Donnan approaches. Based on an integrated diffusion and sorption model of Ochs et al. (2001), which accounts for electrostatic and viscoelectric effects, Tachi and Yotsuji (2014) modeled I, Na and Cs diffusion in Na-montmorillonite. The same model was used by Fukatsu et al. (2021) to model Na and Cs diffusion in Ca-montmorillonite, but they additionally accounted for different interlayer pore sizes. Appelo et al. (2010) modeled anion and cation diffusion in Opalinus Clay using a dual porosity approach. However, different geometrical factors for different ions had to be applied to describe the experimental data. Soler et al. (2019) also used a dual porosity approach to investigate the ionic strength-dependent diffusion of anion and cations in a field experiment in Opalinus Clay. Larger diffusion coefficients in the diffuse layer had to be attributed to K and Cs, but not Na, Mg and Ca to match the experimental data. All of these studies had to make more or less well-founded assumptions of how much of the total surface charge is compensated in the diffuse layer, which affects the ion concentrations in the diffuse layer. Tinnacher et al. (2016) compared different diffuse layer models (dual porosity model of Appelo and Wersin (2007); single porosity models of Birgersson and Karnland (2009), Gonçalvès et al. (2007), Leroy and Revil (2004) and Tachi and Yotsuji (2014)) with respect to their ability to predict cation and anion diffusion on a (molecular) pore-scale and on the macroscopic scale. They found that only the dual porosity model of Appelo and Wersin (2007) can be consistent with their results on both scales, while all other single porosity models, which assume all pore water being diffuse layer water, cannot.

7 Molecular dynamics simulations of ion retention and transport

In the last decades molecular dynamics simulations were established as very useful techniques to investigate clay-water interactions in nanometer-sized pores. Molecular dynamics simulations can be applied to determine properties and structure of clay mineral surfaces and diffusive behavior of water and ions in the vicinity of the clay mineral surfaces. Molecular dynamics simulations have been used for instance to investigate the structural properties of the diffuse layer (Tournassat et al., 2009) and the Stern layer (Bourg et al., 2017), cation and water diffusion in smectite interlayer (Bourg and Sposito, 2010; Churakov, 2013; Holmboe and Bourg, 2014; Kosakowski et al., 2008), dehydration effects of smectite suspensions (Underwood and Bourg, 2020) and the adsorption behavior of Na and Cs onto illite particles (Lammers et al., 2017). They can support the interpretation of experimental data by contributing additional structural and thermodynamic information and explore research questions, for which no experimental data or measurement techniques exist (Churakov and Gimmi, 2011; Gimmi and Churakov, 2019).

Molecular dynamics simulations compute the thermodynamic and transport properties of a classical many-body system (Frenkel and Smit, 2002). The trajectory (the movement in space and time) of atoms is calculated by Newton's equation of motion. The interactions between atoms are determined by electrostatic forces (described by Coulomb's law), short-range van der Waals forces (for example described by the Lennard-Jones potential functions) and intramolecular forces, which arise from bond stretching and bending of atomic bonds. The parameters describing these forces are derived empirically from experimental crystal structure data or from ab initio methods, as Hartree-Fock or density functional theory, which solve the Schrödinger equation to obtain interaction energies and forces. The ClayFF force field (Cygan et al., 2004) has been proven to describe the above mentioned atom-atom interactions realistically and is therefore a widely used force field in clay science.

Molecular dynamics simulations describe the time-dependent evolution of atom positions and velocities, which can be linked via the application of statistical mechanics to time- and ensemble-averaged macroscopic thermodynamic properties of the system, such as for example pressure, temperature, volume and energy (Allen and Tildesley, 1987). The thermodynamic state of a system is uniquely defined by a set of extensive and intensive state variables referred to as statistical ensembles. The two most common statistical ensembles used in molecular dynamics studies investigating clay-water interactions are the NVT (constant number of particles embedded in a constant volume at constant temperature) and the NPT (constant number of particles under constant pressure and temperature) ensembles. Further thermodynamic and transport (e.g., self-diffusion coefficients) quantities of interest can be derived by analyzing the equilibrium trajectory of atoms and molecules in the system.

8 Motivation and outline

Until now, the modeling of cation diffusion in clays remains somewhat incomplete and inconsistent. Simple Fickian diffusion models are not able to describe the enhanced cation diffusion and decreased anion diffusion (compared to a water tracer) in a consistent way. More sophisticated models including cation diffusion in the diffuse layer do not predict experimental data at different clay bulk densities (Bourg and Tournassat, 2015). In addition, molecular dynamics studies (Bourg and Sposito, 2011; Tinnacher et al., 2016; Tournassat et al., 2009) showed that cations adsorbed in the Stern layer, as outer- or inner-sphere complex, as well as water in the Stern layer, maintain a certain mobility. So cations adsorbed in the Stern layer most likely contribute to the overall mass flux measured in diffusion experiments Their mobility should therefore be included when modeling cation diffusion in clays. However, the contribution of Stern layer diffusion has not received much attention and has rarely been considered in models yet. Therefore, there is a need to develop more complex models that include all relevant transport processes. Only in this way, a more consistent description of transport of different ions in clays might be possible.

In this thesis, transport codes were further developed in order to arrive at models for cation diffusion in clays that have a more predictive character. These models also provide insight into the significance of the different diffusion mechanisms or diffusion environments in clays at different environmental conditions (e.g., clay density, pore water chemistry).

As a first step, a multi-site surface diffusion model (Gimmi and Kosakowski, 2011) was implemented in the reactive transport code Flotran and applied to Cs diffusion in Opalinus Clay (Chapter 2). This model can account for the effects of varying Cs background concentrations on the Cs diffusion behavior. Then, a model which combines diffusion in the free bulk water, in a diffuse (Donnan) layer region, in the interlayer and in the Stern layer was developed and implemented in Flotran by combining the multi-site surface diffusion model (Chapter 2) with a Donnan approach for the diffuse layer (Gimmi and Alt-Epping, 2018). This combined model was then applied to HTO, Cl, Na, Sr and Cs diffusion data in Volclay bentonite (Chapter 3) and Opalinus Clay (Chapter 4). Results of Cs diffusion in Opalinus Clay showed that Cs seems to retain a certain mobility even when sorbed on frayed-edge sites, which was not obvious. In order to check the latter result at a more detailed level, the mobility of Cs on edges of illite clay particles was investigated in a molecular dynamics study using a jump diffusion model (Chapter 5).

References

Allen M. P. and Tildesley D. J. (1987). *Computer simulation of liquids*. Oxford University Press Inc, New York 1987.

Appelo C. A. J. Van Loon L. R. and Wersin, P. (2010). Multicomponent diffusion of a suite of tracers (HTO, Cl, Br, I, Na, Sr, Cs) in a single sample of Opalinus Clay. *Geochimica et Cosmochimica Acta* **74**(4), 1201–1219. https://doi.org/10.1016/j.gca.2009.11.013

Appelo C. A. J. and Wersin P. (2007). Multicomponent diffusion modeling in clay systems with application to the diffusion of tritium, iodide, and sodium in opalinus clay. *Environmental Science and Technology* **41**(14), 5002–5007. https://doi.org/10.1021/es0629256

Bergaya F., and Lagaly G. (2006). Chapter 1 General Introduction: Clays, Clay Minerals, and Clay Science. *Developments in Clay Science*, *1*(C), 1–18. https://doi.org/10.1016/S1572-4352(05)01001-9

Birgersson M., and Karnland O. (2009). Ion equilibrium between montmorillonite interlayer space and an external solution — Consequences for diffusional transport. *Geochimica et Cosmochimica Acta* **73**(7), 1908–1923. https://doi.org/10.1016/j.gca.2008.11.027

Bolt G. H. (1979a). Chapter 1: The Ionic Distribution in the Diffuse Double Layer. In *Developments in Soil Science* (Vol. 5, Issue PART B). https://doi.org/10.1016/S0166-2481(08)70656-1

Bolt G. H. (1979b). Chapter 3: Theories of Cation Adsorption by Soil Constituents: Distribution Equilibrium in Electrostatic Fields. In *Developments in Soil Science* (Vol. 5, Issue PART B). https://doi.org/10.1016/S0166-2481(08)70658-5

Bourg I. C., Lee S. S., Fenter P. and Tournassat C. (2017). Stern Layer Structure and Energetics at Mica-Water Interfaces. *Journal of Physical Chemistry* C **121**(17), 9402–9412. https://doi.org/10.1021/acs.jpcc.7b01828

Bourg I. C. and Sposito, G. (2010). Connecting the molecular scale to the continuum scale for diffusion processes in smectite-rich porous media. *Environmental Science and Technology* **44**(6), 2085–2091. https://doi.org/10.1021/es903645a

Bourg I. C. and Sposito G. (2011). Molecular dynamics simulations of the electrical double layer on smectite surfaces contacting concentrated mixed electrolyte (NaCl-$CaCl_2$) solutions. *Journal of Colloid and Interface Science* **360**(2), 701–715. https://doi.org/10.1016/j.jcis.2011.04.063

Bourg I. C. and Tournassat C. (2015). Self-Diffusion of Water and Ions in Clay Barriers. In *Developments in Clay Science* (Vol. 6). Elsevier. https://doi.org/10.1016/B978-0-08-100027-4.00006-1

Bradbury M. H. and Baeyens B. (1997). A mechanistic description of Ni and Zn sorption on Part II: modelling. *Journal of Contaminant Hydrology* **27,** 223–248. https://doi.org/10.1016/S0169-7722(97)00008-9

Bradbury M. H. and Baeyens B. (2000). A generalised sorption model for the concentration dependent uptake of caesium by argillaceous rocks. *Journal of Contaminant Hydrology* **42**(2–4), 141–163. https://doi.org/10.1016/S0169-7722(99)00094-7

Brigatti M. F., Galan E. and Theng B. K. G. (2006). Chapter 2 Structures and Mineralogy of Clay Minerals. *Developments in Clay Science*, *1*(C), 19–86. https://doi.org/10.1016/S1572-4352(05)01002-0

Brouwer E., Baeyens B., Maes A. and Cremers A. (1983). Cesium and rubidium ion equilibria in illite clay. *Journal of Physical Chemistry* **87**(7), 1213–1219. https://doi.org/10.1021/j100230a024

Carnie S. L. and Torrie G. M. (1984). The Statistical Mechanics of the Electrical Double Layer. In I. Prigogine and S. A. Rice (Eds.), *Advances in Chemical Physics* (pp. 141–253). https://doi.org/doi:10.1002/9780470142806.ch2

Chen W. L., Grabowski R. C. and Goel S. (2022). Clay Swelling: Role of Cations in Stabilizing/Destabilizing Mechanisms. *ACS Omega* **7**(4), 3185–3191. https://doi.org/10.1021/acsomega.1c04384

Churakov S. V. (2013). Mobility of Na and Cs on montmorillonite surface under partially saturated conditions. *Environmental Science and Technology* **47**(17), 9816–9823. https://doi.org/10.1021/es401530n

Churakov S. V. and Dähn R. (2012). Zinc adsorption on clays inferred from atomistic simulations and EXAFS spectroscopy. *Environmental Science and Technology* **46**(11), 5713–5719. https://doi.org/10.1021/es204423k

Churakov S. V. and Gimmi T. (2011). Up-scaling of molecular diffusion coefficients in clays: A two-step approach. *Journal of Physical Chemistry C* **115**(14), 6703–6714. https://doi.org/10.1021/jp112325n

Crank J. (1975). *The Mathematics of Diffusion* (2nd ed.). Clarendon Press Oxford. https://doi.org/10.1021/ja01562a072

Cygan R. T., Liang J.-J. and Kalinichev A. G. (2004). Molecular Models of Hydroxide, Oxyhydroxide, and Clay Phases and the Development of a General Force Field. *The Journal of Physical Chemistry B* **108**(4), 1255–1266. https://doi.org/10.1021/jp0363287

Davis J. A., James R. O. and Leckie J. O. (1978). Surface Ionization and Complexation at the Oxide/Water Interface. *Journal of Colloid and Interface Science* **63**(3), 480–499. https://doi.org/10.1016/S0021-9797(78)80009-5

Dzombak D. A. and Hudson R. J. M. . (1995). Ion Exchange The Contributions of Diffuse Layer Sorption and Surface Complexation. In *Advances in Chemistry* (Vol. 26, Issues 3–4, p. 288). https://doi.org/10.1524/zpch.1960.26.3_4.288

Elprince A. M., Vanselow A. P. and Sposito G. (1980). Heterovalent, Ternary Cation Exchange Equilibria: NH_4^+ -Ba^{2+} -La^{3+} Exchange on Montmorillonite. *Soil Science Society of America Journal* **44**(5), 964–969. https://doi.org/10.2136/sssaj1980.03615995004400050018x

Frenkel D. and Smit B. (2002). *Understanding Molecular Simulation, From Algorithms to Applications* (2nd ed.). Academic Press.

Fukatsu Y., Yotsuji K., Ohkubo T. and Tachi Y. (2021). Diffusion of tritiated water, $^{137}Cs^+$, and $^{125}I^-$ in compacted Ca-montmorillonite: Experimental and modeling approaches. *Applied Clay Science* **211**(May), 106176. https://doi.org/10.1016/j.clay.2021.106176

Gaines G. L. and Thomas H. C. (1953). Adsorption studies on clay minerals. II. A formulation of the thermodynamics of exchange adsorption. *The Journal of Chemical Physics* **21**(4), 714–718. https://doi.org/10.1063/1.1698996

Gapon E. N. (1933). Theory of exchange adsorption in soils. *Journal of General Chemistry (USSR)* **3**(2), 144–152.

Gimmi T. and Kosakowski G. (2011). How mobile are sorbed cations in clays and clay rocks? *Environmental Science and Technology* **45**(4), 1443–1449. https://doi.org/10.1021/es1027794

Gimmi T., Waber H. N., Gautschi A. and Rübel A. (2007). Stable water isotopes in pore water of Jurassic argillaceous rocks as tracers for solute transport over large spatial and temporal scales. *Water Resources Research* **43**(4), 1–16. https://doi.org/10.1029/2005WR004774

Gimmi T. and Alt-Epping P. (2018). Simulating Donnan equilibria based on the Nernst-Planck equation. *Geochimica et Cosmochimica Acta* **232**, 1–13. https://doi.org/10.1016/j.gca.2018.04.003

Gimmi T. and Churakov S. V. (2019). Water retention and diffusion in unsaturated clays: Connecting atomistic and pore scale simulations. *Applied Clay Science* **175**, 169–183. https://doi.org/10.1016/j.clay.2019.03.035

Glaus M. A., Aertsens M., Maes N., Van Laer L. and Van Loon L. R. (2015). Treatment of boundary conditions in through-diffusion: A case study of $^{85}Sr^{2+}$ diffusion in compacted illite. *Journal of Contaminant Hydrology* **177–178**, 239–248. https://doi.org/10.1016/j.jconhyd.2015.03.010

Glaus M. A., Baeyens B., Bradbury M. H., Jakob A., Van Loon L. R. and Yaroshchuk A. (2007). Diffusion of ^{22}Na and ^{85}Sr in montmorillonite: Evidence of interlayer diffusion being the dominant pathway at high compaction. *Environmental Science and Technology* **41**(2), 478–485. https://doi.org/10.1021/es061908d

Glaus M. A., Frick S., Rossé R. and Van Loon L. R. (2011). Consistent interpretation of the results of through-, out-diffusion and tracer profile analysis for trace anion diffusion in compacted montmorillonite. *Journal of Contaminant Hydrology* **123**(1–2), 1–10. https://doi.org/10.1016/j.jconhyd.2010.11.009

Glaus M. A., Rossé R., van Loon L. R. and Yaroshchuk A. E. (2008). Tracer diffusion in sintered stainless steel filters: Measurement of effective diffusion coefficients and implications for diffusion studies with compacted clays. *Clays and Clay Minerals* **56**(6), 677–685. https://doi.org/10.1346/CCMN.2008.0560608

Gonçalvès J., Rousseau-Gueutin P. and Revil A. (2007). Introducing interacting diffuse layers in TLM calculations: A reappraisal of the influence of the pore size on the swelling pressure and the osmotic efficiency of compacted bentonites. *Journal of Colloid and Interface Science* **316**(1), 92–99. https://doi.org/10.1016/j.jcis.2007.07.023

González Sánchez F., Van Loon L. R., Gimmi T., Jakob A., Glaus M. A. and Diamond L. W. (2008). Self-diffusion of water and its dependence on temperature and ionic strength in highly compacted montmorillonite, illite and kaolinite. *Applied Geochemistry* **23**(12), 3840–3851. https://doi.org/10.1016/j.apgeochem.2008.08.008

Guggenheim S., Martin R. T., Alietti A., Drits V. A., Formoso M. L. L., Galán E., Köster H. M., Morgan D. J., Paquet H., Watanabe T., Bain D. C., Ferrell R. E., Bish D. L., Fanning D. S., Kodama H. and Wicks F. J. (1995). Definition of clay and clay mineral: Joint report of the AIPEA nomenclature and CMS

nomenclature committees. *Clays and Clay Minerals* **43**(2), 255–256. https://doi.org/10.1346/CCMN.1995.0430213

Holmboe M. and Bourg I. C. (2014). Molecular dynamics simulations of water and sodium diffusion in smectite interlayer nanopores as a function of pore size and temperature. *Journal of Physical Chemistry C* **118**(2), 1001–1013. https://doi.org/https://doi.org/10.1021/jp408884g

Holmboe M., Wold S. and Jonsson M. (2012). Porosity investigation of compacted bentonite using XRD profile modeling. *Journal of Contaminant Hydrology* **128**(1–4), 19–32. https://doi.org/10.1016/j.jconhyd.2011.10.005

Jakob A., Sarott F.-A. and Spieler P. (1999). Diffusion and sorption on hardened cement pastes - experiments and modelling results. *PSI-Bericht Nr. 99-05,* 1–194.

Kéri A., Dähn R., Marques Fernandes M., Scheinost A. C., Krack M. and Churakov S. V. (2020). Iron Adsorption on Clays Inferred from Atomistic Simulations and X-ray Absorption Spectroscopy. *Environmental Science and Technology* **54**(19), 11886–11893. https://doi.org/10.1021/acs.est.9b07962

Kosakowski G., Churakov S. V. and Thoenen T. (2008). Diffusion of Na and Cs in montmorillonite. *Clays and Clay Minerals* **56**(2), 190–206. https://doi.org/10.1346/CCMN.2008.0560205

Lammers L. N., Bourg I. C., Okumura M., Kolluri K., Sposito G. and Machida M. (2017). Molecular dynamics simulations of cesium adsorption on illite nanoparticles. *Journal of Colloid and Interface Science* **490**, 608–620. https://doi.org/10.1016/j.jcis.2016.11.084

Leroy P. and Revil A. (2004). A triple-layer model of the surface electrochemical properties of clay minerals. *Journal of Colloid and Interface Science* **270**(2), 371–380. https://doi.org/10.1016/j.jcis.2003.08.007

Leroy P., Revil A., Altmann S. and Tournassat C. (2007). Modeling the composition of the pore water in a clay-rock geological formation (Callovo-Oxfordian, France). *Geochimica et Cosmochimica Acta* **71**(5), 1087–1097. https://doi.org/10.1016/j.gca.2006.11.009

Lewis D. R. (1949). Ion Exchange Reactions of Clays. *Properties of Clays*, 54–69.

Lichtner P. C. (2007). *Flotran User's Manual: Two-Phase Nonisothermal Coupled Thermal-Hydrological-Chemical (THC) Reactive Flow and Transport Code, Version 2.0*.

Lichtner P. C. (1996). Chapter 1: CONTINUUM FORMULATION OF MULTICOMPONENT-MULTIPHASE REACTIVE TRANSPORT. *Reactive Transport in Porous Media*, edited by P. C. Lichtner, C. I. Steefel and E. H. Oelkers, Berlin, Boston: De Gruyter, 1996, pp. 1-82. https://doi.org/10.1515/9781501509797-004

Maes N., Salah S., Jacques D., Aertsens M., Van Gompel M., De Cannière P. and Velitchkova N. (2008). Retention of Cs in Boom Clay: Comparison of data from batch sorption tests and diffusion experiments on intact clay cores. *Physics and Chemistry of the Earth* **33**, S149–S155. https://doi.org/10.1016/j.pce.2008.10.002

Matusewicz M., Pirkkalainen K., Liljeström V., Suuronen J.-P., Root A., Muurinen A., Serimaa R. and Olin M. (2013). Microstructural investigation of calcium montmorillonite. *Clay Minerals* **48**(2), 267–276. https://doi.org/10.1180/claymin.2013.048.2.08

Mazurek M., Alt-Epping P., Bath A., Gimmi T., Waber H. N., Buschaert S., Cannière P. De, Craen M., Gautschi A., Savoye S., Vinsot A., Wemaere I. and Wouters L. (2011). Natural tracer profiles across argillaceous formations. *Applied Geochemistry* **26**(7), 1035–1064.

Melkior T., Gaucher E. C., Brouard C., Yahiaoui S., Thoby D., Clinard C., Ferrage E., Guyonnet D., Tournassat C. and Coelho D. (2009). Na^+ and HTO diffusion in compacted bentonite: Effect of surface chemistry and related texture. *Journal of Hydrology* **370**(1–4), 9–20. https://doi.org/10.1016/j.jhydrol.2009.02.035

Melkior T., Yahiaoui S., Motellier S., Thoby D. and Tevissen E. (2005). Cesium sorption and diffusion in Bure mudrock samples. *Applied Clay Science* **29**(3–4), 172–186. https://doi.org/10.1016/j.clay.2004.12.008

Missana T., Benedicto A., García-Gutiérrez M., and Alonso U. (2014). Modeling cesium retention onto Na-, K- and Ca-smectite: Effects of ionic strength, exchange and competing cations on the determination of selectivity coefficients. *Geochimica et Cosmochimica Acta* **128**, 266–277. https://doi.org/10.1016/j.gca.2013.10.007

Montoya V., Baeyens B., Glaus M. A., Kupcik T., Marques Fernandes M., Van Laer L., Bruggeman C., Maes N. and Schäfer T. (2018). Sorption of Sr, Co and Zn on illite: Batch experiments and modelling including Co in-diffusion measurements on compacted samples. *Geochimica et Cosmochimica Acta* **223**, 1–20. https://doi.org/10.1016/j.gca.2017.11.027

Nagra (n.d.). *Types of radioactive waste*. Retrieved January 18, 2023, from https://nagra.ch/en/knowledge-centre/types-of-radioactive-waste/

Nagra (2002). Project Opalinus Clay. Safety Report: Demonstration of disposal feasibility for spent fuel, vitrified high-level waste and long-lived intermediate-level waste (Entsorgungsnachweis). *Technical Report - Nagra*, *02–05*.

Nagra (2014a). Etappe 2: Vorschlag weiter zu untersuchender geologischer Standortgebiete mit zugehörigen Standortareal - Geologische Grundlagen - Dossier VI Barriereneigenschaften der Wirt-und Rahmengesteine SGT. *Nagra Technischer Bericht, NTB 14-02 Dossier VI*.

Nagra (2014b). SGT Etappe 2: Vorschlag weiter zu untersuchender geologischer Standortgebiete mit zugehörigen Standortarealen für die Oberflächenanlage - Geologische Grundlagen - Dossier I - Einleitung und Zusammenfassung. *Nagra Technischer Bericht, NTB 14-02*.

Norrish K. (1954). The swelling of montmorillonite. *Discussions of the Faraday Society* **18**, 120–134. https://doi.org/10.1039/DF9541800120

Ochs M., Lothenbach B., Wanner H., Sato H. and Yui M. (2001). An integrated sorption-diffusion model for the calculation of consistent distribution and diffusion coefficients in compacted bentonite. *Journal of Contaminant Hydrology* **47**(2–4), 283–296. https://doi.org/10.1016/S0169-7722(00)00157-1

Ohkubo T., Ibaraki M., Tachi Y. and Iwadate Y. (2016). Pore distribution of water-saturated compacted clay using NMR relaxometry and freezing temperature depression; effects of density and salt concentration. *Applied Clay Science* **123**, 148–155. https://doi.org/10.1016/j.clay.2016.01.014

Ohkubo T., Yamazaki A., Fukatsu Y. and Tachi Y. (2021). Pore distribution of compacted Ca-montmorillonite using NMR relaxometry and cryoporometry: Comparison with Na-

montmorillonite. *Microporous and Mesoporous Materials* **313**, 110841. https://doi.org/10.1016/j.micromeso.2020.110841

Parkhurst D. L. and Appelo C. A. J. (2013). Description of input and examples for PHREEQC Version 3– a computer program for speciation,batch-reaction, one-dimensional transport, and inverse geochemical calculations. In *U.S. Geological Survey Techniques Methods, book 6* (p. 497). https://doi.org/10.1097/00000446-195210000-00005

Poinssot C., Baeyens B. and Bradbury M. H. (1999). Experimental and modelling studies of caesium sorption on illite. *Geochimica et Cosmochimica Acta* **63**(19–20), 3217–3227. https://doi.org/10.1016/S0016-7037(99)00246-X

Pusch R. (2001). The microstructure of MX-80 clay with respect to its bulk physical properties under different environmental conditions. SKB Technical Report TR-01-08.

Pusch R. (2006). Chapter 11.4 Clays and Nuclear Waste Management. *Developments in Clay Science*, *1*(C), 703–716. https://doi.org/10.1016/S1572-4352(05)01023-8

Revil A., Leroy P. and Titov K. (2005). Characterization of transport properties of argillaceous sediments: Application to the Callovo-Oxfordian argillite. *Journal of Geophysical Research: Solid Earth* **110**(6), 1–18. https://doi.org/10.1029/2004JB003442

Sawhney B. L. (1972). Selective sorption and fixation of cations by clay minerals. A review. *Clays and Clay Minerals* **20**(2), 93–100. https://doi.org/10.1346/CCMN.1972.0200208

Shackelford C. D. (1991). Laboratory diffusion testing for waste disposal - A review. In *Journal of Contaminant Hydrology* (Vol. 7, Issue 3, pp. 177–217). https://doi.org/10.1016/0169-7722(91)90028-Y

Shainberg I., Alperovitch N. I. and Keren R. (1987). Charge density and Na-K-Ca exchange on smectites. *Clays and Clay Minerals* **35**(1), 68–73. https://doi.org/10.1346/ccmn.1987.0350109

Soler J. M., Steefel C. I., Gimmi T., Leupin O. X. and Cloet V. (2019). Modeling the Ionic Strength Effect on Diffusion in Clay. the DR-A Experiment at Mont Terri. *ACS Earth and Space Chemistry* **3**(3), 442–451. https://doi.org/10.1021/acsearthspacechem.8b00192

Steefel C. I., Appelo C. A. J., Arora B., Jacques D., Kalbacher T., Kolditz O., Lagneau V., Lichtner P. C., Mayer K. U., Meeussen J. C. L., Molins S., Moulton D., Shao H., Šimůnek J., Spycher N., Yabusaki S. B. and Yeh G. T. (2015). Reactive transport codes for subsurface environmental simulation. In *Computational Geosciences* (Vol. **19**, Issue 3). https://doi.org/10.1007/s10596-014-9443-x

Steefel C. I. and Maher K. (2009). Fluid-Rock Interaction: A Reactive Transport Approach. *Reviews in Mineralogy and Geochemistry* **70**(1), 485–532. https://doi.org/10.2138/rmg.2009.70.11

Steefel C. I. (2009). *CrunchFlow: User's manual*. Earth Sciences Division Lawrence Berkeley National Laboratory. http://www.csteefel.com/CrunchFlowIntroduction.html

Tachi Y. and Yotsuji K. (2014). Diffusion and sorption of Cs^+, Na^+, I^- and HTO in compacted sodium montmorillonite as a function of porewater salinity: Integrated sorption and diffusion model. *Geochimica et Cosmochimica Acta* **132**, 75–93. https://doi.org/10.1016/j.gca.2014.02.004

The Federal Assembly of the Swiss Confederation. (2003). *Nuclear Energy Act*. 1–40.

Tinnacher R. M., Holmboe M., Tournassat C., Bourg I. C. and Davis J. A. (2016). Ion adsorption and diffusion in smectite: Molecular, pore, and continuum scale views. *Geochimica et Cosmochimica Acta* **177**, 130–149. https://doi.org/10.1016/j.gca.2015.12.010

Tournassat C. and Appelo C. A. J. (2011). Modelling approaches for anion-exclusion in compacted Na-bentonite. *Geochimica et Cosmochimica Acta* *75*(13), 3698–3710. https://doi.org/10.1016/j.gca.2011.04.001

Tournassat C., Bourg I. C., Steefel C. I. and Bergaya F. (2015). Surface Properties of Clay Minerals. *Developments in Clay Science*, *6*, 5–31. https://doi.org/10.1016/B978-0-08-100027-4.00001-2

Tournassat C., Chapron Y., Leroy P., Bizi M. and Boulahya F. (2009). Comparison of molecular dynamics simulations with triple layer and modified Gouy-Chapman models in a 0.1 M NaCl-montmorillonite system. *Journal of Colloid and Interface Science* **339**(2), 533–541. https://doi.org/10.1016/j.jcis.2009.06.051

Tournassat C. and Steefel C. I. (2015). Ionic Transport in Nano-Porous Clays. *Reviews in Mineralogy and Geochemistry, Pore-Scale Geochemical Processes, 80*, 287–329. https://doi.org/https://doi.org/10.2138/rmg.2015.80.0

Underwood T. R. and Bourg I. C. (2020). Large-scale molecular dynamics simulation of the dehydration of a suspension of smectite clay nanoparticles. *Journal of Physical Chemistry C* **124**(6), 3702–3714. https://doi.org/10.1021/acs.jpcc.9b11197

Van Loon L. R., Baeyens B. and Bradbury M. H. (2005). Diffusion and retention of sodium and strontium in Opalinus clay: Comparison of sorption data from diffusion and batch sorption measurements, and geochemical calculations. *Applied Geochemistry* **20**(12), 2351–2363. https://doi.org/10.1016/j.apgeochem.2005.08.008

Van Loon L. R., Baeyens B. and Bradbury M. H. (2009). The sorption behaviour of caesium on Opalinus Clay: A comparison between intact and crushed material. *Applied Geochemistry* **24**(5), 999–1004. https://doi.org/10.1016/j.apgeochem.2009.03.003

Van Loon L. R. and Eikenberg J. (2005). A high-resolution abrasive method for determining diffusion profiles of sorbing radionuclides in dense argillaceous rocks. *Applied Radiation and Isotopes* **63**(1), 11–21. https://doi.org/10.1016/j.apradiso.2005.02.001

Van Loon L. R., Soler J. M. and Bradbury M. H. (2003). Diffusion of HTO, $^{36}Cl^-$ and $^{125}I^-$ in Opalinus Clay samples from Mont Terri: Effect of confining pressure. *Journal of Contaminant Hydrology* **61**(1–4), 73–83. https://doi.org/10.1016/S0169-7722(02)00114-6

Van Loon Luc R. and Glaus M. A. (2008). Mechanical compaction of smectite clays increases ion exchange selectivity for cesium. *Environmental Science and Technology* **42**(5), 1600–1604. https://doi.org/10.1021/es702487m

Van Loon Luc R., Glaus M. A. and Müller W. (2007). Anion exclusion effects in compacted bentonites: Towards a better understanding of anion diffusion. *Applied Geochemistry* **22**(11), 2536–2552. https://doi.org/10.1016/j.apgeochem.2007.07.008

Van Loon Luc R. and Müller W. (2014). A modified version of the combined in-diffusion/abrasive peeling technique for measuring diffusion of strongly sorbing radionuclides in argillaceous rocks: A test study on the diffusion of caesium in Opalinus Clay. *Applied Radiation and Isotopes* **90**, 197–202. https://doi.org/10.1016/j.apradiso.2014.04.009

Vanselow A. P. (1932). The utilization of the base-exchange reaction for the determination of activity coefficients in mixed electrolytes. *Journal of the American Chemical Society* **54**(4), 1307–1311. https://doi.org/10.1021/ja01343a005

Wersin P., Soler J. M., Van Loon L., Eikenberg J., Baeyens B., Grolimund D., Gimmi T. and Dewonck S. (2008). Diffusion of HTO, Br^-, I^-, Cs^+, $^{85}Sr^{2+}$ and $^{60}Co^{2+}$ in a clay formation: Results and modelling from an in situ experiment in Opalinus Clay. *Applied Geochemistry* **23**(4), 678–691. https://doi.org/10.1016/j.apgeochem.2007.11.004

Wigger C. and Van Loon L. R. (2017). Importance of interlayer equivalent pores for anion diffusion in clay-rich sedimentary rocks. *Environmental Science and Technology* **51**(4), 1998–2006. https://doi.org/10.1021/acs.est.6b03781

Wigger C. and Van Loon L. R. (2018). Effect of the pore water composition on the diffusive anion transport in argillaceous, low permeability sedimentary rocks. *Journal of Contaminant Hydrology*, **213**, 40–48. https://doi.org/10.1016/j.jconhyd.2018.05.001

Yu C., Gonçalvès J. and Matray J. (2018). Bayesian inversion of a chloride profile obtained in the hydraulically undisturbed Opalinus Clay: Mass transport and paleo-hydrological implications. *Applied Geochemistry* **93**, 178–189.

Chapter 2:
On the concentration-dependent diffusion of sorbed cesium in Opalinus Clay

(published in Geochimica et Cosmochimica Acta 298, 149–166 (2021);

available at: https://doi.org/10.1016/j.gca.2021.01.012)

Available online at www.sciencedirect.com

ScienceDirect

Geochimica et Cosmochimica Acta 298 (2021) 149–166

Geochimica et Cosmochimica Acta

www.elsevier.com/locate/gca

On the concentration-dependent diffusion of sorbed cesium in Opalinus Clay

Philipp Krejci [a,b,*], Thomas Gimmi [a,b], Luc Robert Van Loon [a]

[a] *Laboratory for Waste Management, Nuclear Energy and Safety, Paul Scherrer Institute, CH-5232 Villigen, Switzerland*
[b] *Rock-Water Interaction, Institute of Geological Sciences, University of Bern, CH-3012 Bern, Switzerland*

Received 20 June 2020; accepted in revised form 11 January 2021; available online 27 January 2021

Abstract

Cation diffusion coefficients in clayey materials partly appear to be greater than diffusion coefficients of water tracers. The measured values vary between experiments performed at different salinities or different tracer concentrations. This effect is especially pronounced for cations that sorb strongly on the clay surfaces, such as Cs. The observations illustrate the difficulties in applying Fick's law to cation diffusion in clays and demonstrate the need to find a consistent description of cation diffusion in clays that can be used to predict experiments performed at different conditions. In order to consistently describe Cs diffusion in Opalinus Clay, a multi-site surface diffusion model was implemented in the continuum-scale reactive transport code Flotran. The model combines pore and surface diffusion in one single diffusion coefficient, which accounts for the diffusion of sorbed cations along the clay surfaces.. The contribution from surface diffusion to the diffusion coefficient is directly coupled to the sorption behavior via the derivative of the sorption isotherm. The model parameters include the surface mobilities, which are specific for each cation and sorption site. To derive surface mobilities for Cs, in-diffusion experiments were conducted at eight different stable Cs background concentrations. A set of surface mobilities for Cs on three sorption sites in Opalinus Clay was estimated by fitting the surface diffusion model simultaneously to these experimental data. Moreover, the sensitivity of the model to sorption parameters and surface mobilities was evaluated. The surface diffusion model with the estimated surface mobilities was then successfully tested against independent experimental data for Cs in Opalinus Clay, illustrating the model's predictive capabilities.

Keywords: Opalinus Clay; Cesium; Sorption; Diffusion; Surface diffusion; Reactive transport modeling

1. INTRODUCTION

There is a worldwide interest to use clays and claystones as sealing components for waste disposal sites. In Switzerland, Opalinus Clay (OPA), an argillaceous rock, is considered as potential host rock for a radioactive waste repository (Nagra, 2002). The low hydraulic conductivity (10^{-10}–10^{-15} m s^{-1}) restricts migration of solutes through clay formations, such as OPA, essentially to diffusive processes only (Gimmi et al., 2007; Mazurek et al., 2011; Yu et al., 2018). The sorption capacity of clay for various cations or contaminants of interest as well as the detailed mechanisms of the sorption process have been investigated in numerous studies (Elprince et al., 1980; Neal and Cooper, 1983; Shainberg et al., 1987; Fletcher and Sposito, 1989; Helios et al., 1995; Staunton and Roubaud, 1997; Tournassat et al., 2007; Robin et al., 2015; Montoya et al., 2018; Siroux et al., 2018; Fernandes and Baeyens, 2019). For Cs, sorption on clays has been found to be non-linear in a complex way, which was attributed to the existence of different sorption sites. Various multi-site sorption models (Poinssot et al., 1999; Bradbury and Baeyens, 2000; Savoye et al., 2012; Benedicto et al., 2014;

* Corresponding author at: Paul Scherrer Institute, OFLA/207, CH-5232 Villigen, Switzerland.
E-mail address: philipp.krejci@psi.ch (P. Krejci).

https://doi.org/10.1016/j.gca.2021.01.012
0016-7037/

Chen et al., 2014; Missana et al., 2014a; Missana et al., 2014b; Cherif et al., 2017) have been developed in order to characterize the sorption behavior of Cs onto different clays. Most of these models considered cation exchange as the main sorption process. It was generally found that soils and sediments have a comparably small number of high affinity sites where Cs sorbs preferentially, and a larger number of sites with lower affinity for Cs (Fuller et al., 2014). Often, the high affinity sites were attributed to frayed edges of illite (FES), whereas the sites with lower affinity were attributed to planar sites (PS), that is, to sites on external or internal basal planes of illite and smectites, with the charge arising from isomorphous substitution.

In Opalinus Clay, Cs sorption can be described by a generalized three-site ion exchange model (Bradbury and Baeyens, 2000; Van Loon et al., 2009). This model is based on the sorption properties of illite (Poinssot et al., 1999) but also includes planar sites of other clay phases (e.g., illite/smectite mixed layers) according to the measured cation exchange capacity (CEC). Following Poinssot et al. (1999), Type II sites (TTS) with intermediate capacity and strong to intermediate affinity for Cs are distinguished in addition to FES and PS. Zachara et al. (2002) used a two-site model, similar to Poinssot et al. (1999), to describe Cs sorption in Handford sediments. Steefel et al. (2003) modified this model by adding a second FES for a more sensitive fit. Chen et al. (2014) applied the generalized three-site model (FES, TTS, and PS) successfully to samples from the Callovo-Oxfordian (COx) clay-rich formation with differing mineral compositions. They concluded that only PS should be attributed to illite/smectite mixed layer minerals. More recently Cherif et al. (2017) compared sorption of Cs on many different clay minerals and developed a model with two sites (one ion exchange site, one surface complexation site) each on illite, montmorillonite, and kaolinite. As different sorption affinity parameters (selectivities, equilibrium constants) were derived for each of these minerals, this essentially represents a six-site model for a multi-mineral clay. Surprisingly, they considered a pH-dependent SC model for frayed edge sites on illite, which is at odds with the widely accepted idea that Cs has a highly specific affinity to these sites due to its large size and low hydration energy (Sawhney, 1972; Brouwer et al., 1983; Poinssot et al., 1999; Bradbury and Baeyens, 2000). In any case, the distinction of different sites in the aforementioned multi-site sorption models is empirically based on the shape of the adsorption isotherms, mostly without any evidence from spectroscopic methods. This is especially true for the low capacity sites.

Model concepts for cation sorption have also been developed by considering interactions between a charged, planar surface and the surrounding electrolyte solution. In the classical Gouy-Chapman diffuse double-layer model (Huang and Stumm, 1973; Singh and Uehara, 1999), the negative surface charge (representing the first layer of the model) is compensated by a swarm of electrostatically attracted cations, with decreasing concentration with distance from the surface such that electrostatic and thermal forces are balanced. The modified Gouy-Chapman model (Carnie and Torrie, 1984; Sposito, 1992; Tournassat et al., 2009) accounts for the fact that ions have a finite size; the origin of the diffuse layer is thus shifted by one ion radius from the charged surface. The Gouy-Chapman-Stern model (Bowden et al., 1977; Westall and Hohl, 1980) includes an innermost compact layer (Stern layer) with more specifically adsorbed cations, followed by the diffuse layer; resulting in a triple-layer model (cf. Fig. 1). The Grahame model or other triple-layer models (Davis et al., 1978; Leroy and Revil, 2004; Leroy et al., 2007) also assume a specific layer of cations next to the surface. The layer of sorbed cations next to the surface in these models can be considered as Stern layer, without referring explicitly to the strength or type of interaction. This surface layer may consist of cations forming inner-sphere complexes (i.e., without an intervening water molecule) or outer-sphere complexes. Cations in the surface layer and in the diffuse layer may be considered as sorbed in the sense that they compensate the surface charges. One should keep in mind, however, that the diffuse layer typically contains an excess of cations, depending on the equilibrium electrolyte concentration. Far away from the surface, the ion concentrations reach the values of this electrolyte concentration. Thus, cations can generally occur in the two counter layers (Stern or surface layer, diffuse layer) as well as in so-called 'free' pore water, which is the charge neutral electrolyte solution (Fig. 1).

The traditional approach to model cation diffusion in clays is based on the simple Fick's law. In this approach, only cations in 'free' pore water contribute to diffusion, while any sorbed cations are considered as immobile, with

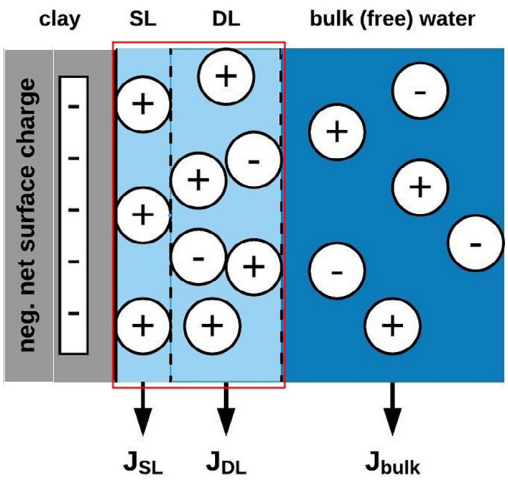

Fig. 1. Schematic representation of the concept of a triple-layer model: Cations are sorbed (light blue domain) on the negatively charged clay surfaces (grey) in the Stern layer (SL) and the diffuse layer (DL) close to the clay surface. The latter contains an excess of cations. In the bulk water (or 'free' pore water; dark blue domain) ions are not affected by electrostatic forces resulting from the negatively charged clay surfaces. Each domain may contribute to the overall mass flux j in a surface diffusion model. Here, we only distinguish between sorbed cations (red frame) and cations in the pore water, with an (average) surface mobility of sorbed cations. (For interpretation of the references to colour in this figure legend, the reader is referred to the web version of this article.)

no distinction between different sites or types of sorption. This means that sorbed cations, including those in the DL, do not add to the overall mass flux. However, this approach often appears to be problematic when evaluating cation diffusion experiments in clays. Especially for strongly sorbing ions, such as Cs, diffusion coefficients are often higher than diffusion coefficients of neutral tracers (e.g. tritiated water, HTO). For example, Jakob et al. (2009) found the effective diffusion coefficient of Cs in Opalinus Clay to be one order of magnitude greater than that of HTO, Melkior et al. (2005) found similar results for Callovo-Oxfordian clay, whereas Wersin et al. (2008) found a 3 times higher and Van Loon et al. (2004b) a four times higher effective diffusion coefficient for Cs than for HTO in Opalinus Clay. These observations are inconsistent with simple Fick's law.

One explanation for this phenomenon is the excess of cations in the diffuse layer which leads to an enhanced mass flux. However, models including DL diffusion on the basal planes of the clay platelets also cannot describe the diffusion behavior of Cs in OPA consistently, and bulk diffusion coefficients still have to be adapted to the experimental data (Appelo et al., 2010; Soler et al., 2019). Tachi and Yotsuji (2014) found the modeled Cs diffusion coefficient at an ionic strength of 0.01 M about matching the experimental value when applying a DL diffusion model to Cs diffusion in compacted sodium montmorillonite, while it underestiamted the values at higher ionic strengths.

A more general explanation for the discrepancy between experimental results and classical Fickian diffusion theory is the movement of any sorbed cations along the clay surfaces, without referring to a specific type of sorption (Jenny and Overstreet, 1939; van Schaik et al., 1966; Cheung, 1990; Berry and Bond, 1992; Eriksen et al., 1999; Gimmi and Kosakowski, 2011). This process is called surface diffusion, with the term referring to the diffusion of any sorbed cations, including those in the DL. Although DL cations are mobile, Stern layer cations are generally considered to be immobile. However, some mobility has been attributed to these cations in order to be able to match conductivity or electrophoretic data (Lyklema et al., 1998; Revil et al., 1998; Lyklema, 2001; Leroy and Revil, 2004; Weber and Stanjek, 2017). From a mechanistic perspective, surface diffusion can be considered as ions moving from one adsorption site to another (Jenny and Overstreet, 1939; Revil et al., 1998; Lyklema, 2001).

Gimmi and Kosakowski (2011) compiled a large set of cation diffusion data in clays and soils in order to evaluate the mobility of sorbed cations. They found a distinct surface mobility for each cation. However, Cs data were concentration-dependent, and different surface mobilities were given for low and high Cs background concentrations. The concentration-dependent mobility was attributed to the different sorption sites for Cs, which dominate at different Cs concentrations. Therefore, they proposed a generalized multi-site surface diffusion model. This model considers a (partial) mobility of the cation on each of the sorption sites or domains.

In this study, we present the application of a multi-site surface diffusion model to Cs diffusion data in Opalinus Clay. The model was implemented in the reactive transport code Flotran (Lichtner, 2007). Specific in-diffusion experiments at different Cs background concentrations were conducted in order to estimate the sorption-site-specific surface mobilities of Cs. The sensitivity of simulations to model parameters was evaluated and the model was tested against other Cs diffusion data in Opalinus Clay.

2. MODELING APPROACH

2.1. Formalism of the multi-site surface diffusion model

At the pore scale, surface diffusion occurs in parallel to diffusion in the bulk pore water (Gimmi and Kosakowski, 2011). Therefore, the total cation mass flux can be written as the sum of the contributions from pore diffusion, described by Fick's first law, and surface diffusion:

$$j_{tot} = j_p + j_s = -\varepsilon \frac{D_0}{\tau_p} \frac{\partial C}{\partial x} - \rho_{bd} \frac{D_{s0}}{\tau_s} \frac{\partial S}{\partial x} \tag{1}$$

where j_p and j_s are the fluxes for the pore and surface regions (Fig. 1), C is the concentration in solution, S is the sorbed concentration per mass of dry solid, D_0 is the cation diffusion coefficient in bulk water, D_{s0} is the intrinsic surface diffusion coefficient for a flat surface, ε is the total (water filled) porosity, ρ_{bd} is the bulk dry density, τ_p and τ_s account for the tortuous pathway in the pore water and on the surface, respectively, and $\partial C/\partial x$ and $\partial S/\partial x$ are the concentration gradients in the pore water and on the surface. The balance equation is:

$$\left(\varepsilon + \rho_{bd} \frac{\partial S}{\partial C}\right) \frac{\partial C}{\partial t} = \frac{\partial}{\partial x}\left(\varepsilon \frac{D_0}{\tau_p} \frac{\partial C}{\partial x}\right) + \frac{\partial}{\partial x}\left(\rho_{bd} \frac{D_{s0}}{\tau_s} \frac{\partial S}{\partial x}\right) \tag{2}$$

Neglecting the second term on the right hand side in Eqs. (1) and (2) results in the classical Fickian diffusion model with the effective diffusion coefficient D_e being $D_e = \varepsilon D_p = \varepsilon D_0/\tau_p$, and the pore diffusion $D_p = D_0/\tau_p$. Eq. (1) can also be used to describe the flux at the sample scale as long as the tortuosities are representative for this scale. If we assume local equilibrium between pore and surface concentrations, pore and surface diffusion fluxes can be combined in a single term that depends on the concentration gradient $\partial C/\partial x$ only, using the relation $\partial S/\partial x = (\partial S/\partial C)(\partial C/\partial x)$. This relationship is, however, only valid if S depends uniquely on C, as is typically the case for trace concentrations where the background concentrations of other cations participating in sorption remain about constant. More generally, the surface concentration gradient of a cation k, $\partial S_k/\partial x$, can be given as:

$$\frac{\partial S_k}{\partial x} = \sum_j \left(\frac{\partial S_k}{\partial C_j}\right)\left(\frac{\partial C_j}{\partial x}\right) = \left(\sum_j \left(\frac{\partial S_k}{\partial C_j}\right)\left(\frac{\partial C_j}{\partial C_k}\right)\right)\left(\frac{\partial C_k}{\partial x}\right) \tag{3}$$

where $\partial S_k/\partial C_j$ are the derivatives of the sorbed concentration of cation k with respect to the concentrations of the cations j in solution and $\partial C_j/\partial x$ are the concentration gradients of the cations j. Here, we focus on the case of constant background cations where $\partial C_{j\neq k}/\partial x \approx 0$, but the surface diffusion model was implemented according to the general form of Eq. (3).

Substituting Eq. (3) into Eq. (1), the total flux of the surface diffusion model depends then on a single, combined diffusion coefficient. If multiple sorption sites i are present, we have

$$D_{e,comb} = \frac{\varepsilon D_0}{\tau_p} + \rho_{bd} \sum_i \frac{\mu_{sk,i} D_0}{\tau_s} \left(\sum_j \left(\frac{\partial S_{k,i}}{\partial C_j} \right) \left(\frac{\partial C_j}{\partial C_k} \right) \right) \quad (4)$$

In the above relation, $\mu_{sk,i}$ is the relative surface mobility of the cation k on site i. When species concentrations or solution composition are not constant over the domain or time span of interest, the local derivative terms, and therefore $D_{e,comb}$, become space- and time-dependent. As different $D_{e,comb}$ have to be used for different ions in the surface diffusion model, a multi-species diffusion approach is required. Thus, diffusion has to be described by the Nernst-Planck equation, which is implemented in Flotran. The relative surface mobility $\mu_{sk,i}$ is equal to the ratio $D_{s0,i}/D_0$. In other words, it is a measure for the average diffusive mobility of a cation sorbed on site i on a flat surface in comparison to its diffusive mobility in water. For constant background concentrations ($\partial C_{j \neq k}/\partial x \approx 0$ or $\partial C_{j \neq k}/\partial C_k \approx 0$), this relation simplifies to (Gimmi and Kosakowski, 2011):

$$D_{e,comb} = \frac{\varepsilon D_0}{\tau_p} + \rho_{bd} \sum_i \frac{\mu_{s,i} D_0}{\tau_s} \frac{\partial S_i}{\partial C} \quad (5)$$

where the subscript k for the sorbing cation of interest has been dropped. Gimmi and Kosakowski (2011) assumed that $\tau_s = \tau_p$, which was justified in view of the closeness of surface and pore diffusion pathways. Also, the effective cation porosity is set equal to the total (water-filled) porosity $\varepsilon = \varepsilon_w$, because cations and water occupy the same pore space (external and interlayer pores). The first term in Eqs. (4) and (5) stands for diffusion in the pore water, while the second term accounts for diffusion along the clay particle surfaces. Surface diffusion may occur on each of the available sorption sites i for a certain cation, according to the sorption model and the value of the surface mobility $\mu_{s,i}$. The multi-site surface diffusion coefficient sums up the contributions of all sorption sites i to the overall mass flux.

2.2. Cs sorption model for Opalinus Clay

The sorption behavior of Cs in OPA can be described by the generalized three-site sorption model (GCS) of Bradbury and Baeyens (2000), where Cs sorption is linked to the illite mineral content of the clay. The site-specific derivatives of the sorption isotherm $\partial S_i/\partial C$ needed in Eq. (5) (or the more complicated sum term over all cations j in Eq. (4)) are calculated from the GCS. The calculation of these terms based on a general cation exchange reaction is explained in the Appendix A. The GCS proposes that Cs sorbs via cation exchange reactions onto three different sorption sites: Planar sites (PS), Type II-sites (TTS) and Frayed-edge sites (FES). Frayed-edge (0.25%) and Type II (20%) site capacities were fixed according to the illite mineral content in the OPA specimen and a reference illite with a CEC of 0.2 eq kg^{-1}. The planar site capacity was taken to be 0.095 eq kg^{-1} for Mont Terri Opalinus Clay (Bradbury and Baeyens, 1998), which accounts for the sum of all clay minerals (e.g. illite-smectite mixed layers) participating in Cs sorption. TTS and FES site capacities were calculated to $9.2 \cdot 10^{-3}$ eq kg^{-1} and $1.15 \cdot 10^{-4}$ eq kg^{-1}, respectively, taking an illite content of 23%. The mineralogical and pore water composition of OPA are summarized in Table 1. Selectivity coefficients (uncertainty of ±0.2 log K units) for the cation exchange reactions are given by Bradbury and Baeyens (1998) and Van Loon et al. (2009) (Table 2).

3. DIFFUSION EXPERIMENTS

3.1. Experimental setup

Diffusion experiments were performed in order to determine the surface mobilities of Cs in Opalinus Clay. The idea was to determine Cs tracer diffusion at several different, about constant stable Cs (Cs-133) background concentrations. In each experiment, Cs tracer diffusion was expected to be dominated by sorption and surface diffusion of certain sites only. For this purpose, small rock columns were presaturated with a given Cs background concentration. Then,

Table 1
Mineralogical composition (range according to Bradbury and Baeyens (1998) and Lauber et al. (2000)) and pore water composition of OPA.

Mineralogical composition		Pore water composition	
Minerals	wt%	Element	Concentration
Calcite	8–11	Na (M)	$2.4 \cdot 10^{-1}$
Dolomite/ankerite	1.5–2.5	K (M)	$1.61 \cdot 10^{-3}$
Siderite	3–5	Ca (M)	$2.58 \cdot 10^{-2}$
Quartz	10–14	Mg (M)	$1.69 \cdot 10^{-2}$
Albite	0.5–2	Cl (M)	$3 \cdot 10^{-1}$
K-feldspar	1.5–3	SO_4 (M)	$1.41 \cdot 10^{-2}$
Pyrite	1.7	Alkalinity (M)	$4.76 \cdot 10^{-4}$
Phyllosilicates		pH	7.6
Illite	16–26		
Illite/smectite mixed layers	6–22		
Kaolinite	17–32		
Clorite	5–12		

Table 2
Cation exchange reactions and selectivity coefficients used in the GCS.

Cation exchange reactions	Selectivity coefficients (log K_C)
Na-FES + Cs ↔ Cs-FES + Na	7.0**
Na-FES + K ↔ K-FES + Na	2.4**
Na-TTS + Cs ↔ Cs-TTS + Na	3.2**
Na-TTS + K ↔ K-TTS + Na	2.1**
Na-PS + Cs ↔ Cs-PS + Na	1.6**
Na-PS + K ↔ K-PS + Na	1.1**
2Na-PS + Ca ↔ Ca-PS + 2Na	0.67*
2Na-PS + Mg ↔ Mg-PS + 2Na	0.59*
2Na-PS + Sr ↔ Sr-PS + 2Na	0.67***

* Bradbury and Baeyens (1998).
** Van Loon et al. (2009).
*** For Sr the same value as for Ca was taken.

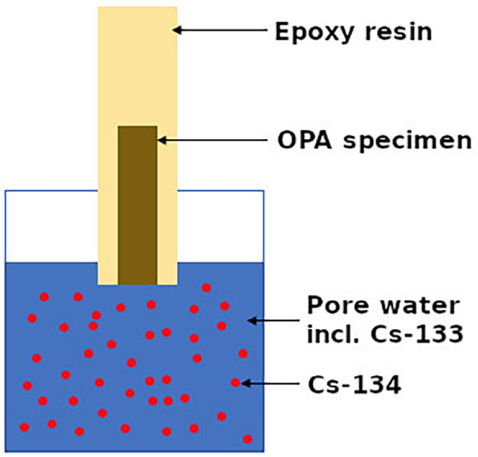

Fig. 2. Schematic presentation of the diffusion set up used for the in-diffusion experiments.

in-diffusion of a Cs tracer (Cs-134) into the same column was monitored. The Opalinus Clay specimen used in these experiments were from the Mont Terri Rock Laboratory (St. Ursanne, Switzerland). The specimen originate from the borehole drilled for the DI-A field experiment (Wersin et al., 2004). The setup of the experiment is similar to that of Van Loon and Müller (2014) (Fig. 2). Small cylindrical specimen were subcored parallel to the bedding plane from a single larger core. The small bore cores were embedded in an epoxy resin (Epofix, Streurs, Germany). After hardening, the resin at one front side of the core was removed. This end of the specimen was contacted for 2 months at 25 ± 1 °C with 100 mL synthetic pore water suited for OPA at the sampling site (Table 1) containing different concentrations of stable cesium between 10^{-2} M and $3.5 \cdot 10^{-8}$ M (Table 3). Simplified calculations showed that after 2 months clearly different levels of Cs-133 concentrations are reached in the clay specimen close to the reservoir. The geometrical parameters of the specimens are given in Table 4.

Table 3
Concentrations of Cs-133 in synthetic pore water used to pre-saturate the Opalinus Clay specimen and concentrations of Cs-134 for the in-diffusion experiments.

Specimen	Cs-133 (M)	Cs-134 Bq dm^{-3}	Cs-134 (M)
1	10^{-2}	10^{7}	$1.56 \cdot 10^{-9}$
2	10^{-3}	$5 \cdot 10^{6}$	$7.70 \cdot 10^{-10}$
3	10^{-4}	$3 \cdot 10^{6}$	$4.68 \cdot 10^{-10}$
4	10^{-5}	$2 \cdot 10^{6}$	$3.11 \cdot 10^{-10}$
5	10^{-6}	$3 \cdot 10^{5}$	$4.68 \cdot 10^{-11}$
6	$3 \cdot 10^{-7}$	$3 \cdot 10^{5}$	$4.68 \cdot 10^{-11}$
7	10^{-7}	10^{5}	$1.56 \cdot 10^{-11}$
8	$3.5 \cdot 10^{-8}$	10^{5}	$1.56 \cdot 10^{-11}$

After 2 months of resaturation and equilibration, the specimens were contacted with 100 mL solution of similar composition but spiked with Cs-134 tracer (Table 3). After 7 days in-diffusion, the profiles of Cs-134 in the OPA specimens were analysed using the abrasive technique described in Van Loon and Müller (2014). The abrasive paper used was P400 (Siawatt fc, SIA abrasives, Switzerland). The thickness of the sampled layers varied between ~100 μm and 200 μm. The uncertainty on the diffusion distance was calculated as described in Van Loon and Müller (2014). The total concentration of Cs-134 per dry mass of the removed rock was determined by γ-counting.

3.2. Derivation of model parameter values

3.2.1. General model parameters

Diffusion was modeled by applying species-dependent pore diffusion coefficients for all ions, while the contribution of surface diffusion was only added to the Cs diffusion coefficient. Aquatic complexes and competitive sorption were taken into account by considering geochemical equilibrium in solution and between solution and clay surfaces using the activity model of Davies (Eq. (A2)) (Stumm and Morgan, 1996).

A Cs diffusion coefficient in bulk water $D_{0,Cs}$ of $2 \cdot 10^{-9}$ m^2 s^{-1} (Flury and Gimmi, 2018) was used for all simulations. The porosity ε and the bulk dry density ρ_{bd} were calculated from the geometric in-diffusion data (Table 4) using a grain density of OPA of 2.7 g mL^{-1}. The tortuosities τ_p and τ_s were approximated with τ_w for a water tracer (Gimmi and Kosakowski, 2011) taking the same value of 6.14 for all experiments from Appelo et al. (2010). At the interface between reservoir and OPA specimen a constant concentration boundary condition was taken, whereas a no flux boundary was used to describe the boundary at the other end of the specimen.

3.2.2. Sorption model

All experiments were modeled using the given pore water composition and a single sorption isotherm according to the generalized Cs sorption model of Bradbury and Baeyens (2000). The default parameters for sorption (site capacities, selectivities) were those from the literature given in Section 2.2. The Cs-134 concentration in the reservoir was approximately constant during the experiment (less

Table 4
Geometrical characteristics of the OPA cores used in the diffusion experiments.

Specimen	Diameter (mm)	Length (mm)	Mass dry (g)	Bulk dry density (g mL^{-1})	Porosity (–)
1	2.61	12.52	0.1519	2.268	0.160
2	2.60	12.64	0.1522	2.268	0.160
3	2.60	11.11	0.1344	2.278	0.156
4	2.61	12.62	0.1538	2.278	0.156
5	2.62	10.63	0.1310	2.286	0.153
6	2.61	11.94	0.1463	2.286	0.153
7	2.60	12.19	0.1450	2.240	0.170
8	2.61	11.85	0.1444	2.286	0.153

than 1% of the initial mass of Cs-134 in the reservoir diffused into the specimen). The comparison of the reservoir Cs-134 concentration with that of the first data point of the in-diffusion profiles, which was adjacent to the reservoir solution, allows an independent estimation of the Cs-134 sorption at different Cs background concentrations. These points were compared with the default sorption isotherm based on the literature data, and site capacities were adapted when considered necessary. To do so, the stable Cs sorbed concentration was calculated from the corresponding stable Cs aqueous background concentration by using the distribution coefficient derived from the Cs-134 aqueous and sorbed concentrations. The natural heterogeneity of OPA at the centimeter scale can lead to local variations of the illite or smectite contents, which then directly affect the local sorption capacities of the different specimen drilled from the same core sample. Furthermore, selectivity coefficients were also modified – within their given uncertainty – in order to better match the isotherm data. As stated, a single sorption isotherm was finally used for all eight experiments, but it may also be justified to use slightly different site capacities for each separate specimen in response to local heterogeneity.

3.2.3. Surface mobilities

The surface mobilities were estimated by fitting the surface diffusion model visually to the experimental in-diffusion profiles. A sequential procedure was used. At the highest $C_{Cs,bg}$ of 10^{-2} M, FES and TTS are mostly occupied by stable Cs and $\partial S_{FES}/\partial C$ and $\partial S_{TTS}/\partial C$ tend to be negligibly small. Therefore, only the mobility on the planar sites significantly contributes to the overall mass flux. Accordingly, the data at this highest background concentration are most sensitive to μ_{PS}, and the value of this parameter was determined from these profile data and kept constant for the modeling of the other experiments. Second, the value for μ_{TTS} was estimated mainly based on the data at intermediate to high concentrations, where $\partial S_{FES}/\partial C$ still is negligible. Finally, the μ_{FES} value was derived mainly with a focus on the data at the lowest background concentration of $3.5 \cdot 10^{-8}$ M, leading in the end to a single set of surface mobilities.

3.2.4. Sensitivity to model parameters

Some correlation exists between the three surface mobilities, as well as between these parameters and the isotherm parameters. In order to get a feeling for these correlations, three sets of sensitivity simulations were performed, where the effect of a variation of the sorption capacities, the selectivities, and the surface mobilities were investigated. These sensitivity simulations served also to check effects of possible specimen heterogeneities with respect to these parameters.

3.2.5. Global parameter estimation

In order to better judge the validity of the sorption and diffusion parameters, the site capacities, selectivity coefficients and surface mobilities for Cs (in total 9 parameters) were also estimated with a global optimization procedure. To do so, the open-source library NLopt (Johnson, 2019) for non-linear optimization was used. The sum of the squared error between model and experimental data (diffusion profiles) was minimized applying the ESCH algorithm (da Silva et al., 2010). This is an evolutionary algorithm for global optimization implemented in the NLopt library. The squared errors between model and data values were weighted by the corresponding squared uncertainty (error) of the diffusion data points. The optimization procedure was limited to 20,000 iterations to find the global optimum of all parameters simultaneously for seven out of the eight experiments (excluding that at $C_{Cs,bg}$ 10^{-7} M, which has some peculiarities, see below).

4. RESULTS

4.1. Modification of the sorption isotherm

The usage of the original (default) isotherm parameters (Section 3.2.2) was not satisfactory, especially for low stable Cs background concentration $C_{Cs,bg}$; sorption as derived from the first three profile points was overestimated for most experiments (Fig. 3). Therefore, the site capacities as well as the ${}^{Cs}_{Na}K_c$ values were slightly modified to better match the experimental data, the latter within the range of their uncertainty (Table 5). The CEC of the PS and TTS had to be decreased by ~25%, compared to the original isotherm (Van Loon et al., 2009), and the CEC of the FES by ~50%, respectively, in order to approximately match all eight experiments simultaneously (Fig. 3). The modification significantly lowered the sorbed amount of Cs at low $C_{Cs,bg}$. However, sorption remained slightly overestimated for $C_{Cs,bg}$ of $3.5 \cdot 10^{-8}$ M, while for the experiment with $C_{Cs,bg}$ of 10^{-7} M the large difference between the first three data points, which may hint to heterogeneity within

the specimen, precludes a unique match anyway. The modified isotherm parameters were then used for the simulations carried out to estimate the surface mobilities.

The used specimen were small (Table 4). Thus, the scatter of the data with respect to a single isotherm may be partly due to heterogeneity between the specimen (or heterogeneity within the specimen for $C_{Cs,bg}$ of 10^{-7} M). Heterogeneity is expected to affect mainly site capacities through local variations of mineralogical composition. Selectivities, even though not representing real thermodynamic parameters, are considered as more fundamental than capacities, but it is clear that they also can depend on mineralogical variations.

One has to keep in mind that the sorption isotherm affects also the effective diffusion coefficient in a surface diffusion model, because of the coupling to its derivative. Accordingly, a variation of the sorption parameters will also influence the respective diffusion profiles.

4.2. Surface mobilities determined from in-diffusion profiles

From the data at the highest $C_{Cs,bg}$ of 10^{-2} M, a value of $3.3 \cdot 10^{-2}$ was estimated for μ_{PS}; best agreement with the experiments at intermediate to high concentrations was found when using a mobility of zero for the Type II sites, whereas a mobility on the FES of $1.5 \cdot 10^{-3}$ was necessary to fit the data for low $C_{Cs,bg}$.

Fig. 4 shows the experimental and modeled Cs-134 diffusion profiles for the eight experiments. Reasonable matches between experimental data and model were obtained for the high $C_{Cs,bg}$ of 10^{-2} M, 10^{-3} M, 10^{-4} M and 10^{-5} M (with the first point appearing as an outlier at 10^{-5} M). For $3.5 \cdot 10^{-8}$ M Cs, sorption near the inlet (first three points) was slightly overestimated, whereas for $C_{Cs,bg}$ of 10^{-6} M it was slightly underestimated near the inlet and the diffusion profile was too flat. For $3 \cdot 10^{-7}$ M $C_{Cs,bg}$ the model matches the experimental data only near the inlet but then overestimates the sorbed Cs-134 concentration (except for the last point). Finally, a reasonable match for $C_{Cs,bg}$ 10^{-7} M could not be achieved. At this $C_{Cs,bg}$, the first measurement point exhibits a very high concentration compared to the rest of the profile. This behavior cannot be described appropriately by diffusion into a homogeneous rock specimen.

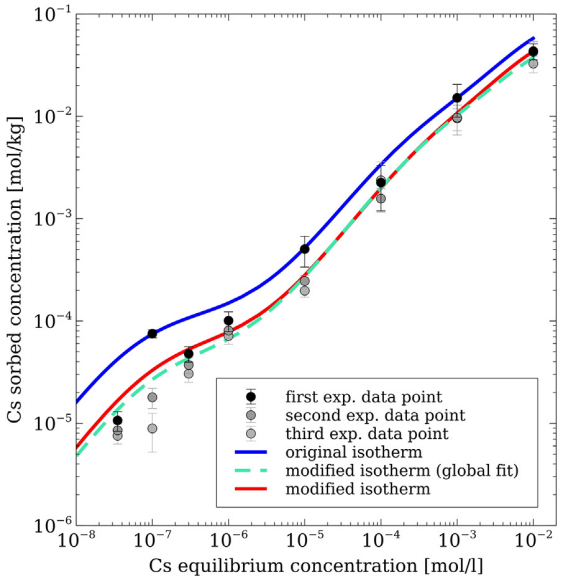

Fig. 3. Cs sorption isotherms with original parameters (blue line, section 2.2), and with optimized parameters (red line, cyan dashed line for global fit, Table 5); Experimental data: black and grey dots with error bars for the first three data points of the measured in-diffusion profile. (For interpretation of the references to colour in this figure legend, the reader is referred to the web version of this article.)

4.3. Global parameter estimation

The globally estimated model parameter values are in good agreement with the values obtained by the visual fit (Table 5). Site capacities of PS and FES from the global fit were found to be about 20% lower, those for the TTS about 10% higher than those from the visual fit. Both fitting procedures led to the same selectivity coefficients. The different site capacities result in a slightly different Cs sorption isotherm (Fig. 3). At low $C_{Cs,bg}$ of $3.5 \cdot 10^{-8}$ M to $3 \cdot 10^{-7}$ M the global fit tends to better match the isotherm data, whereas for 10^{-6} M sorption is underestimated. At mid-range concentrations both modified isotherms are about identical and for highest $C_{Cs,bg}$ sorption is slightly lower for the global fit. The surface mobilities were found to be nearly identical on the PS and about 20% lower on the FES compared to the visual fit. A very small mobility of $5.3 \cdot 10^{-4}$ was estimated for the TTS. The diffusion profiles for the global fit exhibit only small, hardly significant differences compared to those of the visual fit (Fig. 4). For all $C_{Cs,bg}$ the global fit parameters lead to slightly lower total Cs-134 concentrations over the diffusion distance. The differences of both fits increase with decreasing $C_{Cs,bg}$. These results show that a global fitting routine can be successfully applied to optimize the parameters for a complex diffusion-sorption behavior. In addition, the results corroborate the validity of the step-wise visual fit procedure, on which the following discussion will focus.

5. DISCUSSION

5.1. Sensitivity of the surface diffusion model to sorption parameters

Because of the direct coupling of the effective diffusion coefficient of the surface diffusion model to the sorption isotherm through the derivative term $\partial S/\partial C$, the diffusion behavior is sensitive to the choice of sorption parameters. In order to evaluate the influence of the sorption parameters on the simulated diffusion profiles, the CEC of the sorption sites was varied by ±40% and the selectivity coefficients by ±0.2 log ${}^{Cs}_{Na}K_c$ units (Figs. 5–7). A positive variation of the sorption parameters leads to higher effective diffusion coefficients and vice versa (Eqs. (5), (A5) and (A6)).

Table 5
Optimized values of the site capacities, selectivity coefficients and site-specific surface mobilities of Cs in Opalinus Clay. Left values: step-wise visual fitting; right values: global fit.

Parameter	PS		TTS		FES	
	Visual Fit	Global Fit	Visual Fit	Global Fit	Visual Fit	Global Fit
CEC [eq kg^{-1}]	$7 \cdot 10^{-2}$	$5.8 \cdot 10^{-2}$	$7.0 \cdot 10^{-3}$	$7.8 \cdot 10^{-3}$	$6.15 \cdot 10^{-5}$	$4.8 \cdot 10^{-5}$
${}^{Cs}_{Na}K_c$ [–]	1.6	1.60	3.0	3.01	6.8	6.82
surface mobility μ_s [–]	$3.3 \cdot 10^{-2}$	$3.4 \cdot 10^{-2}$	~0	$5.3 \cdot 10^{-4}$	$1.5 \cdot 10^{-3}$	$1.2 \cdot 10^{-3}$

A variation of the CEC of each site appears as a shift of the isotherm in a log-log plot along the y-axis (Fig. 5a). This leads to identical trends in the profiles at all $C_{Cs,bg}$ (Fig. 6). At the specimen-reservoir interface, where the OPA specimen is in equilibrium with the constant concentration in the reservoir, the difference between the base case and the upper and lower variation is equal to ±40%. With increasing distance from the interface, the variations approximate the base case faster or slower depending on the $C_{Cs,bg}$.

The variations of the sorption isotherm parameters affect the diffusion profiles differently in the surface diffusion model compared to a classical Fickian diffusion model having a single, constant diffusion coefficient. For a model with a constant diffusion coefficient a positive variation of CEC and/or ${}^{Cs}_{Na}K_c$ leads to a steeper diffusion profile, a negative variation to a flatter profile. For the surface diffusion model, the same trend appears when varying the CEC. However, the trend is less pronounced, because it is partly compensated by the larger effective diffusion coefficient calculated for a higher CEC (and vice versa) (see Eqs. (5), (A5) and (A6)).

The upper and lower variation of ${}^{Cs}_{Na}K_c$ lead to a different behavior. An increase or decrease of all ${}^{Cs}_{Na}K_c$ tends to shift the isotherm in a log-log plot along the x-axis to the left or to the right, respectively (Fig. 5b). Thus, little change in sorption (and thus in the effective diffusion coefficient) occurs in regions where the isotherm is flat (e.g., near saturation of a site) as compared to steep regions. As a consequence, the effect of a variation of all ${}^{Cs}_{Na}K_c$ on the simulated profiles clearly varies depending on $C_{Cs,bg}$ (Fig. 7). It does so in a complex manner because of the superposition of the three sorption sites and because $C_{Cs,bg}$ is not fully constant but decreases slightly along each diffusion profile. Therefore, depending on $C_{Cs,bg}$, the variations depart from the base case (10^{-3} M, 10^{-5} M, 10^{-6} M, $3 \cdot 10^{-7}$ M, 10^{-7} M) or approximate to the base case (10^{-2} M, 10^{-4} M, $3.5 \cdot 10^{-8}$ M) with increasing distance from the interface.

The variable influence of the sorption parameters on the shape of the diffusion profiles over the entire penetration distance clearly illustrates the difficulty to find an appropriate set of CEC and ${}^{Cs}_{Na}K_c$. We limited the range of selectivity coefficients to the given uncertainty of ± 0.2 log K units, and required the simulation to match the first data point of the profile within its uncertainty. It is possible that other sets of sorption parameters (and correspondingly other values for the surface mobilities) exist that describe the data similarly. However, it appears justified to restrict the values of the sorption parameters to the range of well-established data from the literature, which then restricts the values of surface mobilities to a relatively small range. In any case, the set of sorption parameters that was finally used led to an appropriate fit of the diffusion profiles with the estimated surface mobilities.

Because of the small size of the OPA rock specimens (diameter: 2.6 mm; length: 12 mm), the mineralogical composition, and therefore the illite/smectite content as well as the selectivities, can vary from specimen to specimen or within a specimen due to the natural heterogeneity of Opalinus Clay at the centimeter to (sub)millimeter scale. From Figs. 6 and 7 we can see that local variations of CEC and/or ${}^{Cs}_{Na}K_c$ could indeed be responsible for the scatter between the specimens or within a single specimen.

5.2. Sensitivity of surface diffusion model to surface mobilities

The site-specific surface mobilities determined from the experimental data were varied by ±20% in order to evaluate their influence on the diffusion profiles. At the specimen-reservoir interface the variations do not differ from the base case (Fig. 8), because the reservoir volume (100 mL, ratio to pore volume ~13′000) was large enough such that the reservoir concentration of Cs remained approximately constant, independent of the used μ_{si}. Larger and smaller μ_{si} lead to flatter and steeper profiles, respectively. Accordingly, the variations diverge with increasing penetration distance for all experiments. The surface mobilities are constant model parameters, such that their variation by ±20% leads to a 20% higher or lower contribution of the surface diffusion term to the effective diffusion coefficient. The effect is thus similar to a corresponding variation of the constant diffusion coefficient in the classical Fickian diffusion model, but not fully equivalent, because of dependence of $D_{e,comb}$ in our model on the slightly variable background Cs concentrations.

5.3. Average mobilities and comparison to existing data

One set of site-specific surface mobilities was found to describe the Cs diffusion behavior in Opalinus Clay. There are no reference data against which the present set of surface mobilities can be directly compared. However, it is possible to calculate the average mobility of Cs in OPA by weighting the site-specific mobilities with their average sorption capacity ratio. The average mobility can then be directly compared to the surface mobilities determined for

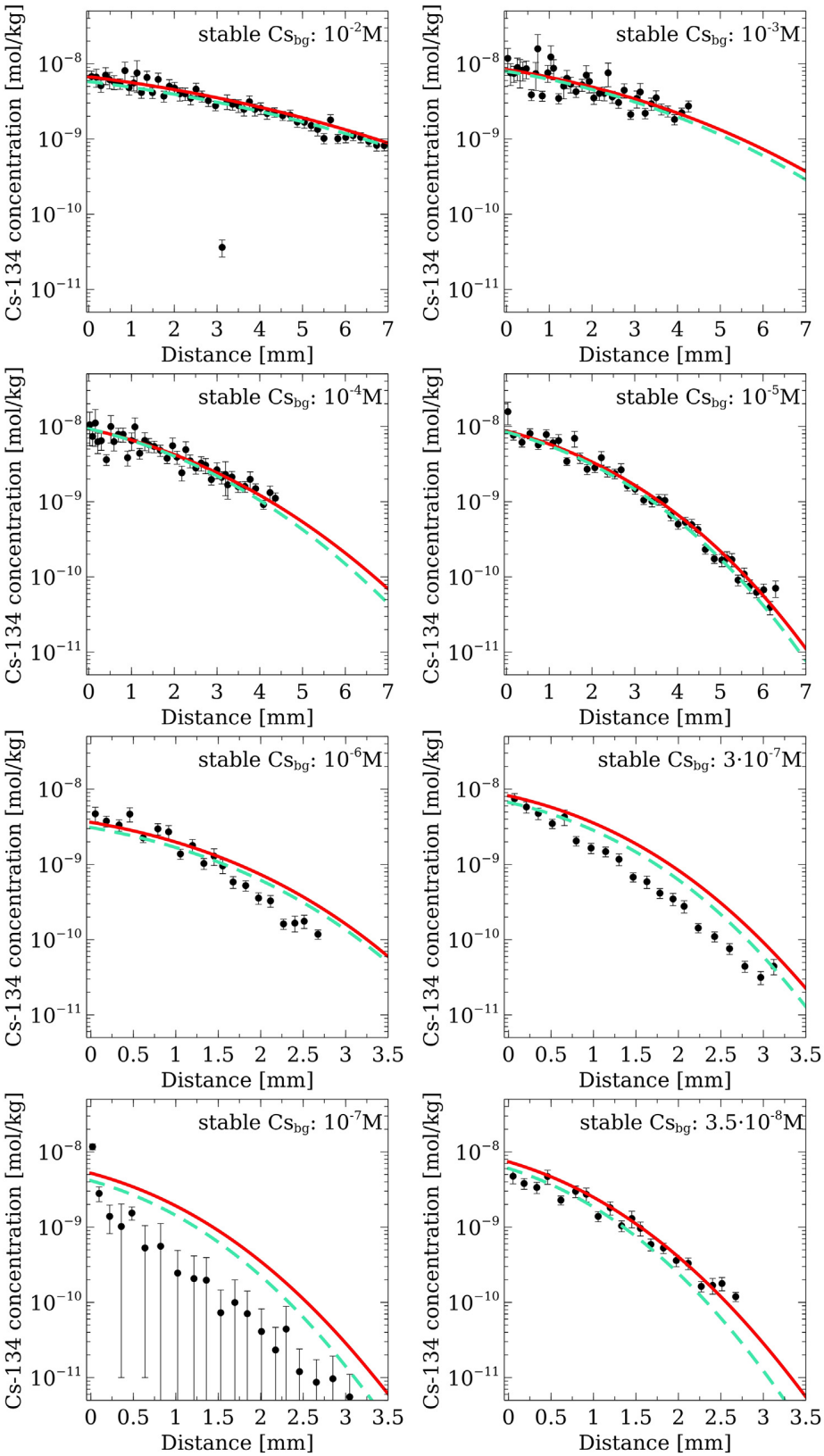

Fig. 4. Total (sorbed plus aqueous) Cs-134 concentration profiles for the experiments with $C_{Cs,bg}$ of 10^{-2} M, 10^{-3} M, 10^{-4} M, 10^{-5} M, 10^{-6} M, $3 \cdot 10^{-7}$ M, 10^{-7} M, and $3.5 \cdot 10^{-8}$ M. Red line: Three-site surface diffusion model with three surface mobilities fitted simultaneously to all data sets. Cyan dashed line: Three-site surface diffusion model with globally fitted parameters. Black dots with error bars: experimental data. The same concentration range is used on the y-axis in all plots, whereas profiles over 7 mm and 3.5 mm are shown on the x-axis for the first four and the last four plots, respectively. (For interpretation of the references to colour in this figure legend, the reader is referred to the web version of this article.)

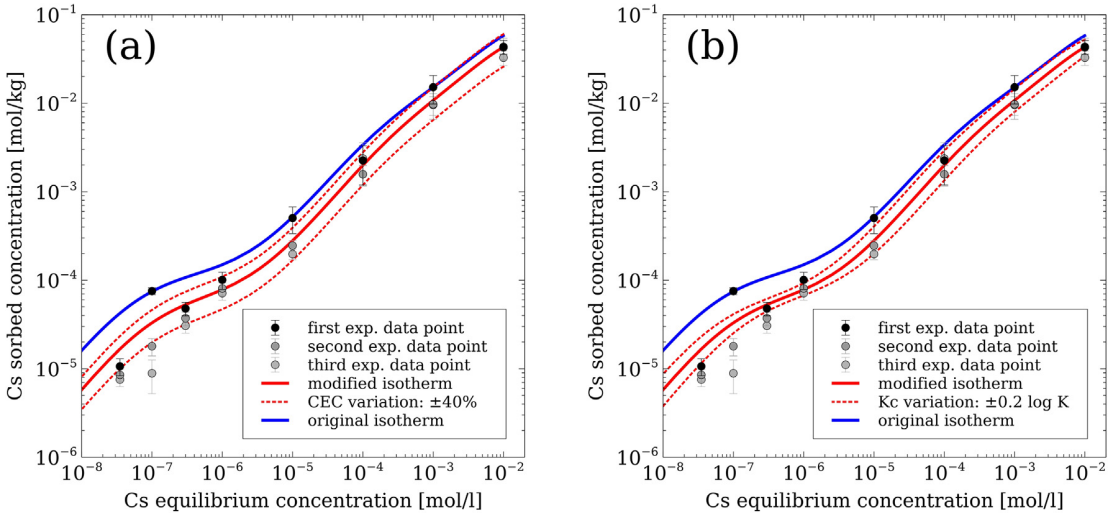

Fig. 5. Variation of CEC (left) and ${}^{Cs}_{Na}K_c$ (right): Cs sorption isotherms with original parameters (blue line, Section 2.2), with optimized parameters (red solid line, Table 5), and variations of the CEC and ${}^{Cs}_{Na}K_c$ of the modified isotherm (dotted red lines). Experimental data: Black and grey dots with error bars. (For interpretation of the references to colour in this figure legend, the reader is referred to the web version of this article.)

a large set of diffusion data in clays in Gimmi and Kosakowski (2011). The average mobility can be written as (Gimmi and Kosakowski, 2011):

$$\mu_{av} = \sum \frac{\kappa_i}{\kappa} \mu_{s,i} \tag{6}$$

with $\kappa = \sum \kappa_i$ and κ_i being the sorption capacity ratio for site i:

$$\kappa_i = \frac{\rho_{bd}}{\varepsilon} \frac{\partial S_i}{\partial C} \tag{7}$$

Table 6 shows the average mobilities for the different in-diffusion experiments. For high $C_{Cs,bg}$, the contribution of surface diffusion is dominated by the mobility on the planar sites ($\mu_{PS} = 3.3 \cdot 10^{-2}$), as expected. The calculated average mobilities for high Cs are in good agreement with the range of 1–4 · 10^{-2} determined in Gimmi and Kosakowski (2011). This finding confirms the validity of the estimated mobility on the planar sites. Kosakowski et al. (2008) performed molecular dynamics simulations determining Na and Cs diffusion in montmorillonite. They found values of μ_{PS} for monohydrated interlayers similar to ours (~0.002–0.1). This is plausible, because considering the high bulk dry density of OPA (~2.3 g mL^{-1}), mostly monohydrated interlayers are expected in OPA. With the estimated μ_{PS} and the derived (close to) zero mobility of Cs on the TTS, the experiments can be described down to a $C_{Cs,bg}$ of 10^{-6} M. A larger mobility on the TTS would result in a worse match of the data for the mid-range concentrations. The average mobilities derived here for Cs at trace conditions (~0.002 at very low Cs concentrations) in OPA are significantly larger than average values ($2 \cdot 10^{-4}$–$4 \cdot 10^{-4}$) found by Gimmi and Kosakowski (2011), but similar to their maximum values. The surface mobility of $1.5 \cdot 10^{-3}$ attributed here to the FES, which is dominant at low Cs, is comparably large. Such a high surface mobility on FES may not be expected considering the strong sorption of Cs on these sites (high ${}^{Cs}_{Na}K_c$), but is clearly required to describe the experimental data at low $C_{Cs,bg}$ (<10^{-6} M).

The site-specific surface mobilities may incorporate geometrical effects of the surface topology. By assuming $\tau_s = \tau_w$ we neglect the differences of surface and pore diffusion pathways for Cs. As a result, any deviation of the tortuosities between these pathways is accounted for in the fitted values of the surface mobilities.

5.4. Comparison with a classical diffusion model

The experimental data were also modeled with a classical Fickian diffusion model using the modified Cs-isotherm, in order to demonstrate the differences to a surface diffusion model. For every experiment, an effective diffusion coefficient of Cs $D_{e,Cs}$ was fitted separately to match the corresponding profile data. All fitted $D_{e,Cs}$ were larger than typical effective water tracer diffusion coefficients parallel to bedding, by a factor of 3 to 21 (Table 7; with an effective diffusion coefficient of a water tracer $D_{e,HTO}$ being $6 \cdot 10^{-11}$ m^2 s^{-1}). The fitted $D_{e,Cs}$ show a concentration dependency with increasing values from high to low $C_{Cs,bg}$. The different values of the diffusion coefficients demonstrate the difficulties using a classical Fickian diffusion model for describing Cs diffusion in OPA. The experiments cannot be described consistently with a single diffusion coefficient.

In contrast, the observations can be easily explained with the surface diffusion model. From $C_{Cs,bg}$ of 10^{-2} M to 10^{-5} M or 10^{-6} M, the relative diffusion coefficient $D_{e,Cs}/D_{e,HTO}$ increases from 3 to 5 (Table 7). At 10^{-2} M $C_{Cs,bg}$ planar sites approach saturation. This means that the derivative $\partial S_{PS}/\partial C$ is smaller at 10^{-2} M $C_{Cs,bg}$ compared to the lower $C_{Cs,bg}$ of 10^{-3} M, 10^{-4} M and 10^{-5} M (Table 6).

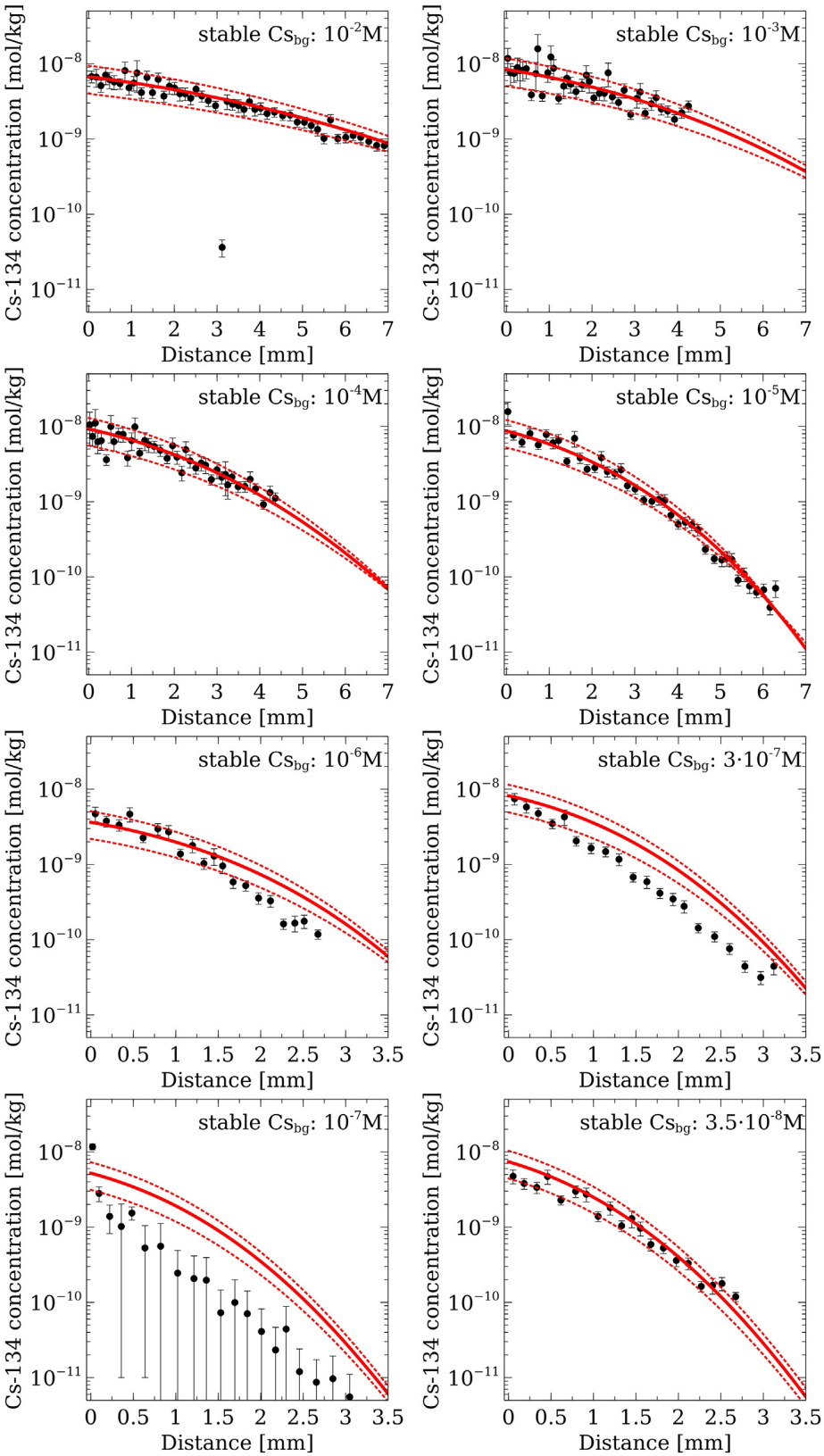

Fig. 6. Variation of CEC: Total Cs-134 concentration profiles for the eight experiments with different $C_{Cs,bg}$ as given in each plot. Red solid line: base case of three-site surface diffusion model; Red dotted lines: upper and lower CEC-variation of the surface diffusion model; Black dots with error bars: experimental data. (For interpretation of the references to colour in this figure legend, the reader is referred to the web version of this article.)

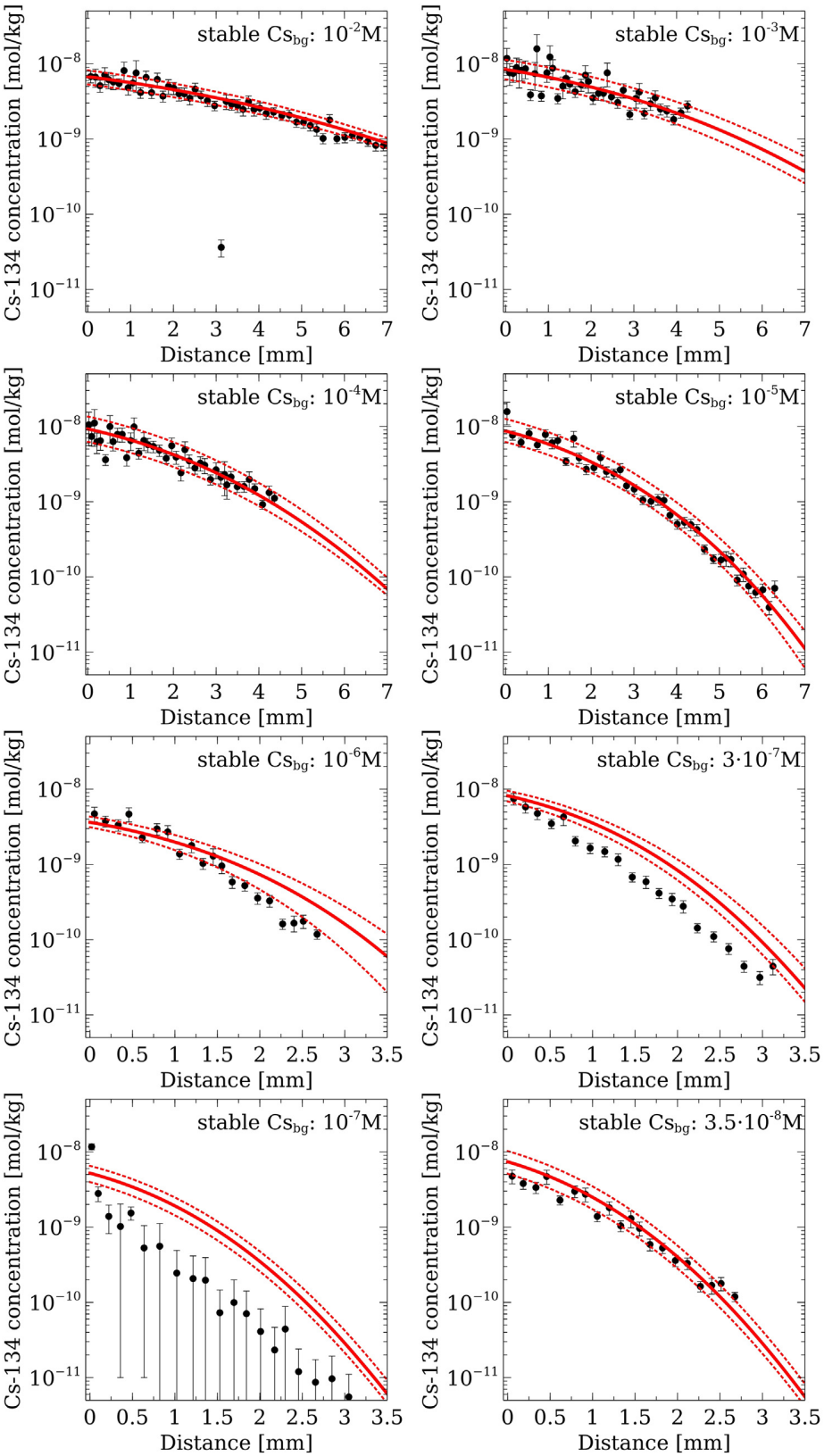

Fig. 7. Variation of ${}^{Cs}_{Na}K_c$: Total Cs-134 concentration profiles for the eight experiments with different $C_{Cs,bg}$ as given in each plot. Red solid line: base case of three-site surface diffusion model; Red dotted lines: upper and lower ${}^{Cs}_{Na}K_c$-variation of the surface diffusion model; Black dots with error bars: experimental data. (For interpretation of the references to colour in this figure legend, the reader is referred to the web version of this article.)

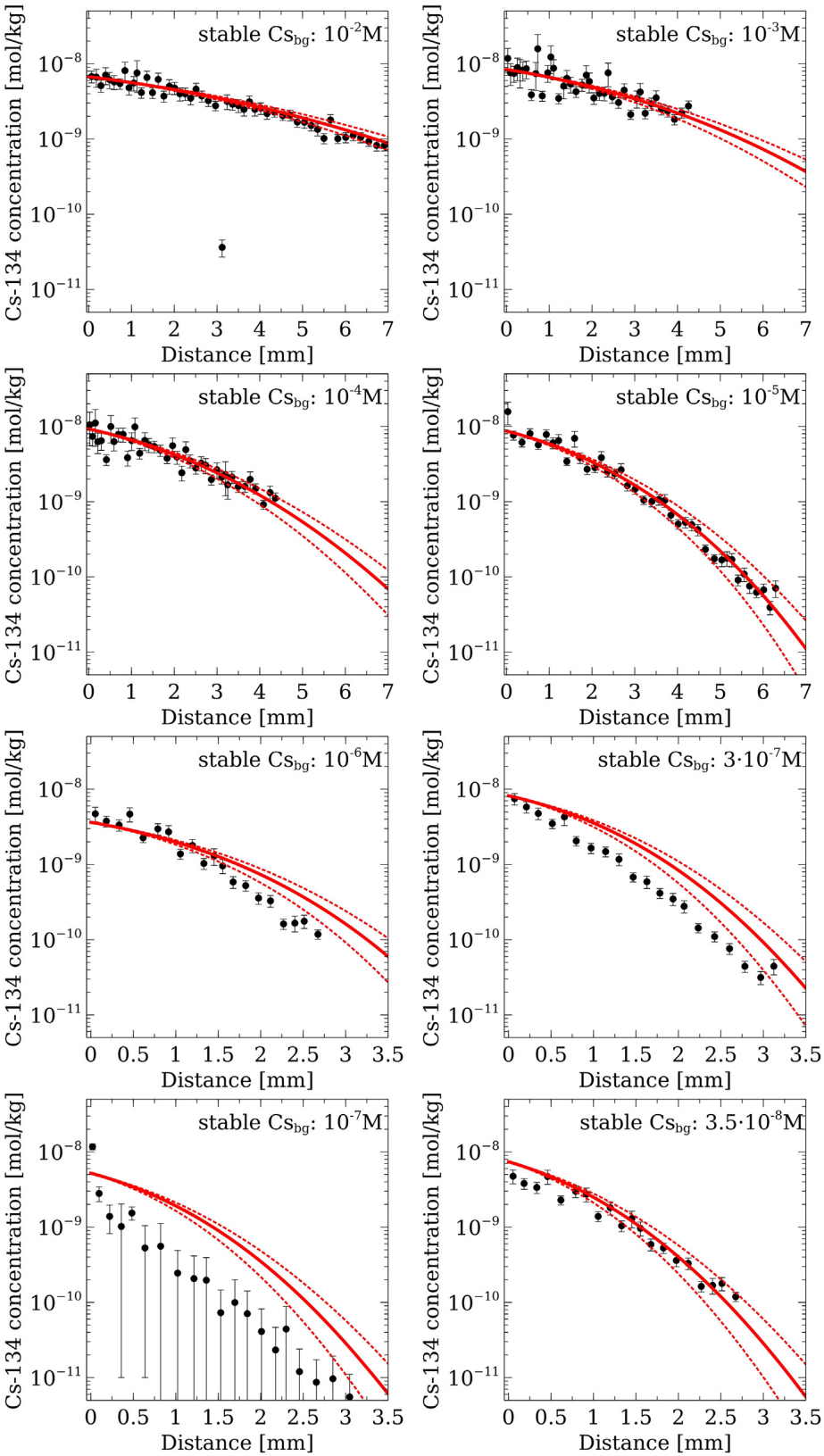

Fig. 8. Variation of surface mobilities: *Total* Cs-134 concentration profiles for the eight experiments with different $C_{Cs,bg}$ as given in each plot. Red solid line: Three-site surface diffusion model; Red dotted lines: upper and lower μ_{si}-variation of the surface diffusion model; Black dots with error bars: experimental data. (For interpretation of the references to colour in this figure legend, the reader is referred to the web version of this article.)

Table 6
Values of the derivatives of the sorption isotherm and capacity ratios for PS, TTS and FES and resulting average surface mobilities calculated for each experiment.

$C_{Cs,bg}$	$\partial S_{PS}/\partial C$	κ_{PS}/κ	$\partial S_{TTS}/\partial C$	κ_{TTS}/κ	$\partial S_{FES}/\partial C$	κ_{FES}/κ	μ_{av}
10^{-2} M	5.13	0.8253	1.08	0.1732	0.01	0.0014	0.027
10^{-3} M	7.93	0.5050	7.68	0.4895	0.09	0.0055	0.017
10^{-4} M	8.29	0.2989	18.52	0.6679	0.92	0.0332	0.010
10^{-5} M	8.33	0.1882	21.54	0.4865	14.40	0.3253	0.0067
10^{-6} M	8.30	0.0634	21.70	0.1656	101.02	0.7710	0.0033
$3 \cdot 10^{-7}$ M	8.30	0.0248	21.75	0.0649	304.83	0.9103	0.0022
10^{-7} M	8.48	0.0157	22.20	0.0412	508.55	0.9431	0.0019
$3.5 \cdot 10^{-8}$ M	8.30	0.0123	21.76	0.0323	643.57	0.9554	0.0018

At the latter concentrations, Cs sorption is about linear for the PS and the value of $\partial S_{PS}/\partial C$ is about constant, which is the reason for the constant effective diffusion coefficient in this concentration region. The ratio of $\partial S_{PS}/\partial C$ at 10^{-2} M and at 10^{-3} M to 10^{-5} M is ~0.6, which equals about the ratio of the relative diffusion coefficients in Table 7. The increasing diffusion coefficients at low $C_{Cs,bg}$ corroborate the findings of a non-negligible surface mobility of Cs sorbed on the FES in the surface diffusion model. Without a mobility of Cs on FESs, the surface diffusion model is not able to reproduce the experimental data or the large relative diffusion coefficient at the lowest Cs background concentrations.

5.5. Indications for diffuse and Stern layer diffusion

According to Appelo et al. (2010) 45% of the charge of the total CEC in OPA is compensated in the diffuse-layer. Wigger and Van Loon (2018) found that about 40% of the total porosity of OPA has to be attributed to DL (or Donnan) pores in order to describe anion exclusion effects. Therefore, DL effects certainly play a relevant role in diffusion of charged species. The surface diffusion model here does not directly account for diffusion in the DL; any DL effects are included indirectly in the average surface mobilities. A DL model can predict a dependency of diffusion on the ionic strength of the solution. However, a model including just DL sorption and diffusion cannot account for a dependence of diffusion on the Cs background concentration as observed here, and it would also predict equal effects for equally charged ions such as Cs and Na. In the experiments here, the solution composition with respect to the major ions was identical, except for the different Cs background, which is small compared to the total ion concentration. Then, neither a significant variation of the thickness of the diffuse layer for the different experiments, nor a variation of the diffusion coefficients in the DL, nor a variation of the distribution ratio of Cs between the DL and external pore water is expected. Accordingly, a DL-only model cannot reproduce the observed Cs concentration dependency of diffusion.

Table 7
Modeled effective Cs diffusion coefficient for the classical Fickian diffusion model and ratio of the Cs diffusion coefficient to the effective diffusion coefficient of a water tracer.

$C_{Cs,bg}$	$D_{e,Cs}$ (m^2 s^{-1})	$D_{e,Cs}/D_{e,HTO}$
10^{-2} M	$1.8 \cdot 10^{-10}$	3
10^{-3} M	$3 \cdot 10^{-10}$	5
10^{-4} M	$3 \cdot 10^{-10}$	5
10^{-5} M	$3 \cdot 10^{-10}$	5
10^{-6} M	$3 \cdot 10^{-10}$	5
$3 \cdot 10^{-7}$ M	$4.8 \cdot 10^{-10}$	8
10^{-7} M	$6 \cdot 10^{-10}$	10
$3.5 \cdot 10^{-8}$ M	$1.3 \cdot 10^{-9}$	21

Furthermore, in Cs diffusion studies with Cs reservoir concentrations of 10^{-3} M (Appelo et al., 2010) and $2 \cdot 10^{-4}$ M (Soler et al., 2019), where a model with DL diffusion was applied besides specific Cs sorption, bulk diffusion coefficients of Cs still had to be increased. This observation suggests that an additional diffusion process on PSs, which are dominant at these concentrations, contributes to the overall diffusive flux. Appelo et al. (2010) attributed this additional process to interlayer diffusion. The process may generally be related to a mobility of cations sorbed more specifically. Experimental data for Cs sorption onto muscovite (Lee et al., 2012) and molecular dynamics studies of Cs sorption on illite (Lammers et al., 2017) showed that Cs sorbs as inner-sphere complex on the respective basal planes, that is, in the Stern layer. This means that μ_{PS} incorporates not only DL diffusion, but also (to some degree) Stern layer diffusion. Such (partial) Stern layer diffusion becomes even more distinct at low $C_{Cs,bg}$, where FESs dominate sorption. There, a mobility of sorbed Cs on the FES (and therefore a higher effective diffusion coefficient) is required to match the experimental data. At these low $C_{Cs,bg}$, the proportion of specifically sorbed Cs (with higher selectivity) becomes larger, and Stern layer diffusion (or diffusion of more specifically sorbed Cs) can contribute proportionally more to the overall diffusive flux. However, to evaluate in more detail the contributions from diffuse and Stern layer diffusion, separate modeling of the experiments with a model considering also a DL is necessary.

5.6. Test of the model: Application to different Cs diffusion data in Opalinus Clay

The surface diffusion model with the estimated set of surface mobilities was finally tested against data of an independent, radial through-diffusion experiment for Cs in Opalinus Clay (Appelo et al., 2010). The experimental setup is described in detail in Van Loon et al. (2004a). The initial Cs concentration in the high concentration reservoir was 10^{-3} M. During the course of 1500 days, the reservoir

concentration decreased to approximately 10^{-5} M. The Cs flux at the outer boundary of the OPA specimen was measured. For our modeling the original Cs-isotherm parameters (Van Loon et al., 2009) were used, applying a CEC of 0.117 eq kg^{-1} for the PS as derived in Appelo et al. (2010). The sorption selectivity coefficients (Van Loon et al., 2009) were slightly adapted (±0.05 log K units) within the range of their uncertainty. Other model parameters (porosity, bulk dry density, tortuosity of water tracer) were taken from Appelo et al. (2010), and the surface mobilities as determined here. The surface diffusion model shows good agreement with the trend of the experimentally determined Cs flux (Fig. 9). However, the simulated arrival of the Cs front is somewhat delayed and the flux from the peak until day 1000 is slightly overestimated compared to the experimental data. To account for the delay either the pore diffusion coefficient can be increased or sorption can be decreased, but both modifications lead to a too high peak of the breakthrough curve. Appelo et al. (2010), when fitting a model including diffusion in the DL to the experimental data, observed exactly the same discrepancies. They explained the early arrival front compared to their simulation by the existence of dead-end pores, leading to physical kinetics of sorption. Also, they had to distribute the surface charges unequally between the open and the postulated dead-end pores. We did not include any dead-end pores in our model, because the early breakthrough could also result from experimental details not considered appropriately in the modeling. Irrespective of the dead-end pores, their fitted Cs diffusion coefficient is rather large, leading to a tortuosity much smaller than that for HTO. They interpreted this high diffusion coefficient (low tortuosity) as being the result of additional interlayer or surface diffusion of Cs (besides some ion pairing in the DL), a process not considered in their model. Having largely different tortuosities for Cs and HTO is unexpected, as (pore) diffusion of both occurs in the whole pore water. The overall good match between the experimental data and our surface diffusion model, using a tortuosity for Cs identical to that of HTO, is a proof that indeed this process is relevant for Cs. Furthermore, the test of the surface diffusion model with independently estimated surface mobilities was successful. There was no need to change surface mobilities compared to our calibration experiments, nor to adapt the Cs pore diffusion coefficient to any value that is difficult to defend (value of $D_{p,Cs}$ used here: $3.36 \cdot 10^{-10}$ m^2 s^{-1}). Therefore, the surface diffusion model appears to be capable to predict Cs diffusion in Opalinus Clay.

The experiment was additionally modeled using the classical Fickian diffusion model. Here, the effective Cs diffusion coefficient had to be fitted to $3.75 \cdot 10^{-10}$ m^2 s^{-1}, a value about 7 times larger than the effective diffusion coefficient of HTO. This again shows the inconsistency that arises when using the classical Fickian diffusion model for modeling Cs diffusion in Opalinus Clay.

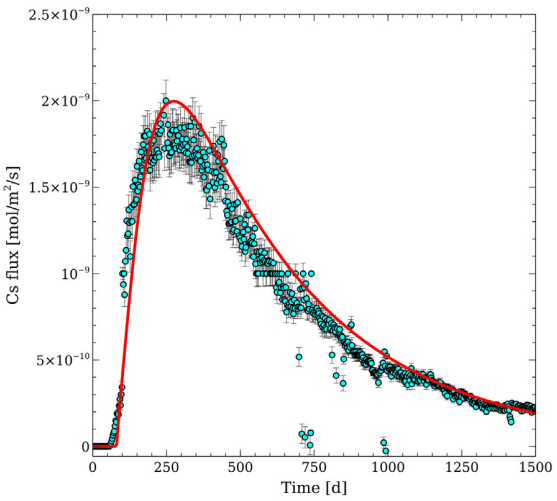

Fig. 9. Cs flux at the outer boundary of an Opalinus Clay specimen used in a radial diffusion experiment described in Appelo et al. (2010); Red line: surface diffusion model; Cyan dots with error bars: experimental data. (For interpretation of the references to colour in this figure legend, the reader is referred to the web version of this article.)

6. SUMMARY AND CONCLUSIONS

A multi-site surface diffusion model was implemented in the reactive transport code Flotran. In-diffusion experiments for Cs-134 in Opalinus Clay were conducted at different stable Cs background concentrations. Diffusion properties of Cs-134 clearly depended on the stable Cs background concentration. A single set of three site-specific surface mobilities could be estimated by fitting the surface diffusion model simultaneously to the data of the eight in-diffusion experiments. Parameters for the adsorption isotherm, only slightly adapted compared to literature values (within the given uncertainty range), led to a good match with the isotherm data points derived from our experiments. The results show that a multi-site surface diffusion model can describe the concentration-dependent Cs diffusion in Opalinus Clay consistently based on a single set of surface mobilities, while the Cs pore diffusion coefficient could be calculated from that in water and the assumed tortuosity of a water tracer. The observed concentration dependency of Cs diffusion cannot be explained by a classical diffusion model or by models including diffusion in the DL only. With a classical Fickian diffusion model, diffusion coefficients that depend on the Cs background concentration would be obtained. Sensitivities of the surface diffusion model to sorption parameters and surface mobilities were evaluated. Finally, the surface diffusion model with the estimated surface mobilities could successfully predict an other, independent Cs diffusion experiment in Opalinus Clay.

Even though the surface diffusion model was successfully applied to two data sets (the eight in-diffusion and the radial-diffusion experiments), it is clear that the presented surface diffusion model has limitations and has to be further improved. Site-specific surface mobilities of cations that compete with Cs for sorption in Opalinus Clay should probably be included for a more accurate description of Cs diffusion and sorption in situations with variable

pore water chemistry. Additionally, the application of molecular modeling of cation diffusion at clay surfaces could support the determination and/or validation of cation surface mobilities (e.g., Bourg and Sposito, 2011). Finally, at present the model focuses only on cations and does not consider effects of anion exclusion. Accordingly, a combination with a model that takes into account anion exclusion, such as DL models, is required. The combination of diffusion of cations that are specifically sorbed (e.g., in the Stern layer), diffusion in the DL and diffusion in free pore water could eventually lead to a consistent and more detailed model including all known diffusive processes in clays.

Declaration of Competing Interest

The authors declare that they have no known competing financial interests or personal relationships that could have appeared to influence the work reported in this paper.

ACKNOWLEDGMENTS

Financial support by the Swiss National Science Foundation (grant no. 200021_166287) is kindly acknowledged. We thank Dr. Bart Baeyens, Dr. Dan Miron and Dr. Wilfried Pfingsten for the fruitful discussions.

APPENDIX A

A.1. Calculation of the derivative term $\partial S/\partial C$ of the sorption isotherm

A general cation exchange reaction between cations A and B onto a sorption site can be written as:

$$\equiv S_B z_A + z_B C_A^{z_A} \Longleftrightarrow \equiv S_A z_B + z_A C_B^{z_B}$$

where C_A and C_B are the concentrations in solution, z_A and z_B are their charges and $\equiv S_A$ and $\equiv S_B$ are the sorbed concentrations on a cation exchange site.

The corresponding mass action law after the Gaines-Thomas convention (Gaines and Thomas, 1953) is:

$${}^{k}_{1}K_c = \frac{N_k^{z_1} a_1^{z_k}}{N_1^{z_k} a_k^{z_1}} \tag{A1}$$

where ${}^{k}_{1}K_c$ is the selectivity coefficient of cation k with respect to the reference cation 1, z is the cation charge, N is the fractional occupancy on the exchanger solid, i.e., the moles charge of cation k on the exchanger per cation exchange capacity, and a is the cation activity. The activity is related to the concentration C via:

$$a = \gamma C \tag{A2}$$

where γ is the activity coefficient. The sorbed concentration S_k of cation k (in moles per mass of dry solid) is related to the fractional occupancy according to

$$S_k = \frac{CEC}{z_k} N_k \tag{A3}$$

Rearranging Eq. (A1) for N_k leads to an expression for the fractional occupancy N_k of cation k:

$$N_k = \left(\frac{N_1}{a_1}\right)^{\frac{z_k}{z_1}} \left({}^{k}_{1}K_c\right)^{1/z_1} a_k \tag{A4}$$

Thus, N_k depends on the activity a_k and charge z_k of cation k in solution, on the selectivity coefficient ${}^{k}_{1}K_c$, and on the fractional occupancy, the activity and the charge of the reference cation 1. The partial derivative $\partial N_k/\partial a_k$ is then (applying the chain rule):

$$\frac{\partial N_k}{\partial a_k} = \left(\frac{N_1}{a_1}\right)^{\frac{z_k}{z_1}} \left({}^{k}_{1}K_c\right)^{1/z_1} \left(1 + \frac{z_k}{z_1}\frac{a_k}{N_1}\frac{\partial N_1}{\partial a_k} - \frac{z_k}{z_1}\frac{a_k}{a_1}\frac{\partial a_1}{\partial a_k}\right) \tag{A5}$$

The dependency of a_1 on a_k or the partial derivative $\partial a_1/\partial a_k$, respectively, is most often very small and can be neglected. The combination of Eq. (A3) and Eq. (A5) results in the derivative of the sorption isotherm:

$$\frac{\partial S_k}{\partial a_k} = \frac{CEC}{z_k}\frac{\partial N_k}{\partial a_k} \tag{A6}$$

The sum of the fractions of all competing cations for an exchange site is equal to 1 (full surface site coverage):

$$\sum_{i}^{imax} N_i = 1 \tag{A7}$$

Combining Eq. (A4) and Eq. (A7) we obtain an equation for N_1 as a function of all cation activities and selectivity coefficients:

$$N_1 + \sum_{i=2}^{imax} \left(\frac{N_1}{a_1}\right)^{\frac{z_i}{z_1}} \left({}^{i}_{1}K_c\right)^{1/z_1} a_i - 1 = 0 \tag{A8}$$

For homoionic exchange ($z_i/z_1 = 1$), Eq. (A8) can be solved analytically, but in general, N_1 is obtained numerically by using the secant method (or any other suitable method) to find the root. The partial derivative $\partial N_1/\partial a_k$ is then obtained also numerically by varying a_k in Eq. (A8). With N_1 and $\partial N_1/\partial a_k$, we can then derive the required derivatives according to Eqs. (A5) and (A6). The derivatives $\partial S_k/\partial C_j$ appearing in the more sophisticated Eqs. (3) and (4) are evaluated numerically accordingly by varying a_j instead of a_k.

APPENDIX B. SUPPLEMENTARY MATERIAL

Supplementary data to this article can be found online at https://doi.org/10.1016/j.gca.2021.01.012.

REFERENCES

Appelo C. A. J., Van Loon L. R. and Wersin P. (2010) Multicomponent diffusion of a suite of tracers (HTO, Cl, Br, I, Na, Sr, Cs) in a single sample of Opalinus Clay. *Geochim. Cosmochim. Acta* **74**, 1201–1219.

Benedicto A., Missana T. and Fernández A. M. (2014) Interlayer collapse affects on cesium adsorption onto illite. *Environ. Sci. Technol.* **48**, 4909–4915.

Berry J. A. and Bond K. A. (1992) Studies of the extent of surface diffusion in the migration of radionuclides through geological materials. *Radiochim. Acta* **58–59**, 329–336.

Bourg I. C. and Sposito G. (2011) Molecular dynamics simulations of the electrical double layer on smectite surfaces contacting concentrated mixed electrolyte (NaCl-$CaCl_2$) solutions. *J. Colloid Interface Sci.* **360**, 701–715.

Bowden J. W., Posner A. M. and Quirk J. P. (1977) Ionic adsorption on variable charge mineral surfaces. Theoretical-charge development and titration curves. *Aust. J. Soil Res.* **15**, 121–136.

Bradbury M. H. and Baeyens B. (2000) A generalised sorption model for the concentration dependent uptake of caesium by argillaceous rocks. *J. Contam. Hydrol.* **42**, 141–163.

Bradbury M. H. and Baeyens B. (1998) A physicochemical characterisation and geochemical modelling approach for determining porewater chemistries in argillaceous rocks. *Geochim. Cosmochim. Acta* **62**, 783–795.

Brouwer E., Baeyens B., Maes A. and Cremers A. (1983) Cesium and rubidium ion equilibria in illite clay. *J. Phys. Chem.* **87**, 1213–1219.

Carnie, S. L. and Torrie G. M. (1984) The Statistical Mechanics of the Electrical Double Layer. In Advances in Chemical Physics (eds. I. Prigogine and S. A. Rice). pp. 141–253.

Chen Z., Montavon G., Ribet S., Guo Z., Robinet J. C., David K., Tournassat C., Grambow B. and Landesman C. (2014) Key factors to understand in-situ behavior of Cs in Callovo-Oxfordian clay-rock (France). *Chem. Geol.* **387**, 47–58.

Cherif M. A., Martin-Garin A., Gérard F. and Bildstein O. (2017) A robust and parsimonious model for caesium sorption on clay minerals and natural clay materials. *Appl. Geochem.* **87**, 22–37.

Cheung S. C. H. (1990) A new interpretation of measured ionic diffusion coefficient in compacted bentonite-based materials. *Eng. Geol.* **28**, 369–378.

Davis J. A., James R. O. and Leckie J. O. (1978) Surface ionization and complexation at the oxide/water interface. *J. Colloid Interface Sci.* **63**, 480–499.

Elprince A. M., Vanselow A. P. and Sposito G. (1980) Heterovalent, ternary cation exchange equilibria: NH_4^+ -Ba^{2+} -La^{3+} exchange on montmorillonite. *Soil Sci. Soc. Am. J.* **44**, 964–969.

Eriksen T. E., Jansson M. and Molera M. (1999) Sorption effects on cation diffusion in compacted bentonite. *Eng. Geol.* **54**, 231–236.

Fernandes M. M. and Baeyens B. (2019) Cation exchange and surface complexation of lead on montmorillonite and illite including competitive adsorption effects. *Appl. Geochem.* **100**, 190–202.

Fletcher P. and Sposito G. (1989) The chemical modelling of clay/electrolyte interactions for montmorillonite. *Clay Miner.*, 375–391.

Flury M. and Gimmi T. (2018) 6.2 Solute Diffusion. In Methods of Soil Analysis (eds. J. H. Dane and G. C. Topp). pp. 1323–1351.

Fuller A. J., Shaw S., Peacock C. L., Trivedi D., Small J. S., Abrahamsen L. G. and Burke I. T. (2014) Ionic strength and pH dependent multi-site sorption of Cs onto a micaceous aquifer sediment. *Appl. Geochem.* **40**, 32–42.

Gaines G. L. and Thomas H. C. (1953) Adsorption studies on clay minerals. II. A formulation of the thermodynamics of exchange adsorption. *J. Chem. Phys.* **21**, 714–718.

Gimmi T. and Kosakowski G. (2011) How mobile are sorbed cations in clays and clay rocks?. *Environ. Sci. Technol.* **45** 1443–1449.

Gimmi T., Waber H. N., Gautschi A. and Rübel A. (2007) Stable water isotopes in pore water of Jurassic argillaceous rocks as tracers for solute transport over large spatial and temporal scales. *Water Resour. Res.* **43**, 1–16.

Helios Rybicka E., Calmano W. and Breeger A. (1995) Heavy metals sorption/desorption on competing clay minerals; an experimental study. *Appl. Clay Sci.* **9**, 369–381.

Huang C.-P. and Stumm W. (1973) Specific adsorption of cations on hydrous γ-Al_2O_3. *J. Colloid Interface Sci.* **43**, 409–420.

Jakob A., Pfingsten W. and Van Loon L. (2009) Effects of sorption competition on caesium diffusion through compacted argillaceous rock. *Geochim. Cosmochim. Acta* **73**, 2441–2456.

Jenny H. and Overstreet R. (1939) Surface migration of ions and contact exchange. *J. Phys. Chem.* **43**, 1185–1196.

Johnson S. G. (2019) The NLopt nonlinear-optimization package. http://github.com/stevengj/nlopt.

Kosakowski G., Churakov S. V. and Thoenen T. (2008) Diffusion of Na and Cs in montmorillonite. *Clays Clay Miner.* **56**, 190–206.

Lammers L. N., Bourg I. C., Okumura M., Kolluri K., Sposito G. and Machida M. (2017) Molecular dynamics simulations of cesium adsorption on illite nanoparticles. *J. Colloid Interface Sci.* **490**, 608–620.

Lauber M., Baeyens B. and Bradbury M. H. (2000) Physico-chemical characterisation and sorption measurements of Cs, Sr, Ni, Eu, Th, Sn and Se on Opalinus Clay from Mont Terri. PSI Bericht No. 00-10, Paul Scherrer Institut, Villigen, NAGRA NTB 00-11, Nagra, Wettingen, Switz.

Lee S. S., Fenter P., Nagy K. L. and Sturchio N. C. (2012) Monovalent ion adsorption at the muscovite (001)-solution interface: Relationships among ion coverage and speciation, interfacial water structure, and substrate relaxation. *Langmuir* **28**, 8637–8650.

Leroy P. and Revil A. (2004) A triple-layer model of the surface electrochemical properties of clay minerals. *J. Colloid Interface Sci.* **270**, 371–380.

Leroy P., Revil A., Altmann S. and Tournassat C. (2007) Modeling the composition of the pore water in a clay-rock geological formation (Callovo-Oxfordian, France). *Geochim. Cosmochim. Acta* **71**, 1087–1097.

Lichtner P. C. (2007) Flotran User's Manual: Two-Phase Non-isothermal Coupled Thermal-Hydrological-Chemical (THC) Reactive Flow &Transport Code, Version 2.0.

Van Loon L. R., Baeyens B. and Bradbury M. H. (2009) The sorption behaviour of caesium on Opalinus Clay: A comparison between intact and crushed material. *Appl. Geochem.* **24**, 999–1004.

Van Loon L. R. and Müller W. (2014) A modified version of the combined in-diffusion/abrasive peeling technique for measuring diffusion of strongly sorbing radionuclides in argillaceous rocks: A test study on the diffusion of caesium in Opalinus Clay. *Appl. Radiat. Isot.* **90**, 197–202.

Van Loon L. R., Soler J. M., Müller W. and Bradbury M. H. (2004a) Anisotropic diffusion in layered argillaceous rocks: A case study with Opalinus Clay. *Environ. Sci. Technol.* **38**, 5721–5728.

Van Loon L. R., Wersin P., Soler J. M., Eikenberg J., Gimmi T., Hernán P., Dewonck S. and Savoye S. (2004b) In-situ diffusion of HTO, $^{22}Na^+$, Cs^+ and I^- in Opalinus Clay at the Mont Terri underground rock laboratory. *Radiochim. Acta* **92**, 757–763.

Lyklema J. (2001) Surface conduction. *J. Phys. Condens. Matter.* **13**, 5027–5034.

Lyklema J., Rovillard S. and De Coninck J. (1998) Electrokinetics: The properties of the stagnant layer unraveled. *Langmuir* **14**.

Mazurek M., Alt-epping P., Bath A., Gimmi T., Waber H. N., Buschaert S., Cannière P., De Craen M., De Gautschi A., Savoye S., Vinsot A., Wemaere I. and Wouters L. (2011) Natural tracer profiles across argillaceous formations. *Appl. Geochem.* **26**, 1035–1064.

Melkior T., Yahiaoui S., Motellier S., Thoby D. and Tevissen E. (2005) Cesium sorption and diffusion in Bure mudrock samples. *Appl. Clay Sci.* **29**, 172–186.

Missana T., Benedicto A., García-Gutiérrez M. and Alonso U. (2014a) Modeling cesium retention onto Na-, K- and Ca-smectite: Effects of ionic strength, exchange and competing cations on the determination of selectivity coefficients. *Geochim. Cosmochim. Acta* **128**, 266–277.

Missana T., García-Gutiérrez M., Benedicto A., Ayora C. and De-Pourcq K. (2014b) Modelling of Cs sorption in natural mixed-clays and the effects of ion competition. *Appl. Geochem.* **49**, 95–102.

Montoya V., Baeyens B., Glaus M. A., Kupcik T., Marques Fernandes M., Van Laer L., Bruggeman C., Maes N. and Schäfer T. (2018) Sorption of Sr, Co and Zn on illite: Batch experiments and modelling including Co in-diffusion measurements on compacted samples. *Geochim. Cosmochim. Acta* **223**, 1–20.

Nagra (2002) Project Opalinus clay: safety report—demonstration of disposal feasibility for spent fuel, vitrified high-level waste and long-lived intermediate-level waste (Entsorgungsnachweis). Nagra technical report NTB-02-05. Nagra, Wettingen, Switzerland.

Neal C. and Cooper D. M. (1983) Extended version of Gouy-Chapman electrostatic theory as applied to the exchange behavior of clay in natural waters. *Clays Clays Miner.* **31**, 367–376.

Poinssot C., Baeyens B. and Bradbury M. H. (1999) Experimental and modelling studies of caesium sorption on illite. *Geochim. Cosmochim. Acta* **63**, 3217–3227.

Revil A., Cathles L. M., Losh S. and Nunn J. A. (1998) Electrical conductivity in shaly sands with geophysical applications. *J. Geophys. Res.* **103**, 23925–23936.

Robin V., Tertre E., Beaufort D., Regnault O., Sardini P. and Descostes M. (2015) Ion exchange reactions of major inorganic cations (H+, Na+, Ca2+, Mg2+ and K+) on beidellite: Experimental results and new thermodynamic database. Toward a better prediction of contaminant mobility in natural environments. *Appl. Geochem.* **59**, 74–84.

Savoye S., Beaucaire C., Fayette A., Herbette M. and Coelho D. (2012) Mobility of cesium through the callovo-oxfordian claystones under partially saturated conditions. *Environ. Sci. Technol.* **46**, 2633–2641.

Sawhney B. L. (1972) Selective sorption and fixation of cations by clay minerals. A review. *Clays Clay Miner.* **20**, 93–100.

van Schaik J. C., Kemper W. D. and Olsen S. R. (1966) Contribution of adsorbed cations to diffusion in clay-water systems. *Soil Sci. Soc. Am. J.* **30**, 17–22.

Shainberg I., Alperovitch N. I. and Keren R. (1987) Charge density and Na-K-Ca exchange on smectites. *Clays Clay Miner.* **35**, 68–73.

da Silva Santos C. H., Gonçalves M. S. and Hernandez-Figueroa H. E. (2010) Designing novel photonic devices by bio-inspired computing. *IEEE Photon. Technol. Lett.* **22**, 1177–1179.

Singh U. and Uehara G. (1999) Electrochemistry of the double layer: Principles and applications to soils. In *Soil Physical Chemistry* (ed. D. L. Sparks), Second Edition. CRC Press, Boca Raton, pp. 1–46.

Siroux B., Wissocq A., Beaucaire C., Latrille C., Petcut C., Calvaire J., Tabarant M., Benedetti M. F. and Reiller P. E. (2018) Adsorption of strontium and caesium onto an Na-illite and Na-illite/Na-smectite mixtures: Implementation and application of a multi-site ion-exchange model. *Appl. Geochem.* **99**, 65–74.

Soler J. M., Steefel C. I., Gimmi T., Leupin O. X. and Cloet V. (2019) Modeling the ionic strength effect on diffusion in clay. The DR-A Experiment at Mont Terri. *ACS Earth Sp. Chem.* **3**, 442–451.

Sposito G. (1992) The Diffuse-Ion Swarm Near Smectite Particles Suspended in 1:1 Electrolyte Solutions: Modified Gouy-Chapman Theory and Quasicrystal Formation eds. P. F. Low, J. K. Mitchell, G Sposito, H. van Olphen, N. Güven, and R. M. Pollastro. Clay-Water Interface its Rheol. Implic. 4, 128–155.

Staunton S. and Roubaud M. (1997) Adsorption of ^{137}Cs on montmorillonite and illite: Effect of charge compensating cation, ionic strength, concentration of Cs, K and fulvic acid. *Clays Clay Miner.* **45**, 251–260.

Steefel C. I., Carroll S., Zhao P. and Roberts S. (2003) Cesium migration in Hanford sediment: A multisite cation exchange model based on laboratory transport experiments. *J. Contam. Hydrol.* **67**, 219–246.

Stumm W. and Morgan J. J. (1996) *Aquatic Chemistry*, third edit. John Wiley & Sons Inc., New York.

Tachi Y. and Yotsuji K. (2014) Diffusion and sorption of Cs^+, Na^+, I^- and HTO in compacted sodium montmorillonite as a function of porewater salinity: Integrated sorption and diffusion model. *Geochim. Cosmochim. Acta* **132**, 75–93.

Tournassat C., Gailhanou H., Crouzet C., Braibant G., Gautier A., Lassin A., Blanc P. and Gaucher E. C. (2007) Two cation exchange models for direct and inverse modelling of solution major cation composition in equilibrium with illite surfaces. *Geochim. Cosmochim. Acta* **71**, 1098–1114.

Tournassat C., Chapron Y., Leroy P., Bizi M. and Boulahya F. (2009) Comparison of molecular dynamics simulations with triple layer and modified Gouy-Chapman models in a 0.1 M NaCl-montmorillonite system. *J. Colloid Interface Sci.* **339**, 533–541.

Weber C. and Stanjek H. (2017) Low-frequency electrical conductivity of aqueous kaolinite suspensions: surface conductance, electrokinetic potentials and counterion mobility. *Clay Miner.* **52**, 299–313.

Wersin P., Van Loon L. R., Soler J. M., Yllera A., Eikenberg J., Gimmi T., Hernán P. and Boisson J. Y. (2004) Long-term diffusion experiment at Mont Terri: First results from field and laboratory data. *Appl. Clay Sci.* **26**, 123–135.

Wersin P., Soler J. M., Van Loon L., Eikenberg J., Baeyens B., Grolimund D., Gimmi T. and Dewonck S. (2008) Diffusion of HTO, Br^-, I^-, Cs^+, $^{85}Sr^{2+}$ and $^{60}Co^{2+}$ in a clay formation: Results and modelling from an in situ experiment in Opalinus Clay. *Appl. Geochem.* **23**, 678–691.

Westall J. and Hohl H. (1980) A comparison of electrostatic models for the oxide/solution interface. *Adv. Colloid Interface Sci.* **12**, 265–294.

Wigger C. and Van Loon L. R. (2018) Effect of the pore water composition on the diffusive anion transport in argillaceous, low permeability sedimentary rocks. *J. Contam. Hydrol.* **213**, 40–48.

Yu C., Gonçalvès J. and Matray J. (2018) Bayesian inversion of a chloride profile obtained in the hydraulically undisturbed Opalinus Clay: Mass transport and paleo-hydrological implications. *Appl. Geochem.* **93**, 178–189.

Zachara J. M., Smith S. C., Liu C., McKinley J. P., Serne R. J. and Gassman P. L. (2002) Sorption of Cs^+ to micaceous subsurface sediments from the Hanford site, USA. *Geochim. Cosmochim. Acta* **66**, 193–211.

Associate editor: Christophe Tournassat

Correction note

This short note serves to identify and correct an error that occurred when implementing a surface diffusion model into the transport code Flotran (Krejci et al., 2021). Luckily, the error has only relatively minor consequences. We outline briefly the source of the error, we explain the way it is corrected, and we discuss the consequences of this error with regard to the values of estimated transport parameters.

The cation mass flux of the surface diffusion model is calculated in Flotran using concentration gradients. According to Eq. (1) in Krejci et al. (2021), the flux equation of the surface diffusion model is:

$$j_{tot} = j_p + j_s = -\varepsilon \frac{D_0}{\tau_p} \frac{\partial C}{\partial x} - \rho_{bd} \frac{D_{s0}}{\tau_s} \frac{\partial S}{\partial x} \tag{C1}$$

Here, the sorbed concentration gradient $\partial S/\partial x$ is expressed by:

$$\frac{\partial S}{\partial x} = \frac{\partial S}{\partial C} \frac{\partial C}{\partial x} \tag{C2}$$

where $\partial S/\partial C$ is the derivative of the sorption isotherm.

Then the mass flux can be written as:

$$j_{tot} = j_p + j_s = -\varepsilon \frac{D_0}{\tau_p} \frac{\partial C}{\partial x} - \rho_{bd} \frac{D_{s0}}{\tau_s} \frac{\partial S}{\partial C} \frac{\partial C}{\partial x} \tag{C3}$$

Chemical reactions such as aquatic complexation or cation exchange reactions, in contrast, were calculated using ion activities. As a consequence, the derivative of the sorption isotherm $\partial S/\partial a$ was calculated considering cation activities (see Eqs. (A5) and (A6) in Krejci et al. (2021)).

In Krejci et al. (2021), the derivative of the sorption isotherm $\partial S/\partial a$ was falsely inserted into Eq. (C3). Correctly, the derivative based on the cation concentration $\partial S/\partial C$ should be used. In order to judge the effect of this erroneous implementation, the relationship between $\partial S/\partial a$ and $\partial S/\partial C$ is investigated in the following paragraph.

The activity gradient $\partial a/\partial x$ can be developed as follows:

$$\frac{\partial a}{\partial x} = \frac{\partial (C\gamma)}{\partial x} = \gamma \frac{\partial C}{\partial x} + C \frac{\partial \gamma}{\partial x} = \gamma \left(\frac{\partial C}{\partial x} + C \frac{\partial \ln \gamma}{\partial x} \right) \tag{C4}$$

This leads to:

$$\partial a = \gamma (\partial C + C \partial \ln \gamma) \tag{C5}$$

Using Eq. (C5), the derivative of the sorption isotherm with regard to activities can be written as

$$\frac{\partial S}{\partial a} = \frac{\partial S}{\gamma (\partial C + C \partial \ln \gamma)} \tag{C6}$$

Considering approximately constant activity coefficients in the direction of diffusion (as for instance for tracer experiments), Eq. (C6) reduces to:

$$\frac{\partial S}{\partial a}=\frac{1}{\gamma}\frac{\partial S}{\partial C} \text{ and } \frac{\partial S}{\partial C}=\gamma\frac{\partial S}{\partial a} \quad \text{(C7)}$$

From Eq. (C7) it can be seen that, under conditions of negligible gradients of the activity coefficient, the derivative of the sorption isotherm with respect to concentrations $\partial S/\partial C$ and required in Eq. (C3) is smaller or larger by a factor γ than the derivative with respect to activities $\partial S/\partial a$.

As a consequence, the derivatives of the sorption isotherms determined in Krejci et al. (2021) (Table 6) are a factor $1/\gamma$ too high. In turn, this has also an effect on the values of the site-specific Cs surface mobilities derived from the experimental data.

The combined effective diffusion coefficient of the multi-site surface diffusion model is expressed by Eq. (5) in Krejci et al. (2021):

$$D_{e,comb}=\frac{\varepsilon D_0}{\tau_p}+\rho_{bd}\sum_i \frac{\mu_{s,i}D_0}{\tau_s}\frac{\partial S_i}{\partial C} \quad \text{(C8)}$$

From Eq. (C8) it can be seen that the combined effective diffusion coefficient depends on the product of the derivatives of the sorption isotherm $\partial S_i/\partial C$ and the site-specific surface mobilities μ_i. In order to obtain the same combined effective diffusion coefficient when using the correct derivatives of the sorption isotherm $\partial S_i/\partial C$, the site-specific surface mobilities μ_i derived in Krejci et al. (2021) (Table 5) have to be multiplied by a factor of $1/\gamma$. For the values of activity coefficients in the investigated system of Krejci et al. (2021), this means that the listed surface mobilities should be multiplied by a factor of 1.36.

The multi-site surface diffusion model implemented in Flotran was corrected by replacing $\partial S/\partial a$ with $\partial S/\partial C$.

Chapter 3:
A diffusion model that includes transport in the diffuse layer, the Stern layer and the interlayer region: Application to HTO, Cl, Na, Sr, and Cs diffusion in Volclay bentonite

(Manuscript ready for submission)

A diffusion model that includes transport in the diffuse layer, the Stern layer and the interlayer region: Application to HTO, Cl, Na, Sr, and Cs diffusion in Volclay bentonite

Philipp Krejci[a,b,], Thomas Gimmi[a,b], Luc Robert Van Loon[a], Martin Glaus[a]*

[a]*Laboratory for Waste Management, Nuclear Energy and Safety, Paul Scherrer Institut, CH-5232 Villigen, Switzerland*

[b]*Rock-Water Interaction, Institute of Geological Sciences, University of Bern, CH-3012 Bern, Switzerland*

*Corresponding author at: Paul Scherrer Institute; *E-mail address*: philipp.krejci@psi.ch (P. Krejci)

Abstract

The diffusive flux of cations is enhanced and that of anions is decreased compared to that of water tracers in bentonite or other clays, as a result of electrostatic interactions between ions and the charged clay surfaces. Clays are often used or foreseen as barriers in waste disposal in order to protect the environment from hazardous materials. A consistent description of diffusion of various ions and uncharged species is important in this context, especially if long-term interactions between clays and other materials shall be predicted by reactive transport simulations. Here, diffusion of a suite of tracers (HTO, Cl, Na, Sr and Cs) in Volclay bentonite was investigated. Experimental through-diffusion data at different bentonite dry densities were described with models of increasing complexity. First, 'standard' empirical single ion transport models (uncoupled, simple Fickian diffusion) were applied for each density. These models served as reference cases for comparisons. For sorbing tracers (Na, Sr, Cs), surface diffusion models were used in a next step, where average surface mobilities for the cations were determined based on comparisons with transport parameters from HTO diffusion. Finally, a more complex model was developed in order to describe anion and cation diffusion in a coupled way. This model accounts for locally parallel diffusion in different environments, namely in 'free' water unaffected by surface charges, in diffuse (Donnan) layer water, within the Stern layer, and within interlayer water (DL-SL-IL model). This coupled model requires additional parameters related to the bentonite microstructure as well as to cation mobilities in the Stern layer and in the interlayer. The latter were taken from literature. Microstructural parameters were constrained in a manner that overall anion exclusion matches anion accessible porosities found by the simple Fickian diffusion model. This was possible with a reasonable choice of microstructure parameters that are consistent with literature values. A good agreement between the experimental data and the simulated diffusion coefficients of the DL-SL-IL model was found. Thus, cation diffusion coefficients for the different bentonite densities could be predicted well based on literature surface mobilities and microstructural parameters. The latter had to be constrained, however, by HTO and Cl diffusion data.

1 Introduction

Montmorillonite is the main component of Volclay bentonite. Pore water in montmorillonite and bentonite is to a large extent located in interlayers, but it occupies also pores on external surfaces of montmorillonite or other particles. Experimental porosity investigations with magnetic resonance (NMR) and small-angle X-ray scattering spectroscopy (SAXS) in MX80 bentonite and Ca-montmorillonite (Matusewicz et al., 2013; Muurinen et al., 2013; Matusewicz and Olin, 2019) suggest that the total pore space can be divided into an external or interparticle pore space and an interlayer pore space. Interlayer pore sizes of Na- and Ca-montmorillonite were estimated by X-ray diffraction (XRD) and NMR relaxometry (Ohkubo et al., 2016; Ohkubo et al., 2021) and XRD (Holmboe et al., 2012) for different degrees of compaction. Under high compaction, 1-3 hydrated (water) layers were found, while for less compacted Na-montmorillonite even a 4-layer hydration state has been reported. The interlayer pore size distribution was generally found to be dependent on clay dry density, prevailing cation, and ionic strength of the pore solution.

Adsorption of alkali and alkaline earth metals in bentonite and montmorillonite are usually described by cation exchange models (e.g., Bradbury and Baeyens, 2002; Missana, 2007; Van Loon and Glaus, 2008; Missana et al., 2014; Siroux et al., 2017). Missana (2007) found a 1-site cation exchange model sufficient for describing Ca and Sr sorption in FEBEX bentonite, while a 2-site model was necessary to explain concentration dependent sorption of Cs (Missana et al., 2014). The second site was attributed to sorption on clay edges, which are dominant at low Cs concentrations. Siroux et al. (2017) developed a three-site cation exchange model in order to describe adsorption of Sr and Cs in Na-MX80 bentonite, where the third site accounts for increased sorption above a pH of about 8. Van Loon and Glaus (2008) found sorption of Cs in compacted Volclay bentonite to increase with increasing dry density. They explained this observation with changes in the thermodynamics of ion exchange at different degrees of mechanical compaction, that is, with a preference of cations with low hydration tendency over those with high hydration tendency in the smaller interlayer space at high bulk densities. Even though these models are able to quantitatively describe cation sorption in batch experiments, they do not give a detailed insight into cation distributions close to the surface and possible consequences on cation transport.

Theoretical models consider electrostatic interaction between the negatively charged clay surfaces and ions in pore solution. Diffuse double layer (DL) models (Tournassat et al., 2009) describe the excess of cations and the depletion of anions in the diffuse swarm using the Poisson-Boltzmann equation. Triple layer models (Davis et al., 1978; Leroy and Revil, 2004; Leroy et al., 2007) include an additional Stern layer (SL), where cations are more specifically sorbed as inner-sphere surface complexes (ISSC) or outer-sphere surface complexes (OSSC). The triple-layer structure has been confirmed in molecular dynamics (MD) simulation studies (Marry et al., 2008; Tournassat et al., 2009; Bourg and Sposito, 2011; Tinnacher et al., 2016; Lammers et al., 2017), where ion distributions showed distinct density peaks with distance from clay surfaces, which were attributed to ISSC/OSSC (Stern layer) and diffuse layer, respectively. In addition, MD simulations revealed that cations maintain a significant mobility in the Stern layer (Tournassat et al., 2009; Bourg and Sposito, 2011; Tinnacher et al., 2016) as well as in interlayers of smectites (Kosakowski et al., 2008; Bourg and Sposito, 2010; Holmboe and Bourg, 2014).

Diffusion of water, cations and anions in clays and clay rocks have been widely studied (Kozaki et al., 1998; Kozaki et al., 1999; Molera and Eriksen, 2002; Glaus et al., 2007; Van Loon et al., 2007; González Sánchez et al., 2008; Melkior et al., 2009; Appelo et al., 2010; Glaus et al., 2010; Gimmi and Kosakowski, 2011; Bourg and Tournassat, 2015; Tinnacher et al., 2016; Wigger and Van Loon, 2018; Fukatsu et al., 2021). Results of these studies revealed that diffusion of cations is enhanced (i.e., shows a larger flux)

while diffusion of anions is reduced in comparison to that of a water tracer. Therefore, when applying a simple Fickian diffusion model, comparably high (cation) and low (anion) effective diffusion coefficients were obtained. Diffusion coefficients of water, anions and cation tracers in bentonite all exhibit a decrease with increasing bentonite dry density, but to different degrees (Bourg and Tournassat, 2015). To explain the different behavior of cations, anions and water tracers, more sophisticated models were developed and applied. Based on pore structure and interlayer diffusivity Bourg et al. (2007) and Bourg and Sposito (2010) described diffusion of Na, Sr and Cs in bentonite clays. Anion exclusion on a pore scale was modeled for bentonite with different dry densities and at different ionic strenghts by Tournassat and Appelo (2011) using microstructure information, considering DL effects and assuming interlayer being devoid of anions. Tachi and Yotsuji (2014) used an integrated sorption and diffusion model (Ochs et al., 2001) inlcuding DL diffusion and accounting for viscoelectric effects to model I, Na and Cs diffusion in Na-montmorillonite. Fukatsu et al. (2021) extended this model for Ca-montmorillonite by accounting for a heterogeneous pore structure. Soler et al. (2019) modeled anion and cation diffusion in Opalinus Clay with a dual continuum approach dividing the porosity in bulk and diffuse layer water. However, none of these models explicitly accounted for diffusion in the Stern layer nor in the interlayer. Moreover, it is unclear how the dry density of the bentonite affects the relative importance of the different diffusion pathways, including the distribution of the different interlayer hydration states.

Here, through-diffusion experiments in Volclay Bentonite at different bentonite dry densities (1.3, 1.6 and 1.9 kg L^{-1}) with HTO, Cl, Na, Sr and Cs tracers were investigated. Experimental results were evaluated with classical Fickian diffusion models for HTO and Cl and with a surface diffusion model (SD) for the cations Na, Sr and Cs. The parameters derived in this way varied with the dry density of the bentonite. In order to describe anion and cation diffusion in a more consistent way for all densities, a model including transport in the diffuse layer, the Stern layer, and the interlayer (DL-SL-IL) besides transport in ‘free’ pore water was implemented in the continuum scale reactive transport code Flotran (Lichtner, 2007). The model is based on bentonite microstructure parameters combined with anion exclusion data and with Stern layer mobilities and interlayer mobilities taken from the literature. Predicted effective diffusion coefficients of this model for Na, Sr and Cs were compared to values determined from experimental data by the simple SD model.

2 Modeling approaches

2.1 Surface diffusion model

A fairly simple way to describe the experimental cation diffusion data in bentonite is the application of a surface diffusion model (Gimmi and Kosakowski, 2011; Krejci et al., 2021). This model incorporates, in addition to pore diffusion, the mass fluxes that result from enrichment of cations close to the clay surfaces. Their contributions are represented with one model parameter, the surface mobility μ_s. At the local scale, pore and surface fluxes follow parallel pathways, but at the sample scale they follow also serial pathways, when considering the small particle sizes compared to a typical sample size. Equilibrium between both regions can be presumed because of their closeness. Then, the total mass flux for constant background concentrations can be written as:

$$j_{tot} = j_p + j_s = -\varepsilon \frac{D_0}{G} \frac{\partial C}{\partial x} - \rho_{bd} \frac{\mu_s D_0}{G} \frac{\partial S}{\partial C} \frac{\partial C}{\partial x} \quad (1)$$

where j_p and j_s are the fluxes for the pore and surface regions, C is the concentration in solution, S is the sorbed concentration per mass of dry solid, D_0 is the cation diffusion coefficient in bulk water, ε is the total (water accessible) porosity, ρ_{bd} is the bulk dry density, G is the so-called geometrical factor ('tortuosity') and accounts for the tortuous and constricted pathway in the pore water, $\partial S/\partial C$ is the derivative of the sorption isotherm, and $\partial C/\partial x$ is the concentration gradient in the pore water. The product of ρ_{bd} and S equals the total sorbed amount (e.g., in moles) per bulk sample volume.

One problem when splitting the flux into separate fluxes of two or multiple transport domains as in Eq. (1) is the assignment of tortuosities (geometrical factors G) to each domain. As noted by Gimmi and Kosakowski (2011), these tortuosities are only defined at the global scale of a sample, where we have a parallel and serial combination of the pathways, but not at the local scale for a single domain. We assume here that identical tortuosities apply to the different pathways in Eq. (1), as in Gimmi and Kosakowski (2011), because the domains are considered to be in close contact and solutes to be in local equilibrium. However, this assumption may be an oversimplification and introduces uncertainty. The balance equation then is:

$$\left(\varepsilon + \rho_{bd} \frac{\partial S}{\partial C}\right) \frac{\partial C}{\partial t} = \frac{\partial}{\partial x}\left(\varepsilon \frac{D_0}{G}\right) \frac{\partial C}{\partial x} + \frac{\partial}{\partial x}\left(\rho_{bd} \frac{\mu_s D_0}{G}\right) \frac{\partial S}{\partial C} \frac{\partial C}{\partial x} \quad (2)$$

Neglecting the second term on the right hand side in Eq. (1) and Eq. (2) one obtains the equations of the classical Fickian diffusion model with the effective diffusion coefficient D_e being $D_e = \varepsilon D_p = \varepsilon D_0/G$, and the pore diffusion coefficient $D_p = D_0/G$.

The SD model was implemented in the reactive transport code Flotran using an implicit approach where pore and surface diffusion are combined in a single diffusion coefficient:

$$D_{e,comb} = \frac{\varepsilon D_0}{G} + \rho_{bd} \frac{\mu_s D_0}{G} \frac{\partial S}{\partial C} \quad (3)$$

The SD model, as written here, is based on the assumption that cations can diffuse in the same pore space as water plus in a surface layer, and therefore the porosity accessible to cations in the first term of Eq. (1) is the same as that for water $\varepsilon = \varepsilon_w$. As mentioned, the geometrical factor G is a 'global' parameter at the sample scale and is typically derived from experimental diffusion data.

2.2 Combined DL-SL-IL model

In order to gain a more detailed insight into the diffusive processes of cations in bentonite, and also to be able to predict the dependence of the diffusion behavior for a variation of the bentonite dry densities or the solution ionic strength, a more sophisticated model is necessary. Here, a new model is developed that accounts for cation fluxes in free (bulk, uncharged) water, in the diffuse layer, in the Stern layer, and in the interlayer space of smectites. Conceptually, the model splits the total pore space into an external pore space, which includes bulk, diffuse layer and Stern layer space, and an interlayer pore space, which may be characterized by a distribution of widths or hydration states. Again, it is assumed that the bulk, diffuse and Stern layer fluxes are parallel and the pore environments are locally in equilibrium. Local equilibrium is also assumed between the interlayer pore space and the pore water of the external pores. The total mass flux of the DL-SL-IL model is then written as:

$$\begin{aligned} j_{tot} &= j_{free} + j_{DL} + j_{SL} + j_{IL} \\ &= \left(-\varepsilon_{free} - \varepsilon_{DL}\frac{C_{DL}}{C} - \mu_{SL}\rho_{bd}\frac{\partial S_{SL}}{\partial C} - \sum_i \mu_{IL,i}\rho_{bd}\frac{\partial S_{IL,i}}{\partial C} \right) \frac{D_0}{G_{DL,SL,IL}}\frac{\partial C}{\partial x} \end{aligned} \quad (4)$$

where ε_{free} and ε_{DL} are the porosities of the pore space not influenced by the surface and in the DL, respectively, and $G_{DL,IL,SL}$ is the geometrical factor of the DL-SL-IL model. Stern layer and interlayer fluxes are described via their derivatives of the sorption isotherms $\partial S_{SL,IL,i}/\partial C$ and their specific mobilities $\mu_{SL,IL,i}$. The sum for the interlayer contributions originates from considering a distribution of interlayer hydration states i (i.e., average number of water layers). Note that the product of $\rho_{bd} S_{SL,IL,i}$ equals the sorbed amount (e.g., moles) in the Stern layer or an interlayer i per bulk sample volume, and that this product could equally be expressed as $\varepsilon_{SL,IL,i} C_{SL,IL,i}$, i.e., as porosity of the corresponding pore environment multiplied by the corresponding concentration. Here, no explicit Stern layer pore volume is considered, and it is assumed that the total porosity ε_{tot} is the sum of ε_{free}, ε_{DL} and all $\varepsilon_{IL,i}$ (and possibly, see section 4, an additional porosity of interlayer-equivalent pores). A combined diffusion coefficient for the DL-SL-IL model can be derived from Eq. (4):

$$D_{DL,SL,IL} = \left(\varepsilon_{free} + \varepsilon_{DL}\frac{C_{DL}}{C} + \mu_{SL}\rho_{bd}\frac{\partial S_{SL}}{\partial C} + \sum_i \mu_{IL,i}\rho_{bd}\frac{\partial S_{IL,i}}{\partial C}\right)\frac{D_0}{G_{DL,SL,IL}} \quad (5)$$

The cation concentrations in the diffuse layer C_{DL} are determined by the amount of charge compensated in the diffuse layer. C_{DL} can be approximated by a Donnan approach where ion concentrations are averaged over the volume of the diffuse layer and expressed via a Boltzmann type distribution:

$$C_{DL} = C e^{-zF\frac{\Psi_D}{RT}} \quad (6)$$

where Ψ_D is the Donnan potential, z is the charge of the ion, F is the Faraday constant, R is the universal gas constant and T is the temperature. The distribution (enrichment or depletion) factor is defined as $\xi = C_{DL}/C$. The Donnan potential Ψ_D can be obtained from a charge balance:

$$\sum_i z_i C_{i,DL} = Q \quad (7)$$

where Q is the net surface charge compensated in the DL per Donnan volume:

$$Q = \frac{CEC_{DL}\rho_{bd}}{\varepsilon_{DL}} \quad (8)$$

Here CEC_{DL} is the fraction of the total cation exchange capacity that is compensated by ions in the diffuse layer.

Anion diffusion is modeled by the same equation (Eq. (5)), but assuming zero anion concentrations in the Stern layer and in the interlayer pore space (consisting of a few water layers only at the considered dry densities). Also, a different geometrical factor than for water or cations has to be taken into account. This is a consequence of the fact that G or the tortuosity is a property at the sample scale that depends on the network of pathways, which is different for anions compared to cations or water tracers

The DL-SL-IL model is implemented in the reactive transport code Flotran. In order to model diffusion in free and DL water in parallel, an additional ('virtual') dimension is added to the simulation set up. Free and DL cells are treated to be in equilibrium with each other. In the DL cells an immobile negative charge is added to mimic the surface charge compensated in the diffuse layer (Gimmi and Alt-Epping, 2018), and the flux of ion concentrations are calculated using the Nernst-Planck equation. This leads then to the desired Donnan behavior of this cell. Equilibrium concentrations in the Stern layer and in interlayers are modeled via cation exchange on different mineral sites. The Stern layer mineral site is placed within the diffuse layer cell, while the interlayer mineral sites are placed in the free pore water cells. Overall 'sorption', that is, the overall distribution of ions in DL, SL and IL environments of the DL-SL-IL model should be equal to that of a cation exchange model for any comparisons. As DL sorption does not reflect the ion specific selectivities reported for ion exchange models (when assuming identical activity coefficients in DL and free pore water, as generally done), selectivity coefficients for the Stern layer were adapted such that the total of DL and SL cation concentrations match the distribution of a representative cation exchange model. Site specific mobilities of cations in the Stern layer and in the interlayer water, which allow to consider a mobility of these 'sorbed' ions, are incorporated in a combined diffusion coefficient according to Eq. (5), i.e., using the same approach as in the SD model. The validation of the implementation of the DL-SL-IL model in the code is found in Appendix A1.

3 Application of Fickian and SD models to experimental results

3.1 Diffusion experiments and model input parameters

The Fickian and SD models were applied to experimental data of HTO, Cl, Na and Sr and Cs diffusion in Volclay bentonite reported by Glaus et al. (2017). The mineral composition and the pore water compositions at different dry densities for Volclay bentonite can be found in the appendix in Tables A1-A4. Experiments were carried out using a through-diffusion set-up. The cylindrical bentonite specimen had a diameter of 25.6 mm and a height of 10.4 mm for HTO, Cl and Na experiments and 5.3 mm for Sr and Cs experiments. Initial tracer concentrations in the upstream reservoir are found in Table A5. The detailed experimental set-up and description can be found in Van Loon et al. (2003) and Glaus et al. (2017). Tracer concentrations in the upstream reservoir, the tracer flux at the downstream boundary as well as the total concentration profile for the cations Na, Sr and Cs at the end of the experiment were measured.

The experimental fluxes in the through-diffusion experiments were modeled by considering the upstream reservoir, the filters and the bentonite clay specimen. Downstream, a zero-concentration boundary condition was applied for HTO and Cl. For the cations Na, Sr and Cs the measured concentrations were used as downstream boundary conditions, because a zero-concentration boundary condition may lead to systematically underestimated effective diffusion coefficients (Glaus et al., 2015). Chemical reactions (aquatic complexes and ion exchange reactions) were calculated based on activities $a = \gamma C/C_0$, where C_0 is the reference concentration equal to unity and the activity coefficient γ being described by the model of Davies (Stumm and Morgan, 1996). Ion specific bulk diffusion coefficients used for modeling are listed in Table 1. Filter diffusion coefficients were adapted within the value range of fresh and used filters given by Glaus et al. (2008) (Table A6).

Table 1: Species specific bulk diffusion coefficients used in modeling.

	D_0 [m^2 s^{-1}]
HTO*	$2.236 \cdot 10^{-9}$
Cl^-*	$2.03 \cdot 10^{-9}$
Na^+*	$1.33 \cdot 10^{-9}$
$NaSO_4^-$**	$1.23 \cdot 10^{-9}$
Sr^{2+}*	$0.794 \cdot 10^{-9}$
$SrSO_4$**	$0.65 \cdot 10^{-9}$
Cs^+*	$2.06 \cdot 10^{-9}$
* from Flury and Gimmi (2018) ** from Applin and Lasaga (1984)	

Sorption for all cations is described by a one-site cation exchange model. A general cation exchange reaction between cations *A* and *B* with their respective charges z_A and z_B onto a surface sorption site $\equiv S$ can be written as:

$$\equiv S - z_B A^{z_A} + z_A B^{z_B} \Leftrightarrow \equiv S - z_A B^{z_B} + z_B A^{z_A} \quad (9)$$

The cation exchange capacity was calculated from the smectite content of the Volclay bentonite (71%) and the cation exchange capacity of montmorillonite being 0.85 eq kg^{-1} (Bradbury and Baeyens, 1997). Selectivity coefficients for the cations present in the pore water are taken from literature data, except for Sr, where selectivity was fitted to the concentration profiles (Table 2). The derivative of the

sorption isotherm $\partial S/\partial C$ was calculated from the one-site cation exchange model numerically. A detailed description of the calculation can be found in Krejci et al. (2021). The same parameters were used for all simulations, except for the different Cs selectivity coefficients that account for a reported bentonite density dependence.

Table 2: Selectivity coefficients used in the cation exchange model with respect to Na.

Cation	Selectivity coefficient log(K_C)
Na	0.00*
K	0.75*
Ca	0.58*
Mg	0.52*
Sr	1.00**
Cs	1.44/1.65/2.55***
* from Bradbury and Baeyens (2002) upper bound of estimated values ** adapted to match sorbed concentration profile ***from Van Loon and Glaus (2008) (slightly adapted)	

3.2 Results of HTO and Cl diffusion

From upstream reservoir concentration and downstream flux data, porosities and geometrical factors of HTO and Cl were determined (Table 3 and Figures 1, A2 and A4). Reasonable matches between experimental data and the simple Fickian diffusion model were achieved. Accessible porosities of HTO and Cl decreased while geometrical factors increased with increasing bentonite dry density. Steady-state diffusion data of HTO showed some fluctuations, which made a precise determination of porosity and geometrical factor difficult. However, for the two replicate HTO experiments per bentonite dry density the same porosity ε_{HTO} was determined. The values are in good agreement with porosities calculated from mineralogy (see section 4, Eq. (11), Table 7) except for the highest bentonite dry density (about 20% difference). For further analysis with the SD model and DL-SL-IL model the porosity based on the mineralogy was used at the highest bentonite dry density and geometrical factors were recalculated to match the steady-state mass flux (Table 3 values in brackets).

Table 3: HTO and Cl accessible porosities and geometrical factors. Values in brackets represent porosity based on mineralogy and corresponding tortuosity.

ρ_{bd} [kg L^{-1}]	1.3	1.6	1.9
ε_{HTO}	0.54	0.43	0.39 (0.33)
G_{HTO}	7.93	12.12	25.32 (21.51)
ε_{Cl}	0.125	0.045	0.019
G_{Cl}	13.61	29.41	107.53

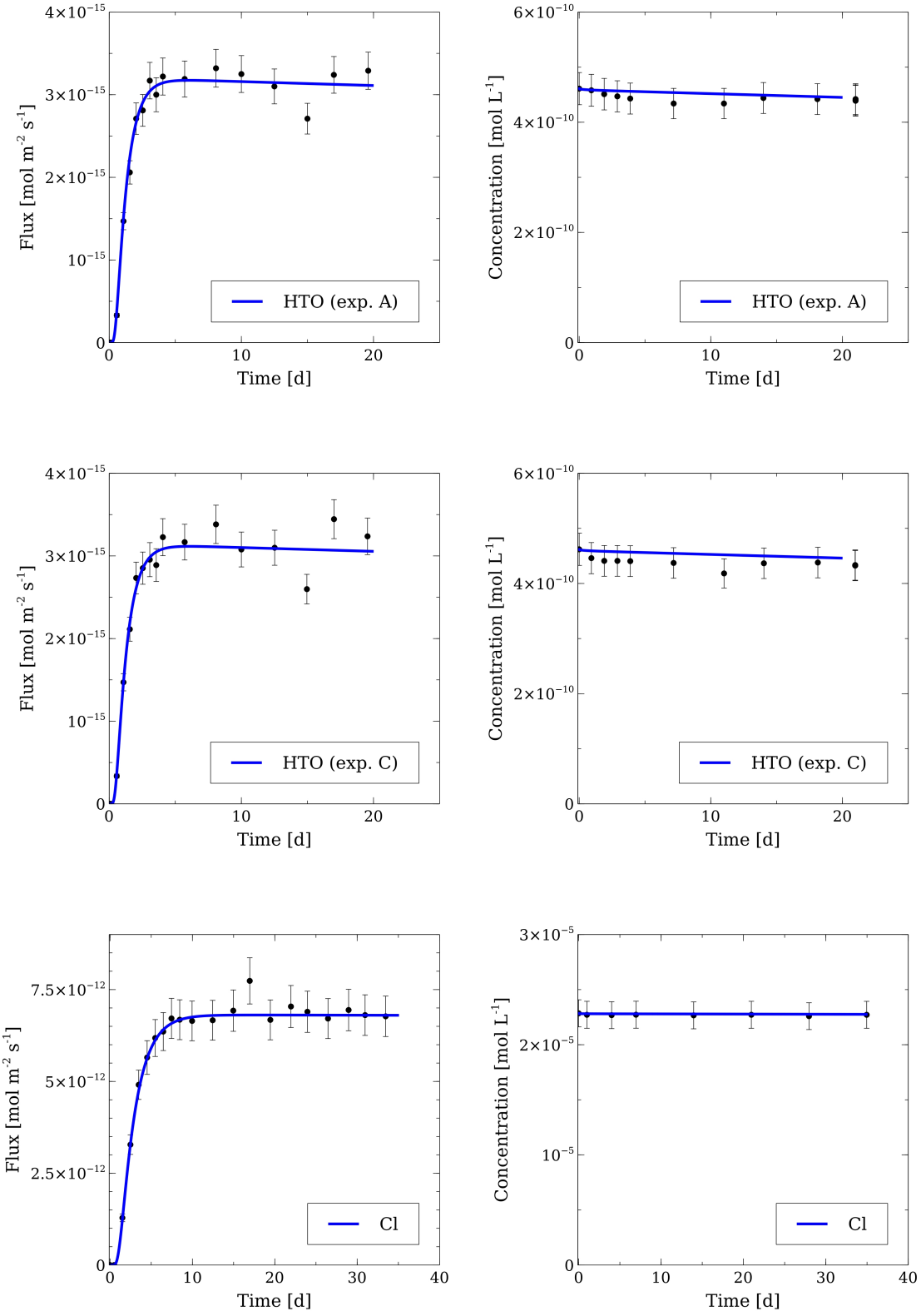

Figure 1: Flux at downstream boundary (first column) and concentration in upstream reservoir (second column) for HTO (first two rows) and Cl (third row) at 1.6 kg L^{-1} bentonite dry density. Black dots with error bars: experimental data; blue line: Fickian diffusion model. Results for the other dry densities are shown in the Appendix in Figs. A2 and A4.

3.3 Results of Na, Sr and Cs diffusion

The porosity ε_{HTO} and the geometrical factor G_{HTO} determined by HTO diffusion are used as input parameter for the surface diffusion model. So, the only unknowns are the surface mobilities of Na, Sr and Cs, which were determined by fitting the SD model to the experimental data (upstream reservoir concentration, downstream flux and sorbed concentration profile) (Figures 2, A3 and A5). The three different pore waters exhibited significant amounts of $NaSO_4^-$ (10%, 9% and 6% of total Na) and $SrSO_4$ (56%, 52% and 42% of total Sr) for the dry densities 1.3, 1.6 and 1.9, respectively, which were considered in the modeling with different diffusion coefficients (Table 1). For all cations fitted mobilities decreased with increasing bentonite dry density (Table 4). Mostly good, partly reasonable, agreement between experimental data and the fitted SD model was achieved (Figures 2, A3 and A5). The discontinuities in the flux curves are a result of the downstream concentration boundary condition. At all bentonite dry densities sorbed Cs concentrations showed a significant decrease close to the filters. This decrease may result from a decreased bentonite dry density close to filters (Van Loon et al., 2007). Such effects are not included in the SD model. Other than that, $\partial S_{Cs}/\partial C_{Cs}$ is in very good agreement with distribution coefficients reported by Van Loon and Glaus (2008).

Table 4: Surface mobilities of Na, Sr and Cs determined with the SD model and derivatives of the sorption isotherms based on the one site cation exchange model. Also shown are effective diffusion coefficients that result from the fitted parameters of the SD model, or equally from a direct fit of the data with the simple Fickian diffusion model.

ρ_{bd} [kg L^{-1}]	1.3	1.6	1.9
μ_{Na}	0.675	0.568	0.475
μ_{Sr}	0.364	0.301	0.204
μ_{Cs}	0.061	0.034	0.010
$\frac{\partial S_{Na}}{\partial C_{Na}}$	2.49	2.21	1.77
$\frac{\partial S_{Sr}}{\partial C_{Sr}}$	28.2	22.0	14.0
$\frac{\partial S_{Cs}}{\partial C_{Cs}}$	68.6	98.6	626
$D_{e,Na}$ [m^2 s^{-1}]	$4.6 \cdot 10^{-10}$	$2.7 \cdot 10^{-10}$	$1.2 \cdot 10^{-10}$
$D_{e,Sr}$ [m^2 s^{-1}]	$1.4 \cdot 10^{-9}$	$7.2 \cdot 10^{-10}$	$2.1 \cdot 10^{-10}$
$D_{e,Cs}$ [m^2 s^{-1}]	$1.5 \cdot 10^{-9}$	$9.8 \cdot 10^{-10}$	$1.2 \cdot 10^{-9}$

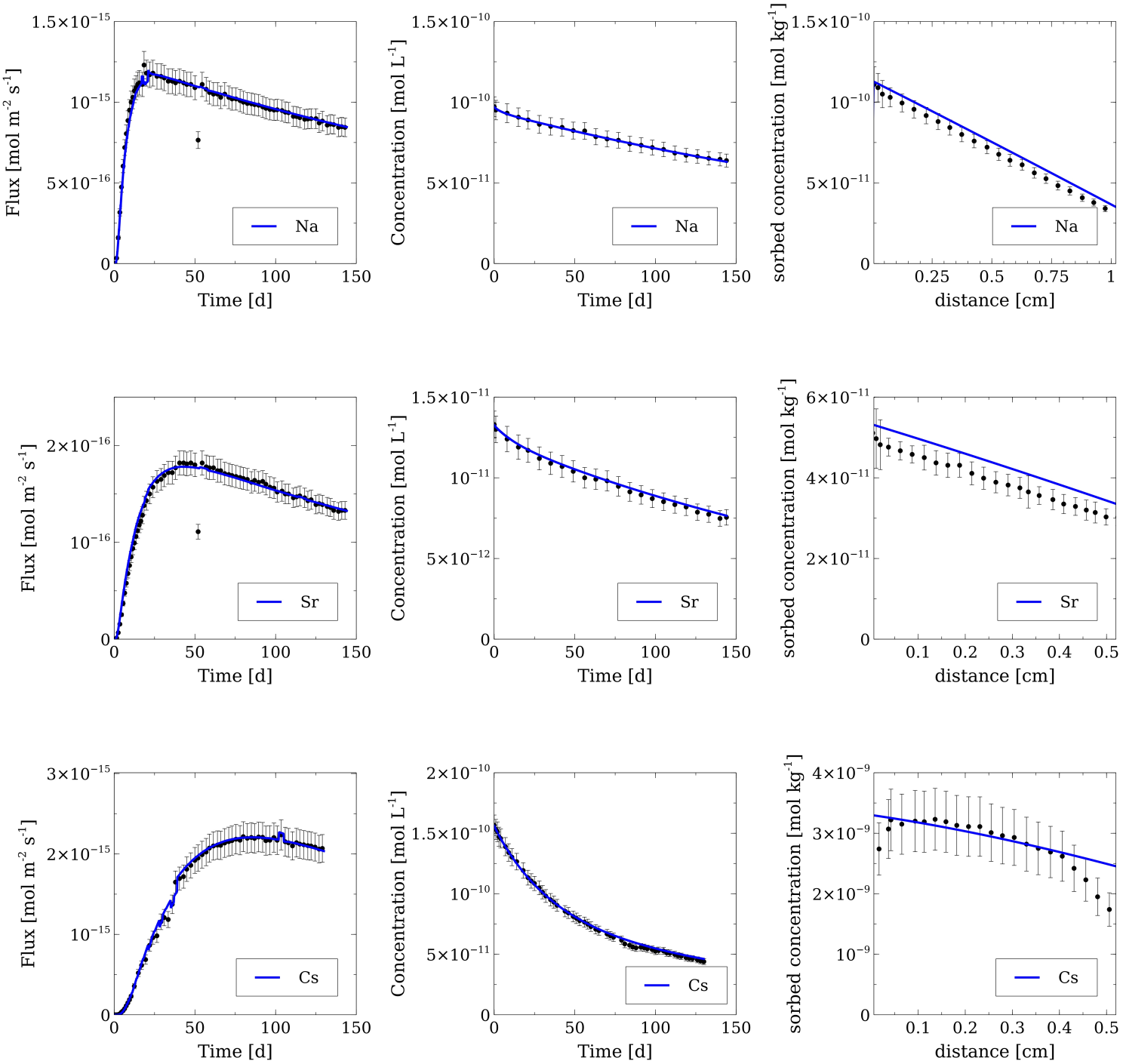

Figure 2: Flux at downstream boundary (first column), concentration in upstream reservoir (second column) and total (sorbed + aqueous) concentration profile (last column) for Na (first row), Sr (second row), and Cs (third row) at 1.6 kg L^{-1} bentonite dry density. Black dots with error bars: experimental data; blue line: surface diffusion model. Results for the other dry densities are shown in the Appendix in Figs. A3 and A5.

4 Application of DL-SL-IL model to experimental results and discussion

The anion accessible porosities derived from the experiments by applying Fick's law are in good agreement with values from other experiments (Van Loon et al., 2007), and the mobilities of Na, Sr and Cs derived by applying the SD model are in good agreement with average mobilities reported by Gimmi and Kosakowski (2011). The cation mobilities seem well constrained as data and model show good agreement. However, their physical meaning, and therefore their predictive capability, is limited; they provide only a phenomenological description of experimental data at each bulk dry density, but cannot explain the variations between different densities. Such variations could be linked to variable contributions of different diffusion pathways (e.g., diffuse layer, Stern layer, interlayer) depending on the bulk dry density. Accordingly, a more predictive model should be able to quantify the significance of different pathways on the overall solute flux. The DL-SL-IL model explicitly accounts for these different contributions.

In order to compare the DL-SL-IL model with the experimental data or, more precisely, with the effective diffusion coefficients derived from the experimental data by the SD model, the combined effective diffusion coefficient of the DL-SL-IL model (Eq. (5)) is directly calculated by assuming equilibrium between concentrations in all water phases. For the calculation we make use of the fact that the overall sorption, and therefore the overall derivative of the sorption isotherm $\partial S_{tot}/\partial C$, is given by the one-site cation exchange model. This overall derivative must equal the sum of the sorption contributions of DL, SL and IL. The derivatives of the sorption isotherm for the various interlayer environments $\partial S_{IL,i}/\partial C$ were calculated by multiplying $\partial S_{tot}/\partial C$ with the fraction of CEC compensated in each interlayer environment. Thereby, it was assumed that the DL and SL sites (exposed to the external pore space) and the different interlayer sites have the same selectivity for the cations Na and Sr. For Cs, the same selectivity as in the SD model was used for the DL and SL sites, but, as Cs exhibits a preference for smaller interlayers expressed by higher selectivity coefficient (Van Loon and Glaus, 2008). Individual selectivities were attributed to the different interlayer environments (Table A7). The selectivities of Cs for the different interlayer environments were calculated in a way that the weighted (by individual interlayer abundance) sum of all interlayer selectivities equals the overall selectivity used in the SD model at each bentonite dry density (Table 2). For the pore water at the different bentonite dry densities the distribution factor ξ and the Stern layer fraction $(\partial S_{SL}/\partial C)/(\partial S_{tot}/\partial C)$ were derived from Donnan equilibrium calculations including a cation exchange site representing the Stern layer. The selectivities of this cation exchange site were adapted (Table A8) so that the overall adsorption in DL and SL matched the distribution of cations predicted by the one-site cation exchange model. Here, it was assumed that the activity coefficient in the diffuse layer is the same as in bulk water. This assumption is, however, arbitrary (Tournassat and Steefel, 2019) as the activity coefficients in the diffuse layer cannot be measured.

The determination of the distribution factor ξ and the fractions of Stern layer and the interlayer environments requires detailed knowledge of the bentonite microstructure, namely the distribution of the porosity and the charge over the different pore environments.

4.1 Bentonite pore structure model

The two key microstructural parameters to describe the bentonite structure are the stack size n_c and the distribution of the different interlayer hydration states. They determine the external and internal surface area and porosity, respectively. However, there exists no such data specific to compacted

Volclay bentonite. Therefore, literature data from montmorillonite, the main component of Volclay bentonite, is taken. From these data combined with anion exclusion data for Volclay bentonite (Van Loon et al., 2007), a model of the pore space is derived. From mass balance considerations the anion accessible porosity can be calculated from the sum of the free bulk porosity ε_{free} and the DL porosity ε_{DL} multiplied by the distribution factor of Cl ξ^{Cl}.

$$\varepsilon_a = \varepsilon_{free} + \varepsilon_{DL}\,\xi^{Cl} \tag{10}$$

where ξ^{Cl} is a function of CEC_{DL} and ε_{DL}, see Eqs. (6), (7) and (8).

The pore space model was constrained so that Eq. (10) matches the Cl accessible porosity determined with the Fickian diffusion model (Table 3). Stack sizes and interlayer pore size distributions were taken from the range of literature values so that this condition was met. Table 5 shows a summary of the results of the pore space model and of one alternative configuration, which are both derived in the next subsections.

Table 5: Diffuse layer parameters used to fulfill the mass balance in Eq. (10) (parameters of the alternative pore space model in brackets).

ρ_{bd} [kg L^{-1}]	1.3	1.6	1.9
ε_{free}	0.01 (0.08)	0.004 (0.03)	0.001 (0.014)
ε_{DL}	0.21 (0.14)	0.096 (0.07)	0.047 (0.034)
CEC_{DL} [mol_c kg^{-1}]	0.0476 (0.084)	0.029 (0.094)	0.0188 (0.097)
ξ	1.83 (2.95)	2.3 (4.82)	2.65 (6.56)

4.1.1 Bentonite microstructure

Pusch (2001) reported stack sizes for Na-montmorillonite around 3-5. Higher stack sizes n_c of 6-8 were found by Matusewicz et al. (2013) for Ca-montmorillonite, independent of the clay dry density. In Volclay bentonite pore water is dominated by Na ions, therefore the stack size used in the model was chosen to be 4.5. Under high compaction 1 WL (water layer), 2 WL and 3 WL hydration states are present in montmorillonite (Holmboe et al., 2012; Ohkubo et al., 2016; Ohkubo et al., 2021), and their distribution strongly depends on the clay dry density, the prevailing cations in the pore water and to some extent on the ionic strength. Bourg et al. (2006) accounted for the dry density effects based on data of Kozaki et al. (1998) by a linear transition from 3 WL to 2 WL between dry densities of Na-montmorillonite of 1.3 kg L^{-1} and 1.6 kg L^{-1}. Tournassat and Appelo (2011) added an ionic strength dependency to this model estimated from data of Kozaki et al. (1998), Kozaki et al. (2001) and Kozaki et al. (2008). More recent studies (Ohkubo et al., 2016; Ohkubo et al., 2021), however, suggested that ionic strength effects may be less significant under high compaction. At very high compaction of 1.8 kg/L, Holmboe et al. (2012) found about 33% 1 WL interlayers in Na-montmorillonite. An exact quantification of the interlayer water distribution is difficult considering the non-homoionic pore water of Volclay bentonite and also pore size distributions for Na-montmorillonite estimated by XRD measurements at a given dry density (Holmboe et al., 2012; Ohkubo et al., 2021) differ significantly. For the lowest bentonite dry density, a configuration of the interlayer water distribution was chosen (Table 6) that lies between a pure 3 WL configuration (100% 3 WL, 0 % 2 WL) and a combination of 55% 3 WL and 45% 2 WL that would have been estimated with the model of Tournassat and Appelo (2011). For the medium bentonite dry density fractions of 85% 2 WL and 15% 3 WL were used, similar to the findings of Ohkubo et al. (2016). At the highest bentonite dry density, 40% 1 WL and 60% 2 WL were taken, which is between the findings of Holmboe et al. (2012) and estimated values of Van Loon et al. (2007).

Table 6: Distribution of interlayer spacings used in the microstructure model and partial montmorillonite dry density $\rho_{bd,Mont}$ (Eq. (A1)).

ρ_{bd} [kg L^{-1}]	$\rho_{bd,Mont}$ [kg L^{-1}]	1 WL	2 WL	3 WL
1.3	1.11	0	20	80
1.6	1.42	0	85	15
1.9	1.73	40	60	0

4.1.2 Porosity distribution

The total porosity (Table 7) of Volclay bentonite at the different dry densities is calculated by:

$$\varepsilon_{tot} = 1 - \frac{\rho_{bd}}{\rho_g} \tag{11}$$

where ρ_g is the bentonite grain density, taken to be 2.84 kg L^{-1}.

The total specific surface area of the montmorillonite fraction in Volclay bentonite was taken to be 770 m^2 g^{-1}, in agreement with values calculated from the montmorillonite crystal structure (Tournassat and Appelo, 2011; Holmboe et al., 2012; Leroy et al., 2015). The interlayer surface area can be calculated according to Tournassat and Appelo (2011):

$$A_{IL} = \frac{a \times b\,(n_c - 1)}{n_c} \frac{N_A}{M_W} \tag{12}$$

where $a \times b$ is the surface area of the montmorillonite unit cell with a value of 46.7 Å^2 (Holmboe et al., 2012), N_A is the Avogadro constant ($6.022 \cdot 10^{23}$ molecules mol^{-1}) and M_W is the molecular weight of montmorillonite taken to be 733 g mol^{-1}. This results in an interlayer surface area of about 590 m^2 g^{-1}. The external basal surface area is the difference between the total and the interlayer surface area (180 m^2 g^{-1}). As adsorption of Na, Sr and Cs was well explained without considering edge sorption (c.f. 3.3), the edge surface area was neglected.

The total porosity can be described as the sum of external ε_{ext} and interlayer ε_{IL} porosity :

$$\varepsilon_{tot} = \varepsilon_{ext} + \varepsilon_{IL} = \varepsilon_{free} + \varepsilon_{DL} + \varepsilon_{ext,inacc} + \varepsilon_{IL} \tag{13}$$

Here, the external porosity is further subdivided into the free bulk porosity ε_{free}, the diffuse layer porosity ε_{DL} and an external, but anion inaccessible (interlayer-equivalent) porosity $\varepsilon_{ext,inacc}$. The derivation of these porosities is shown in the following paragraphs.

The total interlayer porosity (Table 7) is calculated as the sum over the different interlayer hydration states according to their fractions p_i (Table 6):

$$\varepsilon_{IL} = \sum \frac{p_i A_{IL,i} t_{IL,i}}{2} w_{mont} \rho_{bd} \tag{14}$$

where the interlayer distances t_{IL} are 0.32 nm, 0.64 nm and 0.92 nm for 1 WL, 2 WL and 3 WL interlayers, respectively, and w_{mont} is the montmorillonite weight fraction in Volclay bentonite. In the pore model presented here, it is assumed that anions do not enter the pore space between the layers. This can be justified by MD simulations of Tournassat et al. (2016), which showed that anions do not enter 2 WL interlayers and are depleted 20-fold in 3 WL interlayers, which is rather low, such that, it hardly leads to a significant effect on anion mass fluxes.

Van Loon et al. (2007) measured anion exclusion for variable NaCl solutions (ranging from 0.01 M to 1 M) using different techniques for the same Volclay bentonite densities as used here. From highest NaCl concentration (1 M) they derived a maximum anion accessible porosity $\varepsilon_{max,Cl}$ (Table 7). Diffuse

double layer effects at such high ionic strength are negligible, as most charge is compensated in the Stern layer and diffuse layer thickness is very small. Therefore, one can expect that this value of $\varepsilon_{max,Cl}$ represents the whole external pore space.

In addition, a free (bulk) porosity ε_{free} (not influenced by surface charge) (Table 7) is approximated from results at lowest NaCl concentrations of 0.01 M, where the diffuse double layer effect is high.

The diffuse layer porosity ε_{DL} is then taken to be the difference between the maximum accessible porosity and the free bulk porosity:

$$\varepsilon_{DL} = \varepsilon_{max,Cl} - \varepsilon_{free} \quad (15)$$

However, the experimentally determined external porosity (assumed to be equal to $\varepsilon_{max,Cl}$) and the interlayer porosity ε_{IL} (calculated from microstructure data) do not sum up to the total porosity ε_{tot} (Table 7). This discrepancy was also described by several other authors (Tournassat and Appelo, 2011; Matusewicz et al., 2013; Wigger and Van Loon, 2017; Wigger and Van Loon, 2018). Matusewicz et al. (2013) found stack sizes determined by XRD and SAXS being independent of dry density in Ca-montmorillonite, while stack sizes (and therefore interlayer porosity) determined by anion exclusion significantly increased at high dry density. Their explanation was that at high densities the distance between disordered platelets becomes small enough to exclude anions and this effect cannot be captured by XRD measurements. Tournassat and Appelo (2011) hypothesized that under high compaction rearrangement of clay platelets occurs leading to distances between adjacent surfaces in the order of interlayer spacings and accounted for that by an increased stack size. Wigger and Van Loon (2017) and Wigger and Van Loon (2018) had to introduce a so-called interlayer-equivalent porosity or bottleneck porosity, respectively in order to match experimental data on anion exclusion in Opalinus Clay. Here, in our model the stack size was not increased as it is rather unclear how disordered platelets in the external pore space rearrange with increasing density, e.g., parallel orientation of clay stacks with an interlayer-like distance or creation of bottleneck situations blocking interconnectivity of bigger pores. To account for the discrepancy an external, but anion-inaccessible porosity $\varepsilon_{ext,inacc} = \varepsilon_{tot} - \varepsilon_{IL} - \varepsilon_{max,Cl}$ was introduced and calculated from the difference between the total porosity and ε_{IL} and $\varepsilon_{max,Cl}$. The external porosity is then $\varepsilon_{ext} = \varepsilon_{max,Cl} + \varepsilon_{ext,inacc}$. A surface area proportional to its porosity fraction is attributed to $\varepsilon_{ext,inacc}$. Without any knowledge about its detailed nature, its diffusion behavior for HTO, Na, Sr and Cs is assumed to be the same as that for a 2 WL interlayer pore. Alternatively, $\varepsilon_{ext,inacc}$ may be interpreted as a Stern layer porosity devoid of anions. In this case the whole external surface area is attributed to the diffuse and the Stern layer, as these compartments are considered to occur next to each other and not in series. In the following both a pore structure model with $\varepsilon_{ext,inacc}$ and with a Stern layer porosity (alternative pore model) are investigated.

Table 7: Porosities derived for the different pore environments. In the alternative model, $\varepsilon_{ext,inacc}$ is considered to represent the Stern layer porosity.

ρ_{bd} [kg L^{-1}]	ε_{tot}	ε_{IL}	ε_{free}	$\varepsilon_{max,Cl}$	$\varepsilon_{ext,inacc}$
1.3	0.54	0.24	0.01	0.22	0.08
1.6	0.43	0.225	0.004	0.1	0.105
1.9	0.33	0.2	0.001	0.048	0.082

4.1.3 Charge distribution

Charge distribution between diffuse and Stern layer can be approximated by a surface complexation reaction (Wersin et al., 2008; Appelo et al., 2010; Tinnacher et al., 2016):

$$Su^- + Na^+ \Leftrightarrow SuNa \quad (16)$$

with $\log K_{SuNa}$ being the respective surface complexation constant. Results of MD simulations of a montmorillonite nanopore in Na dominated pore water at ionic strength of I=0.1 M (Tinnacher et al., 2016) showed about 40%-50% of surface charge being compensated in the Stern layer. Therefore, $\log K_{SuNa}$ was chosen to be 0.9, which results in 45% charge compensation in the Stern layer at I=0.1 M.

From the Na concentration in the pore water and the surface complexation constant the fraction of charge compensated in the diffuse layer (Table 8) can be calculated:

$$f_{DL} = \frac{1}{1 + K_{SuNa}[Na]^+} \quad (17)$$

Table 8: Fraction of charge compensated in the diffuse layer at the different bentonite dry densities for the different pore chemistries (Tables A2-A4).

ρ_{bd} [kg L^{-1}]	1.3	1.6	1.9
f_{DL}	0.46	0.42	0.36

The total cation exchange capacity is distributed equally over the total specific surface area as external CEC and interlayer CEC:

$$CEC_{tot} = CEC_{ext} + CEC_{IL} \quad (18)$$

The external CEC is further subdivided between the DL, SL and anion-inaccessible pore space according to the charge fraction f_{DL} and the respective volumes, which leads to:

$$\begin{aligned} CEC_{ext} &= CEC_{DL} + CEC_{SL} + CEC_{inacc} \\ &= \left(f_{Dl}\frac{\varepsilon_{max,Cl}}{\varepsilon_{ext}} + \left(1 - f_{Dl}\right)\frac{\varepsilon_{max,Cl}}{\varepsilon_{ext}} + \frac{\varepsilon_{ext,inacc}}{\varepsilon_{ext}}\right) CEC_{ext} \end{aligned} \quad (19)$$

In the case where the anion-inaccessible pore space is interpreted as Stern layer porosity (alternative pore model), $\varepsilon_{ext,inacc}$ is set to zero and the ratio $\varepsilon_{max,Cl}/\varepsilon_{ext}$ is set to one in Eq. (19). The interlayer CEC is distributed over the different interlayer porosities according to their fractions p_i (Table 6):

$$CEC_{IL} = (p_{1WL} + p_{2WL} + p_{3WL}) CEC_{IL} \quad (20)$$

4.1.4 Site-specific mobilities for cations and water tracers

Specific mobilities for the Stern layer and different interlayers were taken from literature when available (Table 9 (bracket values)). Mobility values of 1 WL, 2 WL and 3 WL interlayer for HTO and Na were taken from Holmboe and Bourg (2014), for Sr and Cs from Bourg and Sposito (2010). The latter literature data has however a large uncertainty, and therefore, mobilities of Sr and Cs were allowed to vary in the given range of uncertainty in order to achieve a better match with the experimentally determined mobilities. The Stern layer mobility of Na was taken from Tinnacher et al. (2016). For Sr a similar mobility as for Ca (Bourg and Sposito, 2011) was used, as both cations have similar diffusion coefficient, similar water chemistry, and similar adsorption behavior. No literature data is available for the Stern layer mobility of Cs; it was therefore treated to have the same value as in a 3 WL interlayer, because for Na and Sr Stern layer and 3 WL interlayer mobilities show very similar values. The mobility $\mu_{ext,inacc}$ is set to that of a 2W interlayer in the basic pore model (cf. 4.1.2). In the case where $\varepsilon_{ext,inacc}$ is interpreted as Stern layer porosity (alternative pore model) the mobility $\mu_{ext,inacc}$ in Eq. (21) is set to the Stern layer mobility of water of 0.66 (Tinnacher et al., 2016).

Table 9: Site specific mobilities used in the DL-SL-IL model, literature values in brackets. The asterisk indicates the Stern layer mobility of HTO used in the alternative pore model.

mobility	1 WL	2 WL	3 WL	Stern layer
μ_{HTO}	0.08 (~0.08)	0.35 (~0.35)	0.5 (~0.5)	- (0.66)*
μ_{Na}	0.05 (~0.5)	0.3 (~0.3)	0.475 (~0.475)	0.5 (~0.5)
μ_{Sr}	0 (0±0.0001)	0.1 (0.093 ± 0.055)	0.25 (0.167 ± 0.099)	0.3 (~0.3)
μ_{Cs}	0.004 (0.009 ± 0.005)	0.01 (0.049 ± 0.041)	0.05 (0.077 ± 0.065)	0.05 (as 3 WL)

4.1.5 Geometrical factor

Because water has a lower mobility in bentonite interlayer (Table 9) than in bulk water, the geometrical factor G_{HTO} derived from HTO diffusion and used in the SD model is overestimated, as it does not account for the decreased water mobility in the interlayer environment. The DL-SL-IL model uses a corrected geometrical factor $G_{DL,IL,SL}$, which is written as:

$$G_{DL,IL,SL}=\left(\sum_i \mu_{i\,WL} f_{i\,WL}+\mu_{ext,inacc} f_{ext,inacc}+\left(1-\sum_i f_{i\,WL}-f_{ext,inacc}\right)\mu_{ext}\right)G_{HTO} \quad (21)$$

where μ are the mobilities of water in the different pore environments and f are the respective porosity fractions. The mobility of water in the external (anion accessible) pore space is assumed to be equal to that of bulk water ($\mu_{ext}=1$, as for cations).

4.2 Comparison of experimental data with predictions based on the DL-SL-IL model

The comparison between experimental data, represented by the combined effective diffusion coefficients of Na, Sr and Cs fitted from the diffusion experiments (Eq. (3), Table 4), and the ones predicted by the DL-SL-IL via Eq. (5) model shows good agreement (Figures 3, 4 and 5). Predicted $D_{DL,IL,SL}$ values are within a 15% error of the values fitted from the diffusion experiments with the SD or the Fickian model, except for Cs at highest bentonite dry density, where the predicted value from the DL-SL-IL model is higher by a factor of about two and a factor of three for the alternative pore model. For the alternative pore model Sr diffusion at highest bentonite density was also overestimated by 50%. The reason for this big difference of Cs diffusion coefficients is not clear. The lower clay bulk density towards the filter boundaries is not considered in the evaluation of the experimental data, and may affect the diffusive behavior. It also has to be noted that the available mobility data for Cs (Table 9) has large uncertainty. Another reason that may play a role is that Cs sorption on edge sites should also be taken into account (Missana et al., 2014), even though the experimental data here (Figures 2, A3, A5) could be well described with a 1-site cation exchange model. The results for Na are remarkable, because its site-specific mobilities were well constrained by MD simulation results. Diffusion coefficients were highest for Cs and lowest for Na for all bentonite densities. As Na and Cs are both singly charged, the large difference between Na and Cs diffusion coefficients cannot be explained by a model including a diffuse layer only, unless largely different activities within this diffuse layer are assigned.

The combined DL-SL-IL model allows also to compare relative contributions of the different pore environments to the effective diffusion coefficient of the cations. These comparisons are shown in Tables 10, A9 and A10 for both pore models. As expected from the large smectite content of the Volclay bentonite, for all cations at all densities interlayer diffusion mostly turned out to be dominant in the model with $\varepsilon_{ext,inacc}$ and no Stern layer porosity, except for Cs at highest dry density where Stern layer diffusion was dominant. For Cs, Stern layer diffusion became increasingly important with increasing bentonite dry density. Stern layer diffusion is also important for Sr. It makes up for about 20% of the total diffusivity at all dry densities, because Sr is comparably concentrated within the Stern layer (Table 11) and also has a relatively high mobility there. Diffusion in the DL was least important for Cs, as most Cs is located in the Stern layer. Stern layer adsorption of Na (Table 11) increases with increasing bentonite dry density, because the fraction of charge compensated in the DL decreases with dry density (Table 8). As Sr and Cs are much more selective, they are hardly influenced by this decrease of the fraction of charge compensated in the diffuse layer.

For the alternative pore model, Stern layer diffusion and diffuse layer diffusion become more important for all cations, because the surface charge of the total external surface area (Eq. (19)) is attributed to diffuse and Stern layer. Consequently, Stern layer diffusion was most important for Cs at intermediate and highest bentonite density, and diffuse layer and Stern layer diffusion was most important for Sr at highest bentonite density.

Comparison of effective diffusion coefficients of the two alternative pore models shows very good agreement at low and intermediate bentonite density. However, the DL-SL-IL model with the alternative pore model overestimates Sr and Cs diffusion coefficients at highest bentonite dry density. The two different pore models may be viewed as variation of pore size distribution of external pore space. The first pore model including $\varepsilon_{ext,inacc}$ accounts for a part of the external porosity that has pore sizes similar to interlayer pores and a part with somewhat bigger pores, while the alternative pore model does not include interlayer-like pores, but instead attributes this volume to the Stern layer. The comparison of the effective diffusion coefficients of Sr and Cs calculated for both pore models at highest bentonite density suggests that the pore size distribution of the external pore space is indeed not uniform and significant parts of the external pore space has pore sizes equivalent to interlayer pore sizes. Attributing this volume to the Stern layer leads then to an overestimation of the diffusion coefficients because of the larger cation mobilities within the Stern layer as compared to the otherwise assumed properties of a 2WL interlayer (Table 9). However, exact knowledge of the distribution of the external pore space in bentonite clays and its properties would be required for a more detailed analysis.

Table 10: Relative contributions (in %) to the effective diffusion coefficient (Eq. (5)) of the DL-SL-IL model at a bentonite dry density of 1.6 kg L^{-1} (alternative pore model in brackets; in this model, no external, inaccessible porosity exists).

	1 WL	2 WL	3 WL	ext,inacc	DL	SL
Na	0 (0)	56 (50)	16 (14)	10 (–)	10 (19)	8 (17)
Sr	0 (0)	44 (33)	19 (15)	8 (–)	8 (23)	21 (29)
Cs	0 (0)	40 (31)	16 (12)	7 (–)	5 (7)	32 (50)

Table 11: Percentage of Na, Sr and Cs distributed in the Stern layer on external surfaces (alternative pore model in brackets).

ρ_{bd} [kg L^{-1}]	1.3	1.6	1.9
Na	39 (47)	49 (59)	60 (72)
Sr	91 (86)	89 (81)	87 (77)
Cs	98 (98)	99 (99)	~100 (~100)

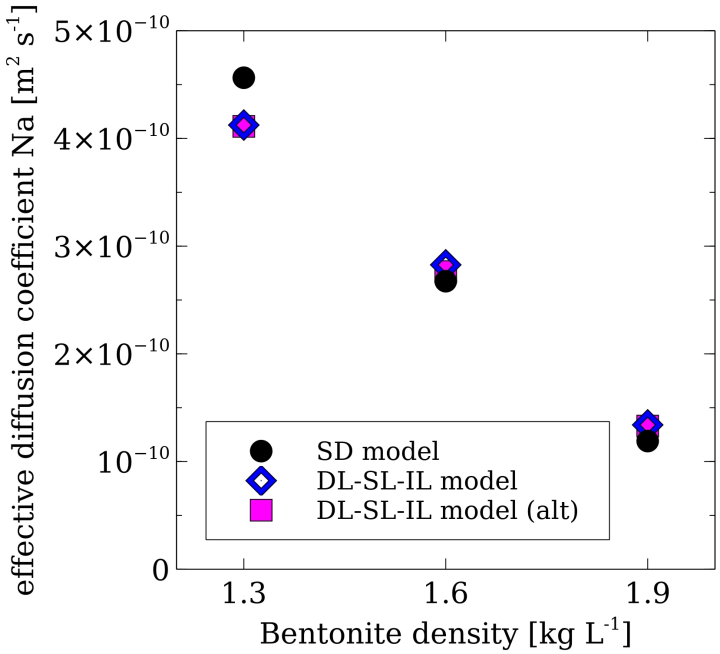

Figure 3: Comparison of effective diffusion coefficients determined from diffusion experiments with a simple Fickian (or an SD) diffusion model (black dots) and predicted by the DL-SL-IL model (blue diamonds and magenta squares for the alternative pore model) for Na.

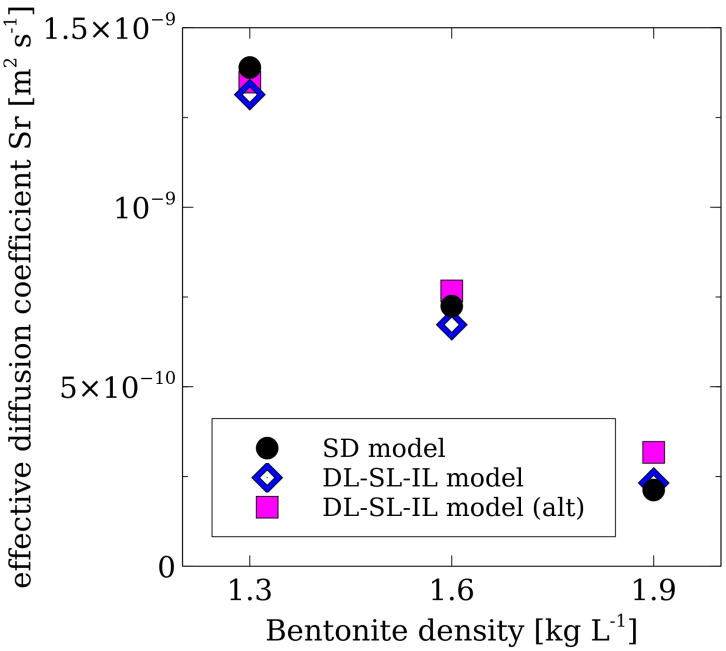

Figure 4: Comparison of effective diffusion coefficients determined from diffusion experiments with a simple Fickian (or an SD) diffusion model (black dots) and predicted by the DL-SL-IL model (blue diamonds and magenta squares for the alternative pore model) for Sr.

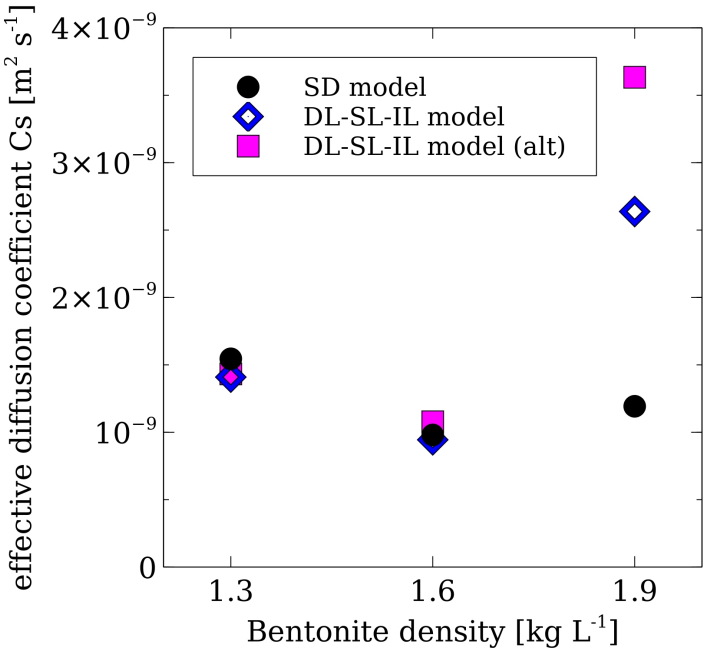

Figure 5: Comparison of effective diffusion coefficients determined from diffusion experiments with a simple Fickian (or an SD) diffusion model (black dots) and predicted by the DL-SL-IL model (blue diamonds and magenta squares for the alternative pore model) for Cs.

5 Summary and conclusions

Experimental through-diffusion data of HTO, Cl, Na, Sr and Cs in Volclay bentonite at different dry densities were modeled. A Fickian diffusion model was applied to determine water and anion accessible porosities as well as geometrical factors (tortuosities). A surface diffusion model was used to derive an average surface mobility of Na, Sr and Cs from experimental data. The experimental data could be well described with these models. However, these models have no predictive capability, as their input parameters are not linked to structural and chemical parameters that may vary in different systems. A new model was developed and implemented in the reactive transport code Flotran. It accounts for diffusion in the diffuse layer, in the Stern layer, and in the interlayer space of clays. This model is mostly based on microstructural information (porosities and charge distribution in these pore environments) and values of cation mobilities in the Stern layer and interlayer environments that were derived from the available literature. However, it also needs parameters that currently cannot (geometrical factor of water and anion) or not easily be constrained by independent data (maximal anion accessible porosity, cation exchange selectivities for the different pore environments). We showed that this model is able to predict anion accessible porosities with reasonable assumptions about the pore structure. Effective diffusion coefficients of Na, Sr and Cs predicted by the DL-SL-IL model were compared to diffusion coefficients derived from experimental data with a simple surface diffusion model, and a good agreement was found. A successful (but challenging) link between diffusion of water, anions and cations was made. Overall, the DL-SL-IL model can be a powerful predictive tool for anion and cation diffusion when detailed information about the clay microstructure and cation mobilities are available.

Acknowledgments

Financial support for the project by the Swiss National Science Foundation (grant no. 200021_166287) is kindly acknowledged. The co-authors acknowledge also partial financial support by Nagra, the Swiss Cooperative for the Disposal of Radioactive Waste.

Appendix

A1 Verification of implementation of the DL-SL-IL model in Flotran

The implementation of the DL-SL-IL model was validated by comparing simulation results for Na fluxes at medium dry density with those obtained by the simple SD model, whose correct implementation was already verified (Krejci et al., 2021). The simulations were carried out with a zero-concentration boundary condition and with parameters for the DL-SL-IL model as determined in section 4. Interlayer mobility parameters were slightly adapted so that the effective diffusion coefficient (Eq. (5)) equaled the diffusion coefficient determined in the SD model (Table 4). The comparison shows almost perfect agreement between both models (Figure A1). The tiny difference (less than 1%) at the peak of the breakthrough and at latest simulation times may be the result of rounding errors or slight numerical differences.

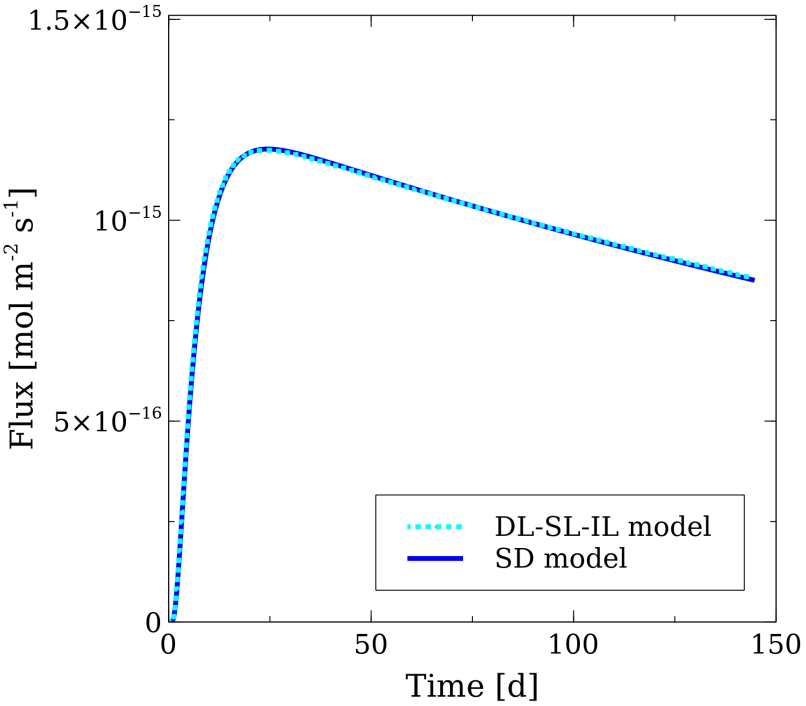

Figure A1: Na flux at a bentonite dry density of 1.6 kg L^{-1}: Comparison of SD model (blue line) and DL-SL-IL model (cyan dotted line).

A2 Experimental data

Table A1: Mineral composition of Volclay bentonite.

Mineral	Weight %
Calcite	3
Dolomite/Ankerite	<2
Siderite	<2
Quartz	4
Albite	10
Feldspar	11
Pyrite	0.7
C_{org}	<0.1
Sheet silicates by difference	71
Illite	0
Smectite	64
Chlorite/Smectite	7

Table A2: Pore water chemistry for dry density 1.3 kg L^{-1}.

Element	Concentration [mol L^{-1}]
Na	1.83E-01
K	2.70E-03
Mg	1.00E-02
Ca	9.20E-03
Sr	8.10E-05
Cl	1.81E-02
SO_4	1.02E-01
C_{inorg}	8.90E-04
F	2.20E-04
pH	8.00E+00
Ionic strength	2.60E-01
log PCO_2	-3.42E+00

Table A3: Pore water chemistry for dry density 1.6 kg L^{-1}.

Element	Concentration [mol L^{-1}]
Na	2.07E-01
K	3.10E-03
Mg	1.20E-02
Ca	9.80E-03
Sr	8.60E-05
Cl	6.18E-02
SO_4	9.50E-02
C_{inorg}	8.00E-04
F	2.20E-04
pH	8.00E+00
Ionic strength	2.90E-01
log PCO_2	-3.47E+00

Table A4: Pore water chemistry for dry density 1.9 kg L^{-1}.

Element	Concentration [mol L^{-1}]
Na	2.54E-01
K	3.70E-03
Mg	1.50E-02
Ca	1.20E-02
Sr	1.10E-04
Cl	1.70E-01
SO_4	7.10E-02
C_{inorg}	5.50E-04
F	1.90E-04
pH	8.00E+00
Ionic strength	3.30E-01
log PCO_2	-3.65E+00

Table A5: Initial tracer concentrations C_0 [mol L^{-1}] for HTO, Cl, Na, Sr and Cs in the upstream reservoir.

ρ_{bd} [kg L^{-1}]	HTO	Cl	Na	Sr	Cs
1.3	$4.60 \cdot 10^{-10}$	$2.35 \cdot 10^{-5}$	$9.67 \cdot 10^{-11}$	$1.33 \cdot 10^{-11}$	$1.58 \cdot 10^{-10}$
1.6	$4.61 \cdot 10^{-10}$	$2.28 \cdot 10^{-5}$	$9.72 \cdot 10^{-11}$	$1.33 \cdot 10^{-11}$	$1.57 \cdot 10^{-10}$
1.9	$4.65 \cdot 10^{-10}$	$2.30 \cdot 10^{-5}$	$1.00 \cdot 10^{-10}$	$1.34 \cdot 10^{-11}$	$1.57 \cdot 10^{-10}$

The partial montmorillonite dry density $\rho_{bd,Mont}$ can be calculated as:

$$\rho_{bd,mont} = \frac{w_{mont}\rho_{bd}}{1 - \frac{(1 - w_{mont})\rho_{bd}}{\rho_{s,acc}}} \quad (A1)$$

where w_{mont} is the mass fraction of montmorillonite in bentonite and $\rho_{s,acc}$ is the solid density of the accessory minerals.

A3 Model parameters and results

Table A6: Effective diffusion coefficients $D_e/10^{-10}$ [m^2 s^{-1}] of Na, Sr and Cs in the filters used for the SD model.

ρ_{bd} [kg L^{-1}]	Na	Sr	Cs
1.3	1.19	1.2	1.4
1.6	0.96	0.794	1.4
1.9	0.64	0.6	1.2

Effective diffusion coefficients in the filters for HTO: $2.236 \cdot 10^{-10}$ m^2 s^{-1} and Cl: $2.03 \cdot 10^{-10}$ m^2 s^{-1}.

Table A7: Calculated Cs selectivity coefficients for different interlayer spacings.

Interlayer spacings	Cs selectivity log K_c
1 WL	2.91
2 WL	1.69
3 WL	1.35

Table A8: Adapted selectivity coefficients for cations in the Stern layer under the condition that the sum of DL and SL cations have the same distribution as that determined by the one-site cation exchange model (alternative pore model in brackets).

K_C	1.3	1.6	1.9
Na	-	-	-
K	1.13 (1.05)	1.03 (0.95)	0.95 (0.88)
Ca	1.01 (0.79)	0.8 (0.48)	0.63 (0.22)
Mg	0.93 (0.69)	0.71 (0.37)	0.53 (0.12)
Sr	1.52 (1.33)	1.33 (1.13)	1.18 (0.98)
Cs	1.87 (1.77)	1.965 (1.88)	2.78 (2.70)

Table A9: Relative contributions (in %) to the effective diffusion coefficient (Eq. (5)) of the DL-SL-IL model at a bentonite dry density of 1.3 kg L^{-1} (alternative pore model in brackets).

	1 WL	2 WL	3 WL	Ext,inacc	DL	SL
Na	0 (0)	10 (10)	66 (61)	4 (-)	12 (18)	7 (11)
Sr	0 (0)	7 (6)	65 (60)	3 (-)	6 (11)	19 (23)
Cs	0 (0)	7 (7)	64 (59)	2 (-)	5 (7)	22 (27)

Table A10: Relative contributions (in %) to the effective diffusion coefficient (Eq. (5)) of the DL-SL-IL model at a bentonite dry density of 1.9 kg L^{-1} (alternative pore model in brackets).

	1 WL	2 WL	3 WL	Ext,inacc	DL	SL
Na	6 (5)	56 (47)	0 (0)	18 (-)	9 (19)	10 (29)
Sr	0 (0)	49 (30)	0 (0)	16 (-)	11 (35)	24 (35)
Cs	30 (19)	7 (4)	0 (0)	16 (-)	1 (1)	46 (76)

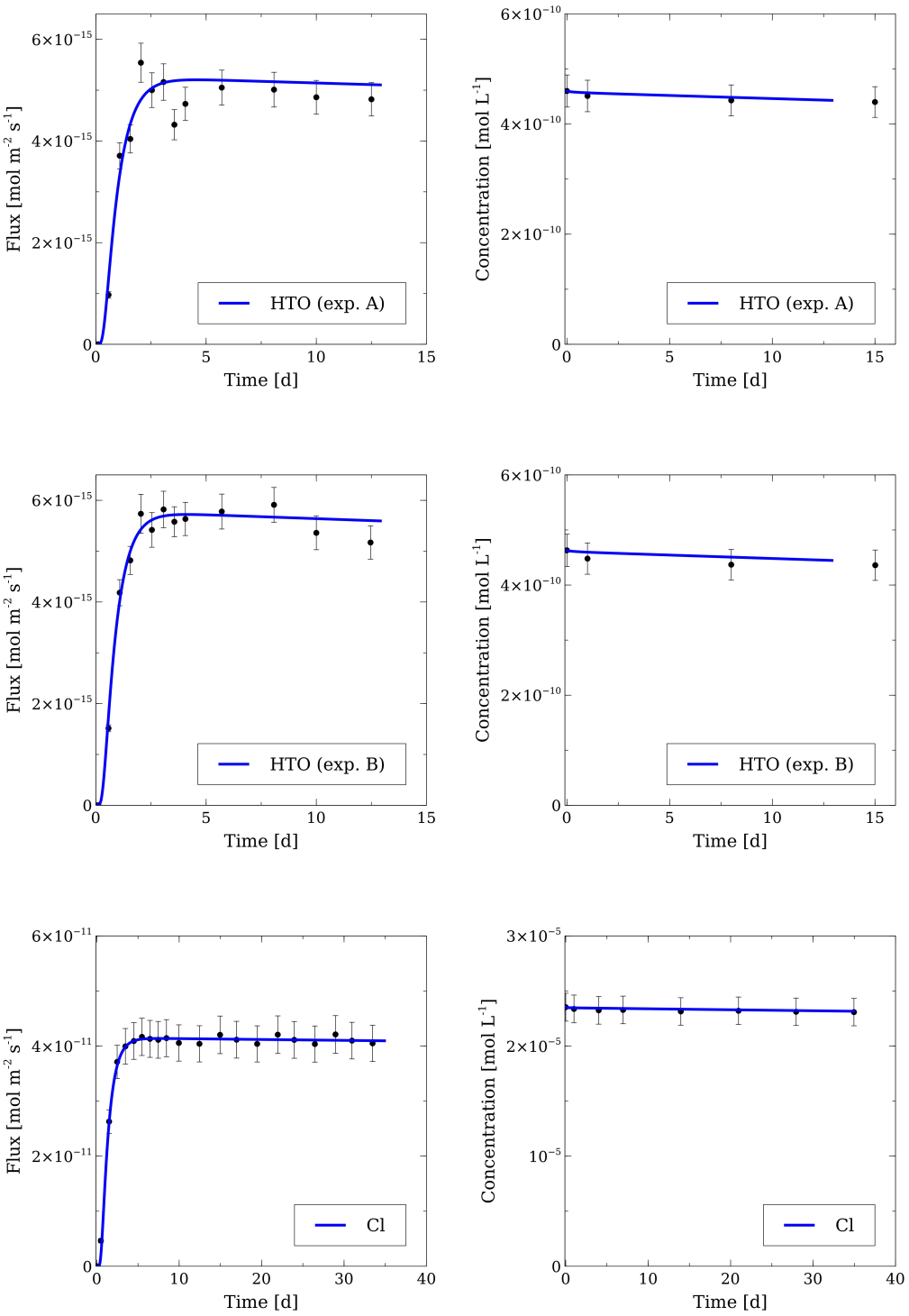

Figure A2: Flux at downstream boundary (first column) and concentration in upstream reservoir (second column) for HTO (first two rows) and Cl (third row) at 1.3 kg L^{-1} bentonite dry density; Black dots with error bars: experimental data; blue line: Fickian diffusion model.

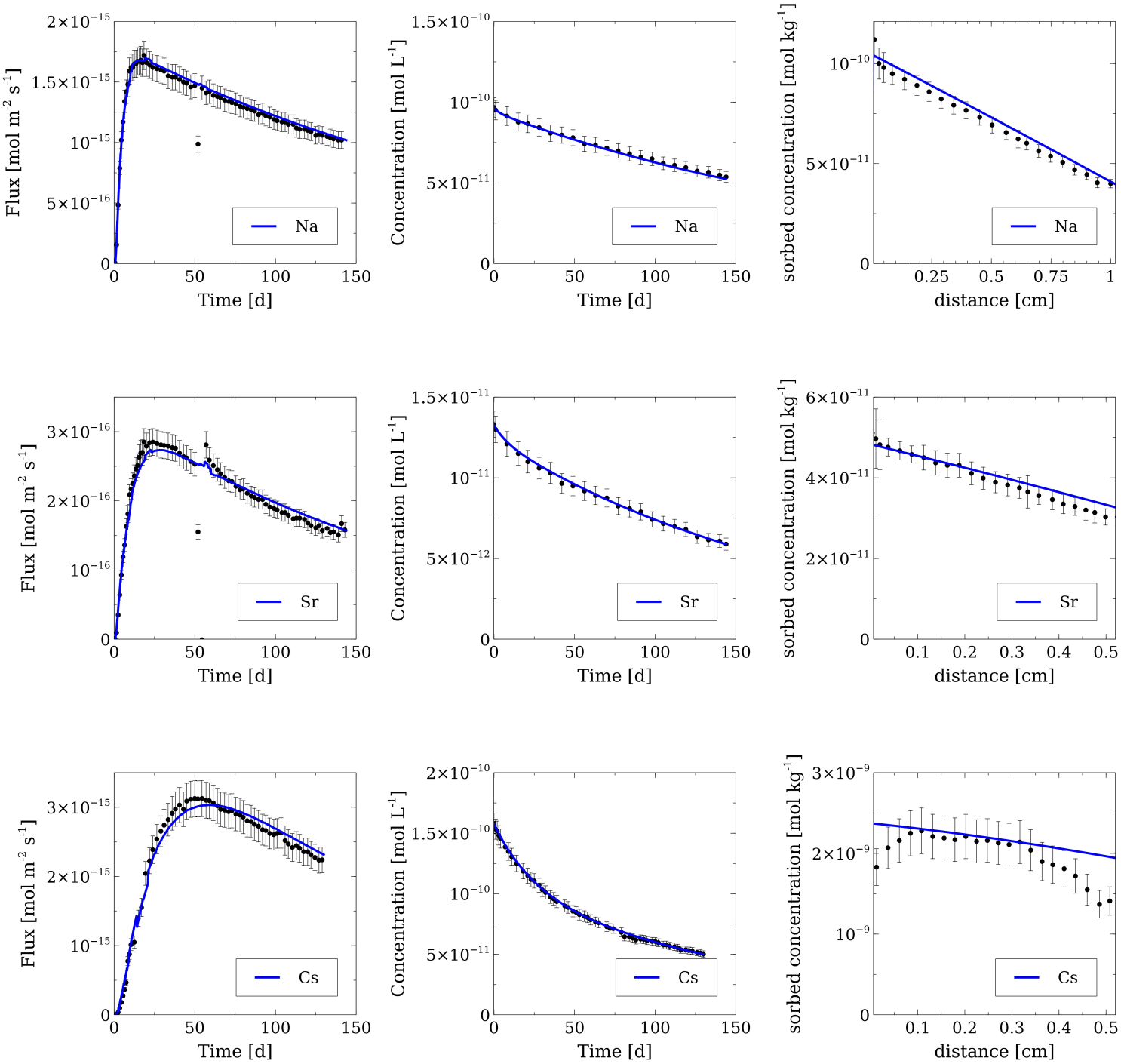

Figure A3: Flux at downstream boundary (first column),concentration in upstream reservoir (second column) and total (sorbed + aqueous) concentration profile for Na (first row), Sr (second row), Cs (third row) at 1.3 kg L^{-1} bentonite dry density; Black dots with error bars: experimental data; blue line: surface diffusion model.

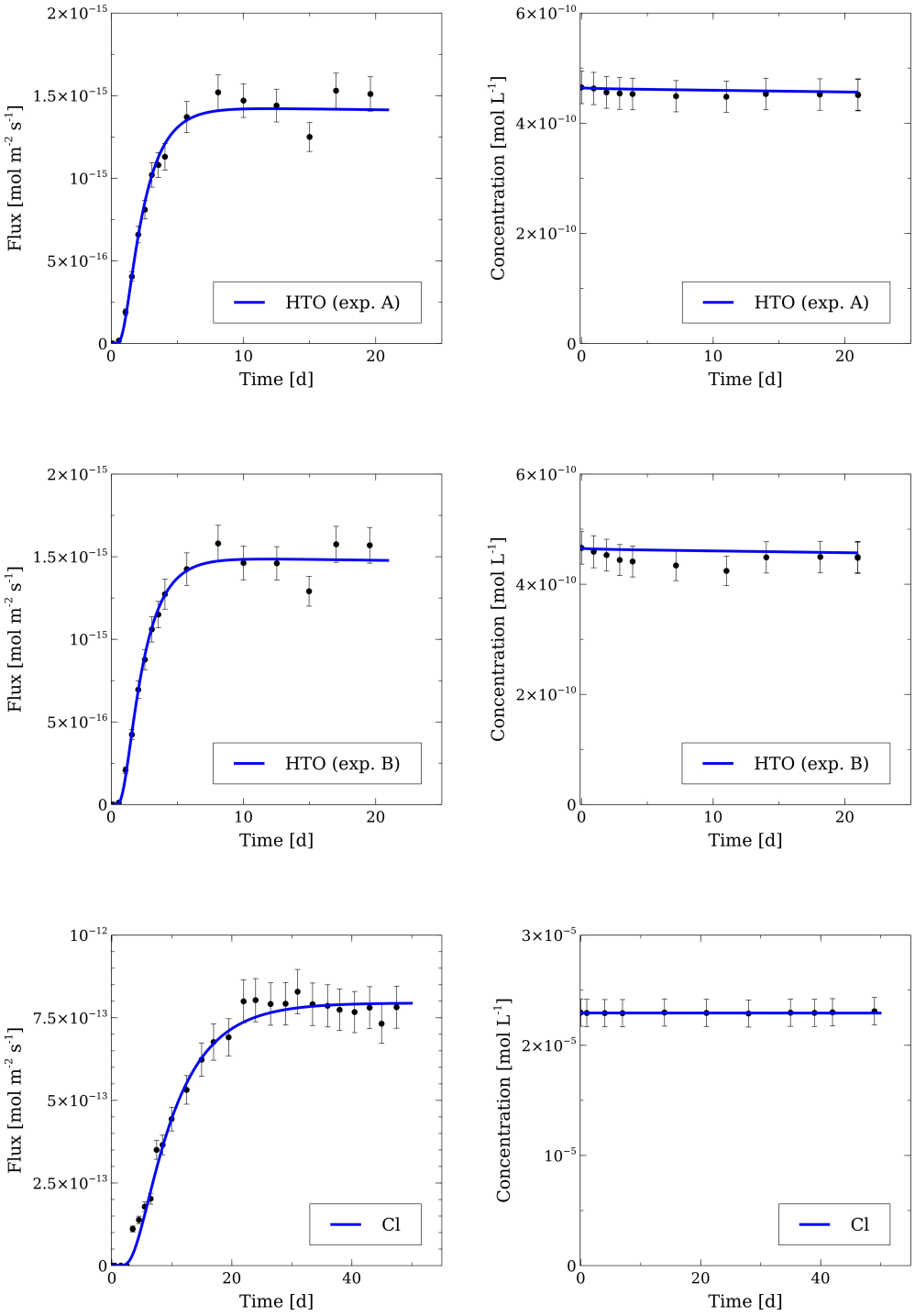

Figure A4: Flux at downstream boundary (first column) and concentration in upstream reservoir (second column) for HTO (first two rows) and Cl (third row) at 1.9 kg L^{-1} bentonite dry density; Black dots with error bars: experimental data; blue line: Fickian diffusion model.

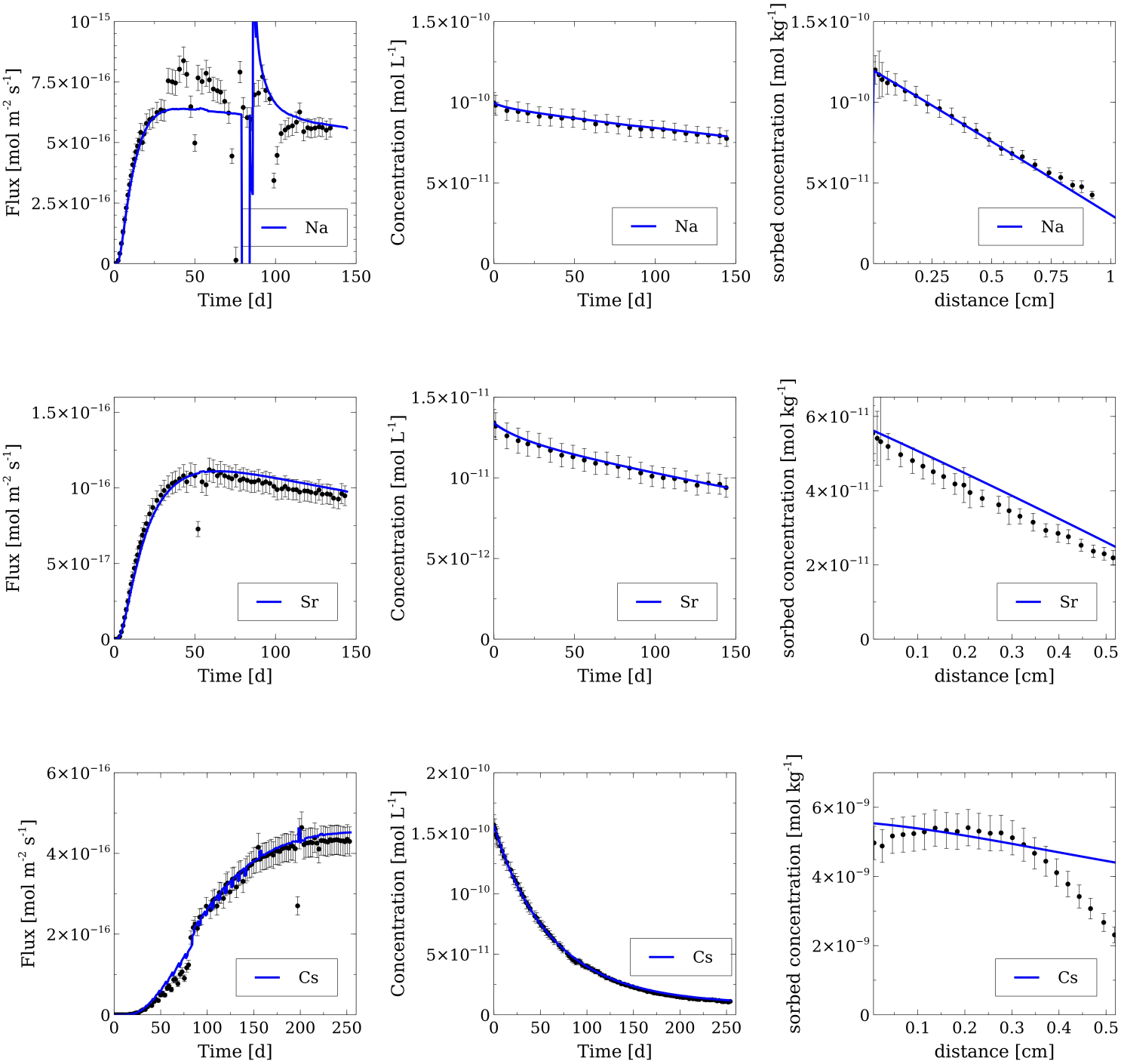

Figure A5: Flux at downstream boundary (first column),concentration in upstream reservoir (second column) and total (sorbed + aqueous) concentration profile for Na (first row), Sr (second row), Cs (third row) at 1.9 kg L^{-1} bentonite dry density; Black dots with error bars: experimental data; blue line: surface diffusion model.

References

Appelo C. A. J., Van Loon L. R. and Wersin P. (2010). Multicomponent diffusion of a suite of tracers (HTO, Cl, Br, I, Na, Sr, Cs) in a single sample of Opalinus Clay. *Geochim. Cosmochim. Acta* **74**, 1201–1219.

Applin K. R. and Lasaga A. C. (1984). The determination of SO42-, NaSO4-, and MgSO40 tracer diffusion coefficients and their application to diagenetic flux calculations. *Geochim. Cosmochim. Acta* **48**, 2151–2162.

Bourg I. C. and Sposito G. (2010). Connecting the molecular scale to the continuum scale for diffusion processes in smectite-rich porous media. *Environ. Sci. Technol.* **44**, 2085–2091.

Bourg I. C. and Sposito G. (2011). Molecular dynamics simulations of the electrical double layer on smectite surfaces contacting concentrated mixed electrolyte (NaCl-$CaCl^2$) solutions. *J. Colloid Interface Sci.* **360**, 701–715. http://dx.doi.org/10.1016/j.jcis.2011.04.063.

Bourg I. C., Sposito G. and Bourg A. C. M. (2007). Modeling cation diffusion in compacted water-saturated sodium bentonite at low ionic strength. *Environ. Sci. Technol.* **41**, 8118–8122.

Bourg I. C., Sposito G. and Bourg A. C. M. (2006). Tracer diffusion in compacted, water-saturated bentonite. *Clays Clay Miner.* **54**, 363–374.

Bourg I. C. and Tournassat C. (2015). Self-Diffusion of Water and Ions in Clay Barriers. In *Developments in Clay Science* (Vol. 6). Elsevier. https://doi.org/10.1016/B978-0-08-100027-4.00006-1

Bradbury M. H. and Baeyens B. (2002). Porewater chemistry in compacted re-saturated MX-80 bentonite: Physico-chemical characterisation and geochemical modelling. *J. Contam. Hydrol.* **61**, 329–338.

Bradbury M. H. and Baeyens B. (1997). A mechanistic description of Ni and Zn sorption on Na-montmorillonite. Part II: Modelling. *J. Contam. Hydrol.* **27**, 223–248.

Davis J. A., James R. O. and Leckie J. O. (1978). Surface Ionization and Complexation at the Oxide/Water Interface. *J. Colloid Interface Sci.* **63**, 480–499.

Flury M. and Gimmi T. (2018). 6.2 Solute Diffusion. In *Methods of Soil Analysis* (eds. J. H. Dane and G. C. Topp). pp. 1323–1351.

Fukatsu Y., Yotsuji K., Ohkubo T. and Tachi Y. (2021). Diffusion of tritiated water, $^{137}Cs^{+}$, and $^{125}I^{-}$ in compacted Ca-montmorillonite: Experimental and modeling approaches. *Appl. Clay Sci.* **211**, 106176. https://doi.org/10.1016/j.clay.2021.106176.

Gimmi T. and Alt-Epping P. (2018). Simulating Donnan equilibria based on the Nernst-Planck equation. *Geochim. Cosmochim. Acta* **232**, 1–13.

Gimmi T. and Kosakowski G. (2011). How mobile are sorbed cations in clays and clay rocks? *Environ. Sci. Technol.* **45**, 1443–1449.

Glaus M. A., Aertsens M., Maes N., Van Laer L. and Van Loon L. R. (2015). Treatment of boundary conditions in through-diffusion: A case study of $^{85}Sr^{2+}$ diffusion in compacted illite. *J. Contam. Hydrol.* **177–178**, 239–248. http://dx.doi.org/10.1016/j.jconhyd.2015.03.010.

Glaus M. A., Baeyens B., Bradbury M. H., Jakob A., Van Loon L. R. and Yaroshchuk A. (2007). Diffusion of ^{22}Na and ^{85}Sr in montmorillonite: Evidence of interlayer diffusion being the dominant pathway at high compaction. *Environ. Sci. Technol.* **41**, 478–485.

Glaus M. A., Frick S. and Van Loon L. R. (2017). Diffusion of Selected Cations and Anions in Compacted Montmorillonite and Bentonite. *PSI Bericht Rep. No. 17-08 Paul Scherrer Inst.*, 85 p.

Glaus M. A., Frick S., Rossé R. and Loon L. R. V. (2010). Comparative study of tracer diffusion of HTO, 22Na+ and 36Cl- in compacted kaolinite, illite and montmorillonite. *Geochim. Cosmochim. Acta* **74**, 1999–2010.

Glaus M. A., Rossé R., van Loon L. R. and Yaroshchuk A. E. (2008). Tracer diffusion in sintered stainless steel filters: Measurement of effective diffusion coefficients and implications for diffusion studies with compacted clays. *Clays Clay Miner.* **56**, 677–685.

González Sánchez F., Van Loon L. R., Gimmi T., Jakob A., Glaus M. A. and Diamond L. W. (2008). Self-diffusion of water and its dependence on temperature and ionic strength in highly compacted montmorillonite, illite and kaolinite. *Appl. Geochemistry* **23**, 3840–3851. http://dx.doi.org/10.1016/j.apgeochem.2008.08.008.

Holmboe M. and Bourg I. C. (2014). Molecular dynamics simulations of water and sodium diffusion in smectite interlayer nanopores as a function of pore size and temperature. *J. Phys. Chem. C* **118**, 1001–1013.

Holmboe M., Wold S. and Jonsson M. (2012). Porosity investigation of compacted bentonite using XRD profile modeling. *J. Contam. Hydrol.* **128**, 19–32. http://dx.doi.org/10.1016/j.jconhyd.2011.10.005.

Kosakowski G., Churakov S. V. and Thoenen T. (2008). Diffusion of Na and Cs in montmorillonite. *Clays Clay Miner.* **56**, 190–206.

Kozaki T., Fujishima A., Sato S. and Ohashi H. (1998). Self-Diffusion of Sodium Ions in Compacted Sodium Montmorillonite. *Nucl. Technol.* **121**, 63–69.

Kozaki T., Inada K., Sato S. and Ohashi H. (2001). Diffusion mechanism of chloride ions in sodium montmorillonite. *J. Contam. Hydrol.* **47**, 159–170.

Kozaki T., Liu J. and Sato S. (2008). Diffusion mechanism of sodium ions in compacted montmorillonite under different NaCl concentration. *Phys. Chem. Earth* **33**, 957–961.

Kozaki T., Sato H., Sato S. and Ohashi H. (1999). Diffusion mechanism of cesium ions in compacted montmorillonite. *Eng. Geol.* **54**, 223–230.

Krejci P., Gimmi T. and Van Loon L. R. (2021). On the concentration-dependent diffusion of sorbed cesium in Opalinus Clay. *Geochim. Cosmochim. Acta* **298**, 149–166. https://doi.org/10.1016/j.gca.2021.01.012.

Lammers L. N., Bourg I. C., Okumura M., Kolluri K., Sposito G. and Machida M. (2017). Molecular dynamics simulations of cesium adsorption on illite nanoparticles. *J. Colloid Interface Sci.* **490**, 608–620. http://dx.doi.org/10.1016/j.jcis.2016.11.084.

Leroy P. and Revil A. (2004). A triple-layer model of the surface electrochemical properties of clay minerals. *J. Colloid Interface Sci.* **270**, 371–380.

Leroy P., Revil A., Altmann S. and Tournassat C. (2007). Modeling the composition of the pore water in a clay-rock geological formation (Callovo-Oxfordian, France). *Geochim. Cosmochim. Acta* **71**, 1087–1097.

Leroy P., Tournassat C., Bernard O., Devau N. and Azaroual M. (2015). The electrophoretic mobility of montmorillonite. Zeta potential and surface conductivity effects. *J. Colloid Interface Sci.* **451**, 21–39. http://dx.doi.org/10.1016/j.jcis.2015.03.047.

Lichtner P. C. (2007). *Flotran User's Manual: Two-Phase Nonisothermal Coupled Thermal-Hydrological-Chemical (THC) Reactive Flow andTransport Code, Version 2.0*., Los Alamos, New Mexico.

Van Loon L. R. and Glaus M. A. (2008). Mechanical compaction of smectite clays increases ion exchange selectivity for cesium. *Environ. Sci. Technol.* **42**, 1600–1604.

Van Loon L. R., Glaus M. A. and Müller W. (2007). Anion exclusion effects in compacted bentonites: Towards a better understanding of anion diffusion. *Appl. Geochemistry* **22**, 2536–2552.

Van Loon L. R., Soler J. M. and Bradbury M. H. (2003). Diffusion of HTO, $^{36}Cl^-$ and $^{125}I^-$ in Opalinus Clay samples from Mont Terri: Effect of confining pressure. *J. Contam. Hydrol.* **61**, 73–83.

Marry V., Rotenberg B. and Turq P. (2008). Structure and dynamics of water at a clay surface from molecular dynamics simulation. *Phys. Chem. Chem. Phys.* **10**, 4802–4813.

Matusewicz M. and Olin M. (2019). Comparison of microstructural features of three compacted and water-saturated swelling clays: MX-80 bentonite and Na- and Ca-purified bentonite. *Clay Miner.* **54**, 75–81.

Matusewicz M., Pirkkalainen K., Liljeström V., Suuronen J.-P., Root A., Muurinen A., Serimaa R. and Olin M. (2013). Microstructural investigation of calcium montmorillonite. *Clay Miner.* **48**, 267–276.

Melkior T., Gaucher E. C., Brouard C., Yahiaoui S., Thoby D., Clinard C., Ferrage E., Guyonnet D., Tournassat C. and Coelho D. (2009). Na^+ and HTO diffusion in compacted bentonite: Effect of surface chemistry and related texture. *J. Hydrol.* **370**, 9–20. http://dx.doi.org/10.1016/j.jhydrol.2009.02.035.

Missana T. and García-Gutiérrez M. (2007). Adsorption of bivalent ions (Ca(II), Sr(II) and Co(II)) onto FEBEX bentonite. Physics and Chemistry of the Earth **32**(8–14), 559–567. https://doi.org/10.1016/j.pce.2006.02.052

Missana T., Benedicto A., García-Gutiérrez M. and Alonso U. (2014). Modeling cesium retention onto Na-, K- and Ca-smectite: Effects of ionic strength, exchange and competing cations on the determination of selectivity coefficients. *Geochim. Cosmochim. Acta* **128**, 266–277.

Molera B. M. and Eriksen T. (2002). Diffusion of $^{22}Na^+$, $^{85}Sr^{2+}$, $^{134}Cs^+$ and $^{57}Co^{2+}$ in bentonite clay compacted to different densities: experiments and modeling. **760**, 753–760.

Muurinen A., Carlsson T. and Root A. (2013). Bentonite pore distribution based on SAXS, chloride exclusion and NMR studies. *Clay Miner.* **48**, 251–266.

Ochs M., Lothenbach B., Wanner H., Sato H. and Yui M. (2001). An integrated sorption-diffusion model for the calculation of consistent distribution and diffusion coefficients in compacted bentonite. *J. Contam. Hydrol.* **47**, 283–296.

Ohkubo T., Ibaraki M., Tachi Y. and Iwadate Y. (2016). Pore distribution of water-saturated compacted clay using NMR relaxometry and freezing temperature depression; effects of density and salt concentration. *Appl. Clay Sci.* **123**, 148–155. http://dx.doi.org/10.1016/j.clay.2016.01.014.

Ohkubo T., Yamazaki A., Fukatsu Y. and Tachi Y. (2021). Pore distribution of compacted Ca-montmorillonite using NMR relaxometry and cryoporometry: Comparison with Na-montmorillonite. *Microporous Mesoporous Mater.* **313**, 110841. https://doi.org/10.1016/j.micromeso.2020.110841.

Pusch R. (2001). The microstructure of MX-80 clay with respect to its bulk physical properties under different environmental conditions. SKB Technical Report TR-01-08.

Siroux B., Beaucaire C., Tabarant M., Benedetti M. F. and Reiller P. E. (2017). Adsorption of strontium and caesium onto an Na-MX80 bentonite: Experiments and building of a coherent thermodynamic modelling. *Appl. Geochemistry* **87**, 167–175.

Soler J. M., Steefel C. I., Gimmi T., Leupin O. X. and Cloet V. (2019). Modeling the Ionic Strength Effect on Diffusion in Clay. the DR-A Experiment at Mont Terri. *ACS Earth Sp. Chem.* **3**, 442–451.

Stumm W. and Morgan J. J. (1996). *Aquatic Chemistry*. third edit., John Wiley and Sons Inc., New York.

Tachi Y. and Yotsuji K. (2014). Diffusion and sorption of Cs+, Na+, I- and HTO in compacted sodium montmorillonite as a function of porewater salinity: Integrated sorption and diffusion model. *Geochim. Cosmochim. Acta* **132**, 75–93. http://dx.doi.org/10.1016/j.gca.2014.02.004.

Tinnacher R. M., Holmboe M., Tournassat C., Bourg I. C. and Davis J. A. (2016). Ion adsorption and diffusion in smectite: Molecular, pore, and continuum scale views. *Geochim. Cosmochim. Acta* **177**, 130–149. http://dx.doi.org/10.1016/j.gca.2015.12.010.

Tournassat C. and Appelo C. A. J. (2011). Modelling approaches for anion-exclusion in compacted Na-bentonite. *Geochim. Cosmochim. Acta* **75**, 3698–3710. http://dx.doi.org/10.1016/j.gca.2011.04.001.

Tournassat C., Bourg I. C., Holmboe M., Sposito G. and Steefel C. I. (2016). Molecular dynamics simulations of anion exclusion in clay interlayer Nanopores. *Clays Clay Miner.* **64**, 374–388.

Tournassat C., Chapron Y., Leroy P., Bizi M. and Boulahya F. (2009a). Comparison of molecular dynamics simulations with triple layer and modified Gouy-Chapman models in a 0.1 M NaCl-montmorillonite system. *J. Colloid Interface Sci.* **339**, 533–541. http://dx.doi.org/10.1016/j.jcis.2009.06.051.

Tournassat C. and Steefel C. I. (2019). Reactive Transport Modeling of Coupled Processes in Nanoporous Media. *Rev. Mineral. Geochemistry* **85**, 75–109.

Wersin P., Soler J. M., Van Loon L., Eikenberg J., Baeyens B., Grolimund D., Gimmi T. and Dewonck S. (2008). Diffusion of HTO, Br^-, I^-, Cs^+, $^{85}Sr^{2+}$ and $^{60}Co^{2+}$ in a clay formation: Results and modelling from an in situ experiment in Opalinus Clay. *Appl. Geochemistry* **23**, 678–691.

Wigger C. and Van Loon L. R. (2018). Effect of the pore water composition on the diffusive anion transport in argillaceous, low permeability sedimentary rocks. *J. Contam. Hydrol.* **213**, 40–48. https://doi.org/10.1016/j.jconhyd.2018.05.001.

Wigger C. and Van Loon L. R. (2017). Importance of interlayer equivalent pores for anion diffusion in clay-rich sedimentary rocks. *Environ. Sci. Technol.* **51**, 1998–2006.

Chapter 4:
A diffusion model that includes transport in the diffuse layer, the Stern layer and the interlayer region: Application to HTO, Cl, Na, Sr, and Cs diffusion in Opalinus Clay

(Manuscript in preparation)

A diffusion model that includes transport in the diffuse layer, the Stern layer and the interlayer region: Application to HTO, Cl, Na, Sr, and Cs diffusion in Opalinus Clay

Philipp Krejci[a,b,*], *Thomas Gimmi*[a,b], *Luc Robert Van Loon*[a]

[a]*Laboratory for Waste Management, Nuclear Energy and Safety, Paul Scherrer Institute, CH-5232 Villigen, Switzerland*

[b]*Rock-Water Interaction, Institute of Geological Sciences, University of Bern, CH-3012 Bern, Switzerland*

*Corresponding author at: Paul Scherrer Institute; *E-mail address*: philipp.krejci@psi.ch (P. Krejci)

Abstract

The diffusion of HTO, Cl, Na, Sr and Cs tracers in Opalinus Clay from Benken and Mont Terri parallel and perpendicular to the bedding was investigated. Diffusion coefficients of anions were lower, those of cations larger than those of water tracers, when normalized by the corresponding diffusion coefficients in bulk water. HTO and Cl accessible porosities and geometrical factors were determined by applying a classical Fickian diffusion model to experimental data. Furthermore, surface mobilities of cations were derived from the data by applying a surface diffusion model. In order to describe the differences between anion and cation diffusion in more detail, the experimentally determined diffusion parameters were also analyzed with a model (DL-SL-IL model) that considers explicitly ion diffusion in the diffuse layer, in the Stern layer, and in the interlayer region in addition to diffusion in bulk pore water. This model is parametrized based on anion exclusion data, from which the distribution of the total (water accessible) porosity and the distribution of charge between the different pore environments is determined. The model is further parametrized with cation specific mobilities in Stern layer and interlayer taken from literature. As cation mobilities in the Stern layer of illite and in the illite/smectite mixed layer are unknown, values determined for Volclay bentonite (chapter 3) were taken and different case scenarios (including the variation of the charge distribution between diffuse and Stern layer, the cation mobility in illite/smectite mixed layer and the activity coefficient in the diffuse layer) were carried out. Predicted diffusion coefficients of the DL-SL-IL model were found to be mostly in good agreement with the experimentally obtained cation diffusion coefficients. The results indicate that this more sophisticated model can describe anion and cation diffusion in a more consistent way than the classical Fickian model or the surface diffusion model.

1 Introduction

Argillaceous rocks, such as Opalinus Clay, have the ability to restrict the migration of radionuclides or other contaminants because of their high sorption capacity and their low hydraulic permeability. For this reason, several countries (i.a., France, Belgium and Switzerland) consider using argillaceous rocks as host rocks for their radioactive waste repository.

The sorption capacity of Opalinus Clay is mostly attributed to its clay minerals, and in particular to illite and illite/smectite mixed layer minerals. Cation adsorption in clays can be described by cation exchange reactions (Lewis, 1949; Elprince et al., 1980; Shainberg et al., 1987; Van Loon et al., 2005; Missana et al., 2014; Siroux et al., 2018). In the case of Cs a three-site cation exchange model (Bradbury and Baeyens, 2000; Van Loon et al., 2009) including adsorption on the planar sites, on intermediate sites and on frayed-edge sites is necessary to explain the concentration-dependent adsorption in Opalinus Clay. Cation exchange models are to be considered as empirical models, as they do not account for the detailed adsorption mechanisms at the clay-water interface.

Close to the negatively charged clay surface cations are adsorbed and anions are excluded. Triple-layer models (Davis et al., 1978; Revil et al., 2005; Leroy et al., 2007) conceptually divide the surface region into the negatively charged surface, the Stern layer and the diffuse layer. In the Stern layer cations can adsorb specifically as inner-sphere complexes and electrostatically as outer-sphere complexes, while anions are assumed to be completely excluded. The diffuse layer consists of a diffuse swarm of cations (with decreasing concentration with distance from the surface) and anions (with increasing concentration with distance from the surface), which compensates the remaining (not compensated in the Stern layer) surface charge. This structure has been corroborated in several molecular dynamics (MD) studies (Tournassat et al., 2009; Bourg and Sposito, 2011; Tinnacher et al., 2016; Lammers et al., 2017). MD simulations also showed that cations and water exhibit a non-zero mobility in the Stern layer (Tournassat et al., 2009; Bourg and Sposito, 2011; Tinnacher et al., 2016).

When applying a simple Fickian diffusion model to experimental data in clays and clay rocks, diffusion coefficients of anions (Van Loon et al., 2003; Descostes et al., 2008; Savoye et al., 2011; Tachi and Yotsuji, 2014) were found to be reduced, while diffusion coefficients of cations (Molera and Eriksen, 2002; Van Loon et al., 2005; Melkior et al., 2007; Jakob et al., 2009) increased, in comparison to diffusion coefficients of water tracers. More sophisticated models including anion and cation diffusion in the diffuse layer were developed and used to describe diffusion of anions (Wigger and Van Loon, 2017; Wigger and Van Loon, 2018) and cations (Appelo et al., 2010; Soler et al., 2019) in Opalinus Clay more consistently. However, at least for strongly sorbing tracers such as Cs these models are not able to match the experimental data. It is thus necessary to further improve the model concepts and to test them on experimental data, if possible, with all required parameters determined independently. That is, the empirical diffusion coefficients have to be underpinned by demonstrating a detailed understanding of the relevant processes.

In this paper diffusion of the tracers HTO, Cl, Na, Sr and Cs in Opalinus Clay from Benken and Mont Terri, in the direction parallel and perpendicular to the clay bedding, was studied. Experimental results of through-diffusion experiments for HTO and Cl were modeled with a classical Fickian diffusion model. Based on the porosity and geometrical factor for HTO, cation diffusion was modeled in a first attempt with a simple surface diffusion model (SD). Effective diffusion coefficients of anions and cations derived by the former models varied for the different pore waters used for the Benken and the Mont Terri Opalinus Clay, and they varied in different ways for the directions parallel and perpendicular to the clay bedding. In order to gain more detailed insight into anion and cation diffusion in Opalinus Clay and to explain the observed differences, a model including diffusion in ‘free’

pore water, in the diffuse layer, in the Stern layer and in interlayers (DL-SL-IL model) was then applied in a second attempt. The model is based on parameters defining the pore structure of the Opalinus Clay and on anion exclusion data of Wigger and Van Loon (2018), as well as on ion specific mobilities of cations in the Stern and interlayer derived from MD simulations for montmorillonite clay minerals. Diffusion coefficients predicted by the DL-SL-IL model of Na, Sr and Cs were finally compared to the values derived from experimental data.

2 Modeling approaches

Diffusion of HTO, Cl, Na, Sr and Cs in Opalinus Clay was modeled using the same modeling approaches as presented in chapter 3. Therefore, section 2 in chapter 3 was adopted here and only slightly adapted when necessary.

2.1 Surface diffusion model

A fairly simple way to describe the experimental cation diffusion data in Opalinus Clay is the application of a surface diffusion model (Gimmi and Kosakowski, 2011; Krejci et al., 2021). This model incorporates, in addition to pore diffusion, the mass fluxes that result from enrichment of cations close to the clay surfaces. Their contributions are represented with one model parameter, the surface mobility μ_s. At the local scale, pore and surface fluxes follow parallel pathways, but at the sample scale they follow also serial pathways, when considering the small particle sizes compared to a typical sample size. Equilibrium between both regions can be presumed because of their closeness. Then, the total mass flux for constant background concentrations can be written as:

$$j_{tot} = j_p + j_s = -\varepsilon \frac{D_0}{G}\frac{\partial C}{\partial x} - \rho_{bd}\frac{\mu_s D_0}{G}\frac{\partial S}{\partial C}\frac{\partial C}{\partial x} \quad (1)$$

where j_p and j_s are the fluxes for the pore and surface regions, C is the concentration in solution, S is the sorbed concentration per mass of dry solid, D_0 is the cation diffusion coefficient in bulk water, ε is the total (water accessible) porosity, ρ_{bd} is the bulk dry density, G is the so-called geometrical factor ('tortuosity') and accounts for the tortuous and constricted pathway in the pore water, $\partial S/\partial C$ is the derivative of the sorption isotherm, and $\partial C/\partial x$ is the concentration gradient in the pore water. It must be pointed out that the product of ρ_{bd} and S equals the total sorbed amount (e.g., in moles) per bulk sample volume.

One problem when splitting the flux into separate fluxes of two or multiple transport domains as in Eq. (1) is the assignment of tortuosities (geometrical factors G) to each domain. As noted by Gimmi and Kosakowski (2011), these tortuosities are only defined at the global scale of a sample, where we have a parallel and serial combination of the pathways, but not at the local scale for a single domain. We assume here that identical tortuosities apply to the different pathways in Eq. (1), as in Gimmi and Kosakowski (2011), because the domains are considered to be in close contact and solutes to be in local equilibrium. However, this assumption may be an oversimplification and introduces uncertainty. The balance equation then is:

$$\left(\varepsilon + \rho_{bd}\frac{\partial S}{\partial C}\right)\frac{\partial C}{\partial t} = \frac{\partial}{\partial x}\left(\varepsilon\frac{D_0}{G}\right)\frac{\partial C}{\partial x} + \frac{\partial}{\partial x}\left(\rho_{bd}\frac{\mu_s D_0}{G}\right)\frac{\partial S}{\partial C}\frac{\partial C}{\partial x} \quad (2)$$

Neglecting the second term on the right hand side in Eq. (1) and Eq. (2) one obtains the equations of the classical Fickian diffusion model with the effective diffusion coefficient D_e being $D_e = \varepsilon D_p = \varepsilon D_0/G$, and the pore diffusion coefficient $D_p = D_0/G$.

The SD model was implemented in the reactive transport code Flotran (Lichtner, 2007) using an implicit approach where pore and surface diffusion are combined in a single diffusion coefficient (Krejci et al., 2021):

$$D_{e,comb} = \frac{\varepsilon D_0}{G} + \rho_{bd}\frac{\mu_s D_0}{G}\frac{\partial S}{\partial C} \quad (3)$$

The SD model, as written here, is based on the assumption that cations can diffuse in the same pore space as water plus in a surface layer, and therefore the porosity accessible to cations in the first term of Eq. (1) is the same as that for water $\varepsilon = \varepsilon_w$. Also, no explicit dependence of the surface mobility μ_s is considered in Eq. (3). As mentioned, the geometrical factor G is a 'global' parameter at the sample scale and is typically derived from experimental diffusion data.

2.2 Combined DL-SL-IL model

In order to gain a more detailed insight into the diffusive processes of cations in Opalinus Clay and also to be able to predict the dependence of diffusion coefficients for different Opalinus Clay pore waters, a more sophisticated model is necessary. Here, a recently developed model for diffusion in bentonite (chapter 3) is adapted for Opalinus Clay. It accounts for cation fluxes in free (bulk, uncharged) water, in the diffuse layer, in the Stern layer, and in the interlayer space of smectites. Conceptually, the model splits the total pore space into an external pore space, which includes bulk, diffuse layer and Stern layer space, and an interlayer pore space; the latter may be characterized by a distribution of widths or hydration states. Again, it is assumed that the bulk, diffuse and Stern layer fluxes are parallel and the pore environments are locally in equilibrium. Local equilibrium is also assumed between the interlayer pore space and the pore water of the external pores. The total mass flux of the DL-SL-IL model is then written as (chapter 3):

$$\begin{aligned} j_{tot} &= j_{free} + j_{DL} + j_{SL} + j_{IL} \\ &= \left(-\varepsilon_{free} - \varepsilon_{DL}\frac{C_{DL}}{C} - \mu_{SL}\rho_{bd}\frac{\partial S_{SL}}{\partial C} - \sum_i \mu_{IL,i}\rho_{bd}\frac{\partial S_{IL,i}}{\partial C} \right) \frac{D_0}{G_{DL,SL,IL}}\frac{\partial C}{\partial x} \end{aligned} \quad (4)$$

where ε_{free} and ε_{DL} are the porosities of the pore space not influenced by the surface and in the DL, respectively, and $G_{DL,IL,SL}$ is the geometrical factor of the DL-SL-IL model. Stern layer and interlayer fluxes are described via their derivatives of the sorption isotherms $\partial S_{SL,IL,i}/\partial C$ and their specific mobilities $\mu_{SL,IL,i}$. The sum for the interlayer contributions originates from considering a distribution of interlayer hydration states i (i.e., average number of water layers). It is to note that the product of $\rho_{bd} S_{SL,IL,i}$ equals the sorbed amount (e.g., moles) in the Stern layer or an interlayer i per bulk sample volume, and that this product could equally be expressed as $\varepsilon_{SL,IL,i} C_{SL,IL,i}$, i.e., as porosity of the corresponding pore environment multiplied by the corresponding concentration. Here, no explicit Stern layer pore volume is considered, and it is assumed that the total porosity ε_{tot} is the sum of ε_{free}, ε_{DL} and all $\varepsilon_{IL,i}$ (and possibly, see section 4, an additional porosity of interlayer-equivalent or bottleneck pores). A combined diffusion coefficient for the DL-SL-IL model can be derived from Eq. (4):

$$D_{DL,SL,IL} = \left(\varepsilon_{free} + \varepsilon_{DL}\frac{C_{DL}}{C} + \mu_{SL}\rho_{bd}\frac{\partial S_{SL}}{\partial C} + \sum_i \mu_{IL,i}\rho_{bd}\frac{\partial S_{IL,i}}{\partial C}\right)\frac{D_0}{G_{DL,SL,IL}} \quad (5)$$

The cation concentrations in the diffuse layer C_{DL} are determined by the amount of charge compensated in the diffuse layer. Moreover, they depend on the charge of a cation as well as on the ratio of cation activity coefficients γ in 'free' bulk water and DL water. C_{DL} can be approximated by a Donnan approach where ion concentrations are averaged over the volume of the diffuse layer and expressed via a Boltzmann type distribution:

$$C_{DL} = C\frac{\gamma_{bulk}}{\gamma_{DL}} e^{-zF\frac{\Psi_D}{RT}} \quad (6)$$

where Ψ_D is the Donnan potential, z is the charge of the ion, F is the Faraday constant, R is the universal gas constant and T is the temperature and γ_{bulk} and γ_{DL} are the activity coefficients in bulk

(free) and DL pore water. The distribution (enrichment or depletion) factor is defined as $\xi = C_{DL}/C$. The Donnan potential Ψ_D can be obtained from a charge balance:

$$\sum_i z_i C_{i,DL} = Q \tag{7}$$

where Q is the net surface charge compensated in the DL per Donnan volume:

$$Q = \frac{CEC_{DL}\rho_{bd}}{\varepsilon_{DL}} \tag{8}$$

Here CEC_{DL} is the fraction of the total cation exchange capacity that is compensated by ions in the diffuse layer.

Anion diffusion is modeled by the same equation (Eq. (5)), but assuming zero anion concentrations in the Stern layer and in the interlayer pore space (consisting of a few water layers only at the considered dry densities of Opalinus Clay). Also, a different geometrical factor than for water or cations has to be taken into account. This is a consequence of the fact that G or the tortuosity is a property at the sample scale that depends on the network of pathways, which is different for anions compared to cations or water tracers.

3 Application of Fickian and SD models to experimental results

3.1 Diffusion experiments and model input parameters

Previously published experimental data of HTO, Cl, Na and Sr diffusion (Van Loon et al., 2004; Appelo et al., 2010) is used to apply a classical Fickian diffusion model and the surface diffusion model. Opalinus Clay specimen from the Mont Terri (MT) Underground Rock Laboratory and from the deep borehole in Benken (BE) were investigated. The experiments were carried out using a radial diffusion set-up for diffusion parallel to the bedding in Opalinus Clay, whereas a through diffusion set-up was used for diffusion perpendicular to the bedding. Concentration in the upstream reservoir as well as the tracer flux at the downstream boundary were measured. The detailed experimental set-up and description can be found in Van Loon et al. (2004) and the mineral compositions as well as the pore water compositions for Opalinus Clay from Mont Terri (Table A1) and Benken (Table A2) are found in the appendix. Van Loon et al. (2004) modeled the diffusion of HTO, Cl and Na in MT and BE Opalinus Clay by applying a Fickian diffusion model, while the Appelo et al. (2010) modeled HTO, Na and Sr diffusion in MT Opalinus Clay parallel to the clay bedding with a more sophisticated model, which included diffusion in 'free' pore water and in the diffuse layer.

Here, diffusion of HTO and Cl was modeled with a classical Fickian diffusion model (first term Eq. (1) and Eq. (2)), diffusion of Na and Sr in the first attempt with the surface diffusion model. Porosity and the geometrical factor determined for HTO diffusion was then used for the modeling of the cations with the surface diffusion model. Upstream reservoir, clay specimen and filters on both sides are explicitly included in the model. For all tracers a zero-concentration boundary condition was applied at the outlet reservoir. Filter diffusion coefficients for the tracers were taken to be 10% of the value of their bulk diffusion coefficients (Table 1), in agreement with a diffusion coefficient for fresh filters according to Glaus et al. (2008). Aquatic complexation and ion exchange are calculated using the activity model of Davies (Stumm and Morgan, 1996), where the activity $a = \gamma(C/C_0)$ is expressed via the of concentration divided by the standard concentration (C_0 is 1 M) times an activity coefficient γ (Table 2). Sorption of Na and Sr was modeled via a 1-site cation exchange model which accounts for adsorption of Na and Sr on the planar (basal) surfaces of Opalinus Clay (Table 3). Appelo et al. (2010) found sorption on one site to be sufficient to describe the diffusion and sorption behavior of Na and Sr in Opalinus Clay, unlike that of Cs, where a 3-site cation exchange model is required (Bradbury and Baeyens, 2000; Van Loon et al., 2009). For the simulations of the experiments on Mont Terri samples a CEC of 0.117 eq kg^{-1} (Appelo et al., 2010) was used; for the experiments on Benken samples a CEC of 0.115 eq kg^{-1} close to a reported value of 0.105 eq kg^{-1} (Van Loon et al., 2005) was used. The selectivity constant for Sr was determined from the flux breakthrough curve. Derivatives of the sorption isotherm were calculated numerically (Krejci et al., 2021).

Table 1: Tracer specific bulk diffusion coefficients (Flury and Gimmi, 2018).

Species	D_0 [m^2 s^{-1}]
HTO	$2.236 \cdot 10^{-9}$
Cl^-	$2.03 \cdot 10^{-9}$
Na^+	$1.33 \cdot 10^{-9}$
Sr^{2+}	$0.794 \cdot 10^{-9}$
Cs^+	$2.06 \cdot 10^{-9}$

Table 2: Ionic strength and activity coefficients for Cl, Na and Sr tracers for MT and BE pore water (Tables A1 and A2) calculated after Davies (Stumm and Morgan, 1996).

	MT	BE
Ionic strength [M]	0.39	0.2
Cl^-	0.7353	0.7522
Na^+	0.7353	0.7522
Sr^{2+}	0.2924	0.3202

Table 3: Cation exchange reactions and selectivity coefficients used in the 1-site cation exchange model.

Cation exchange reactions	Selectivity coefficients (log K_C)
Na-PS + K ↔ K-PS + Na	1.1**
2Na-PS + Ca ↔ Ca-PS + 2Na	0.67*
2Na-PS + Mg ↔ Mg-PS + 2Na	0.59*
2Na-PS + Sr ↔ Sr-PS + 2Na	1.0***
Na-PS + Cs ↔ Cs-PS + Na	1.6**
* (Bradbury and Baeyens, 1998) ** (Van Loon et al., 2009) *** adapted	

3.2 Results of HTO and Cl diffusion

The diffusion data (flux at the downstream side, inlet reservoir concentration) of HTO and Cl could be satisfactorily described with the classical Fickian diffusion model (Figures 1-4). For HTO, the MT specimen showed slightly higher HTO accessible porosities than the BE specimen (Table 4), which is consistent with water-loss determinations for MT (Gimmi et al., 2014) and BE (Gimmi et al., 2007) Opalinus Clay. For both, MT and BE, porosities were found to be the same parallel and perpendicular to the clay bedding. The geometrical factors were found to be significantly higher in the direction perpendicular to the bedding than parallel. Cl accessible porosities and the geometrical factor for Cl were higher than the values found for HTO (Table 4). For MT, Cl accessible porosities were about half that for HTO, for BE about a third of the HTO porosity. Cl accessible porosities parallel and perpendicular were found to be the same for MT and BE, while the geometrical factors were lower for the parallel cases.

Table 4: HTO and Cl accessible porosities and geometrical factors.

	MT		BE	
	Parallel	Perpendicular	Parallel	Perpendicular
ε_{HTO}	0.171	0.171	0.15	0.15
G_{HTO}	6.4	26.2	9.7	60.6
ε_{Cl}	0.084	0.084	0.043	0.043
G_{Cl}	9.8	40.8	23.8	128.2

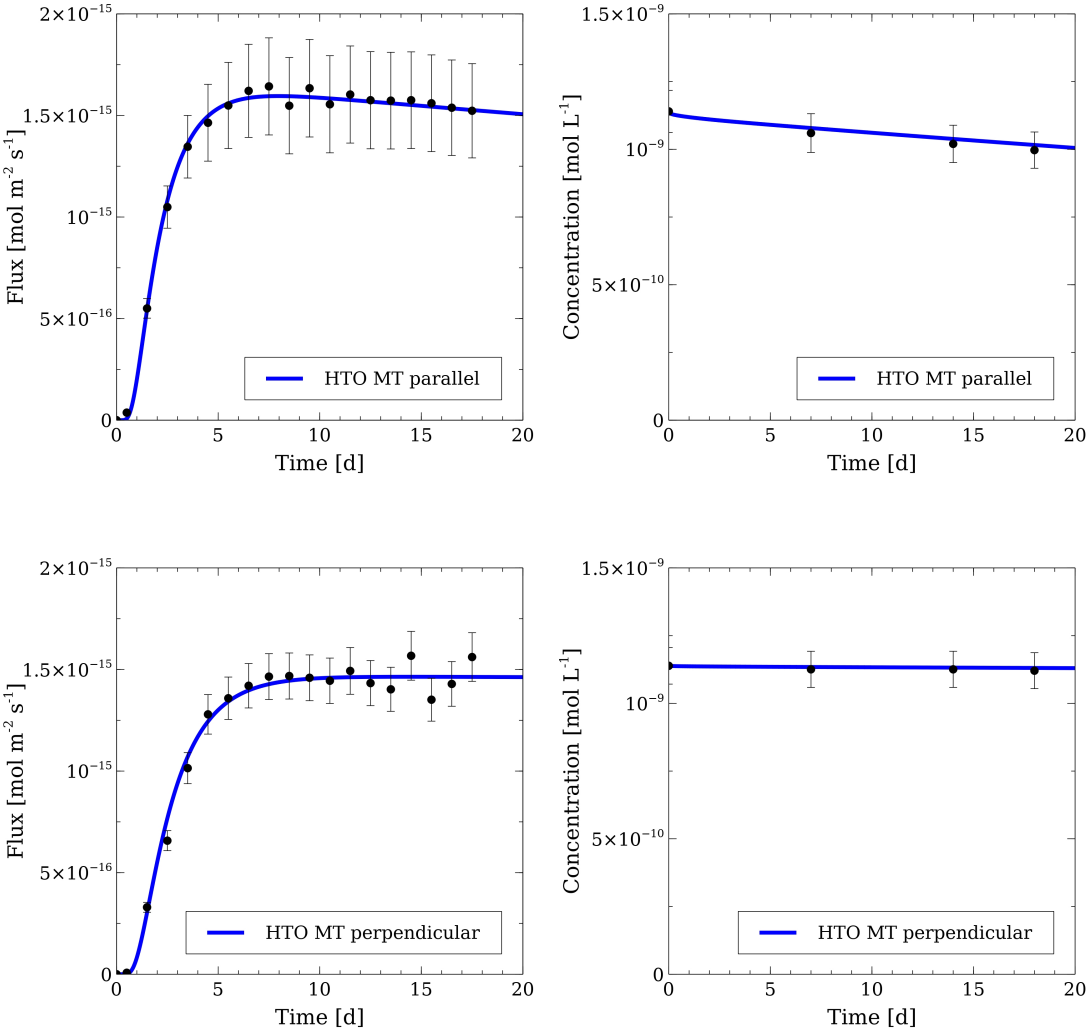

Figure 1: HTO flux at downstream end (left) and HTO upstream reservoir concentration (right) for Mont Terri Opalinus Clay parallel (1st row) and perpendicular (2nd row) to the bedding. Experimental values (dots) and simulations (lines; fitted parameters).

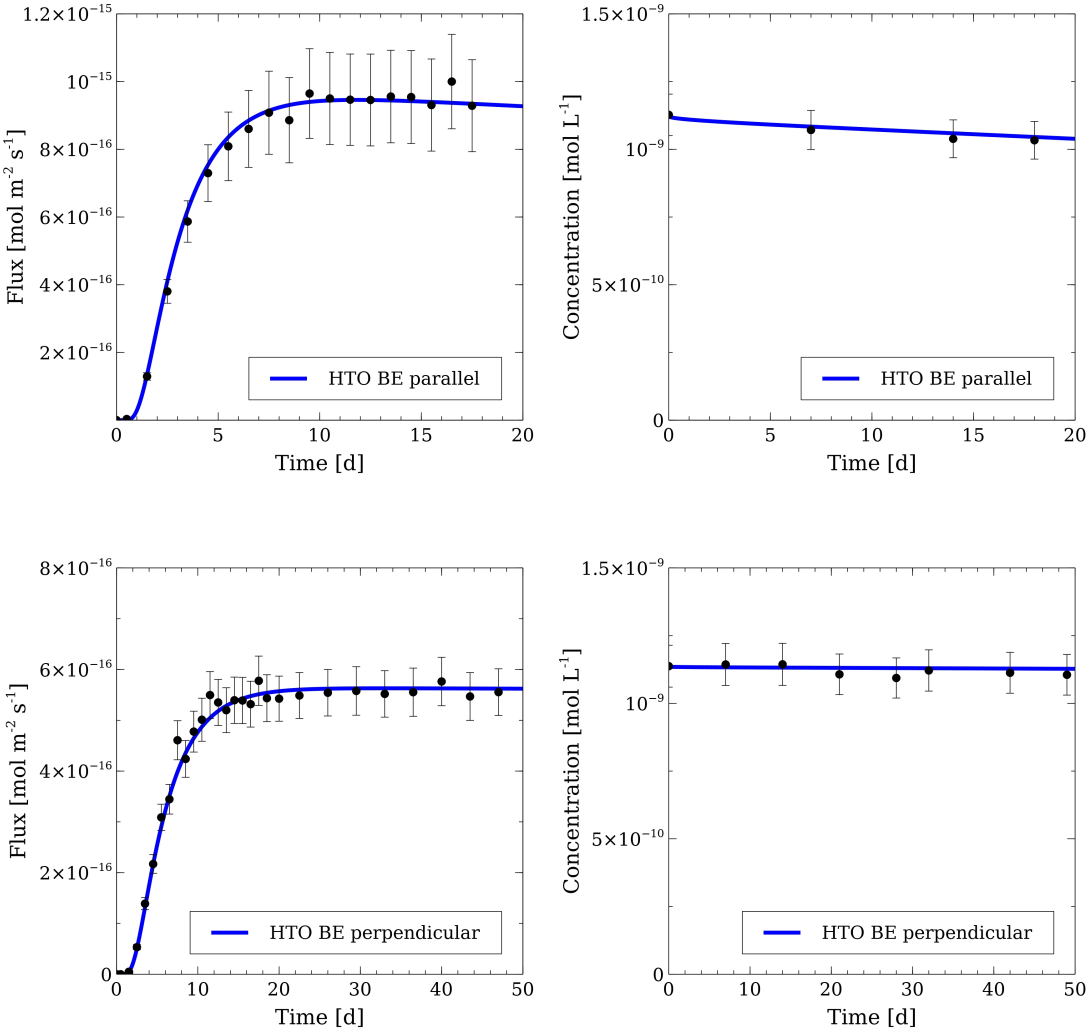

Figure 2: HTO flux at downstream end (left) and HTO upstream reservoir concentration (right) for Benken Opalinus Clay parallel (1st row) and perpendicular (2nd row) to the bedding. Experimental values (dots) and simulations (lines; fitted parameters).

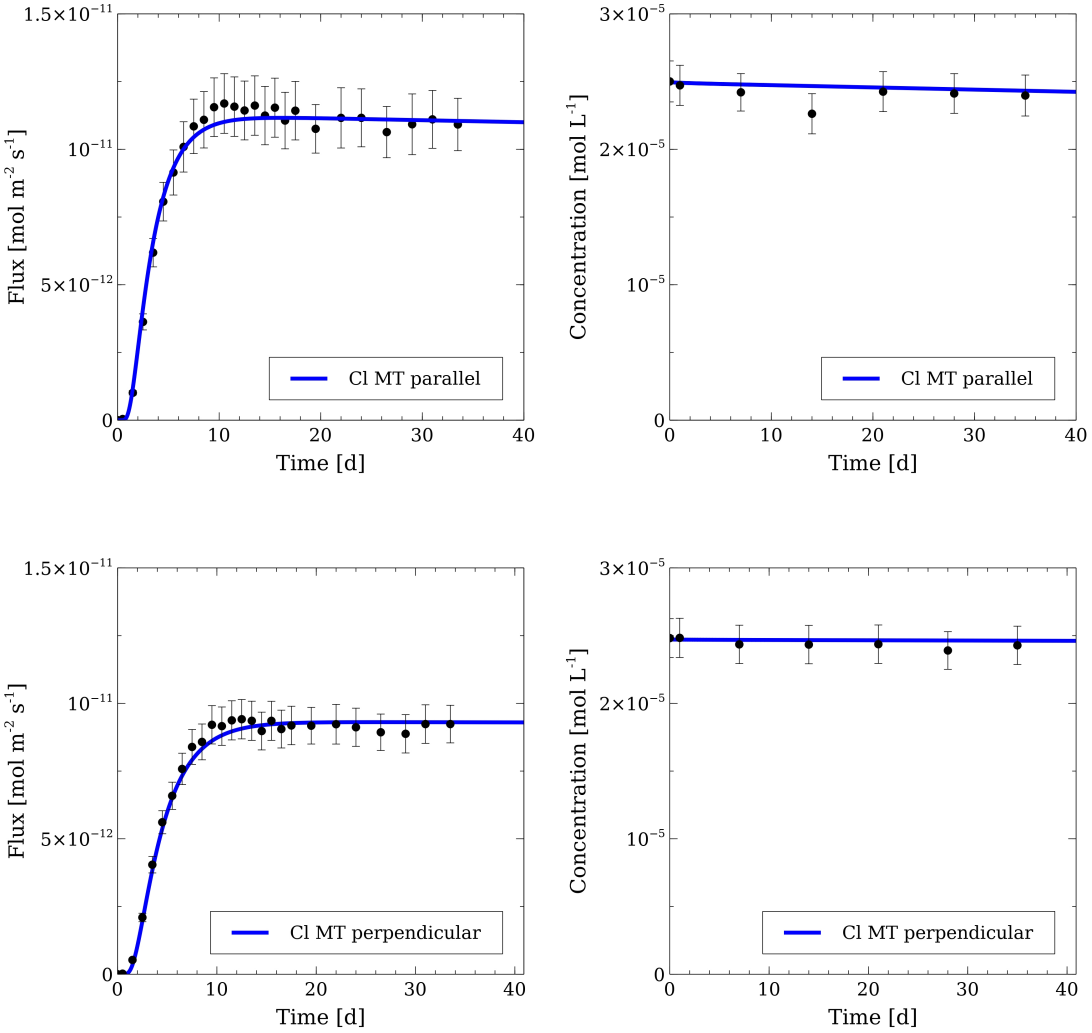

Figure 3: Cl flux at downstream end (left) and Cl upstream reservoir concentration (right) for Mont Terri Opalinus Clay parallel (1st row) and perpendicular (2nd row) to the bedding. Experimental values (dots) and simulations (lines; fitted parameters).

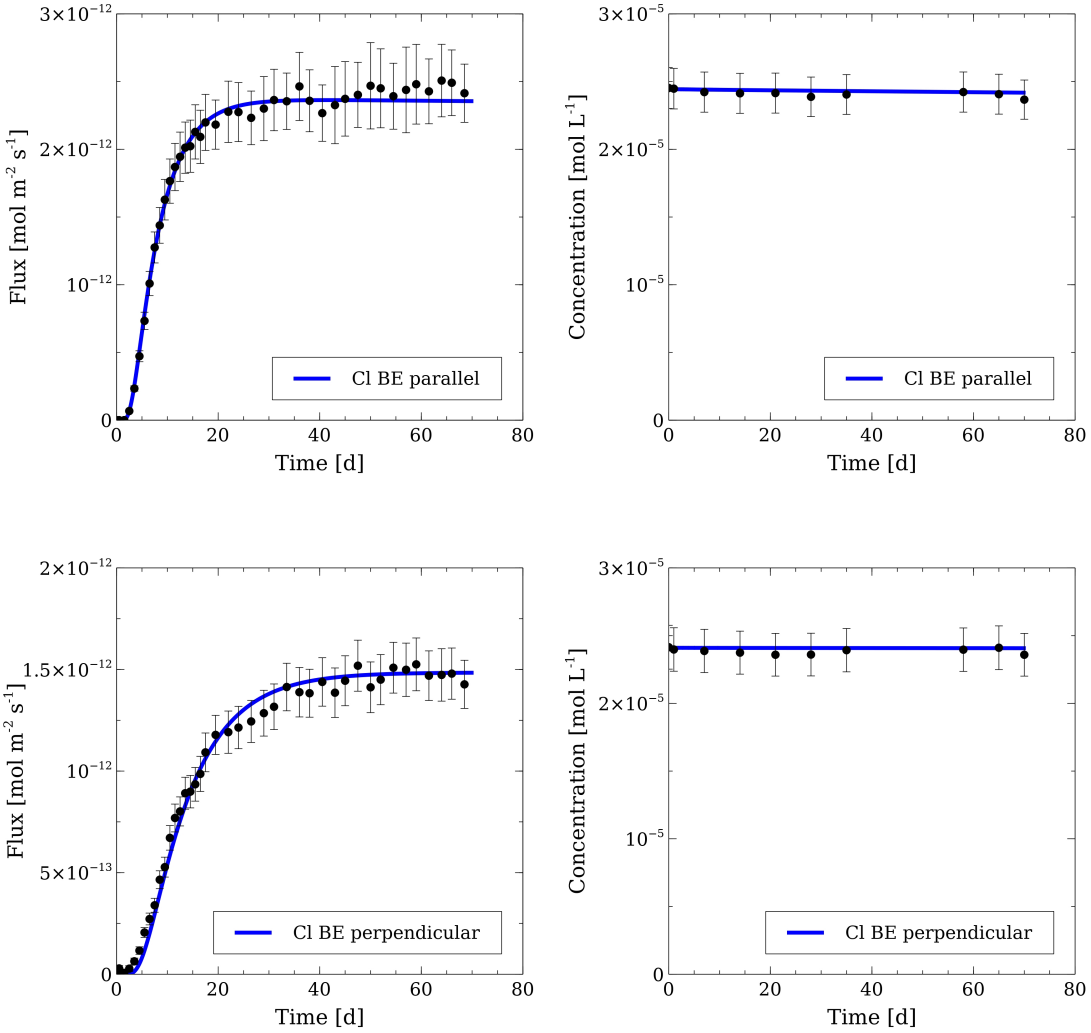

Figure 4: Cl flux at downstream end (left) and Cl upstream reservoir concentration (right) for Opalinus Clay from Benken parallel (1st row) and perpendicular (2nd row) to the bedding. Experimental values (dots) and simulations (lines; fitted parameters).

3.3 Results of Na and Sr diffusion

Na and Sr diffusion data was well described with a surface diffusion model (Figures 5-7): Upstream reservoir concentrations and downstream fluxes were in reasonable agreement with the experimental values. For Sr, a selectivity coefficient of 1.0 was found to match the transient phase of the breakthrough flux curve. For Na diffusion in MT Opalinus Clay perpendicular to the bedding, the CEC had to be reduced to a value of 0.066 eq kg^{-1}, a value about half which was found by Appelo et al. (2010), in order to match the slope in the transient phase of the experimental flux data. Na surface mobilities were found to be higher for BE than for MT, as well as higher parallel to the surface than perpendicular (Table 5). The mobility found for Sr was about one order of magnitude lower than for Na. Cs mobility (a factor 100 lower than the Na mobility) determined in Krejci et al. (2021) (corrected value, see correction note of chapter 2) was also included in Table 5 for comparison and discussion later. Derivatives of the sorption isotherm were higher for BE than for MT and lowest for Na and highest for Cs.

Table 5: Surface mobilities of Na and Sr (derived here), as well as values for Cs (from Krejci et al. (2021)) determined with the SD model, derivatives of the sorption isotherms based on the 1-site cation exchange model and resulting combined effective diffusion coefficients (Eq. (3)).

	MT		BE	
	Parallel	Perpendicular	Parallel	Perpendicular
μ_{Na}	0.57	0.45	0.73	0.55
μ_{Sr}	0.055	-	-	-
μ_{Cs}	0.045	-	-	-
$\frac{\partial S_{Na}}{\partial C_{Na}}$	0.256	0.144	0.384	0.384
$\frac{\partial S_{Sr}}{\partial C_{Sr}}$	1.4	1.4	3.66	3.66
$\frac{\partial S_{Cs}}{\partial C_{Cs}}$	9.3	9.3	13.2	13.2
$D_{e,Na}$ [m^2 s^{-1}]	$1.0 \cdot 10^{-10}$	$1.6 \cdot 10^{-11}$	$1.1 \cdot 10^{-10}$	$1.4 \cdot 10^{-11}$
$D_{e,Sr}$ [m^2 s^{-1}]	$9.8 \cdot 10^{-11}$	-	-	-
$D_{e,Cs}$ [m^2 s^{-1}]	$3.6 \cdot 10^{-10}$	-	-	-

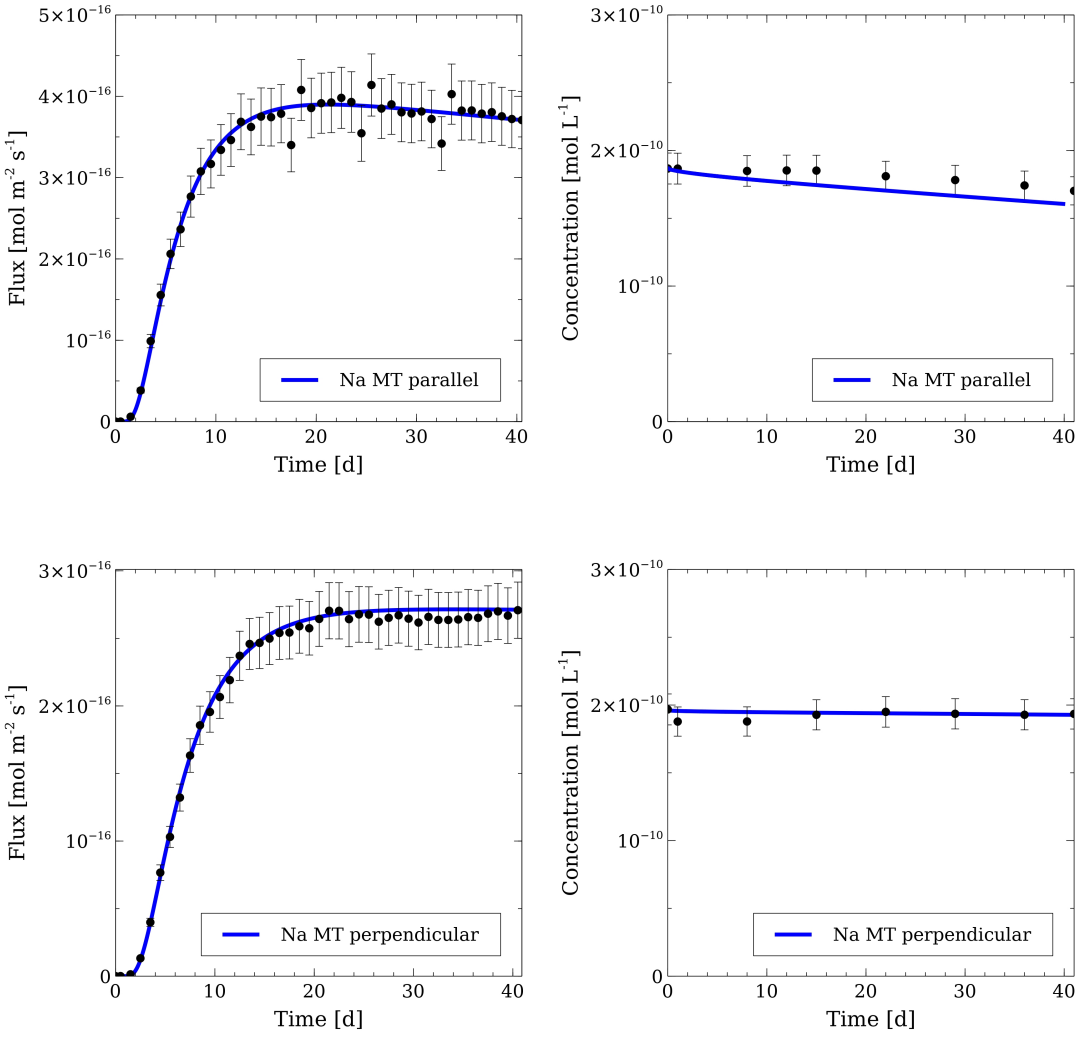

Figure 5: Na flux at downstream end (left) and Na upstream reservoir concentration (right) for Mont Terri Opalinus Clay parallel (1st row) and perpendicular (2nd row) to the bedding. Experimental values (dots) and simulations (lines; fitted parameters).

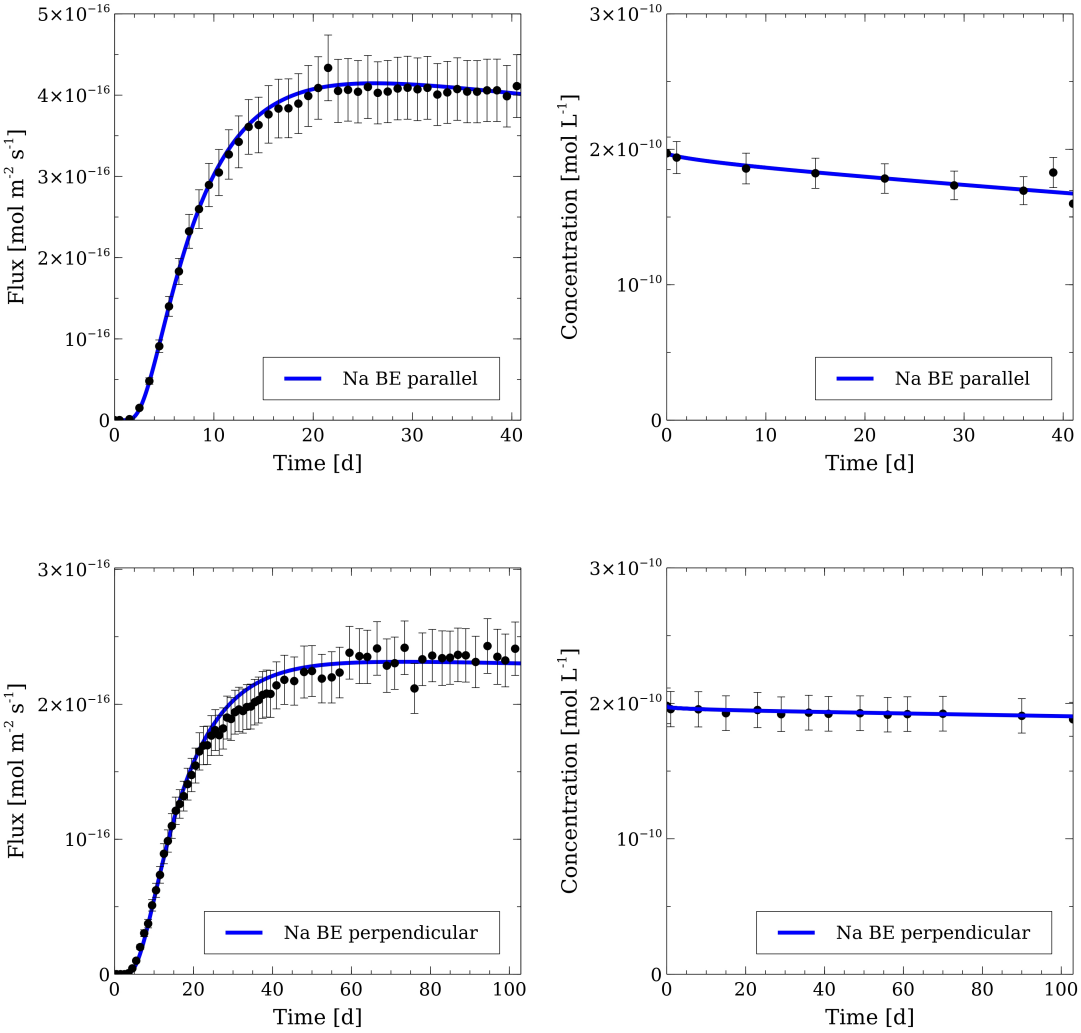

Figure 6: Na flux at downstream end (left) and Na upstream reservoir concentration (right) for Opalinus Clay from Benken parallel (1st row) and perpendicular (2nd row) to the bedding. Experimental values (dots) and simulations (lines; fitted parameters).

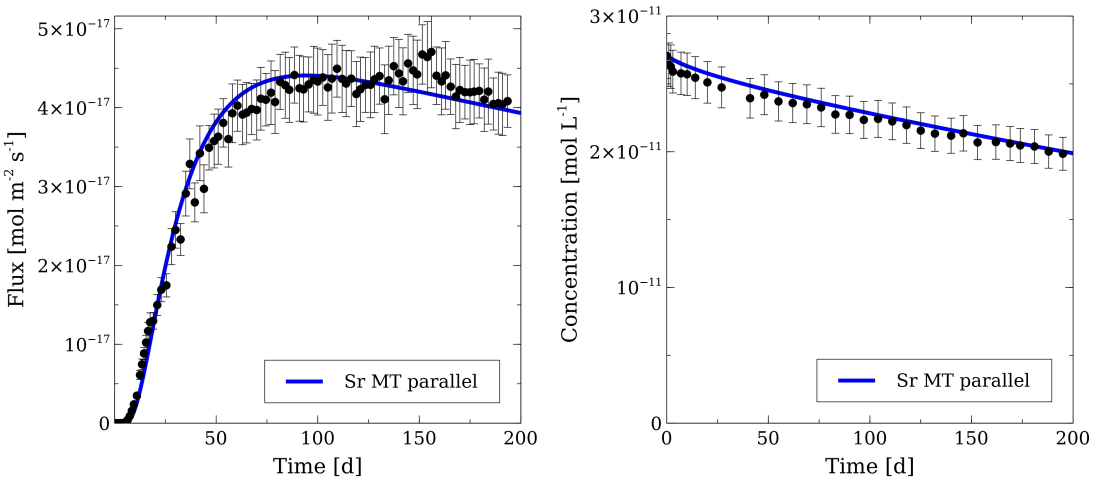

Figure 7: Sr flux at downstream end (left) and Sr upstream reservoir concentration (right) for Mont Terri Opalinus Clay parallel (1st row) and perpendicular (2nd row) to the bedding. Experimental values (dots) and simulations (lines; fitted parameters).

4 Application of DL-SL-IL model to experimental results and discussion

The HTO and Cl accessible porosities found in the previous section are in good agreement with the values determined in Van Loon et al. (2004) and are not affected by the orientation of the bedding. In both orientations the tracers can access the same pore space, as expected. However, geometrical factors for the perpendicular cases are significantly larger than for the parallel ones. This can be explained by the more tortuous diffusion pathways tracers have to take perpendicular to the bedding due to the large aspect ratio of clay particles. The lower Cl accessible porosities compared to HTO can be explained by the effect of the negatively charged surface on the transport of ions. Anions are (partially) excluded from the pore space influenced by the surface charge leading to a lower effective anion accessible porosity. The exclusion effect is more pronounced in the BE experiments, where the ionic strength is lower. In this case, the DL has a bigger extent. In addition, the geometrical factors for Cl are larger compared to those for HTO, because some pores tend to be completely inaccessible for anions (e.g., interlayer pores), which results in a more tortuous pathway for Cl. For cations diffusion coefficients are larger compared to those of HTO, as their mobility in the diffusive layer and most likely in the Stern layer deviates significantly from zero. The higher values of surface mobilities of Na parallel to the bedding compared to perpendicular to the bedding may be explained by a more continuous connection between the clay surfaces parallel to the bedding, while they are less connected in the perpendicular direction. The higher Na surface mobility in BE Opalinus Clay compared to MT, however, shows the limits of the SD model considering a single type of sorption. A more relevant mass flux in the DL compared to that in the 'free' pore water is expected for a lower ionic strength, in parallel to the lower accessibility for Cl, but in the SD model this is accounted for by the larger derivative $\partial S/\partial C$ for the BE samples only. Any dependency of the surface mobility on the ionic strength and sample type cannot be predicted by a single-site SD model, as it treats all sorbed cations as equally mobile.

In order to get a more detailed insight into the diffusion process of cations and anions, a more sophisticated model is necessary. Therefore, the previous results were further analyzed with the combined DL-SL-IL model that accounts for diffusion in bulk water, in the diffuse layer, in the Stern layer and in interlayers. When assuming interlayers and Stern layer being inaccessible for anions, this model describes just anion diffusion in free and DL pore water. Effective cation diffusion coefficients (Table 5) determined from experimental data by the SD model (or, equally, derived from a simple Fickian model) can be compared to the combined diffusion coefficients of the DL-SL-IL model (Eq. (5)).

In order to be able to calculate the combined diffusion coefficient of the DL-SL-IL model, several additional parameters are needed as explained in the following. The overall derivative of the sorption isotherm $\partial S_{tot}/\partial C$ from the 1-site cation exchange model for the planar sorption sites in Opalinus Clay has to be split into the contributions of sorption in the diffuse layer, the Stern layer and the interlayers.

The distribution factor ξ, which accounts for cation adsorption in the diffuse layer, and the fraction of cations adsorbed in the Stern layer $(\partial S_{SL}/\partial C)/(\partial S_{tot}/\partial C)$ are determined from Donnan/Stern layer equilibrium calculations. These calculations include a cation exchange site which represents the Stern layer. The selectivities of this cation exchange site are adapted so that the overall adsorption in DL and SL equals the distribution of cations given by the one-site cation exchange model.

The contributions of interlayer pore environments $\partial S_{IL,i}/\partial C$ are calculated by multiplying the fraction of CEC compensated in each interlayer environment with the overall derivative of the sorption isotherm.

In order to determine the different contributions described above, knowledge about the pore structure (i.e., the relevant porosities) and the charge distribution between different pore environments in Opalinus Clay is required.

4.1 Opalinus Clay pore structure model

4.1.1 Porosity distribution

The basis of the DL-SL-IL model is experimental anion exclusion data from Wigger and Van Loon (2018) and some of the modeling assumption therein. From their anion data the pore structure, the charge distribution between different pore environments and DL properties are determined. While this obviously precludes a validation of the DL-SL-IL model with respect to anion diffusion, it allows then, in the next step, to check its applicability on the cation diffusion data, provided the additionally required cation mobilities can be estimated reasonably.

Similar to Wigger and Van Loon (2018), the total porosity in Opalinus Clay is written as:

$$\varepsilon_{tot} = \varepsilon_{free} + \varepsilon_{DL} + \varepsilon_{bottle} + \varepsilon_{IL} \tag{9}$$

where ε_{free} is the bulk 'free' porosity unaffected by the negative surface charge, ε_{DL} is the porosity of the diffuse layer, ε_{IL} is the interlayer porosity of the illite/smectite mixed layers and ε_{bottle} is the so-called bottleneck porosity. This porosity was introduced to explain the large fraction of the total porosity being inaccessible to Cl even at high ionic strengths, which seems to be larger than just the interlayer porosity. However, the nature of these bottleneck pores is rather unclear. Nevertheless, the experimental data show about 25-40% of the total porosity being inaccessible (ε_{inacc}) to anions even at high ionic strength (> 1 M). Alternatively, this porosity (or at least a part of it) may be attributed to the Stern layer, which is assumed to be mostly devoid of anions. The bulk (free) porosity can be estimated from experimental data at lowest ionic strength to 20-30% of the total porosity. The interlayer porosity of the illite/smectite mixed layers was approximated by:

$$\varepsilon_{IL} = \frac{A_{IL} t_{IL}}{2} w_{smectite} \rho_{bd} \tag{10}$$

where A_{IL} is the internal smectite surface area, t_{IL} is the width of the interlayer and $w_{smectite}$ is the mass fraction of smectite in Opalinus Clay. $w_{smectite}$ can be calculated from the illite/smectite mixed layer content in Opalinus Clay with a smectite content of 15-30% (Wersin et al., 2013) (here we assume about 20%). The total specific surface area of the smectite fraction is assumed to be about 770 $m^2\ g^{-1}$. With an assumed smectite stack size of two the internal smectite surface area is about 380 $m^2\ g^{-1}$. The bottleneck porosity can be written as:

$$\varepsilon_{bottle} = \varepsilon_{inacc} - \varepsilon_{IL} \,. \tag{11}$$

4.1.2 Charge distribution

The charge distribution between diffuse and Stern layer can be expressed by a surface complexation reaction (Wersin et al., 2008; Appelo et al., 2010; Tinnacher et al., 2016):

$$Su^- + Na^+ \Leftrightarrow SuNa \tag{12}$$

with $\log K_{SuNa}$ being the surface complexation constant. A value of 0.7 was used by Appelo et al. (2010) to describe anion and cation diffusion in Opalinus Clay, while from MD simulation results of Tinnacher et al. (2016) in Na-montmorillonite, a value of about 0.9 can be extracted. However, both values are based on montmorillonite data, and application of the values to illite-based clay systems

such as Opalinus Clay may not be valid. Nevertheless, here these values are used, because no data specific to illite is available.

The fraction of charge compensated in the DL (Table 6) can be calculated according to Eq (12) as:

$$f_{DL} = \frac{1}{1 + K_{SuNa}[Na]^{+}} \tag{13}$$

Table 6: Fraction of total surface charge compensated in the DL for Mont Terri and Benken Opalinus Clay for different values of $\log K_{SuNa}$.

$\log K_{SuNa}$	MT	BE
0.9	34%	45%
0.7	46%	57%

The total cation exchange capacity can be distributed over the different pore environments (diffuse layer, Stern layer, bottleneck and interlayer pores) according to their porosity fractions:

$$CEC_{tot} = CEC_{DL} + CEC_{SL} + CEC_{bottle} + CEC_{IL} \tag{14}$$

where

$$CEC_{IL} = \frac{A_{IL}}{A_{tot}} w_{smectite} CEC_{smectite} , \tag{15}$$

$$CEC_{bottle} = \frac{\varepsilon_{bottle}}{\varepsilon_{tot} - \varepsilon_{IL} - \varepsilon_{free}} \left(CEC_{tot} - CEC_{IL}\right) , \tag{16}$$

$$CEC_{DL} = f_{DL}\left(CEC_{tot} - CEC_{IL} - CEC_{bottle}\right) , \tag{17}$$

$$CEC_{SL} = \left(1 - f_{DL}\right)\left(CEC_{tot} - CEC_{IL} - CEC_{bottle}\right) . \tag{18}$$

The smectite cation exchange capacity is about 0.85 eq kg^{-1} (Baeyens and Bradbury, 1997) for Na-montmorillonite. The CEC compensated in the interlayer is calculated from the former value multiplied with the smectite content in Opalinus Clay and the fraction of internal surface area (Eq. (15)). Having CEC_{IL} determined, the charge compensated in the bottleneck pores, the diffuse layer and the Stern layer can be calculated consecutively (Eqs. (16)-(18)).

4.1.3 Variations of the pore structure model

As neither the charge distribution between diffuse and Stern layer in Opalinus Clay nor the interlayer width of the illite/smectite mixed layers as well as the nature of the bottleneck pores are exactly known, different cases were studied. First of all, it was assumed that the bottleneck pores have the same properties as the interlayer pores with regards to diffusion behavior. This means that anions are excluded from the bottleneck pores and the mobility of cations and water tracers in the bottleneck pores is the same as in the interlayer.

Two base cases (case A and B) with different charge distribution between diffuse layer and Stern layer using a $\log K_{SuNa}$ of 0.9 and 0.7, respectively, were studied.

For both base cases the interlayer width was varied between one hydrated water layer WL (case A1 and B1) and two hydrated water layers (case A2 and B2). The interlayer porosity was then calculated using interlayer distances of 0.32nm (1 WL) and 0.64nm (2 WL), respectively.

In the cases A1, B1, A2 and B2, it was assumed that the activity coefficient in the diffuse layer equals the one in 'free' pore water $\gamma_{DL} = \gamma_{bulk}$. However, the assumption of equal activity coefficients in bulk

and DL is arbitrary (Birgersson, 2017; Tournassat and Steefel, 2019). At the clay surface, the elecotrolyte solution is far from being neutral because of the negative electrostatic potential. Therefore, Rytwo (2004) drew the conclusion that the charge screening effect, on which the Debye-Hückel theory is based, is minimized, which then leads to activity coefficients closer to unity in the diffuse layer. Therefore, the cases A2 and B2 were additionally recalculated using $\gamma_{DL}=1$ (these cases are named A3 and B3).

4.1.4 Constraints by experimental anion exclusion data

The pore structure models for the cases A1, B1, A2 and B2 (but not A3 and B3) (Tables 7 and 8) were constrained in a manner that anion accessible porosities derived from the Fickian diffusion model (Table 4) were matched by the mass balance equation:

$$\varepsilon_a=\varepsilon_{free}+\varepsilon_{DL}\xi^{Cl} \tag{19}$$

where ξ^{Cl} is a function of CEC_{DL} and ε_{DL}, see Eqs. (6), (7) and (8). ε_{DL} is given by the pore structure model (Eq. (9)). In order to achieve the same anion accessible porosities as with the simple Fickian model used in the previous section (Table 4), the free porosity ε_{free} and the porosity inaccessible to anions ε_{inacc} were varied within their uncertainty given by the experimental data of Wigger and Van Loon (2018). For the cases A3 and B3 the same pore structure model as for A2 and B2 was used. For the pore structure model of Benken Opalinus Clay ε_{free} was allowed to be smaller than the value derived from the experimental data of Wigger and Van Loon (2018) because of the lesser kaolinite and chlorite content in Benken Opalinus Clay compared to the Opalinus Clay from the Schlattingen deep borehole (similar composition to Mont Terri Opalinus Clay) used in their experiments. Kaolinite and chlorite have significantly lower CEC than illite, and diffusion of ions through their pores is less influenced by electrostatics originating from the negatively charged surfaces. The resulting values of porosity and distribution of the cation exchange capacity are summarized in Tables 7 and 8. Table 9 shows the distribution coefficients in the diffuse layer, calculated for each case based on the pore structure models. The distribution factors for the cases A3 and B3 where $\gamma_{DL}=1$ was used, were significantly lower for Cl (about a factor of 2), and therefore the anion accessible porosity calculated was lower (Table 10).

Table 7: Determined porosities for free (bulk), diffuse layer, bottleneck and interlayer pore environments for the different pore structure models.

		ε_{tot}	ε_{free}	ε_{DL}	ε_{bottle}	ε_{IL}
MT	A1	0.171	0.0496	0.0718	0.046	0.0036
	A2	0.171	0.0513	0.07	0.0424	0.0072
	B1	0.171	0.0513	0.0804	0.0357	0.0036
	B2	0.171	0.0513	0.0821	0.0304	0.0072
BE	A1	0.15	0.0256	0.069	0.052	0.0036
	A2	0.15	0.0256	0.0705	0.047	0.0072
	B1	0.15	0.0256	0.0795	0.0414	0.0036
	B2	0.15	0.0256	0.081	0.0322	0.0072

Table 8: Determined charge distribution in $mol_C\ kg^{-1}$ Opalinus Clay in the different pore environments for the different pore structure models.

		CEC_{tot}	CEC_{free}	$CEC_{DL/SL}$	CEC_{bottle}	CEC_{IL}
MT	A1	0.117	-	0.065	0.041	0.011
	A2	0.117	-	0.066	0.04	0.011
	B1	0.117	-	0.073	0.033	0.011
	B2	0.117	-	0.077	0.029	0.011
BE	A1	0.115	-	0.059	0.045	0.011
	A2	0.115	-	0.063	0.041	0.011
	B1	0.115	-	0.068	0.036	0.011
	B2	0.115	-	0.072	0.032	0.011

Table 9: Distribution factors for Cl, Na, Sr and Cs determined for the different studied cases.

	MT						BE					
	A1	A2	A3	B1	B2	B3	A1	A2	A3	B1	B2	B3
ξ_{Cl}	0.48	0.47	0.23	0.41	0.4	0.19	0.25	0.24	0.12	0.21	0.21	0.1
ξ_{Na}	2.09	2.15	2.35	2.46	2.51	2.85	4.37	4.61	2.99	6.05	6.31	4.4
ξ_{Sr}	4.06	4.15	4.73	4.66	4.74	5.51	16.5	17.3	12.8	22.1	22.9	17.3
ξ_{Cs}	2.09	2.15	2.35	2.46	2.51	2.85	4.37	4.61	2.99	6.05	6.31	4.4

Table 10: Calculated Cl accessible porosities based on the different pore structure models (note: cases A1, A2, B1, B2 are constrained by experimental data).

	MT						BE					
	A1	A2	A3	B1	B2	B3	A1	A2	A3	B1	B2	B3
ϵ_{Cl}	0.084	0.084	0.067	0.084	0.084	0.067	0.043	0.043	0.034	0.043	0.043	0.034

4.1.5 Site-specific mobilities for cations and water tracers

Based on the pore structure models and the cation distribution in the diffuse layer the DL-SL-IL model is applied to cations. The mobility of the cations in the illite Stern layer as well as the behavior in the bottleneck pores, however, is not known. As the bottleneck pores exclude anions, one may assume that the clay surfaces at the entrance of these pores are very close in the range of interlayer widths. Therefore, water and cations in these pores are assumed to have the same diffusion behavior as in interlayer pores. So, the assumption is made that the water and cation mobility of the smectite interlayer applies equally for the bottleneck pores. Moreover, while for montmorillonite, mobility data for Stern layer and interlayer obtained in MD simulations (Bourg and Sposito, 2010; Bourg and Sposito, 2011; Holmboe and Bourg, 2014; Tinnacher et al., 2016) is available, no such data is available for illite. Instead, values (brackets in Table 11) for interlayer and Stern layer for water and cations determined for Volclay bentonite (chapter 3) are used, except for the Stern layer mobility of Sr and Cs, which were used as fitting parameters.

Table 11: Mobilities of HTO, Na, Sr and Cs in 1 and 2 WL montmorillonite interlayer and montmorillonite Stern layer. In brackets: values determined for Volclay bentonite (chapter 3).

mobility	1 WL	2 WL	Stern layer
μ_{HTO}	0.08 (0.08)	0.35 (0.35)	-
μ_{Na}	0.05 (0.05)	0.3 (0.3)	0.5 (0.5)
μ_{Sr}	0 (0)	0.1 (0.1)	0.05 (~0.3)
μ_{Cs}	0.005 (0.004)	0.01 (0.01)	0.045 (~0.05)

4.1.6 Geometrical factor

In the DL-SL-IL model a lower mobility is attributed to water in the illite/smectite interlayer and in the bottleneck pores of Opalinus Clay (Table 11) than in 'free' bulk pore water. Accordingly, the geometrical factor G_{HTO} derived previously from HTO diffusion (Fickian model, assuming equal mobility of HTO in all pores) and used in the SD model cannot be directly applied to the DL-SL-IL model in Eq. (5). Instead, the DL-SL-IL model uses a corrected geometrical factor $G_{DL,IL,SL}$, which is written as:

$$G_{DL,SL,IL} = \left(\mu_{IL} f_{IL} + \mu_{bottle} f_{bottle} + \left(1 - f_{IL} - f_{bottle}\right)\mu_{ext}\right) G_{HTO} \quad (20)$$

where μ are the mobilities of water in the different pore environments, f are the respective porosity fractions, and G_{HTO} is the geometrical factor derived for HTO in section 3 (Table 4). The mobility of water in the external (anion accessible) pore space is assumed to be equal to that of bulk water ($\mu_{ext} = 1$, as for cations).

4.2 Comparison of experimental data with predictions based on the DL-SL-IL model

4.2.1 Predicted effective diffusion coefficients

The comparison between effective diffusion coefficients of Na, Sr and Cs fitted from the diffusion experiments (Eq. (3), Table 5, black symbols in figures 8-10), and the ones predicted by the DL-SL-IL model via Eq. (5) shows good to fair agreement for all cases (Figures 8, 9 and 10). Predicted $D_{DL,IL,SL}$ for Na perpendicular to the bedding for MT Opalinus Clay are found to be up to 50% higher than diffusion coefficients derived from experimental data, while for Benken Opalinus Clay perpendicular to the bedding a good agreement is observed (Figure 8). $D_{DL,IL,SL}$ for Sr in Benken Opalinus Clay perpendicular to the bedding are about a factor of two higher when compared to other experimental data from the literature (Figure 9).

When comparing the results of the different cases studied, the cases B with the lower $\log K_{SuNa} = 0.7$ tend to lead to higher effective diffusion coefficients for Na, Sr and Cs. This can be explained by the fact that in the cases B more charge is compensated in the diffuse layer (Table 6), which leads to increased diffuse layer concentrations and decreased Stern layer concentrations of Na, Sr and Cs. As the mobility in the diffuse layer (here assumed to be the same as in 'free' pore water) is higher than in the Stern layer, the values of the predicted diffusion coefficients increase. This tendency is more pronounced for Sr, because of higher enrichment of bivalent Sr compared to monovalent Na and Cs in the diffuse layer (see Eq. (6)). Overall, the differences between the different cases investigated are rather small for Na

and Cs (within 10-20%), while for the bivalent Sr the differences are more significant. Because of the partly small differences, no definite statement can be made about which one of the different cases studied generates most accurate results.

4.2.2 Relative contributions of different diffusion pathways

The combined DL-SL-IL model also allows to compare relative contributions of the different pore environments to the effective diffusion coefficient of the cations. These comparisons are shown in Tables 12, 13 and 14 for the investigated cases. Diffusion in the diffuse layer plays the most important role for Na and Sr in all cases, while for Cs Stern layer diffusion is most important (60-70%). The contribution to diffusion of the interlayers in I/S mixed layer minerals is very small for all cations (<6%). Diffusion in the bottleneck pores is important for Na and Sr (10-23%) when assuming the same diffusion properties as a 2 WL montmorillonite interlayer. Diffusion in 'free' pore water is important for Na (12-16%) and Sr (7-11%) in MT Opalinus Clay, but not for Cs and not in Benken Opalinus Clay. Cs is mostly insensitive to changes of the charge distribution between diffuse and Stern layer.

4.2.3 Influence of activity coefficients

When assuming $\gamma_{DL}=1$, Na and Cs diffusion in the DL becomes slightly more important, while diffusion of Sr in the diffuse layer is reduced. While diffuse layer concentrations of Na and Cs increase, the concentrations of Sr and of Cl decrease compared to the cases where $\gamma_{DL}=\gamma_{free}$ (Table 9). Considering a Boltzmann distribution and the exponential decay of the surface potential, cation concentrations in the DL are highest closer to the surface, where the potential (and thus its influence on the electrolyte solution) is highest, while further away from the surface, where anion concentrations are increased, the influence of the potential is lower. Therefore, the influence of the potential on the activity coefficient is more pronounced for cations than for anions following the argumentation of Rytwo (2004). Accordingly, it may be appropriate to assume that for cations the assumption of $\gamma_{DL}=1$ is a better choice, while $\gamma_{DL}=\gamma_{bulk}$ may be more accurate for anions.

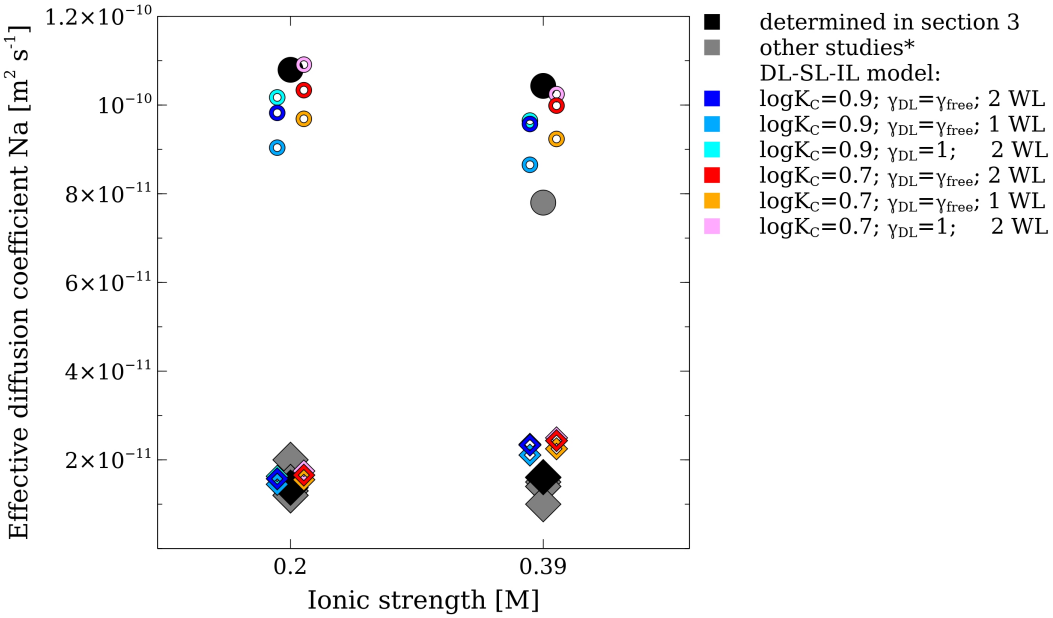

Figure 8: Comparison of effective diffusion coefficients of Na derived from experimental data (black (Table 5) and grey (from other studies)) and predicted by the DL-SL-IL model (medium blue: case A1; dark blue: case A2; light blue: case A3; orange: case B1; red: case B2; pink: case B3) for Opalinus Clay from Benken (0.2 M) and Mont Terri (0.39 M). The circles denote diffusion coefficients parallel to the Opalinus Clay bedding, the diamonds diffusion coefficients perpendicular to the bedding.

* Additional data of Na diffusion coefficients were taken from Gimmi and Kosakowski (2011) and references therein.

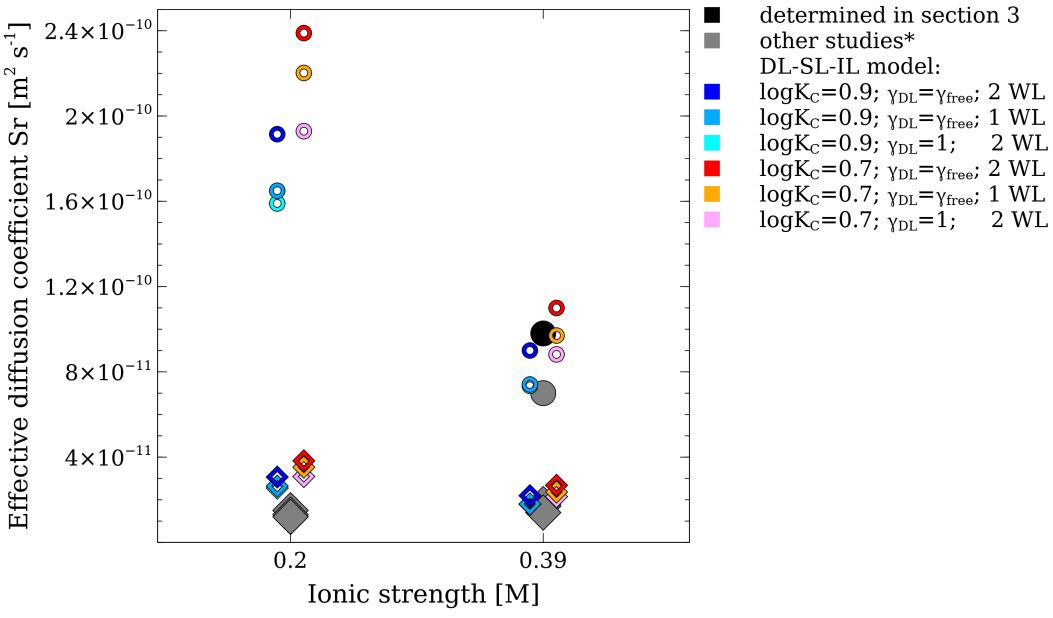

Figure 9: Comparison of effective diffusion coefficients of Sr derived from experimental data (black (Table 5) and grey (from other studies)) and predicted by the DL-SL-IL model (medium blue: case A1; dark blue: case A2; light blue: case A3; orange: case B1; red: case B2; pink: case B3) for Opalinus Clay from Benken (0.2 M) and Mont Terri (0.39 M). The circles denote diffusion coefficients parallel to the Opalinus Clay bedding, the diamonds diffusion coefficients perpendicular to the bedding.

* Additional data of Sr diffusion coefficients were taken from Gimmi and Kosakowski (2011) and references therein.

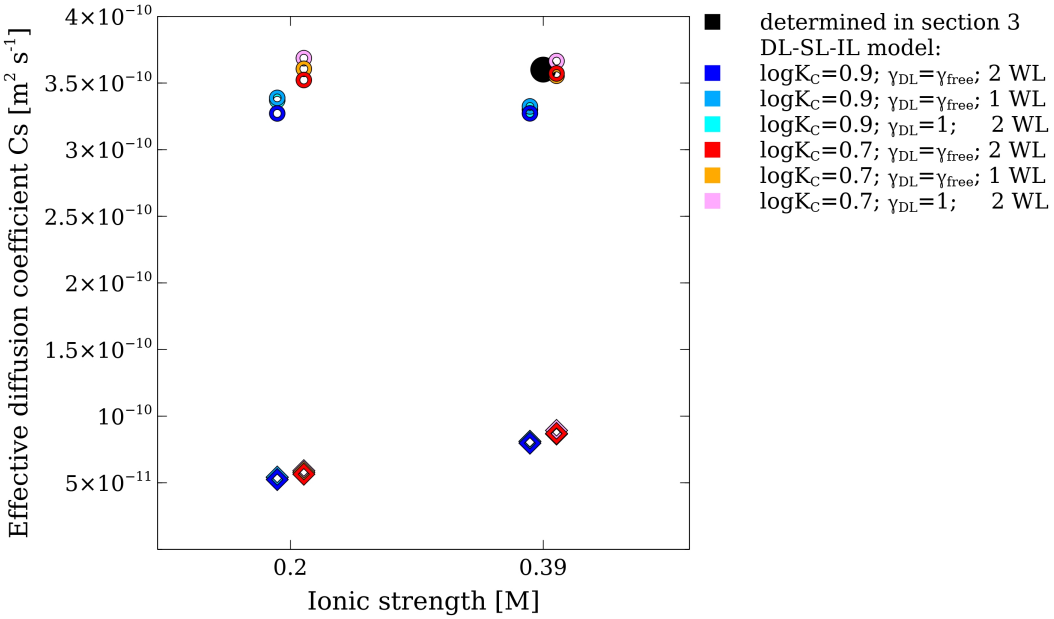

Figure 10: Comparison of effective diffusion coefficients of Cs derived from experimental data (black (Table 5)) and predicted by the DL-SL-IL model (medium blue: case A1; dark blue: case A2; light blue: case A3; orange: case B1; red: case B2; pink: case B3) for Opalinus Clay from Benken (0.2 M) and Mont Terri (0.39 M). The circles denote diffusion coefficients parallel to the Opalinus Clay bedding, the diamonds diffusion coefficients perpendicular to the bedding.

Table 12: Predicted effective diffusion coefficient of the DL-SL-IL model (Eq. (5)) and relative contributions of diffusion in 'free' pore water, the diffuse layer, the Stern layer, bottleneck pores and I/S mixed layers for Na (in %).

Na	case	$D_{DL\text{-}SL\text{-}IL,Na}$ [m^2 s^{-1}]		free	DL	SL	bottleneck	I/S mixed layers
MT		parallel	perpendicular					
	A1	$8.7 \cdot 10^{-11}$	$2.1 \cdot 10^{-11}$	16	49	30	3	1
	A2	$9.6 \cdot 10^{-11}$	$2.3 \cdot 10^{-11}$	14	40	26	16	4
	A3	$9.6 \cdot 10^{-11}$	$2.4 \cdot 10^{-11}$	14	44	23	16	4
	B1	$9.2 \cdot 10^{-11}$	$2.2 \cdot 10^{-11}$	15	56	26	2	1
	B2	$1.0 \cdot 10^{-10}$	$2.4 \cdot 10^{-11}$	12	50	23	10	4
	B3	$1.0 \cdot 10^{-10}$	$2.5 \cdot 10^{-11}$	12	55	19	10	4
BE		parallel	perpendicular					
	A1	$9.0 \cdot 10^{-11}$	$1.4 \cdot 10^{-11}$	6	64	25	4	1
	A2	$9.8 \cdot 10^{-11}$	$1.6 \cdot 10^{-11}$	5	53	20	17	5
	A3	$1.0 \cdot 10^{-10}$	$1.6 \cdot 10^{-11}$	4	59	16	17	4
	B1	$9.7 \cdot 10^{-11}$	$1.6 \cdot 10^{-11}$	5	72	19	3	1
	B2	$1.0 \cdot 10^{-10}$	$1.7 \cdot 10^{-11}$	4	63	17	12	4
	B3	$1.1 \cdot 10^{-10}$	$1.7 \cdot 10^{-11}$	4	69	12	11	4

Table 13: Predicted effective diffusion coefficient of the DL-SL-IL model (Eq. (5)) and relative contributions of diffusion in 'free' pore water, the diffuse layer, the Stern layer, bottleneck pores and I/S mixed layers for Sr (in %).

Sr	case	$D_{DL\text{-}SL\text{-}IL,Sr}$ [m^2 s^{-1}]		free	DL	SL	bottleneck	I/S mixed layers
MT		parallel	perpendicular					
	A1	$7.4 \cdot 10^{-11}$	$1.8 \cdot 10^{-11}$	11	72	17	0	0
	A2	$9.0 \cdot 10^{-11}$	$2.2 \cdot 10^{-11}$	9	55	13	18	5
	A3	$7.3 \cdot 10^{-11}$	$1.8 \cdot 10^{-11}$	11	44	17	23	6
	B1	$9.7 \cdot 10^{-11}$	$2.4 \cdot 10^{-11}$	8	79	13	0	0
	B2	$1.1 \cdot 10^{-10}$	$2.7 \cdot 10^{-11}$	7	68	11	10	4
	B3	$8.8 \cdot 10^{-11}$	$2.1 \cdot 10^{-11}$	8	59	15	13	5
BE		parallel	perpendicular					
	A1	$1.6 \cdot 10^{-10}$	$2.6 \cdot 10^{-11}$	2	86	12	0	0
	A2	$1.9 \cdot 10^{-10}$	$3.1 \cdot 10^{-11}$	1	68	9	17	4
	A3	$1.6 \cdot 10^{-10}$	$2.5 \cdot 10^{-11}$	2	60	12	20	5
	B1	$2.2 \cdot 10^{-10}$	$3.5 \cdot 10^{-11}$	1	90	9	0	0
	B2	$2.4 \cdot 10^{-10}$	$3.8 \cdot 10^{-11}$	1	78	7	10	3
	B3	$1.9 \cdot 10^{-10}$	$3.1 \cdot 10^{-11}$	1	72	10	12	4

Table 14: Predicted effective diffusion coefficient of the DL-SL-IL model (Eq. (5)) and relative contributions of diffusion in 'free' pore water, the diffuse layer, the Stern layer, bottleneck pores and I/S mixed layers for Cs (in %).

Cs	case	$D_{DL\text{-}SL\text{-}IL,Cs}$ [m^2 s^{-1}]		free	DL	SL	bottleneck	I/S mixed layers
MT		parallel	perpendicular					
	A1	$3.3 \cdot 10^{-10}$	$8.1 \cdot 10^{-11}$	6	20	68	5	1
	A2	$3.3 \cdot 10^{-10}$	$8.0 \cdot 10^{-11}$	6	18	64	9	2
	A3	$3.3 \cdot 10^{-10}$	$8.1 \cdot 10^{-11}$	6	20	63	9	2
	B1	$3.6 \cdot 10^{-10}$	$8.7 \cdot 10^{-11}$	6	22	67	3	1
	B2	$3.6 \cdot 10^{-10}$	$8.7 \cdot 10^{-11}$	5	22	65	5	2
	B3	$3.7 \cdot 10^{-10}$	$8.9 \cdot 10^{-11}$	5	24	63	5	2
BE		parallel	perpendicular					
	A1	$3.4 \cdot 10^{-10}$	$5.4 \cdot 10^{-11}$	2	26	65	5	1
	A2	$3.3 \cdot 10^{-10}$	$5.2 \cdot 10^{-11}$	2	25	61	9	2
	A3	$3.4 \cdot 10^{-10}$	$5.4 \cdot 10^{-11}$	2	27	59	9	2
	B1	$3.6 \cdot 10^{-10}$	$5.8 \cdot 10^{-11}$	2	30	63	4	1
	B2	$3.5 \cdot 10^{-10}$	$5.6 \cdot 10^{-11}$	2	28	61	6	2
	B3	$3.7 \cdot 10^{-10}$	$5.9 \cdot 10^{-11}$	2	32	59	6	2

5 Summary and conclusions

Simulations of diffusion experiments with HTO, Na, Sr and Cl in Opalinus Clay samples from the Mont Terri Rock laboratory and from the borehole Benken, both parallel and perpendicular to the bedding, were carried out. Accessible porosities and geometrical factors for HTO and Cl were determined with a classical Fickian diffusion model, while surface mobilities were determined from simulations of Na and Sr with a simple 1-site surface diffusion model. The simulations were in good agreement with the experimental data. Identical accessible porosities parallel and perpendicular to the bedding were found for both HTO and Cl. The geometrical factors perpendicular to the bedding were larger, displaying the anisotropy. Surface mobilities found for Na were higher for BE Opalinus Clay than for MT Opalinus Clay. Also, the mobilities showed an anisotropy, with mobilities for the perpendicular cases being lower. This may be explained with less well-connected surfaces in the perpendicular diffusion direction.

Even though the simulations with these simple models led to good matches with the data, the derived parameters were sample specific, meaning that the models have limited predictive capability with regard to, for instance, variations of the porosity, the ionic strength of the pore solution, or the diffusion direction. In order to get more insight into relevant processes and be able to better interpret the experimentally determined values, the more sophisticated DL-SL-IL model (chapter 3) was applied to the experimental data.

Using anion exclusion data and modeling results of Wigger et al. (2018) in Opalinus Clay, a model for pore structure and charge distribution in Opalinus Clay was derived. The DL-SL-IL model was then applied to diffusion of Na, Sr and Cs. For cations, the model needs additional parameters, including cation mobilities for Stern and interlayer pores. For lack of such data for Opalinus Clay, corresponding values determined for Volclay bentonite (chapter 3) were used. As these model parameters do not necessarily apply to Opalinus Clay, different cases were investigated including a variation of the charge distribution between DL and SL, different activity coefficients in the DL and different pore widths (and therefore different mobilities) of smectite interlayer and bottleneck pores.

Cation diffusion coefficients derived from experimental data were finally compared with calculated effective diffusion coefficients of the DL-SL-IL model. When adapting mobilities of Sr and Cs in the Stern layer compared to values determined in bentonite, good to fair agreement between the diffusion coefficients derived from experimental data and the predictions of the DL-SL-IL model was found. However, a clear statement with regard to the accuracy of the DL-SL-IL model, or with regard to correct values for required parameters, can hardly be made, as the model has too many undetermined parameters and a series of assumptions had to be made. Therefore, the results presented here have to be treated with caution, and further investigations are necessary. Nevertheless, the sensitivity simulations performed for different cases show a comparably small variation, which encourages the further application of such models. Two important aspects that would make the application of the DL-SL-IL model to cation diffusion data in Opalinus Clay more reliable are (1) the determination of diffusion coefficients of cations in the Stern layer of illite clay minerals, and (2) better estimates of the charge distribution between DL and SL in illite clay minerals. This may be done by MD simulations, in a similar manner as it has been done already for montmorillonite (e.g., Bourg and Sposito (2011) or Tinnacher et al. (2016)).

Acknowledgments

Financial support by the Swiss National Science Foundation (grant no. 200021_166287) is kindly acknowledged. The co-authors also acknowledge financial support by Nagra, the Swiss Cooperative for the Disposal of Radioactive Waste.

Appendix

Table A1: Mineralogical composition (range according to (Lauber et al., 2000) and (Bradbury and Baeyens, 1998)) and pore water composition of Mont Terri Opalinus Clay.

Mineralogical composition		Pore water composition	
Minerals	wt.%	Element	Concentration
Calcite	8-11	Na (M)	$2.4 \cdot 10^{-1}$
Dolomite/ankerite	1.5-2.5	K (M)	$1.61 \cdot 10^{-3}$
Siderite	3-5	Ca (M)	$2.58 \cdot 10^{-2}$
Quartz	10-14	Mg (M)	$1.69 \cdot 10^{-2}$
Albite	0.5-2	Cl (M)	$3 \cdot 10^{-1}$
K-feldspar	1.5-3	SO_4 (M)	$1.41 \cdot 10^{-2}$
Pyrite	1.7	Alkalinity (M)	$4.76 \cdot 10^{-4}$
Phyllosilicates		pH	7.6
Illite	16-26	I	0.39
Illite/smectite mixed layers	6-22		
Kaolinite	17-32		
Clorite	5-12		

Table A2: Mineralogical composition and pore water composition of Benken Opalinus Clay.

Mineralogical composition		Pore water composition	
Minerals	wt.%	Element	Concentration
Calcite	16 ± 10	Na (M)	$1.50 \cdot 10^{-1}$
Dolomite/ankerite	1.0 ± 0.4	K (M)	$4.3 \cdot 10^{-3}$
Siderite	4 ± 2.4	Ca (M)	$7.2 \cdot 10^{-3}$
Quartz	20 ± 5	Mg (M)	$5.2 \cdot 10^{-3}$
Albite	1 ± 0.3	Cl (M)	$1. \cdot 10^{-1}$
K-feldspar	1.5-3	SO_4 (M)	$1.0 \cdot 10^{-2}$
Pyrite	2 ± 1	Alkalinity (M)	$3.1 \cdot 10^{-4}$
Phyllosilicates		pH	7.6
Illite	18 ± 6	I	0.2
Illite/smectite mixed layers	14 ± 4		
Kaolinite	17 ± 6		
Clorite	5 ± 2		

References

Appelo C. A. J., Van Loon L. R. and Wersin P. (2010). Multicomponent diffusion of a suite of tracers (HTO, Cl, Br, I, Na, Sr, Cs) in a single sample of Opalinus Clay. *Geochim. Cosmochim. Acta* **74**, 1201–1219.

Baeyens B. and Bradbury M. H. (1997). A mechanistic description of Ni and Zn sorption on Part I: Titration and sorption measurements. **27**, 199–222.

Birgersson M. (2017). A general framework for ion equilibrium calculations in compacted bentonite. *Geochim. Cosmochim. Acta* **200**, 186–200. http://dx.doi.org/10.1016/j.gca.2016.11.010.

Bourg I. C. and Sposito G. (2010). Connecting the molecular scale to the continuum scale for diffusion processes in smectite-rich porous media. *Environ. Sci. Technol.* **44**, 2085–2091.

Bourg I. C. and Sposito G. (2011). Molecular dynamics simulations of the electrical double layer on smectite surfaces contacting concentrated mixed electrolyte (NaCl-CaCl2) solutions. *J. Colloid Interface Sci.* **360**, 701–715. http://dx.doi.org/10.1016/j.jcis.2011.04.063.

Bradbury M. H. and Baeyens B. (2000). A generalised sorption model for the concentration dependent uptake of caesium by argillaceous rocks. *J. Contam. Hydrol.* **42**, 141–163.

Bradbury M. H. and Baeyens B. (1998). A physicochemical characterisation and geochemical modelling approach for determining porewater chemistries in argillaceous rocks. *Geochim. Cosmochim. Acta* **62**, 783–795.

Davis J. A., James R. O. and Leckie J. O. (1978). Surface Ionization and Complexation at the Oxide/Water Interface. *J. Colloid Interface Sci.* **63**, 480–499.

Descostes M., Blin V., Bazer-Bachi F., Meier P., Grenut B., Radwan J., Schlegel M. L., Buschaert S., Coelho D. and Tevissen E. (2008). Diffusion of anionic species in Callovo-Oxfordian argillites and Oxfordian limestones (Meuse/Haute-Marne, France). *Appl. Geochemistry* **23**, 655–677.

Elprince A. M., Vanselow A. P. and Sposito G. (1980). Heterovalent, Ternary Cation Exchange Equilibria: NH_4^+ -Ba^{2+} -La^{3+} Exchange on Montmorillonite. *Soil Sci. Soc. Am. J.* **44**, 964–969.

Flury M. and Gimmi T. (2018). 6.2 Solute Diffusion. In *Methods of Soil Analysis* (eds. J. H. Dane and G. C. Topp). pp. 1323–1351.

Gimmi T. and Kosakowski G. (2011). How mobile are sorbed cations in clays and clay rocks? *Environ. Sci. Technol.* **45**, 1443–1449.

Gimmi T., Leupin O. X., Eikenberg J., Glaus M. A., Van Loon L. R., Waber H. N., Wersin P., Wang H. A. O., Grolimund D., Borca C. N., Dewonck S. and Wittebroodt C. (2014). Anisotropic diffusion at the field scale in a 4-year multi-tracer diffusion and retention experiment - I: Insights from the experimental data. *Geochim. Cosmochim. Acta* **125**, 373–393. http://dx.doi.org/10.1016/j.gca.2013.10.014.

Gimmi T., Waber H. N., Gautschi A. and Rübel A. (2007). Stable water isotopes in pore water of Jurassic argillaceous rocks as tracers for solute transport over large spatial and temporal scales. *Water Resour. Res.* **43**, 1–16.

Glaus M. A., Rossé R., van Loon L. R. and Yaroshchuk A. E. (2008). Tracer diffusion in sintered stainless steel filters: Measurement of effective diffusion coefficients and implications for diffusion studies with compacted clays. *Clays Clay Miner.* **56**, 677–685.

Holmboe M. and Bourg I. C. (2014). Molecular dynamics simulations of water and sodium diffusion in smectite interlayer nanopores as a function of pore size and temperature. *J. Phys. Chem. C* **118**, 1001–1013.

Jakob A., Pfingsten W. and Van Loon L. (2009). Effects of sorption competition on caesium diffusion through compacted argillaceous rock. *Geochim. Cosmochim. Acta* **73**, 2441–2456.

Krejci P., Gimmi T. and Van Loon L. R. (2021). On the concentration-dependent diffusion of sorbed cesium in Opalinus Clay. *Geochim. Cosmochim. Acta* **298**, 149–166. https://doi.org/10.1016/j.gca.2021.01.012.

Lammers L. N., Bourg I. C., Okumura M., Kolluri K., Sposito G. and Machida M. (2017). Molecular dynamics simulations of cesium adsorption on illite nanoparticles. *J. Colloid Interface Sci.* **490**, 608–620. http://dx.doi.org/10.1016/j.jcis.2016.11.084.

Lauber M., Baeyens B. and Bradbury M. H. (2000). Physico-Chemical Characterisation and Sorption Measurements of Cs, Sr, Ni, Eu, Th, Sn and Se on Opalinus Clay from Mont Terri. *PSI Bericht No. 00-10, Paul Scherrer Institut, Villigen, NAGRA NTB 00-11, Nagra, Wettingen, Switz.*

Leroy P., Revil A., Altmann S. and Tournassat C. (2007). Modeling the composition of the pore water in a clay-rock geological formation (Callovo-Oxfordian, France). *Geochim. Cosmochim. Acta* **71**, 1087–1097.

Lewis D. R. (1949). Ion Exchange Reactions of Clays. *Prop. clays*, 54–69.

Lichtner P. C. (2007). *Flotran User's Manual: Two-Phase Nonisothermal Coupled Thermal-Hydrological-Chemical (THC) Reactive Flow and Transport Code, Version 2.0*., Los Alamos, New Mexico.

Van Loon L. R., Baeyens B. and Bradbury M. H. (2005). Diffusion and retention of sodium and strontium in Opalinus clay: Comparison of sorption data from diffusion and batch sorption measurements, and geochemical calculations. *Appl. Geochemistry* **20**, 2351–2363.

Van Loon L. R., Baeyens B. and Bradbury M. H. (2009). The sorption behaviour of caesium on Opalinus Clay: A comparison between intact and crushed material. *Appl. Geochemistry* **24**, 999–1004. http://dx.doi.org/10.1016/j.apgeochem.2009.03.003.

Van Loon L. R., Soler J. M. and Bradbury M. H. (2003). Diffusion of HTO, $^{36}Cl^-$ and $^{125}I^-$ in Opalinus Clay samples from Mont Terri: Effect of confining pressure. *J. Contam. Hydrol.* **61**, 73–83.

Van Loon L. R., Soler J. M., Müller W. and Bradbury M. H. (2004). Anisotropic diffusion in layered argillaceous rocks: A case study with Opalinus Clay. *Environ. Sci. Technol.* **38**, 5721–5728.

Melkior T., Yahiaoui S., Thoby D., Motellier S. and Barthès V. (2007). Diffusion coefficients of alkaline cations in Bure mudrock. *Phys. Chem. Earth* **32**, 453–462.

Missana T., Benedicto A., García-Gutiérrez M. and Alonso U. (2014). Modeling cesium retention onto Na-, K- and Ca-smectite: Effects of ionic strength, exchange and competing cations on the determination of selectivity coefficients. *Geochim. Cosmochim. Acta* **128**, 266–277.

Molera B. M. and Eriksen T. (2002). Diffusion of $^{22}Na^{+}$, $^{85}Sr^{2+}$, $^{134}Cs^{+}$ and $^{57}Co^{2+}$ in bentonite clay compacted to different densities: experiments and modeling. **760**, 753–760.

Revil A., Leroy P. and Titov K. (2005). Characterization of transport properties of argillaceous sediments: Application to the Callovo-Oxfordian argillite. *J. Geophys. Res. Solid Earth* **110**, 1–18.

Rytwo G. (2004). A worksheet model for adsorption/desorption of ions on clay surfaces. In *Interface Science and Technology* (Vol. 1, Issue C). Elsevier Ltd. https://doi.org/10.1016/S1573-4285(04)80040-1

Savoye S., Goutelard F., Beaucaire C., Charles Y., Fayette A., Herbette M., Larabi Y. and Coelho D. (2011). Effect of temperature on the containment properties of argillaceous rocks: The case study of Callovo-Oxfordian claystones. *J. Contam. Hydrol.* **125**, 102–112. http://dx.doi.org/10.1016/j.jconhyd.2011.05.004.

Shainberg I., Alperovitch N. I. and Keren R. (1987). Charge density and Na-K-Ca exchange on smectites. *Clays Clay Miner.* **35**, 68–73.

Siroux B., Wissocq A., Beaucaire C., Latrille C., Petcut C., Calvaire J., Tabarant M., Benedetti M. F. and Reiller P. E. (2018). Adsorption of strontium and caesium onto an Na-illite and Na-illite/Na-smectite mixtures: Implementation and application of a multi-site ion-exchange model. *Appl. Geochemistry* **99**, 65–74.

Soler J. M., Steefel C. I., Gimmi T., Leupin O. X. and Cloet V. (2019). Modeling the Ionic Strength Effect on Diffusion in Clay. the DR-A Experiment at Mont Terri. *ACS Earth Sp. Chem.* **3**, 442–451.

Stumm W. and Morgan J. J. (1996). *Aquatic Chemistry*. third edit., John Wiley and Sons Inc., New York.

Tachi Y. and Yotsuji K. (2014). Diffusion and sorption of Cs^{+}, Na^{+}, I^{-} and HTO in compacted sodium montmorillonite as a function of porewater salinity: Integrated sorption and diffusion model. *Geochim. Cosmochim. Acta* **132**, 75–93. http://dx.doi.org/10.1016/j.gca.2014.02.004.

Tinnacher R. M., Holmboe M., Tournassat C., Bourg I. C. and Davis J. A. (2016). Ion adsorption and diffusion in smectite: Molecular, pore, and continuum scale views. *Geochim. Cosmochim. Acta* **177**, 130–149. http://dx.doi.org/10.1016/j.gca.2015.12.010.

Tournassat C., Chapron Y., Leroy P., Bizi M. and Boulahya F. (2009). Comparison of molecular dynamics simulations with triple layer and modified Gouy-Chapman models in a 0.1 M NaCl-montmorillonite system. *J. Colloid Interface Sci.* **339**, 533–541. http://dx.doi.org/10.1016/j.jcis.2009.06.051.

Tournassat C. and Steefel C. I. (2019). Reactive Transport Modeling of Coupled Processes in Nanoporous Media. *Rev. Mineral. Geochemistry* **85**, 75–109.

Wersin P., Mazurek M., Waber H. N., Rufer D. and Haller A. De (2013). Arbeitsbericht NAB 12-54. *NAGRA Tech. Rep. NAB 12-54*, 343.

Wersin P., Soler J. M., Van Loon L., Eikenberg J., Baeyens B., Grolimund D., Gimmi T. and Dewonck S. (2008). Diffusion of HTO, Br^{-}, I^{-}, Cs^{+}, $^{85}Sr^{2+}$ and $^{60}Co^{2+}$ in a clay formation: Results and modelling from an in situ experiment in Opalinus Clay. *Appl. Geochemistry* **23**, 678–691.

Wigger C. and Van Loon L. R. (2018). Effect of the pore water composition on the diffusive anion transport in argillaceous, low permeability sedimentary rocks. *J. Contam. Hydrol.* **213**, 40–48. https://doi.org/10.1016/j.jconhyd.2018.05.001.

Wigger C. and Van Loon L. R. (2017). Importance of interlayer equivalent pores for anion diffusion in clay-rich sedimentary rocks. *Environmental Science and Technology* **51**(4). https://doi.org/10.1021/acs.est.6b03781

Chapter 5:
Mobility of Cs adsorbed on edges of an illite nanoparticle: A molecular dynamics study

(Manuscript in preparation)

Mobility of Cs adsorbed on edges of an illite nanoparticle: A molecular dynamics study

Philipp Krejci[a,b,], Konstantinos Karalis[c], Thomas Gimmi[a,b], Sergey V. Churakov[a,c]*

[a]*Laboratory for Waste Management, Nuclear Energy and Safety, Paul Scherrer Institute, CH-5232 Villigen, Switzerland*

[b]*Rock-Water Interaction, Institute of Geological Sciences, University of Bern, CH-3012 Bern, Switzerland*

[c]*Mineralogy, Institute of Geological Sciences, University of Bern, CH-3012 Bern, Switzerland*

*Corresponding author at: Paul Scherrer Institute; *E-mail address*: philipp.krejci@psi.ch (P. Krejci)

Abstract

Because of their negatively charged surfaces, clays and clay rocks have a large capability to retain positively charged contaminants. Sorption of cesium onto illite clays has been widely studied, and a particularly strong affinity of cesium to sorb onto illite edge surfaces has been found. The retention properties of illite for any cation depend on the degree of immobilization of the sorbed cation on the clay surfaces. Several studies have shown that alkali and alkaline earth cations are partly mobile and can diffuse along planar surfaces of smectites or illites. To address the question of whether cesium maintains a certain mobility in the vicinity of illite edge surfaces, molecular dynamics (MD) simulations were performed. In particular, they served to (1) identify cesium sorption sites on illite (110) edges at a pH 10, (2) to calculate the potential of mean force (PMF) for the identified sorption sites, and (3) to estimate surface diffusion of the Cs ion using a lattice jump model. Attempt frequencies and activation energies were derived from the PMFs and used to calculate the transition rates for each sorption site. A jump diffusion model combined with an effective medium approach (EMA) was used to calculate the diffusion coefficient of the edge surface. The simulation results revealed three distinct sorption sites with different sorption affinity towards Cs. The surface diffusion coefficient was calculated to be $1.4 \cdot 10^{-11}$ m^2 s^{-1}. This is about a factor of 150 lower than the self-diffusion coefficient in bulk water. Analysis of the uncertainties of the model parameters reveals that the activation energies and effective masses of the Cs aqua complexes are the most sensitive parameters controlling the numerically predicted diffusion coefficients.

1 Introduction

Cesium adsorption onto illite has been addressed by a large number of experimental studies (Brouwer et al., 1983; Comans and Hockley, 1992; Staunton and Roubaud, 1997; Poinssot et al., 1999; Bradbury and Baeyens, 2000; Zachara et al., 2002; Steefel et al., 2003; de Koning and Comans, 2004; Benedicto et al., 2014; Chen et al., 2014; Missana et al., 2014). Various sorption models were constructed and parametrized to match the measured adsorption isotherms. Analyzing the slopes of the isotherms, it was possible to deduce that Cs sorbs in illite onto at least three different sorption sites. Low-affinity sites with high sorption capacity and high-affinity sites with low sorption capacity were attributed to the basal planes of planar external surfaces and to so-called frayed-edge sites, respectively. The third site with intermediate affinity and capacity, which was identified in some studies only, may be related to the anhydrous interlayer in K-bearing illite having slow exchange kinetics (Comans and Hockley, 1992). The capacity of the planar sites is strongly affected by the pore water chemistry, and especially by the concentrations of Ca and probably other bivalent cations, because these cations induce opening of the collapsed, K saturated interlayers and expose planar sorption sites of the interlayers (Benedicto et al., 2014). At low Cs background concentrations, the high-affinity sites dominate the Cs adsorption. The frayed-edge sites are a result of weathering (Jackson et al., 1948; Fuller et al., 2015). They are characterized by a wedge-like expansion and hydration of the initially anhydrous interlayer close to the edge surface. Sorption (Fuller et al., 2015) and desorption (de Koning and Comans, 2004) of Cs on frayed-edge sites strongly depend on the background electrolyte. Experimental results of Fuller et al. (2015) show that initially unweathered K-illite exhibits no increase in interlayer distances, the interlayers remain collapsed. Exchange of electrolyte solution with Ca leads to an expansion (de-collapsing) of the interlayers in the edge regions and formation of frayed edge sites. Subsequent exchange with a Cs electrolyte solution results in exchange of Ca with Cs at the frayed edge sites and a (re-)collapse of the interlayer in the edge regions. However, the influence of mixed electrolytes as occurring in natural systems as well as the degree of illite compaction on frayed-edge site formation is still not understood. Therefore, it is unclear whether the high-affinity sites are indeed exclusively frayed-edge sites or at least to some degree regular collapsed illite edge sites.

Molecular dynamics simulations are a widely used tool to study ion interactions at the clay-water interface and help in the interpretation of experimental data by providing complementary thermodynamic and structural information at the nano-scale. Edge structures of clays were investigated by *ab initio* MD and DFT simulations (Bickmore et al., 2003; Churakov, 2006; Churakov, 2007). Ion distributions and adsorption properties were determined in MD simulations for basal surfaces of smectites (Tournassat et al., 2009; Bourg and Sposito, 2011) and micas (Bourg et al., 2017) in qualitative agreement with theoretical double and triple layer models. Lammers et al. (2017) performed MD simulations of Cs adsorption on basal, interlayer and edge sites of an illite nano-particle finding Cs residence times on collapsed illite edges in the order of up to tens of nanoseconds. Diffusion coefficients derived from MD simulations in hydrated smectite interlayer (Kosakowski et al., 2008; Bourg and Sposito, 2010) as well as in the vicinity of external basal smectite surfaces (Marry et al., 2008; Tournassat et al., 2009; Bourg and Sposito, 2011; Tinnacher et al., 2016) are typically derived based on the Einstein equation for self-diffusion suggesting that in the long-time limit, the mean squared displacement of a particle is a linear function of time and can be derived from the slope of this curve (Allen and Tildesley, 1987). However, this method requires accurate statistics of the mean squared displacement; it tends to become unfeasible if the particles of interest are trapped in specific low energy configurations and the rate of transition events is very low. In such systems, the method is not practical due to the necessity to simulate long physical trajectories.

If adsorbed atoms form strong surface complexes (at sites with a potential energy minimum) their diffusion behavior at the surface can be described as (rare) jumps from an occupied sorption site to a vacant neighboring site. Jump diffusion models are frequently used to describe diffusion in crystalline solids (Auerbach, 2000; Fang et al., 2020). The surface diffusion coefficient depends on the jump rate, which is determined by the effective attempt frequency, the activation energy barrier and the characteristic jump distance between sorption sites (Gomer, 1990).

The evaluation of Cs diffusion experiments in illite-containing clays at low Cs background concentrations, where the high affinity sites dominate adsorption, suggests that Cs diffusion cannot be explained by a simple Fickian diffusion model for transport in the pore water alone, and a non-zero mobility of Cs on the high-affinity sites is necessary to match the experimental data (Gimmi and Kosakowski, 2011; Krejci et al., 2021). Having a non-zero mobility of a cation on high affinity sorption sites is somewhat counterintuitive. In order to resolve the question whether adsorbed Cs at illite edges maintains a certain diffusive mobility, MD simulations on a stack of illite nanoparticles surrounded by water and Cs were performed using the interatomic potential parameters for the (110) illite edge surface proposed by Lammers et al. (2017). First, the preferred Cs-sorption sites were identified from Cs density profiles. Then, MD simulations with a constraint force method (Allen and Tildesley, 1987) were carried out in order to determine the potential of mean force (PMF) of several complexes at the identified sorption sites. Attempt frequencies and activation energies were derived from the PMFs to estimate the transition rates for surface diffusion. Finally, a surface diffusion coefficient for the illite edge surface was derived by applying a jump diffusion model using an effective medium approach in combination with the determined transition rates.

2 Methods

2.1 System set-up

The simulation supercell contains two TOT layers of an illite particle with the structural formula $24\times[K_{0.67}Al_2(Si_{3.33}Al_{0.67})O_{10}(OH)_2]$ per TOT layer, see Figure 1. Isomorphic Al substitutions for Si were distributed randomly, but avoiding neighboring tetrahedral positions. The (110)-type edges (White and Zelazny, 1988; Bickmore et al., 2003; Churakov, 2006) of the illite particle were created in the same way as in Lammers et al. (2017) (hanging and indented sites), see Figure 2. At pH 10, 100% of $Al(OH)_2$ and 25% of SiOH groups are deprotonated according to the intrinsic acidity of OH groups (Churakov and Liu, 2018). Deprotonated SiO^- were not allowed to be neighbors. In order to satisfy the charge balance of the surface complex, being -1*e* per $Al(OH)^-$ or SiO^-, the partial charges of the six oxygen atoms bonded to Al and of four oxygen atoms bonded to Si were scaled accordingly (the residual charge was distributed equally over the oxygen atoms). The (110) edge surface of illite was constructed to mimic the surface speciation at pH 10 with 834 confining water molecules and 24 Cs atoms resulting in a Cs bulk concentration of 0.52 mol L^{-1}.

2.2 MD simulations

Molecular dynamics simulations with periodic boundary conditions in all dimensions were carried out using the code LAMMPS (Plimpton, 1995) in order to determine Cs sorption density profiles and identify preferred sorption sites. Well-established force fields (FF) describing interactions between the atoms in clay systems were used: the rigid SPC/E FF (Berendsen et al., 1987) for water; the CLAYFF (Cygan et al., 2004) for mineral-water with bond parameters for the illite edges parameterized by Lammers et al. (2017); the Smith-Dang parameters for Cs (Smith and Dang, 1994) and the Dang parameters for K (Dang, 1995).

The system was equilibrated for 2 ns in the NPT ensemble followed by a 60 ns long production run carried out with a time step of 0.5 fs. Pressure and temperature were kept at 0.1 MPa and 298 K, respectively by the Nose-Hoover thermostat and barostat. Long-range coulomb interactions were accounted for using the Ewald summation method with the real space cutoff set to 15 Å. The rigid geometry of water molecules was kept using the SHAKE algorithm (Ryckaert et al., 1977). Hydroxyl OH groups as well as edge surface atoms of oxygen, Al and Si were flexible, while the rest of the clay structure was kept fixed throughout the whole simulation trajectory.

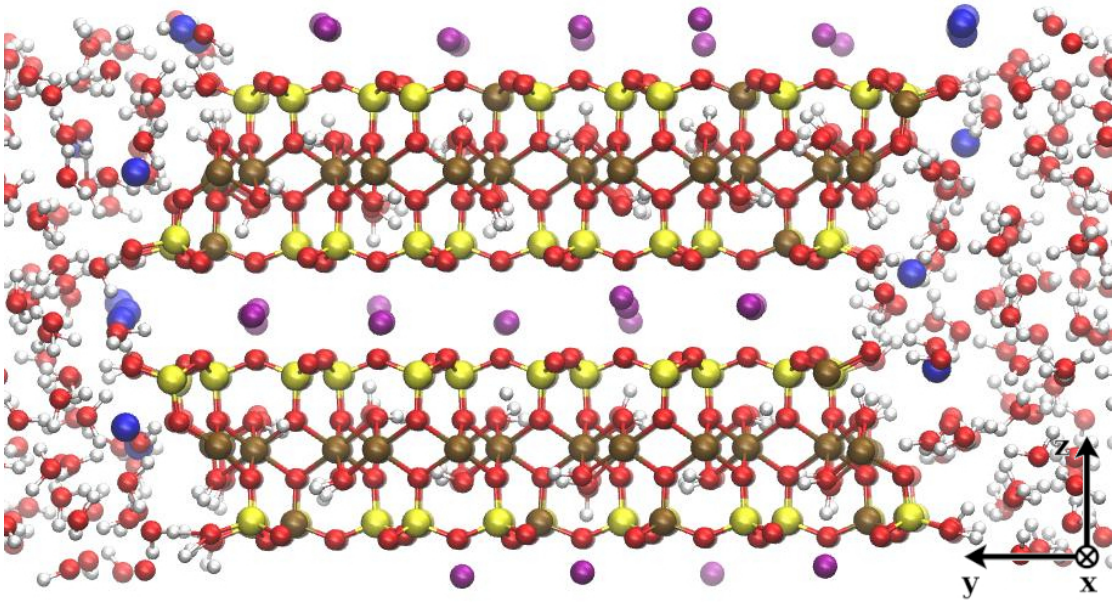

Figure 1: Snapshot of the MD simulation viewed in x-direction of the simulation supercell: The illite particle (Si: yellow, Al: brown, O: red, H: white and interlayer K: purple) in the middle is surrounded by confining water (O: red, H: white) and Cs atoms (blue).

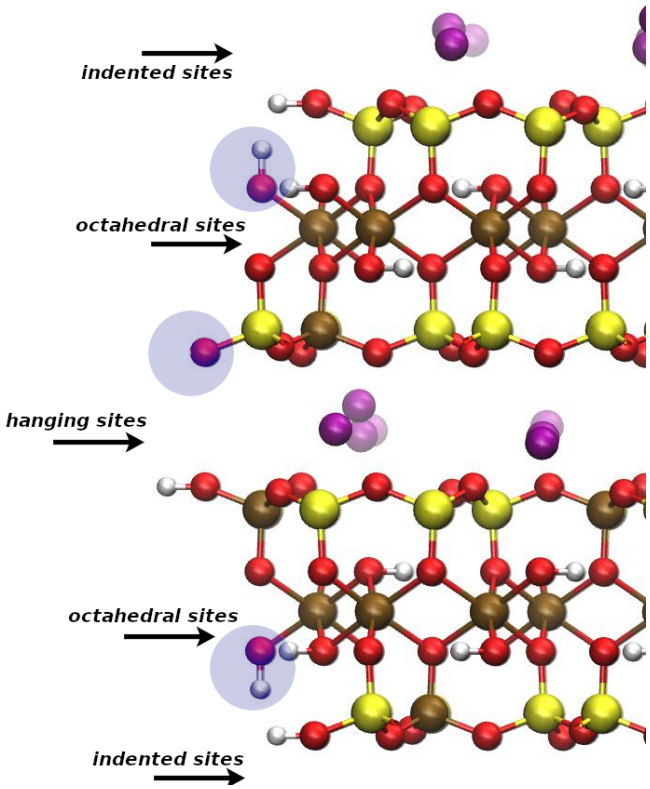

Figure 2: Representation of the illite edge surface structure: Indication of the location of the different sorption sites (hanging, indented and octahedral) and deprotonation (shaded areas).

2.3 Calculation of the potential of mean force

The potential of mean force (PMF) for desorption of different surface complexes of Cs was calculated using a thermodynamic integration method. A sequence of MD simulations, with the component of the Cs coordinate normal to the edge surface fixed at a given distance, were performed. The distance was varied from 0.0 to 8.0 Å with steps of 0.2 Å. For each constrained Cs distance normal to the surface direction a 2 ns run was performed allowing the Cs to move freely in the other directions. The mean force normal to the surface along the reaction coordinate was calculated to derive the potential of mean force $V(\lambda)$ via:

$$V(\lambda)=\int_{o}^{\lambda} -\langle F(x,y,z)\rangle_{\lambda}\, d\lambda \tag{1}$$

where λ is the reaction coordinate and $\langle F(x,y,z)\rangle_{\lambda}$ is the mean force calculated from MD simulations at different positions of the reaction coordinate λ.

2.4 Determination of transition rates

The transition rates Γ_i of a Cs particle leaving a sorption site *i* can be estimated from the profiles of the potential energies, and are described by the Arrhenius law:

$$\Gamma_i=\Gamma_0 \mathrm{e}^{\frac{-E_i^a}{RT}} \tag{2}$$

where Γ_0 is the attempt frequency, E_i^a is the activation energy, T is the temperature and R is the universal gas constant. The activation energy E_i^a is the energy a particle has to overcome to leave the sorption site *i*.

The attempt frequency can be estimated using a harmonic approximation of the potential of mean force in a local minimum corresponding to the adsorbed complex. Here, the harmonic potential is:

$$V(\Delta\lambda)=\frac{1}{2}k\Delta\lambda^2 \tag{3}$$

where k is the force constant and $\Delta\lambda$ is the displacement from the potential minimum. The atomic motion in the harmonic potential is described by:

$$-k\Delta\lambda=\frac{d^2\Delta\lambda}{dt^2} \tag{4}$$

By solving this ordinary differential equation the attempt frequency Γ_0 can be obtained:

$$\Gamma_0=\frac{1}{2\pi}\sqrt{\frac{k}{m^{eff}}} \tag{5}$$

where m^{eff} is an effective mass of the complex which, depending on the diffusion mechanism, may include both the mass of the Cs ion and the H_2O molecules in the first coordination shell.

2.5 Calculation of a jump diffusion coefficient

An effective medium approximation (EMA) is one of several possible approaches to determine the jump surface diffusion coefficient. This concept has been used to describe diffusion in lattice gas models of higher dimensions with disordered site energies or transition rates, respectively (Gartner and Pitis, 1992; Wichmann and Kehr, 1995; Kehr and Wichmann, 1996; Kehr et al., 2005). In order to make use of the effective medium approximation, the edge surface is considered as a two-dimensional square lattice, neglecting the difference in a position normal to the surface as it is small compared to the lateral distances. The solution of self-consistency condition of the EMA provides one effective jump rate, which represents the diffusive system behavior:

$$\left\{ \frac{\Gamma_{eff} - \Gamma_{ij}^{sym}}{(d-1)\Gamma_{eff} + \Gamma_{ij}^{sym}} \right\} = 0 \tag{6}$$

where Γ_{eff} is the effective jump rate of the ion on the surface, Γ_{ij}^{sym} are the symmetric transition rates from site *i* to site *j* (which are calculated from the transition rates Γ_i for the different sorption sites, see below), d is the dimension and the brackets $\{\}$ denote the average over the disordered transition rates Γ_i. An important requirement of this approximation is that the transition rates Γ_i are symmetric. Symmetry of the transition rates can be achieved by applying a detailed balance to the transition rates. For the diffusion of many particles on the square lattice the symmetric transition rates from site *i* to site *j* can be written as (Wichmann and Kehr, 1995; Kehr and Wichmann, 1996; Kehr et al., 2005):

$$\Gamma_{ij}^{sym} = \frac{P_i(1-P_j)}{\{P_i(1-P_i)\}} \Gamma_i \tag{7}$$

where $P_{i,j}$ are the occupancies of site *i* or *j*, respectively.

In the limit of very low surface coverages the system can be approximated by single particle diffusion. Here, the symmetric rates in equilibrium are weighted by the thermal occupancy factors ρ_i:

$$\Gamma_{ij}^{sym} = \rho_i \Gamma_i \tag{8}$$

where ρ_i is inversely proportional to the transition rates Γ_i and written as (Kehr and Wichmann, 1996):

$$\rho_i = \frac{e^{\frac{E_i^a}{RT}}}{\left\{ e^{\frac{E_i^a}{RT}} \right\}} \tag{9}$$

The surface diffusion coefficient can then be calculated using the effective jump rate determined above:

$$D_S = \frac{a^2}{2d} \Gamma_{eff} \tag{10}$$

where a is the average jump length from one site to a neighboring site and *d* is the dimension.

3 Results and discussion

3.1 Cesium distribution on the surface and sorption sites

The probability density maps of Cs and preferential localizations of Cs at the entrance of the anhydrous illite interlayers are shown in Figures 3 and 4. These high affinity Cs positions coincide with the hanging (blue) and indented (red) sorption sites described by Lammers et al. (2017). No entering of Cs into the interlayers was observed during the 60 ns long simulation trajectories. In addition, high density regions were found in the vicinity of the deprotonated $Al(OH)^{-}$-groups with the density peak shifted towards the hanging sites, here referred to as octahedral sorption sites (green). The octahedral sites have not been reported by Lammers et al. (2017). Therefore, we conclude that their existence depends on the deprotonation of the $Al(OH)_2$-groups. Higher Cs densities close to the edge surface are observed up until a y-position of about 6.5 Å from the octahedral edge Al atoms. Beyond this region, the Cs concentration is equal to the one in bulk water, see Figure 3. In total, four hanging, four indented and eight octahedral sorption sites per edge surface were identified, see Figure 4. The location of these positions in the xz-plane are well ordered with almost identical distances between two sorption sites, and the pattern is in good agreement with the crystallographic dimensions in x-direction as the clay structure was built up with four unit cells. The average occupancy of each of the three sorption sites was calculated by counting Cs particles throughout the whole simulation time within a 1.5 Å spherical radius around the center of each sorption site, which was defined by the Cs probability density maximum. Almost 90% of the hanging sites are occupied. At the same time, only 44% of the indented and 25% of the octahedral sites are occupied, respectively (see Table 1). This indicates that Cs has the highest affinity to hanging sites. The sorption affinity is intermediate for the indented sites and the lowest for the octahedral sites. These results are in agreement with Lammers et al. (2017), who also found stronger sorption on hanging sites than on indented sites.

Table 1: Average occupancies of the different sorption sites.

sites	occupancy
hanging	0.89
indented	0.44
octahedral	0.25

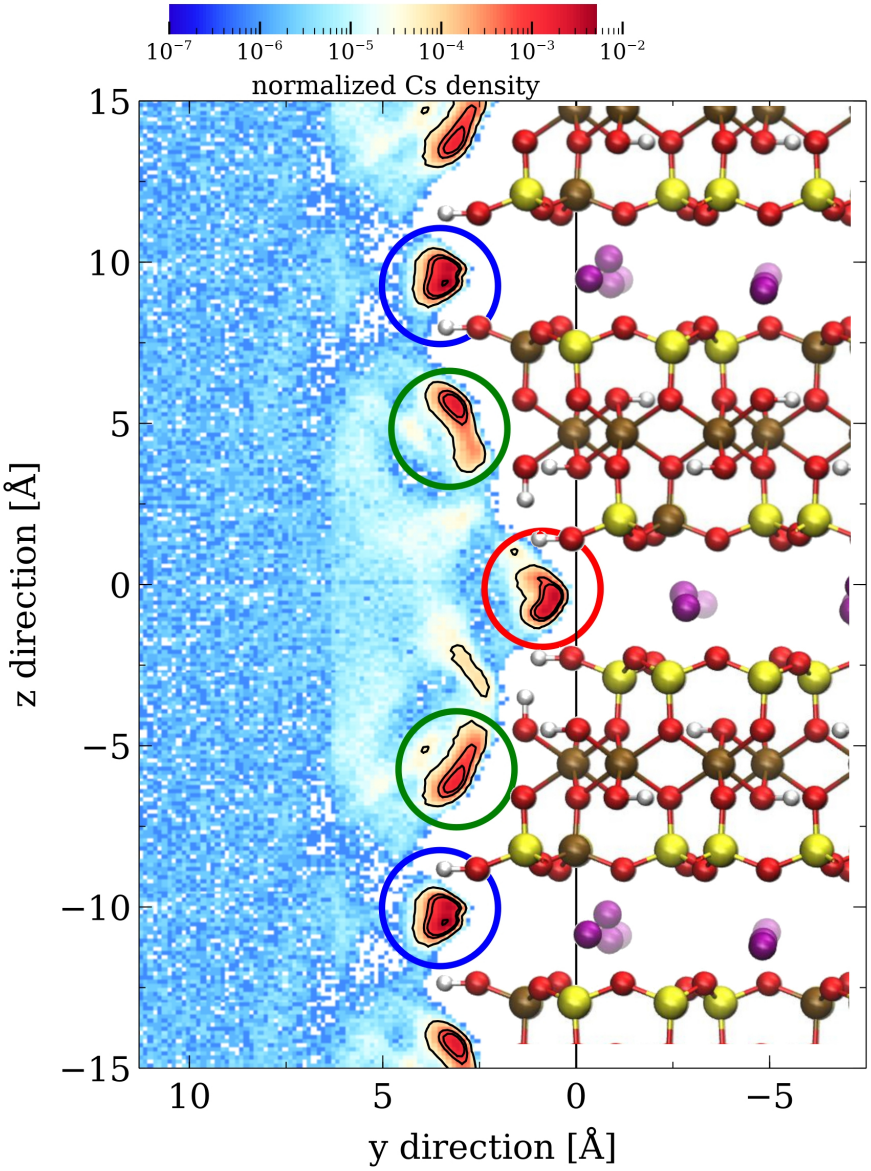

Figure 3: Side view of the illite edge-water interface with the Cs density profile in the yz-plane. The blue circle indicates hanging sites, the red circle indented sites and the green circles octahedral sites. The black vertical line at y = 0 Å denotes the position of octahedral edge Al atoms.

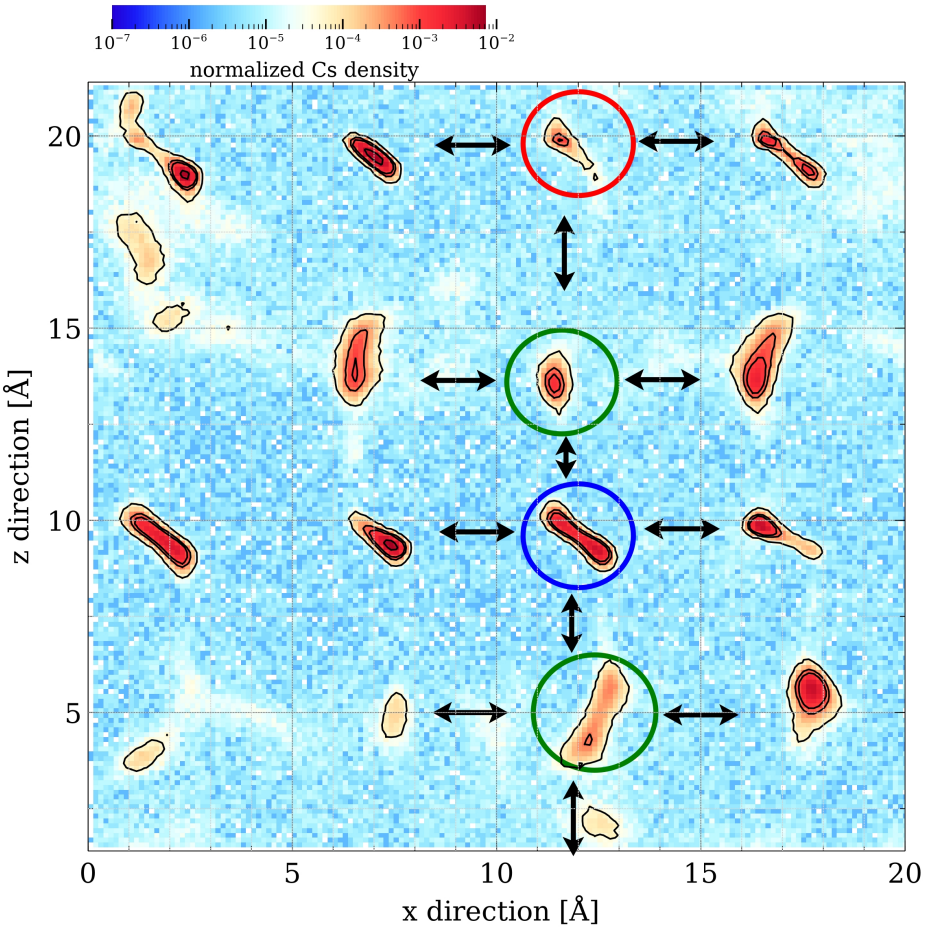

Figure 4: Cs density profile in the xz-plane of the illite particle. The blue circle indicates hanging sites, the red circle indented sites and the green circles octahedral sites (in horizontal direction the sites are the same). The black arrows indicate possible jump pathways to neighboring sorption sites.

3.2 Potential of mean force

For each sorption site four different complexes were randomly picked and the potential of mean force as a function of the distance normal to the surface (in the y-direction, see Figures 1 and 3) was derived by integration of the average forces on Cs ion at the specific locations of the sorption sites, see Eq. (1). The PMF profiles were plotted (Figure 5) as a function of the distance normal to the surface. The reference point located at 0 Å denotes the location of the octahedral Al atoms at the (110) edge (Figure 3).

For the hanging sites, all analyzed complexes exhibit similar PMF profiles (Figure 5a). A distinct minimum is located at about 3.5 Å. The value at the minimum is about −20 to −30 kJ mol^{-1}. The PMF plateaus at zero potential force in the bulk water region at a distance of about 6.5 Å. The PMF for indented sites show a different pattern with a number of local minima and maxima. The first minimum is found at a distance of about 0.8-1.5 Å. For three out of four analyzed complexes, a maximum of the PMF is observed at about 1.8-2.5 Å distance. One of the analyzed complexes does not show a maximum (complex 2). The values of the first minimum of the PMFs of the indented sites exhibit a high variability with values of about −2, −10, −20 and −38 kJ mol^{-1}. For the PMFs with intermediate maximum peaks (i.e., complex 1, 3 and 4, see Figure 5b), a second minimum is found after 2.5-3.5 Å. However, it is difficult to judge the appropriateness of this second minimum because in the MD simulations only the direction normal to the surface was fixed and the Cs atom was allowed to move freely in the other

directions. Therefore, there is the possibility that the investigated Cs atoms moved to the proximity of another (hanging or octahedral) sorption site, which then reflects the second minimum. At 5-6 Å distance bulk water conditions are found. The behavior of octahedral complexes is similar to the hanging sites (Figure 5c), however, the depths of the minima (7-30 kJ mol^{-1}) and minima locations (2.5-3.2 Å) are more variable.

Variations in PMF observed in the simulation can be attributed to the differences in the coordination environment, the protonation state of the surface sites, the charge distribution or even the presence of neighboring sorbed ions. To reveal factors controlling the variability of PMFs, especially for the indented sites, coordination numbers from the corresponding radial distribution functions of the Cs complexes at the minimum of each PMF were calculated for all surface atoms, water and other Cs atoms. The results are shown in the appendix in Figures A1-A3. No clear conclusions could be drawn from the analysis of coordination numbers. For the indented sites this variability may be explained by the deprotonation of a tetrahedral edge oxygen (Figure A2 upper right). For the complex with the deepest minimum (blue line) a deprotonated tetrahedral edge oxygen is close within a distance of 3 Å, while for the complexes with smallest minima (cyan and green lines) the next deprotonated tetrahedral edge oxygen is in a distance of about 7 Å. However, it does not explain the differences with respect to the last complex (red line). Neither any differences for hanging or octahedral sites can be explained by differences in coordination numbers of different surface edge oxygen (Figures A1 and A3).

In order to cross benchmark the PMF calculations with alternative approaches, the PMFs obtained as explained by mean force integration from individual sites were averaged out and compared to the free energy profile corresponding to the average distribution density of Cs ions (Figure 6). The excess free energy F is expressed by

$$\Delta F(y) = RT \ln\left(\frac{C(y)}{C_0}\right) \tag{11}$$

where C_0 is the reference concentration in bulk water and C is the concentration of Cs as a function of the distance to the surface, R is the universal gas constant and T is the temperature.

There is good qualitative and even quantitative (except for the depth of the minima) agreement between both calculations (Figure 6). The averaged PMF obtained by thermodynamic integration shows a deeper minimum in the region about 3.5 Å distance from the surface, where hanging and octahedral sites are present, while the minimum of the indented sites at 1.0 Å is less deep compared to the PMF derived from concentration profiles. Considering the significant standard error of activation energies calculated for indented and octahedral sites (see section 3.3) these differences may be explained by the fact that only 50% of hanging and indented and 25% of octahedral complex sites of the illite clay structure were analyzed for their potential of mean force and the inclusion of all complexes would provide a more precise average.

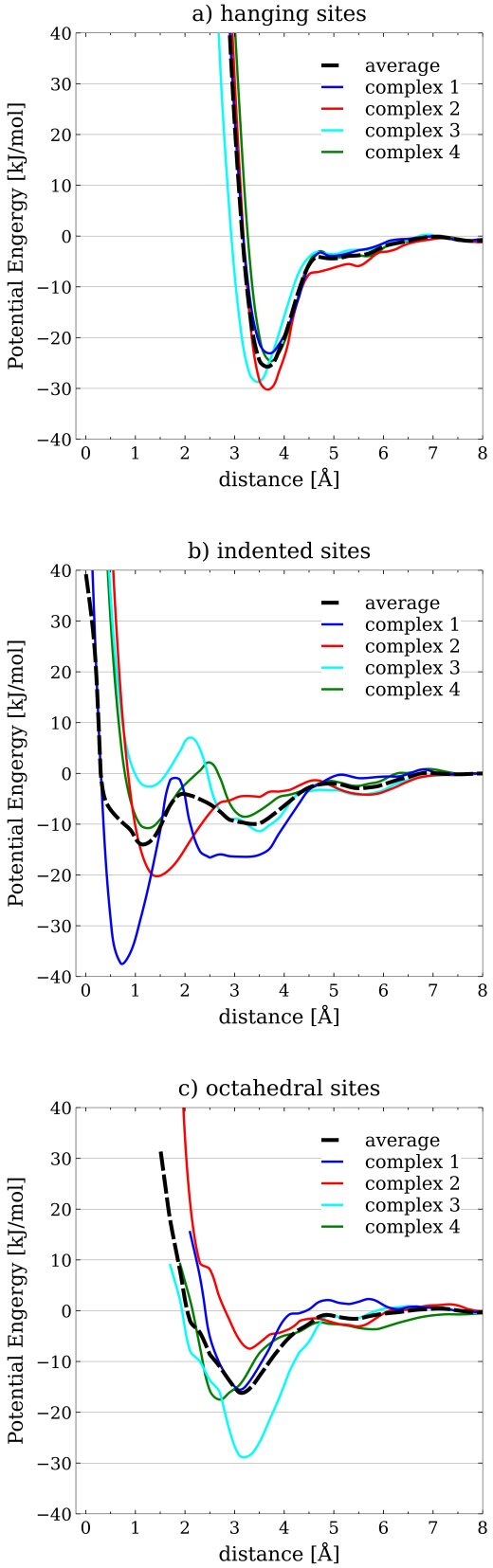

Figure 5: Potential of mean force for four complexes for hanging, indented and octahedral sites and their respective average (black line) with distance from the zero concentration surface at zero Å.

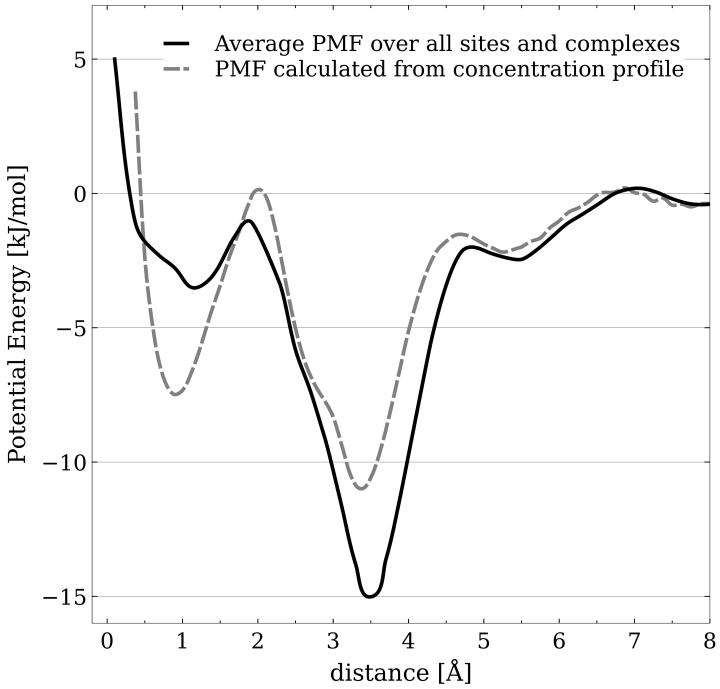

Figure 6: Comparison between averaged PMFs (black line) and the chemical potential calculated from Cs concentrations (grey line).

3.3 Calculation of transition rates

In order to determine the transition rates of a Cs particle leaving a sorption site, at first, the coordination numbers of the first hydration shell CN were calculated from radial distribution functions at the minimum of the PMFs where the complex is located, see Figure A4. Cs complexes at hanging and indented sites were found to be 4-fold coordinated and 7-fold coordinated at octahedral sites. Especially at hanging and indented sites, Cs is significantly less hydrated than in an aqueous solution, where Cs is 8-fold coordinated (Mähler and Persson, 2012). The effective mass of the complex is then calculated by $m^{eff} = m_{Cs} + N\, m_{H_2O}$ with the atomic or molecular mass of Cs of 132.90545 au and H_2O of 18.01494 au. Water in the hydration shell of Cs is weakly bound to the ions, therefore the effective mass m^{eff} is set equal to the atomic mass of Cs to calculate an upper bound estimate of the attempt frequency and respective transition rates (Table A1). The estimation of a lower bound using a CN of eight, equal to the value in the aqueous solution, was not included in the analysis.

To evaluate the attempt frequencies Γ_0 (see Eq. (5)), the minima of the PMFs in Figure 5 were approximated with a harmonic potential (Table 2). The predicted attempt frequencies are very similar for all the sites studied, namely $7.0 \cdot 10^{-11}$ s^{-1}, $8.5 \cdot 10^{-11}$ s^{-1} and $1.0 \cdot 10^{-12}$ s^{-1} for octahedral, indented and hanging sites, respectively.

For indented sites, E_i^a is approximated by the potential difference between the first minimum and the first maximum of the PMFs. For hanging and octahedral sites, E_i^a is assigned to the difference between the minimum of the PMFs and the zero value of potential in the bulk water region (Figure 5 and Table 2). The activation energies are the highest for hanging sites and the lowest for octahedral sites, resulting in the lowest average transition rates for hanging sites and highest for octahedral sites. These results are in qualitative agreement with site occupancies found in section 3.1. Higher activation energies result in lower transition rates, at a site with high activation energy a Cs particle is more likely

to stay at the complex site. Therefore, the occupancy of a low energy site is higher at thermodynamic equilibrium. The critical factor in calculating transition rates is the activation energy as it scales exponentially. So already small differences of E_i^a result in rather high differences of transition rates. The standard error of the attempt frequency E_i^a was calculated for each site and a lower and upper value of the transition rate were calculated in order to account for the variability of E_i^a, Table 2.

Table 2: Attempt frequency, activation energy and resulting transition rate for each investigated complex.

Sites	Attempt frequency Γ_0 [s^{-1}]	Activation energy E_i^a [kJ mol^{-1}]	Standard error of E_i^a [kJ mol^{-1}]	Transition rate Γ [s^{-1}]	Lower bound of Γ [s^{-1}]	Upper bound of Γ [s^{-1}]
hanging	$8.6 \cdot 10^{11}$	23.2	-	$7.4 \cdot 10^{7}$	-	-
	$1.2 \cdot 10^{12}$	30.1	-	$6.5 \cdot 10^{6}$	-	-
	$1.0 \cdot 10^{12}$	28.9	-	$8.7 \cdot 10^{6}$	-	-
	$1.0 \cdot 10^{12}$	24.7	-	$4.8 \cdot 10^{7}$	-	-
Average hanging	$1.0 \cdot 10^{12}$	26.7	1.7	$2.1 \cdot 10^{7}$	$1.1 \cdot 10^{7}$	$4.2 \cdot 10^{7}$
indented	$1.0 \cdot 10^{12}$	36.0	-	$5.0 \cdot 10^{5}$	-	-
	$7.2 \cdot 10^{11}$	18.7	-	$3.8 \cdot 10^{8}$	-	-
	$8.2 \cdot 10^{11}$	9.7	-	$1.7 \cdot 10^{10}$	-	-
	$8.2 \cdot 10^{11}$	12.9	-	$4.6 \cdot 10^{9}$	-	-
Average indented	$8.4 \cdot 10^{11}$	19.3	5.9	$3.5 \cdot 10^{8}$	$3.2 \cdot 10^{7}$	$3.7 \cdot 10^{9}$
octahedral	$6.9 \cdot 10^{11}$	17.9	-	$5.1 \cdot 10^{8}$	-	-
	$6.9 \cdot 10^{11}$	7.5	-	$3.3 \cdot 10^{10}$	-	-
	$8.4 \cdot 10^{11}$	29.4	-	$5.8 \cdot 10^{6}$	-	-
	$6.9 \cdot 10^{11}$	17.5	-	$5.9 \cdot 10^{8}$	-	-
Average octahedral	$7.2 \cdot 10^{11}$	18.1	4.5	$4.9 \cdot 10^{8}$	$8.0 \cdot 10^{7}$	$3.0 \cdot 10^{9}$

3.4 Surface diffusion coefficient

The average transition rates of hanging, indented and octahedral sites were used to calculate Γ_{eff} (Eq. (6)). The black arrows in Figure 4 indicate possible jumps from each site to neighboring sites. It can be easily seen that there is a limited number of types of jumps: one jump hanging to hanging, one indented to indented, one hanging to octahedral and vice versa, one jump indented to octahedral and vice versa and finally two jumps octahedral to octahedral. This set of jumps is representative for the surface and is taken into account calculating Γ_{eff}. Symmetric rates were calculated according to Eq. (7) and Eq. (8) for the actual situation (many particles) and for the low coverage limit case (one particle). In the latter case only four rates were taken into account (one hanging, one indented and two octahedral) as ρ_i only depends on state of the initial site (the denominator in Eq. (9) is the same for all sites). The calculated Γ_{ij}^{sym} were found to be not exactly symmetric in both cases. However, a variation of E_i^a of less than 5% would lead to perfect symmetry. Nonetheless, these values of Γ_{ij}^{sym} were taken to calculate Γ_{eff} via Eq. (6), see Table 3. The effective rate of the mean value calculated for the situation here is $2.2 \cdot 10^8$ s^{-1} and about 3.6 times higher than in the case of the low coverage limit. The reason for that is that sites with a higher E_i^a and therefore lower Γ_i are more likely to be occupied by a Cs atom, so the other Cs atoms in the system jump to sites with lower E_i^a, which results in higher effective rates. Therefore, the surface diffusion coefficient is surface coverage dependent.

At last, the average jump length a has to be determined in order to calculate D_S. One way is to estimate a from the density map in Figure 4. The distance between the sorption sites is about 5 Å within some small variability, also in agreement with the crystal dimensions (4 unit cells in x-direction

with a total width of about 20.8 Å, the dimension of the clay structure in z-direction is 20 Å). In addition, the trajectories of Cs atoms leaving a sorption site, but not entering free bulk water (i.e., which do not cross the boundary at y=6.5 Å in Figure 3), were followed. The results (Figure 7) show that the travel distance after 100-200 ps is limited to 4-5 Å for the hanging and indented sites after a strong increase in the first 50 ps. Cs atoms leaving octahedral sites exhibit slowly increasing travel distance with time and therefore some small mobility within the surface area. The results support the estimated jump length from Figure 4 and an average jump length of 5 Å was taken to calculate the surface diffusion coefficient.

With the model assumptions described above, the surface diffusion coefficient was estimated to be $1.4 \cdot 10^{-11}$ m^2 s^{-1} (Table 3); lower and upper values are $2.3 \cdot 10^{-12}$ m^2 s^{-1} and $8.5 \cdot 10^{-11}$ m^2 s^{-1}, respectively. The ratio to the self diffusion coefficient of Cs in free bulk water leads to a mean relative mobility D_s/D_0 on the illite edge surface of $6.6 \cdot 10^{-3}$. This result is somewhat larger than the value of $1.5 \cdot 10^{-3}$ found for Opalinus Clay by Krejci et al. (2021) and larger than the average value of $5 \cdot 10^{-4}$ compiled from illite diffusion data by Gimmi and Kosakowski (2011). Nevertheless, the calculated value of D_s/D_0 of $1.1 \cdot 10^{-3}$ for the lower limit of the transition rates, as well as the mean value of D_s/D_0 of $1.9 \cdot 10^{-3}$ obtained for the low coverage case, is in good agreement with the one obtained by Krejci et al. (2021), while the lower bound value of $3.4 \cdot 10^{-4}$ for the low coverage case is in good agreement with the average value found by Gimmi and Kosakowski (2011). One reason for the larger mean surface diffusion coefficients found here compared to literature values may be related to the fact that illite occurring in natural systems is exposed to weathering, which can result in a different surface structure compared to the idealized conditions of MD simulations (regular (110) edge). Depending on the pore water solution illite potentially forms frayed-edge sites (Fuller et al., 2015). At these sites interlayers are expanded, which allows hydration of the interlayer and Cs atoms can enter the widened part and get potentially trapped because of successive interlayer collapse. As a result surface diffusion coefficients derived from experimental data in natural clays tend to be lower as they incorporate immobilized Cs at frayed-edge sites. Another reason can be that the continuum-scale approaches used in Gimmi and Kosakowski (2011) and Krejci et al. (2021) assume the same tortuosity for the flow pathways in free bulk water (derived from a water tracer) and along the surfaces. Especially for edge sites, with their complex structure compared to planar (100) surface sites, the actual surface pathways might be more tortuos than those of the free bulk water, which would result in an underestimation of the surface diffusion coefficients. In addition, in natural clay systems different cations, such as e.g., Na and K, are present, which compete with Cs for the occupancy of the sorption sites on illite edges and may cause some blocking effects, which then possibly reduce the Cs mobility at the surface.

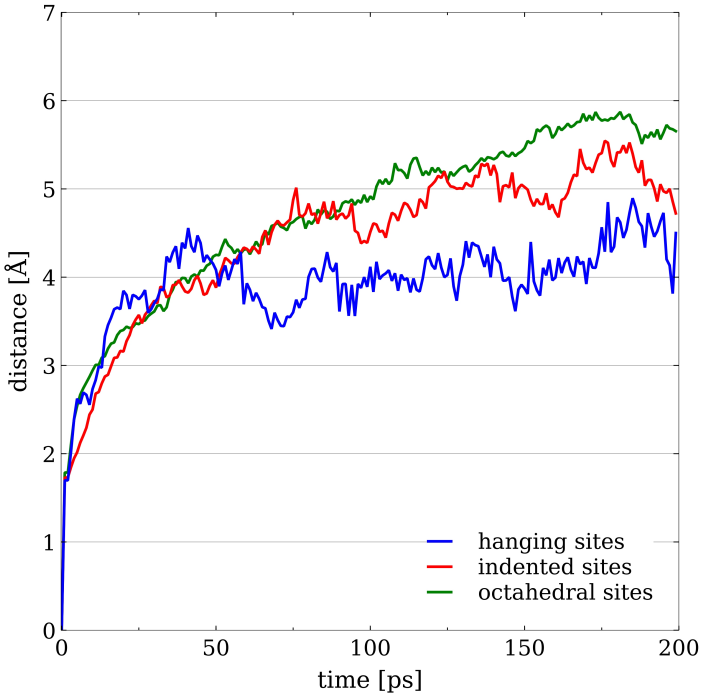

Figure 7: Average travel distance of a Cs atom after leaving a complex (but not entering free bulk water) as a function of time.

Table 3: Effective rate, surface diffusion coefficient and ratio of the Cs surface diffusion coefficient to the self-diffusion coefficient in free bulk water with a value of $2.06 \cdot 10^{-9}$ m^2 s^{-1} (Flury and Gimmi, 2018). Calculated for a many particles case and a single particle case (representation at very low surface coverage).

	Γ_{eff} [s^{-1}]			D_s [m^2 s^{-1}]			D_s/D_0 [-]		
	Mean	Min	Max	Mean	Min	Max	Mean	Min	Max
many particles	$2.2 \cdot 10^{8}$	$3.7 \cdot 10^{7}$	$1.4 \cdot 10^{9}$	$1.4 \cdot 10^{-11}$	$2.3 \cdot 10^{-12}$	$8.5 \cdot 10^{-11}$	$6.6 \cdot 10^{-3}$	$1.1 \cdot 10^{-3}$	$4.1 \cdot 10^{-2}$
single particle	$6.1 \cdot 10^{7}$	$1.1 \cdot 10^{7}$	$3.2 \cdot 10^{8}$	$3.8 \cdot 10^{-12}$	$7.0 \cdot 10^{-13}$	$2.0 \cdot 10^{-11}$	$1.9 \cdot 10^{-3}$	$3.4 \cdot 10^{-4}$	$9.8 \cdot 10^{-3}$

4 Summary and conclusions

The results of the molecular dynamics simulations performed for illite edge surfaces at a pH of 10 revealed that cesium sorbs onto hanging, indented and octahedral sorption sites. Constrained force MD simulations were performed to calculate the potential of the mean force. From the potential profiles, activation energies and attempt frequencies were derived. The different sites are characterized by different activation energies for jump diffusion. The hanging sites have the highest activation energy, while octahedral sites have the lowest. The average transition rate derived for hanging site is more than one order of magnitude lower than the one of the octahedral sites. A surface diffusion coefficient for the illite edge surface was calculated using an effective medium approach. The mean value of the surface diffusion coefficient was found to be larger than the surface diffusion coefficients derived from experimental diffusion data in illite-containing clays. Possible reasons for this discrepancy are that (1) depending on the solution chemistry illite forms frayed-edge sites, where Cs potentially gets immobilized and which may be present in the performed diffusion experiments, (2) the presence of competing ions in the diffusion experiments, which may cause blocking effects, as well as, (3) the methodology of the derivation of surface diffusion coefficients from experimental data, which assumes the same tortuous pathways for both bulk and surface Cs. However, the lower bound values as well as the mean and lower bound values of the low concentration limit case were in good agreement with the published experimental data. Thus, the simulations presented here corroborate the picture that the mobility of cations that compensate surface charges need to be accounted for in transport simulations, even for Cs on illite edge sites.

Transition rates scale exponentially with the activation energies. Therefore, the activation energy is one of the most crucial factor controlling the accuracy of the obtained diffusion coefficient. In this work, the potential of mean force was calculated for only four cesium complexes per sorption site. Therefore, the accuracy of the estimates for diffusion coefficients could be further improved considering a greater number of cesium complexes in a more systematic, but computationally much more expensive study.

The effective medium approximation used in this study is a rather simplified approach. A more rigorous methodology may include kinetic Monte Carlo simulations, e.g., Andersen et al. (2019), where the transition rates determined from the PMFs serve as input.

Finally, different simulations under varying conditions, such as pH, presence of competing ions like K and Cs background concentration should be carried out to capture potential effects on the surface diffusion coefficient.

Acknowledgments

Financial support by the Swiss National Science Foundation (grant no. 200021_166287) is kindly acknowledged.

Appendix

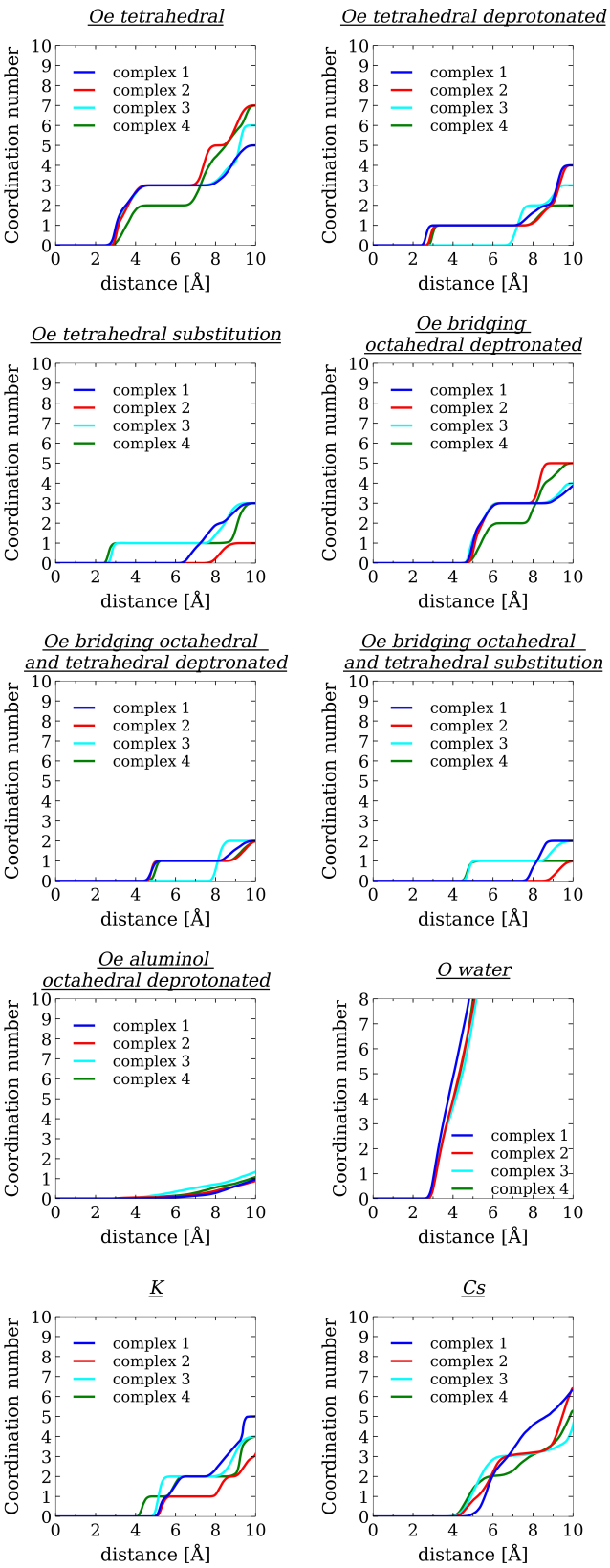

Figure A1: Hanging sites: Coordination numbers at the minimum of the PMF for each complex for all edge surface oxygen, water oxygen, K, Cs.

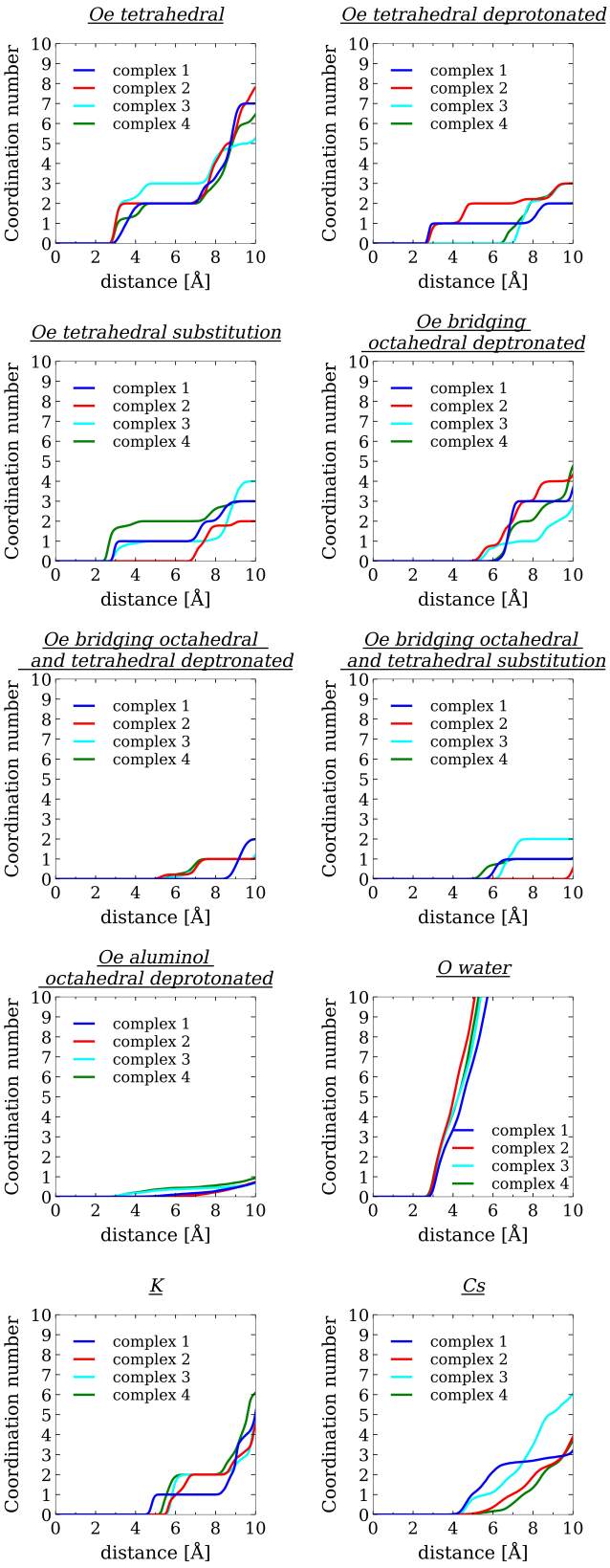

Figure A2: Indented sites: Coordination numbers at the minimum of the PMF for each complex for all edge surface oxygen, water oxygen, K, Cs.

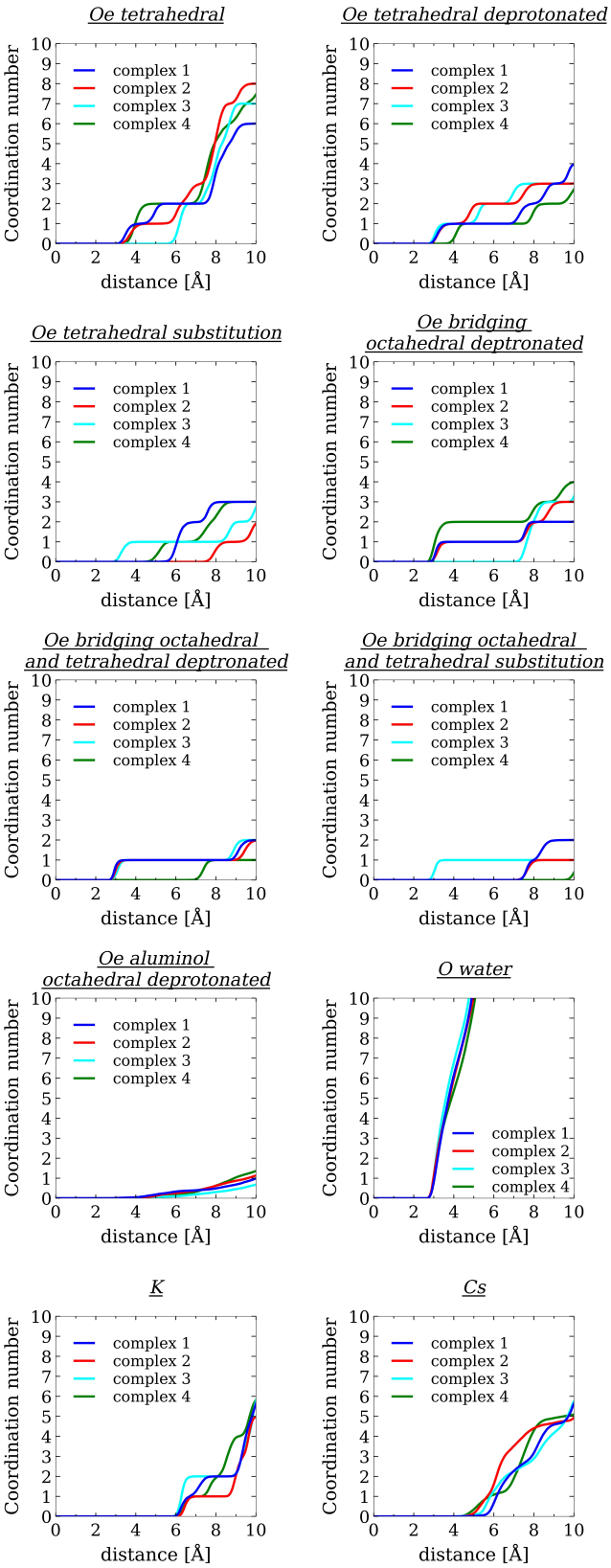

Figure A3: Octahedral sites: Coordination numbers at the minimum of the PMF for each complex for all edge surface oxygen, water oxygen, K, Cs.

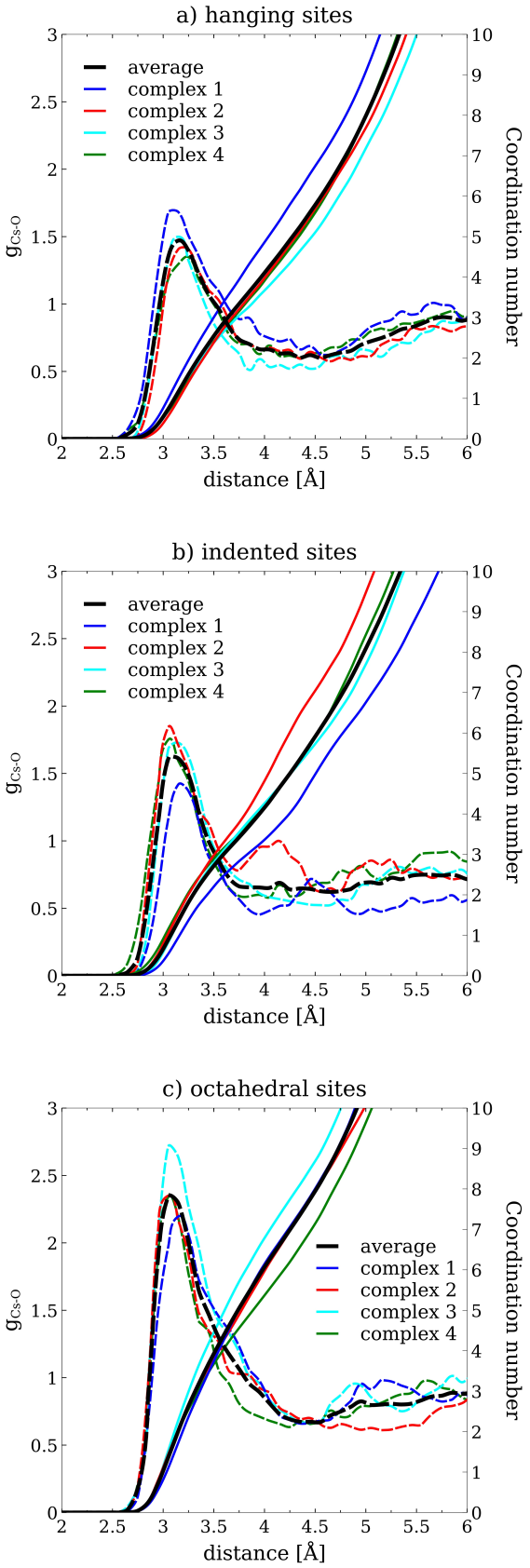

Figure A4: Radial distribution functions (dashed lines) and coordination numbers (full lines) of Cs hydration at the minimum of the PMF for hanging, indented and octahedral sites.

Table A1: Attempt frequency, activation energy and resulting transition rate for each investigated complex for the upper bound case of the attempt frequency where the effective mass equals the atomic mass of Cs.

Sites	Attempt frequency Γ_0 [s^{-1}]	Activation energy E_i^a [kJ mol^{-1}]	Standard error of E_i^a [kJ mol^{-1}]	Transition rate Γ [s^{-1}]	Lower bound of Γ [s^{-1}]	Upper bound of Γ [s^{-1}]
hanging	$1.1 \cdot 10^{12}$	23.2	-	$9.2 \cdot 10^{7}$	-	-
	$1.5 \cdot 10^{12}$	30.1	-	$8.0 \cdot 10^{6}$	-	-
	$1.3 \cdot 10^{12}$	28.9	-	$1.1 \cdot 10^{7}$	-	-
	$1.3 \cdot 10^{12}$	24.7	-	$6.0 \cdot 10^{7}$	-	-
Average hanging	$1.3 \cdot 10^{12}$	26.7	1.7	$2.6 \cdot 10^{7}$	$1.4 \cdot 10^{7}$	$5.2 \cdot 10^{7}$
indented	$1.3 \cdot 10^{12}$	36.0	-	$6.2 \cdot 10^{5}$	-	-
	$9.0 \cdot 10^{11}$	18.7	-	$4.7 \cdot 10^{8}$	-	-
	$1.0 \cdot 10^{12}$	9.7	-	$2.1 \cdot 10^{10}$	-	-
	$1.0 \cdot 10^{12}$	12.9	-	$5.7 \cdot 10^{9}$	-	-
Average indented	$1.0 \cdot 10^{12}$	19.3	5.9	$4.3 \cdot 10^{8}$	$4.0 \cdot 10^{7}$	$4.6 \cdot 10^{9}$
octahedral	$9.6 \cdot 10^{11}$	17.9	-	$7.1 \cdot 10^{8}$	-	-
	$9.6 \cdot 10^{11}$	7.5	-	$4.7 \cdot 10^{10}$	-	-
	$1.2 \cdot 10^{12}$	29.4	-	$8.1 \cdot 10^{6}$	-	-
	$9.6 \cdot 10^{11}$	17.5	-	$8.2 \cdot 10^{8}$	-	-
Average octahedral	$1.0 \cdot 10^{12}$	18.1	4.5	$6.9 \cdot 10^{8}$	$1.1 \cdot 10^{8}$	$4.2 \cdot 10^{9}$

References

Allen M. P. and Tildesley D. J. (1987). *Computer simulation of liquids*., Oxford University Press Inc, New York 1987.

Andersen M., Panosetti C. and Reuter K. (2019). A practical guide to surface kinetic Monte Carlo simulations. *Frontiers in Chemistry* **7**(APR), 1–24. https://doi.org/10.3389/fchem.2019.00202

Auerbach S. M. (2000). Theory and simulation of jump dynamics, diffusion and phase equilibrium in nanopores. *Int. Rev. Phys. Chem.* **19**, 155–198.

Benedicto A., Missana T. and Fernández A. M. (2014). Interlayer collapse affects on cesium adsorption onto illite. *Environ. Sci. Technol.* **48**, 4909–4915.

Berendsen H. J. C., Grigera J. R. and Straatsma T. P. (1987). The missing term in effective pair potentials. *J. Phys. Chem.* **91**, 6269–6271.

Bickmore B. R., Rosso K. M., Nagy K. L., Cygan R. T. and Tadanier C. J. (2003). Ab initio determination of edge surface structures for dioctahedral 2:1 phyllosilicates: Implications for acid-base reactivity. *Clays Clay Miner.* **51**, 359–371.

Bourg I. C., Lee S. S., Fenter P. and Tournassat C. (2017). Stern Layer Structure and Energetics at Mica-Water Interfaces. *Journal of Physical Chemistry* C **121**(17), 9402–9412. https://doi.org/10.1021/acs.jpcc.7b01828

Bourg I. C. and Sposito G. (2010). Connecting the molecular scale to the continuum scale for diffusion processes in smectite-rich porous media. *Environ. Sci. Technol.* **44**, 2085–2091.

Bourg I. C. and Sposito G. (2011). Molecular dynamics simulations of the electrical double layer on smectite surfaces contacting concentrated mixed electrolyte (NaCl-$CaCl_2$) solutions. *J. Colloid Interface Sci.* **360**, 701–715.

Bradbury M. H. and Baeyens B. (2000). A generalised sorption model for the concentration dependent uptake of caesium by argillaceous rocks. *J. Contam. Hydrol.* **42**, 141–163.

Brouwer E., Baeyens B., Maes A. and Cremers A. (1983). Cesium and rubidium ion equilibria in illite clay. *J. Phys. Chem.* **87**, 1213–1219.

Chen Z., Montavon G., Ribet S., Guo Z., Robinet J. C., David K., Tournassat C., Grambow B. and Landesman C. (2014). Key factors to understand in-situ behavior of Cs in Callovo-Oxfordian clay-rock (France). *Chem. Geol.* **387**, 47–58.

Churakov S. V. (2006). Ab initio study of sorption on pyrophyllite: Structure and acidity of the edge sites. *J. Phys. Chem. B* **110**, 4135–4146.

Churakov S. V. (2007). Structure and dynamics of the water films confined between edges of pyrophyllite: A first principle study. *Geochim. Cosmochim. Acta* **71**, 1130–1144.

Churakov S. V. and Liu X. (2018). Quantum-chemical modelling of clay mineral surfaces and clay mineral–surface–adsorbate interactions. In *Developments in Clay Science* (1st ed., Vol. 9). Elsevier Ltd. https://doi.org/10.1016/B978-0-08-102432-4.00003-2

Comans R. N. J. and Hockley D. E. (1992). Kinetics of cesium sorption on illite. *Geochim. Cosmochim. Acta* **56**, 1157–1164.

Cygan R. T., Liang J.-J. and Kalinichev A. G. (2004). Molecular Models of Hydroxide, Oxyhydroxide, and Clay Phases and the Development of a General Force Field. *J. Phys. Chem. B* **108**, 1255–1266.

Dang L. X. (1995). Mechanism and Thermodynamics of Ion Selectivity in Aqueous Solutions of 18-Crown-6 Ether: A Molecular Dynamics Study. *J. Am. Chem. Soc.* **117**, 6954–6960.

Fang T. T., Chen M. I. and Hsu W. D. (2020). Insight into understanding the jump frequency of diffusion in solids. *AIP Adv.* **10**. https://doi.org/10.1063/5.0007178.

Flury M. and Gimmi T. (2018). 6.2 Solute Diffusion. In *Methods of Soil Analysis* (eds. J. H. Dane and G. C. Topp). pp. 1323–1351.

Fuller A. J., Shaw S., Ward M. B., Haigh S. J., Mosselmans J. F. W., Peacock C. L., Stackhouse S., Dent A. J., Trivedi D. and Burke I. T. (2015). Caesium incorporation and retention in illite interlayers. *Appl. Clay Sci.* **108**, 128–134. http://dx.doi.org/10.1016/j.clay.2015.02.008.

Gartner P. and Pitis R. (1992). Occupancy-correlation corrections in hopping. *Phys. Rev. B* **45**, 7739–7749.

Gimmi T. and Kosakowski G. (2011). How mobile are sorbed cations in clays and clay rocks? *Environ. Sci. Technol.* **45**, 1443–1449.

Gomer R. (1990). Diffusion of adsorbates on metal surfaces. *Reports on Progress in Physics* **53***(7)*, 917. https://doi.org/10.1088/0034-4885/53/7/002

Jackson M. L., Tyler S. A., Willis A. L., Bourbeau G. A. and Pennington R. P. (1948). Weathering sequence of clay-size minerals in soils and sediments. I: Fundamental generalizations. *J. Phys. Colloid Chem.* **52**, 1237–1260.

Kehr K. W., Mussawisade K., Schütz G. M. and Wichmann T. (2005). Diffusion of particles on lattices. In *Diffusion in Condensed Matter: Methods, Materials, Models* pp. 745–792.

Kehr K. W. and Wichmann T. (1996). Diffusion coefficients of single and many particles in lattices with different forms of disorder. *Mater. Sci. Forum* **223**–**224**, 151–160.

de Koning A. and Comans R. N. J. (2004). Reversibility of radiocaesium sorption on illite. *Geochim. Cosmochim. Acta* **68**, 2815–2823.

Kosakowski G., Churakov S. V. and Thoenen T. (2008). Diffusion of Na and Cs in montmorillonite. *Clays Clay Miner.* **56**, 190–206.

Krejci P., Gimmi T. and Van Loon L. R. (2021). On the concentration-dependent diffusion of sorbed cesium in Opalinus Clay. *Geochim. Cosmochim. Acta* **298**, 149–166. https://doi.org/10.1016/j.gca.2021.01.012.

Lammers L. N., Bourg I. C., Okumura M., Kolluri K., Sposito G. and Machida M. (2017). Molecular dynamics simulations of cesium adsorption on illite nanoparticles. *J. Colloid Interface Sci.* **490**, 608–620.

Mähler J. and Persson I. (2012). A study of the hydration of the alkali metal ions in aqueous solution. *Inorg. Chem.* **51**, 425–438.

Marry V., Rotenberg B. and Turq P. (2008). Structure and dynamics of water at a clay surface from molecular dynamics simulation. *Phys. Chem. Chem. Phys.* **10**, 4802–4813.

Missana T., García-Gutiérrez M., Benedicto A., Ayora C. and De-Pourcq K. (2014). Modelling of Cs sorption in natural mixed-clays and the effects of ion competition. *Appl. Geochemistry* **49**, 95–102. http://dx.doi.org/10.1016/j.apgeochem.2014.06.011.

Plimpton S. (1995). Fast Parallel Algorithms for Short – Range Molecular Dynamics. *J. Comput. Phys.* **117**, 1–19. http://lammps.sandia.gov.

Poinssot C., Baeyens B. and Bradbury M. H. (1999). Experimental and modelling studies of caesium sorption on illite. *Geochim. Cosmochim. Acta* **63**, 3217–3227.

Ryckaert J. P., Ciccotti G. and Berendsen H. J. C. (1977). Numerical integration of the cartesian equations of motion of a system with constraints: molecular dynamics of n-alkanes. *J. Comput. Phys.* **23**, 327–341.

Smith D. E. and Dang L. X. (1994). Computer simulations of cesium-water clusters: Do ion-water clusters form gas-phase clathrates? *J. Chem. Phys.* **101**, 7873–7881.

Staunton S. and Roubaud M. (1997). Adsorption of ^{137}Cs on montmorillonite and illite: Effect of charge compensating cation, ionic strength, concentration of Cs, K and fulvic acid. *Clays Clay Miner.* **45**, 251–260.

Steefel C. I., Carroll S., Zhao P. and Roberts S. (2003). Cesium migration in Hanford sediment: A multisite cation exchange model based on laboratory transport experiments. *J. Contam. Hydrol.* **67**, 219–246.

Tinnacher R. M., Holmboe M., Tournassat C., Bourg I. C. and Davis J. A. (2016). Ion adsorption and diffusion in smectite: Molecular, pore, and continuum scale views. *Geochim. Cosmochim. Acta* **177**, 130–149.

Tournassat C., Chapron Y., Leroy P., Bizi M. and Boulahya F. (2009). Comparison of molecular dynamics simulations with triple layer and modified Gouy-Chapman models in a 0.1 M NaCl-montmorillonite system. *J. Colloid Interface Sci.* **339**, 533–541. http://dx.doi.org/10.1016/j.jcis.2009.06.051.

White G. N. and Zelazny L. W. (1988). Analysis and Implications of the Edge Structure of Dioctahedral Phyllosilicates. *Clays Clay Miner.* **36**, 141–146.

Wichmann T. and Kehr K. W. (1995). Effective medium theory of collective diffusion of lattice gases in lattices with site energy disorder. *J. Phys. Condens. Matter* **7**, 717–730.

Zachara J. M., Smith S. C., Liu C., McKinley J. P., Serne R. J. and Gassman P. L. (2002). Sorption of Cs^+ to micaceous subsurface sediments from the Hanford site, USA. *Geochim. Cosmochim. Acta* **66**, 193–211.

Chapter 6:
Summary, conclusions and suggestions for future work

In this thesis, diffusion of sorbing cations in clays was investigated, with a main focus on the diffusive mobility of sorbed cations, that is, of cations that are compensating the negative surface charges of clay minerals. While most reactive transport models consider the sorbed species as immobile, this view is in contradiction with many experimental studies of diffusive transport of cations in clays.

At first, a multi-site surface diffusion model was implemented in the continuum-scale reactive transport code Flotran (chapter 2). This model combines the contributions of pore diffusion and the diffusion processes on the clay surfaces in a single diffusion coefficient, which includes surface mobilities as model parameters. The multi-site surface model uses the total (water accessible) porosity and the geometrical factor derived from a water tracer as primary, independent input. The surface mobilities of the different sites are then used as fit parameters to match experimental data. This model was applied to diffusion data of Cs in Opalinus Clay (chapter 2), of Na and Sr in Opalinus Clay (chapter 4), and of Na, Sr and Cs in Volclay bentonite (chapter 3).

As a second step, a more detailed model that accounts for diffusion in 'free' pore water, in the diffuse layer, in the Stern layer and in interlayers (DL-SL-IL model) was implemented in Flotran (chapter 3). It represents a multi-porosity model, but it can also be viewed as a dual porosity model for 'free' uncharged pore water and diffuse layer water, while the contributions of Stern and interlayer are modeled via cation exchange reactions with exchanged ions that have a certain mobility. From this model, a combined diffusion coefficient can be derived (when assuming local equilibrium), which can be directly compared to experimentally determined diffusion coefficients, that is, diffusion coefficients derived from the application of a single-species model using Fick's law. Predictions of the DL-SL-IL model for Na, Sr and Cs diffusion were compared to experimental data of Volclay bentonite (chapter 3) and Opalinus Clay (chapter 4). In chapter 4, effects of assuming different activity coefficients for diffuse layer ions compared to those in free bulk water were also briefly investigated.

Thirdly, the mobility of Cs at illite edge surfaces was investigated by performing molecular dynamics simulations (chapter 5). From these simulations, various Cs adsorption sites in the edge region were identified. Constrained forces MD simulations were used to calculate the potential of mean force (PMF) at the different sites, from which activation energies and attempt frequencies were determined, which in turn were used to calculate a jump diffusion coefficient of Cs at the various illite edge surface sites.

In the following, results of the application of (1) the multi-site surface diffusion model and (2) the DL-SL-IL model to experimental data, as well as the results of (3) the MD simulations of Cs interactions with the illite edge surface are summarized and discussed. At the end of this chapter, possibilities for future research are highlighted.

The multi-site surface diffusion model was successfully applied to Na, Sr and Cs diffusion data in Opalinus Clay and Volclay bentonite. Importantly, this model allowed to describe the concentration-dependent diffusion of Cs in Opalinus Clay (Chapter 2). For Cs, three sorption sites were used following literature data (planar sites, type II sites, frayed-edge sites). A mobility of sorbed Cs on the planar sites as well as on the frayed-edge sites in Opalinus Clay was required to match the diffusion data at different Cs background concentrations. It is somewhat surprising that a mobility of sorbed Cs on the frayed-edge sites had to be assigned, because of the strong surface interaction of Cs expressed by the large selectivity coefficient for these sites. However, the data could not be modeled satisfactorily without assigning a mobility of the frayed-edge site ions. Diffusion of Na and Sr in Opalinus Clay (Chapter 4) was well described with a one-site sorption model (planar sites only), including a mobility of the sorbed cations on the planar sites. The results of Na diffusion revealed that the surface mobility shows an additional anisotropy compared to pore diffusion of a HTO tracer, when evaluating diffusion data parallel and perpendicular to the bedding of Opalinus Clay. Surface mobilities were reduced more than 25% in the direction perpendicular to bedding compared to that parallel to bedding, leading to an

overall stronger anisotropy for Na as compared to HTO. The diffusion and adsorption behavior of Na, Sr and Cs in Volclay bentonite (Chapter 3) was well described when applying the surface diffusion model with a one-site cation exchange model including a surface mobility of the sorbed ions. The surface mobility determined from the data varied for each cation and decreased for all cations with increasing bentonite dry density.

The combined diffusion coefficients of the multi-site sorption and surface diffusion model, with mobilities adapted according to the data, are essentially identical to the directly fitted effective diffusion coefficients of the classical Fickian model. The application of the classical Fickian model results in comparably large cation diffusion coefficients and thus comparably low fitted geometrical factors. These geometry factors then vary for each cation and also differ from those of a water tracer to a different degree, depending on the bulk dry density of the bentonite (or also the ionic strength of the pore solution). This is physically not meaningful. The advantage of the surface diffusion model compared to a classical Fickian diffusion model is that it describes the phenomenon of increased cation diffusion in a more fundamental, but still simple way by accounting for the diffusion processes of sorbed cations. However, the required model parameter, the surface mobility, is still a phenomenological parameter, which varies with the clay dry density (chapter 3), pore water chemistry (chapter 4) or type of clay. For instance, Gimmi and Kosakowski (2011) showed that there is a specific average mobility for each cation, but within a somewhat broad range. Three factors contribute to the observed broad range. One factor is the experimental uncertainty and the natural heterogeneity of the investigated clay samples. The second is that diffusion and sorption data used in this study was mostly derived from tracer transport of single species, where analytical solutions assuming linear adsorption could be used. While this analysis accounts for the effect of the pore water ionic strength on the distribution coefficient, it does not consider the detailed pore water chemistry, which leads for instance to the formation of aquatic complexes with different diffusion coefficients as well as possibly different charge and different sorption properties. This can lead to significant differences in distribution coefficients and also significant differences in estimated surface mobilities. Thirdly, the estimated surface mobility can be seen as an overall mobility including all additional diffusion processes on the surface of clays. The distribution of cations between Stern and diffuse layer depends on the pore water chemistry (ionic strength, types of background ions, type of clay). This leads to varying contributions of diffuse and Stern layer diffusion, and therefore likely to a variation of estimated ‘average’ surface mobilities. Overall, the surface diffusion model is a useful and simple tool to describe cation diffusion in clays approximately, provided that surface mobilities were derived for the conditions of interest. It is, however, not able to predict variable cation diffusion under varying conditions, as shown in Chapters 3 and 4 for different bentonite dry densities and pore waters as well as for Opalinus Clay samples from Benken and Mont Terri.

The more sophisticated DL-SL-IL model allows for a more detailed description and analysis of cation diffusion in clays under varying geochemical conditions. It could be successfully applied to diffusion data in Volclay bentonite and Opalinus Clay. Remarkably good agreement with the experimental data was achieved in Volclay bentonite, where the effect of different bentonite dry densities and pore waters on the cation diffusion coefficients were well explained. This is a promising result with respect to the predictive capabilities of the model. The agreement between the DL-SL-IL model with cation diffusion data in Opalinus Clay was also satisfactory; however, these results have to be treated with some caution, because neither the charge distribution between diffuse and Stern layer in the illite fraction of Opalinus Clay nor the ion-specific mobilities in the illite Stern layer and the interlayers of illite-smectite mixed layer minerals are known. Both were adapted from the values for Volclay bentonite (Chapter 3). The investigation of the dependency of the diffusion coefficients of anions and cations on the variation of the activity coefficient in the diffuse layer (chapter 4) revealed that the variation has a more

pronounced effect on Cl and Sr diffusion, while Na and Cs are less influenced by the variation of the activity coefficient. The model results also revealed that for both, Volclay bentonite and Opalinus Clay, Stern layer diffusion provides a significant contribution to the diffusive flux, which should not be neglected. Especially for Cs in Volclay bentonite and Opalinus Clay and for Sr in Volclay bentonite, Stern layer diffusion was found to be more important than diffusion in the diffuse layer.

In experimental scenarios with constant background pore water concentrations (as is the case in chapter 3 and 4), the combined diffusion coefficient for the DL-SL-IL model can in principle be calculated independently of the experiment (forward simulation, prediction), by calculating Donnan equilibria in order to determine diffuse layer concentrations and distribution of cations between diffuse and Stern layer. The downside of such a detailed model is that it needs more information to be supplied in order to generate useful output. Specifically, the DL-SL-IL model relies on parameters such as total (water accessible) porosity and geometrical factor (here taken from HTO diffusion), anion accessible porosities at different ionic strength to constrain the contributions of different pore environments (here given by Cl diffusion data), a cation adsorption model (i.e., cation selectivities, cation exchange capacity and charge distribution between diffuse and Stern layer; here taken from literature data), microstructural data (i.e., distribution of interlayer porosities, reactive surface area and clay layer stack sizes; here taken from literature data) and ion-specific mobilities in the different pore environments (here taken from results of MD studies). These data, however, can be sparse and/or are associated with some uncertainty. The anion accessible porosities in Volclay bentonite, for example, exhibit a significant uncertainty (Van Loon et al., 2007). Even though a microstructural model could be built up for Volclay bentonite (chapter 3) and Opalinus Clay (chapter 4), the detailed knowledge about the pore structures of Volclay bentonite and Opalinus Clay for varying clay dry density and background pore water solutions is rather limited. Especially, knowledge on the pore-size distributions of external pores in Volclay bentonite, as well as on the pore network connectivity in Opalinus Clay, is not sufficient. Therefore, some uncertainty remains by applying these microstructural models. One can argue that the better predictability that one gains in principle with such more complex, more process-based models has to be paid off by uncertainty regarding the required input parameters. Nevertheless, it is believed that such models considerably contribute to the understanding of the underlying processes, even though they certainly still have many limitations.

Three important (critical) assumptions have been made when applying the DL-SL-IL model to Volclay bentonite and Opalinus clay diffusion data. The first assumption is that the mobility of water in the entire external pore space is set to one (i.e., same bulk diffusion coefficient as in 'free' pore water). However, the mobility of water in the Stern layer (surface bound water) is smaller than one and it reduces the overall mobility of water in a pore significantly (the smaller the pore, the higher the contribution of the surface bound water). For example, MD simulation results of Holmboe and Bourg (2014) showed the overall mobility in a ten water-layer-wide smectite pore is about 0.8. The lack of knowledge of the exact pore-size distribution of external pores prohibits an accurate estimation of an average water mobility in the external pores. The second assumption was that the diffuse layer mobility of all tracers is the same as that in free bulk water. This is not entirely correct, as the mobility of all tracers is slightly decreased (~0.9) in the diffuse layer according to results of MD simulations (Tournassat et al., 2009). However, this effect is not of a significant importance. The third assumption that was made in the application of the DL-SL-IL model, as well as in the multi-site surface diffusion model, is that the tortuous pathway along the surfaces (for all sorbed ions) is approximately the same as that in bulk water. Unfortunately, it is rather difficult to judge the validity of this assumption. Even though pore and surface pathways are in close contact, the pore surface might exhibit some roughness (clay particles not perfectly aligned parallel to the pore direction), which can create differences in the tortuous pathways especially in larger pores, where the tortuous pathway is mainly influenced by the

overall pore direction and not by the local direction of the clay mineral surface. Additionally, pores can have extents corresponding to multiple clay particles (lateral sizes of clay layers). This means that diffuse layer, Stern layer and interlayer may not be continuously connected along the axis parallel to the pore but can potentially be interrupted, which could be translated into a longer tortuous pathway for diffuse layer, Stern layer and interlayer compared to the tortuous pathway of bulk water.

In order to shed some light on the Cs mobility found for the frayed-edge sites of the illite fraction in Opalinus Clay (Chapter 2), MD simulations were performed investigating Cs interactions with illite (110) edge surfaces (Chapter 5). A novel approach was used to determine the Cs diffusion coefficient at the illite edge surface. The methodology of this approach includes the calculation of the PMF for different Cs surface complexes, from which attempt frequencies and activation energies for jump diffusion were derived. Finally, a Cs diffusion coefficient at the illite edge surface was calculated using an effective medium approximation. A significant mobility of Cs on the illite edge sites was found which is comparable, but somewhat larger than values found in chapter 2 or in Gimmi and Kosakowski (2011). As already stated in the last paragraph, the tortuous pathway may be influenced by the surface roughness and disconnection of pore environments. This effect then would be particularly pronounced for clay particle edges, as they do only have a small surface area, which is rather discontinuous. This has to be kept in mind in the direct comparison of the diffusion coefficient or mobility derived here by MD simulations and that derived from experimental data. Even though this new approach generated promising results, there is a potential for further improvement. Firstly, the approach would benefit from better statistics, meaning that a larger number of surface complexes should be evaluated, which would decrease the uncertainty of the derived activation energies significantly. Secondly, the application of Monte-Carlo simulations rather than an effective medium approximation would lead to more robust results, as the three-dimensional edge surface structure as well as the influence of interaction with competing ions could be accounted for. With these improvements, the presented approach may be a powerful tool to investigate situations where diffusion processes are dominated by rare events.

Overall, useful models were extended, newly developed and implemented, from which detailed insights on cation diffusion in clays were gained. The outcome of this work can help to improve the prediction of radionuclide transport in the envisaged multi-barrier system in underground nuclear waste disposal and therefore improve long-term safety considerations.

Nevertheless, further research is necessary to improve the models here proposed for cation diffusion in clays. First of all, the multi-site surface diffusion model should be applied and tested for data of other cations, for example transition metals, which exhibit pH-dependent edge sorption on OH-functional groups.

In the current implementation state the DL-SL-IL model only allows for calculations with constant background concentrations of the pore solutions, as the diffuse layer porosity is fixed throughout the simulations. By coupling the DL porosity to the pore water chemistry, as for example done in CrunchFlow (Soler et al., 2019), the model could be applied to data of experiments with varying background concentrations.

A further improvement of both the multi-site surface diffusion model and the DL-SL-IL model would be the replacement of the implicit approach of a combined diffusion coefficient with an approach that considers cations in the adsorbed phase explicitly as an own species in solution or, more generally, in the balance volume. In this case, diffusion coefficients could be directly attributed to the surface species. This approach would be more versatile. It could incorporate kinetic sorption reactions, because there is no need for the assumption of local equilibrium between the pore solution and all surface phases. In addition, this approach would offer additional possibilities for modeling advective

transport by introducing phase-specific or ion-specific advective mobilities, and therefore also for the evaluation of experimental data of percolation experiments (Chen et al., 2018).

The determination of ion specific mobilities in the Stern layer and in interlayer by MD simulations is a necessary step to generate more robust results when applying the DL-SL-IL model. Mobility data for Sr and Cs in Stern layer and interlayer has to be improved and produced for Volclay bentonite, or generally for montmorillonite. Especially, for the application of the model in Opalinus Clay, no detailed information of charge distribution between Stern layer and diffuse layer as well as regarding cation mobilities in the different pore environments is available, and a series of assumptions had to be made. Therefore, the investigation of charge distribution and cation mobilities on illite surfaces should be the subject of further MD studies. In addition, a discrimination between inner- and outer-sphere complexes (distribution and mobility) may be a further and necessary refinement of the model, which could also be studied through MD simulations.

Last but not least, the effects of a potentially more tortuous surface pathway for water and ions should be quantified. This may be done using an up-scaling approach (Churakov and Gimmi, 2011; Gimmi and Churakov, 2019) where pore scale mobilities for different pore locations (bulk, basal external surface, edge surfaces and interlayer) derived from MD simulations are taken as input for random-walk simulations for simplified or realistic pore structures. From such simulations, geometrical factors for different ions in different types of pore structures can be calculated and compared with each other. This leads to insights into the contributions of different pore environments to the overall transport depending on their connectivities, and, for instance, derived geometrical factors of water, anion and cation tracers could be compared with each other as well as with those derived from experimental data.

References

Chen Y., Glaus M. A., Van Loon L. R. and Mäder U. (2018). Transport of low molecular weight organic compounds in compacted illite and kaolinite. *Chemosphere* **198**, 226–237. https://doi.org/10.1016/j.chemosphere.2018.01.137

Churakov S. V. and Gimmi T. (2011). Up-scaling of molecular diffusion coefficients in clays: A two-step approach. *Journal of Physical Chemistry C* **115**(14), 6703–6714. https://doi.org/10.1021/jp112325n

Gimmi T. and Kosakowski G. (2011). How mobile are sorbed cations in clays and clay rocks? *Environmental Science and Technology* **45**(4), 1443–1449. https://doi.org/10.1021/es1027794

Gimmi T. and Churakov S. V. (2019). Water retention and diffusion in unsaturated clays: Connecting atomistic and pore scale simulations. *Applied Clay Science* **175**, 169–183. https://doi.org/10.1016/j.clay.2019.03.035

Holmboe M. and Bourg I. C. (2014). Molecular dynamics simulations of water and sodium diffusion in smectite interlayer nanopores as a function of pore size and temperature. *Journal of Physical Chemistry C* **118**(2), 1001–1013.

Soler J. M., Steefel C. I., Gimmi T., Leupin O. X. and Cloet V. (2019). Modeling the Ionic Strength Effect on Diffusion in Clay. the DR-A Experiment at Mont Terri. *ACS Earth and Space Chemistry* **3**(3), 442–451. https://doi.org/10.1021/acsearthspacechem.8b00192

Tournassat C., Chapron Y., Leroy P., Bizi M. and Boulahya F. (2009). Comparison of molecular dynamics simulations with triple layer and modified Gouy-Chapman models in a 0.1 M NaCl-montmorillonite system. *Journal of Colloid and Interface Science* **339**(2), 533–541. https://doi.org/10.1016/j.jcis.2009.06.051

Van Loon L. R., Glaus M. A. and Müller, W. (2007). Anion exclusion effects in compacted bentonites: Towards a better understanding of anion diffusion. *Applied Geochemistry* **22**(11), 2536–2552. https://doi.org/10.1016/j.apgeochem.2007.07.008

Declaration of consent

Erklärung

gemäss Art. 18 PromR Phil.-nat. 2019

Name/Vorname:	Krejci Philipp
Matrikelnummer:	08-912-834
Studiengang:	Earth Sciences

Bachelor ☐ Master ☐ Dissertation ☑

Titel der Arbeit:	Diffusion of sorbed cations in clays: Development, improvement and application of new and existing models
LeiterIn der Arbeit:	PD Dr. Thomas Gimmi

Ich erkläre hiermit, dass ich diese Arbeit selbständig verfasst und keine anderen als die angegebenen Quel-len benutzt habe. Alle Stellen, die wörtlich oder sinn-gemäss aus Quellen entnommen wurden, habe ich als solche gekennzeichnet. Mir ist bekannt, dass andern-falls der Senat gemäss Artikel 36 Absatz 1 Buchstabe r des Gesetzes über die Universität vom 5. September 1996 und Artikel 69 des Universitätssta-tuts vom 7. Juni 2011 zum Entzug des Doktortitels be-rechtigt ist.
Für die Zwecke der Begutachtung und der Überprüfung der Einhaltung der Selbständigkeitserklärung bzw. der Reglemente betreffend Plagiate erteile ich der Univer-sität Bern das Recht, die dazu erforderlichen Perso-nendaten zu bearbeiten und Nutzungshandlungen vor-zunehmen, insbesondere die Doktorarbeit zu vervielfäl-tigen und dauerhaft in einer Datenbank zu speichern sowie diese zur Überprüfung von Arbeiten Dritter zu verwenden oder hierzu zur Verfügung zu stellen.

Zürich, 16.01.2023

Ort/Datum

P. Krejci

Unterschrift